Photochemistry and Photophysics of Chemical and Biologically Relevant Systems: Mechanisms, Dynamics and Methodologies

Tesis Doctoral que presenta:
Marco Marazzi

Director de la Tesis Doctoral:
Luis Manuel Frutos Gaite

UNIVERSIDAD DE ALCALÁ
DEPARTAMENTO DE QUÍMICA I
Doctorado en Química Fina

2012

Acknowledgments

First and foremost, I would like to thank my Ph.D. advisor, Luis Manuel. Everything started with a proposal of a Ph.D. project written on a napkin, while drinking some wine on the hills in the nearby of Vienna, during a summer school. I signed that napkin, and I will never regret. Without his scientific guide, made of continuous suggestions and fruitful discussions, this Thesis could not be written.

Also, I thank all former and present members of the RESMOL group. Especially, Obis for his high level intellectual speeches (in different possible languages), Felipe, Manuel, Cris and Alessio for the constant and productive exchange of ideas.

A special thank goes to Roland Lindh, Massimo Olivucci and Mark A. Ratner, who hosted me during my research stays out of Spain, respectively at Uppsala University (Uppsala, Sweden), Bowling Green State University (Bowling Green, Ohio, USA) and Northwestern University (Evanston, Illinois, USA). In BGSU, I am grateful to Samer for his help and useful discussions while at the lab.

My family cannot be out of this list: my mother, my father, my grandmother and my brother are always present when I need them.

For sure I have to mention Jimmy, who was able to stand my "typical theoretician attitudes" at home, apart from a usually hyperactive behavior.

Again, I would like to thank Cris (and maybe also Swedish winter...) for her constant presence and support.

Contents

Prologue

It seems to me that just some days have passed since my first excited-state calculation, a couple of months after starting my Ph.D. program: it was a 2+2 face-to-face cycloaddition of two ethylene molecules.

I could not know, after a Master thesis focused on polymeric complex systems (which I liked, by the way), that a so little system could explain to me so much of the physics and chemistry that I applied and discussed all over my four years of Ph.D. Thesis.

For sure, at that time I did not know that the same exact little system was studied about twenty years earlier resulting in the first relevant publication on the evidence of a conical intersection in excited-state reactivity (*Bernardi et al. 1990*).

Since then, I started to think in terms of intersection hyperspaces, avoided crossings, branching planes, non-adiabatic couplings...

Preface

In this PhD Thesis, the results obtained while performing my graduate student project are organized in eight chapters.

The first chapter is an introduction to the field of photochemistry, posing special attention on its history, potentialities and future perspectives (sections 1.1 and 1.2). It follows a description of hydrogen bonds in biologically relevant systems, including an overview of electron, proton and energy transfer processes (section 1.3). These are fundamental processes to understand the presented mechanisms of photostability and molecular switching (sections 1.4 and 1.5).

In the second chapter, the aims of the Ph.D. project are summarized, in order to help the reader in fully understanding the results obtained.

The methods applied are explained in chapter 3. Especially, a description of multiconfigurational *ab initio* methods (CASSCF and CASPT2, in section 3.1) and quantum mechanics/molecular mechanics methods (section 3.2) is given. How to calculate spectroscopic properties, relaxation pathways, crossings between electronic states and semiclassical dynamics is explained in section 3.3, including a list of the software and packages used.

Chapters 4, 5 and 6 contain all the novel results found during this Ph.D. Thesis: UV-photostability mechanisms in amino acids and proteins are presented in section 4.1, while a novel method to define and quantify the energy transfer between a donor and an acceptor molecule is explained in section 4.2. Chapter 5 contains the description of a methodology to approximate the CASPT2 energy gradient vector for "on the fly" excited-state semiclassical dynamics, which was applied to study a retinal chromophore model. Chapter 6 is dedicated to modulation of the absorption energy, through the systematic study of a series of S-nitrosothiols, that was considered as reference for the development of a method to define the structural substituent effect in the excitation energy of a chromophore (section 6.1). Finally, a method to perform analytical

dynamics with applied external forces was developed and applied to modulate the spectroscopical properties of azobenzene, one of the most common photoswitches.

Summary and conclusions are contained in chapter 7 (English version) and in chapter 8 (Spanish version), in partial fulfillment of the requirements to obtain an "International Doctorate" mention, as established by the "European Higher Education Area" and applied by the University of Alcalá through the RD 1393/2007.

A list of all articles published in peer-reviewed journals is finally added.

Apart from my Ph.D. supervisor, Prof. Dr. Luis Manuel Frutos , I would like to thank all contributors to the results obtained: Prof. Dr. Obis Castaño (chapter 4), Prof. Dr. Roland Lindh and Dr. Isabelle Navizet (subsection 4.1.3), Prof. Dr. Massimo Olivucci, Alessio Valentini and Samer Gozem (chapter 5), Dr. Manuel Temprado (section 6.1), Prof. Dr. Diego Sampedro and Cristina García-Iriepa (see list of publications and subsection 6.1.2), Felipe Zapata (subsection 6.1.2 and section 6.2), Miguel Ángel Fernández-González and Alberto López-Delgado (subsection 6.1.2).

1. Introduction

From up left to right:

Erwin Schrödinger, Manfred Eigen, George Porter,

Ronald George Wreyford Norrish, John A. Pople and Ahmed H. Zewail

1.1 Electromagnetic and Solar Spectra

The electromagnetic spectrum is the range of all possible wavelengths (or frequencies) of electromagnetic radiation. In principle, the electromagnetic spectrum is continuous and infinite, being in practice limited by the Planck length for short wavelengths, and by the size of the universe for long wavelengths.

Nowadays, electromagnetic radiation properties are extensively used for technological and scientific purposes, being of special interest in physics and chemistry for the application to different kinds of spectroscopy, by which it is possible to characterize matter. The electromagnetic spectrum can be divided into different types of radiation, depending on the specific range of wavelengths (or frequencies), therefore broadly defining different regions of the spectrum: radio (>10^8 nm), microwave (10^5–10^8 nm), infrared or IR (750–10^5 nm), visible (390–750 nm), ultraviolet or UV (10–390 nm), X-rays (10^{-2}–10 nm) and gamma rays (<10^{-2} nm).

The Sun, as every object, emits and absorbs part of the electromagnetic radiation. Especially, the Sun radiates light in a broad continuum range including IR, visible and UV regions (Figure 1.1).

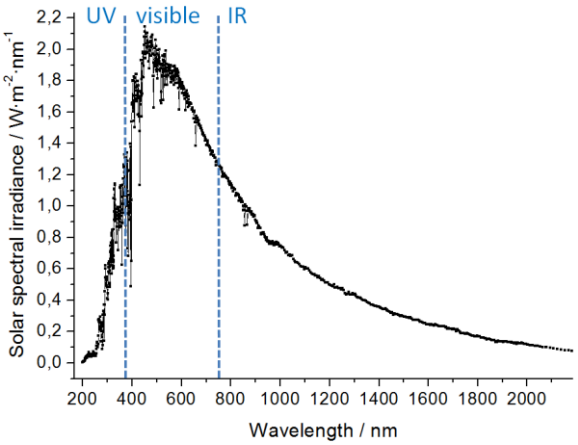

Figure 1.1 Solar spectrum subdivided into UV, visible and IR regions (*ASTM 2008*).

The maximum solar spectral irradiance corresponds to the visible region, with a long tail in the near-IR (750−1400 nm) and short-wavelength-IR (1400-3000 nm) regions. Moreover, a considerable part of the solar spectrum corresponds to near-UV (300−390 nm) and middle-UV (200−300 nm) irradiation.

In this Ph. D. Thesis, the attention is focused on molecular reactivity started by solar irradiation even though, for particular requirements, we can also consider laser sources at specific wavelengths. Indeed, the Sun provides a natural and renewable source of energy which carries advantages and disadvantages: on the one side, solar cells and solar power plants were developed in order to convert solar energy into electrical energy, therefore offering a possible alternative to conventional resources, as oil and gas, *e.g.* by the "Archimede Project" which permitted to build the first concentrated solar power plant to use molten salt for heat transfer and storage (see *www.archimedesolarenergy.it*). In this direction, considerable advances have been made by inorganic solar cells, while organic solar cells are trying to emerge as well (Green et al. 2011; Servaites et al. 2011; Service 2011). Moreover, different classes of photosensitive molecular switches and motors were designed, synthesized and characterized, with broad medical, biological and technological aims (see section 1.5).

On the other side, a major risk for all photoactivated biological processes is UV-radiation exposure, which can cause structural and conformational changes, resulting in a loss of the system function or activity. This, coupled to the ozone depletion phenomena (which results in decline of the total ozone volume in Earth's stratosphere, and therefore in increased UV exposure) leads to a variety of biological and medical consequences, including increases in photoinduced mutations of the genetic material (DNA and messenger-RNA), cataracts and skin cancers.

1.2 Brief History of Photochemistry

The 1967 Nobel Prize in Chemistry was awarded to Manfred Eigen (one half of the Prize), Ronald George Wreyford Norrish and George Porter

(the other half of the Prize) "*for their studies of extremely fast chemical reactions, effected by disturbing the equilibrium by means of very short pulses of energy*". Their pioneering work was oriented towards the development of the instrumentation to study chemical reactions in the microsecond timescale.

The principle that the three scientists applied was simple: perturb the chemical system in order to move it out of equilibrium conditions, and detect the way the system restores to equilibrium or evolves to products, including short-lived molecular species. Eigen developed a sound waves based perturbation technique, while Porter, working with Norrish, designed an apparatus based on UV flashes to perturb systems, generating electronically excited-states (*Van Houten 2002*).

As Porter himself said, it was in World War II, while serving the Royal Naval Volunteer Reserve Special Branch as an Officer and radar scientist working with pulses of electromagnetic radiation, that he started to think about the postgraduate research project that he will realize after the war at the University of Cambridge with Norrish. But it was only in 1947, after looking at how flash lamps were being manufactured at the Siemens factory in Preston (United Kingdom), that he finally realized how to *"study transient phenomena*": a first flash to generate a pulse of energy by which the system could be electronically excited, and a second flash to detect the transient phenomenon. This means that the time passing between the two flashes is the crucial variable determining the resolution of the method (*Farago 1975*).

The original flash photolysis apparatus consisted of a pulsed lamp (a 1 m long quartz tube of 2000 µF charged to 4 kV, which could be discharged in 2 ms) adopted by the Royal Air Force for aerial night-time photography, and a less intense light source as probe flash, in order to measure absorption changes 50 µs after the first flash. The timing was ensured through a mechanical wheel engineered with slits (see Figure 1.2). Previously, "*fast chemical reactions*" were considered the ones studied on the sub-second time scale through stopped-flow instrumentation, developed in the 1920's. Therefore, flash photolysis allowed a substantial advance in science since 1950's, when a millisecond measurement was considered *"far beyond direct physical measurement"* (*Thrush 2003*).

The first experiments conducted by flash photolysis were on triplet-triplet absorption in polyaromatic hydrocarbons, focusing at the kinetics of decay of the triplet state and solvent effects, as presence of oxygen and viscosity of the medium (*Windsor 2003*).

We have to wait almost the end of the century for international recognition of more advanced studies of transient phenomena: in 1999 the Nobel Prize in Chemistry was awarded to Ahmed H. Zewail "*for his studies of the transition states of chemical reactions using femtosecond spectroscopy*". Basically, the brilliant work of Zewail and coworkers consisted in developing techniques for applying laser pulses in the femtosecond time scale (1 fs = 10^{-15} s) to the investigation of chemical reactions, generating snapshots of the ongoing chemical reaction to demonstrate how chemical bonds are formed or broken.

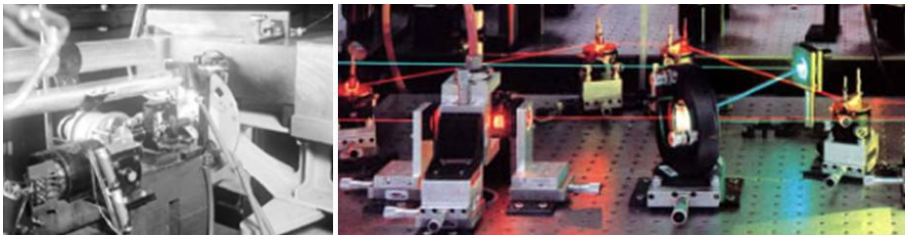

Figure 1.2 Left: the original flash photolysis apparatus (*Thrush 2003*). Right: femtosecond spectroscopy setup in the Laboratory of Molecular Sciences at California Institute of Technology (see *http://www.lms.caltech.edu*).

On the side and together with experimental science, theoretical advances have been made as well, permitting to formulate, predict and validate experimental findings, through mechanistic and dynamical descriptions. Conceptually, most of the photochemistry can be explained and rationalized by means of potential energy surfaces, PESs (see chapter 3). In 1927 it was proposed the so called Born−Oppenheimer approximation, named after Max Born and J. Robert Oppenheimer, by which the wavefunction and energy of a polyatomic average-size molecule can be calculated (*Born and Oppenheimer 1927*). Basically, it permits to separate the total wavefunction into an electronic and a nuclear part:

$$\Psi_{TOT} = \Psi_{electronic} \times \Psi_{nuclear} \qquad \text{Eq. 1.1}$$

Therefore, the electronic Schrödinger equation (corresponding to the $\Psi_{electronic}$ wavefunction) can be solved while keeping fixed the nuclei position. In case the effects of the quantum mechanical nuclear motion have to be introduced, energy derived from the electronic Schrödinger equation is taken as the potential energy for the nuclear Schrödinger equation, which contains only nuclei variables. The success of the Born–Oppenheimer approximation is a consequence of the low ratio between electron and nucleus masses, and consequently of the large ratio between their velocities. This alternative procedure to the calculation of the total time-dependent Schrödinger equation, makes feasible the calculation of molecular wavefunctions.

Within the Born–Oppenheimer adiabatic approximation, PESs determine nuclear motion and, therefore, chemical reactivity. Thermal reactions usually occur on one PES, which describes the electronic ground-state. However, the theoretical treatment of any photochemical reaction requires at least two PESs to be taken into account, *i.e.* the ground-state and one or more electronically excited-states. This leads to two different possible scenarios: PESs never cross (*e.g.* in case of fluorescence) or do actually cross through conical intersections or avoided crossings. If the former case can be correctly treated by the Born–Oppenheimer approximation, the same is not true for surface crossings, where the Born–Oppenheimer approximation is not valid, as demonstrated by John von Neumann, Eugene P. Wigner (*von Neumann and Wigner 1929*) and Clarence Zener (*Zener 1932*). Radiationless relaxation of excited-states, ultrafast intersystem crossing and photoinduced isomerization of polyatomic molecules are typical phenomena associated with violation of the Born–Oppenheimer approximation.

Later on, theoreticians as Edward Teller (*Teller 1937*), Walter Kauzmann (*Kauzmann 1957*) and Theodor Förster (*Förster 1970*) accepted the concept of PESs, anyway without attempting to characterize these points. It was Howard E. Zimmerman (*Zimmerman 1966*), by reformulating the Woodward−Hoffman rules, to explain that, in the Hückel approximation, ground and excited PESs can cross at a point located on a symmetry-forbidden path of a pericyclic reaction, finally clarifying the

different nature of thermal and photochemical reactions of such type. Five years later, Ralph C. Dougherty generalized Zimmerman's conclusion (*Dougherty 1971*).

The next stage of development required the extensive use of computers, by which polyatomic studies could be carried out, and a comparison with experimental findings more likely to happen. At this point the theoretical and computational photochemistry community becomes to enlarge: several groups studied conical intersections imposed by symmetry, while Lionel Salem extended Zimmerman's work from a qualitative to a quantitative level (*Salem 1974*).

Therefore, theoretical and computational advances are making possible, at the present state-of-the-art, a qualitative understanding of organic photochemistry unforeseeable fifty years ago. But, as usual in science, there are limits to the existing experimental and theoretical methods, which create new challenges and future perspectives. On the experimental side, the development of attosecond spectroscopy (1 as = 10^{-18} s) makes the scientific community believing that "*attochemistry*" may soon be possible, by probing and tracking the real-time motion of electrons (*Bucksbaum 2007; Cavalieri et al. 2007; Smirnova 2010*). On the theoretical and computational side, many efforts are being directed towards acquisition of a quantitative picture, in order to predict photochemical reactivity aspects not only in a qualitative way. Especially, mechanistic and semi-classical dynamics methods are being applied to a large area of possible applications, proposing new mechanisms and reporting about the importance and relevance of the intersection space exploration. Solvent effects are introduced by different possible schemes, in order to reach a more realistic description (see chapter 3). Nonetheless, qualitative levels of theory can be used in order to develop new methodologies, at least in a first benchmarking stage.

I hope that the present Thesis can be considered, at least up to a certain extent and within all the limits to be valued, part of the present history of photochemistry.

1.3 Hydrogen Bonds in Biologically Relevant Systems

Hydrogen bonding interactions play a crucial role in chemical, physical and biological processes like enzyme catalysis, crystal engineering, condensed supramolecular chemistry, proton transfer, etc. Especially, the concept of hydrogen bonding became fundamental in biochemistry about sixty years ago, thanks to the correct proposals of α-helix and β-sheet primary structural motifs in protein secondary structure *(Pauling and Corey 1951*), and of the DNA double helix structure (*Watson and Crick 1953*) (Figure 1.3). Nowadays, the role of hydrogen bonds is well known to be crucial in determining the conformation and biological function of proteins (*Cantor and Schimmel 1980; Jeffrey and Saenger 1991*). There are different types of hydrogen bond interaction: strong hydrogen bonds (bond energy > 10 kcal·mol^{-1}) are usually characterized by a positively charged donor group or by a negatively charged acceptor group, *e.g.* $O^{+}\cdots H-O$ or $O-H\cdots O^{-}$. Such hydrogen bonds provoke the formation of excessively rigid structures to participate in most of biochemical functions, since they would essentially block any biological process (*Watson 1965*). Therefore, essential biological interactions are determined by weak hydrogen bonds (bond energy < 10 kcal·mol^{-1}).

Especially, hydrogen bonding is important in determining the three-dimensional structure of proteins and nucleic acids, which folding and unfolding into specific shapes has direct consequences on biochemical and physiological fundamental functions. In particular, the CO and NH groups of the protein backbone, which can form hydrogen bonds between different amino acids of the same polypeptide chain, mainly determine the type of secondary structure within the proteins (α-helix, β-sheet, etc.); additionally, hydrogen bond interactions within amino acid side-groups help in forming the tertiary structure. Moreover, hydrogen bonds within proteins are crucial in the enzymatic activity via recognition of substrates in the binding region of protein complexes *(Dobson and Hore 1998; Lyon et al. 2002; Pal and Zewail 2004*), and in the catalysis of chemical reactions, as carbonic anhydrase (*Lu and Voth 1998*), serine protease (*Warshel et al. 1989; Li et al. 1998*) and alcohol dehydrogenase (*Sekhar and Plapp 1988*). In DNA, the typical double helix structure is mainly due to hydrogen bonding between

the base pairs, which enables replication by forming a couple of DNA complementary strands, being this process the basis for biological inheritance.

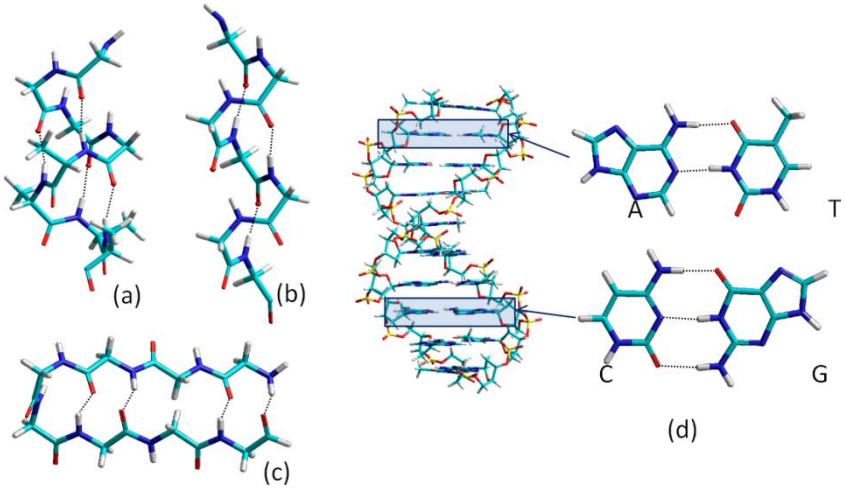

Figure 1.3 Examples of main biochemical motifs keeping their tridimensional structure and function thanks to hydrogen bonds. In proteins: α-helix, with i+4→i hydrogen bonding pattern (**a**); 3_{10} helix, with i+3→i hydrogen bonding pattern (**b**); β-hairpin, composed by two antiparallel β-strands connected by a β-turn (**c**). All polypeptide sequences are $(Glycine)_n$. In DNA: adenine (A) and thymine (T) base pair present two hydrogen bonds, while cytosine (C) and guanine (G) present three hydrogen bonds (**d**).

The hydrogen bond energy can be considered a combination of different components: electrostatic attraction, exchange repulsion, polarization, charge transfer character, dispersion and the coupling term which is important only for short hydrogen bonds length (*Kitaura and Morokuma 1976*).

1.3.1 Electron and Proton Transfer Processes

One of the most important properties related to hydrogen bonds is that they were shown to facilitate proton transfer in the ground-state

(*Zundel 1992*). For example, the high electrical conductivity of water could be explained by proton transfer: H_3O^+ and OH^- are formed as defects which can move by "*structural diffusion*" across the O···H−O hydrogen bonds network (*Eigen and de Maeyer 1958*). Therefore, electron transfer (ET) and proton transfer (PT) processes, both in ground and excited-state, are crucial in understanding biochemical properties of hydrogen-bonded molecules. Apart from single ET and PT processes, different mechanisms were proposed theoretically and experimentally: stepwise ET followed by PT (ETPT), stepwise PT followed by ET (PTET) and concerted proton coupled electron transfer (PCET). These mechanisms correspond to net transfer of a hydrogen atom, being eventually possible the stabilization of a hydrogen transferred product, or being more feasible a reverse path back to the reactant, *i.e.* unidirectional or bidirectional ETPT, PTET, PCET (Figure 1.4).

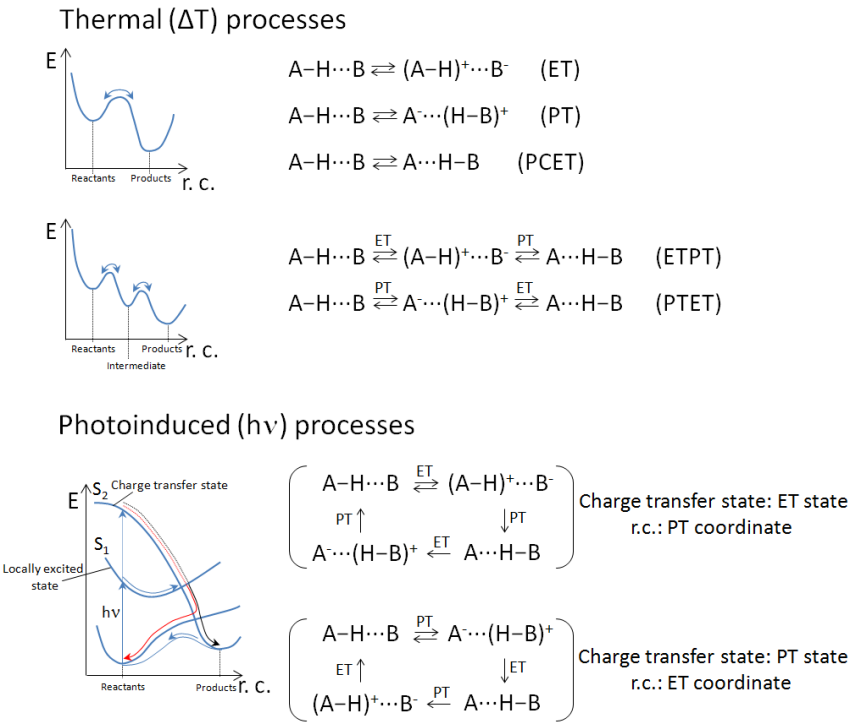

Figure 1.4 Possible electron transfer (ET) and proton transfer (PT) processes induced thermally and photochemically in a hydrogen-bonded moiety (A–H···B), including stepwise (ETPT, PTET) and concerted (PCET) mechanisms. Formation of products ($(A–H)^+\cdots B$, $A^-\cdots(H–B)^+$, A···H–B), as well as reversion of the path back to A–H···B, is shown by schemes of the energy as function of the relevant reaction coordinate (r.c.), and by the corresponding chemical formulae. For photoinduced processes, excitation to a local excited singlet state (S_1) or directly to the charge transfer singlet state (S_2) are considered (vertical arrows), followed by reactant restoration (red path) or photoproduct formation (black path).

Thermal processes proceed on the ground-state PES, being the limiting factor the activation energy from reactants to products (or, in case of ETPT and PTET, from reactants to intermediates and from intermediates to products), determined by the corresponding transition states. Ground-state electron and proton transfer reactivity mediated by hydrogen bonds in biochemical environments has been discussed throughout the literature, including single ET (*Marcus and Eyring 1964; Kuki 1991; Therien et al. 1991; Ye and Ladik 1993; Basilevsky et al. 1994; Barbara et al. 1996; Bixon and Jortner 1999; Herz et al. 1999*), single PT (*Lowdin 1965; Umeyama et al. 1984; Warshel et al. 1989; Li et al. 1998; Lu and Voth 1998; Braeuer et al. 2002; Tautermann et al. 2003; Matsui et al. 2007; Matsui et al. 2009*) and

differently coupled ET and PT *(Cukier 1996; Cukier and Nocera 1998; Soudackov and Hammes-Schiffer 1999; 1999; Decornez and Hammes-Schiffer 2000; Soudackov and Hammes-Schiffer 2000; Hammes-Schiffer 2001; Sjöedin et al. 2005; Irebo et al. 2008; Hammes-Schiffer 2009; Johannissen et al. 2009*).

Photoinduced processes require excited-state PESs to be described: two main types of excited-states are shown in Figure 1.4: locally excited-states and charge transfer states. For simplicity, only one locally excited singlet state (S_1) and one charge transfer singlet state (S_2) are shown, being in general possible the occurrence of more excited-states, differently crossing (or not) between them. The charge transfer state can describe the transfer of one electron or of one proton between the hydrogen bonded moieties, therefore being the population of the charge transfer state the limiting factor to initiate any process. Once irradiating the reactants (supposedly in the Franck–Condon region), the vertical excitation can populate a locally excited-state or directly a charge transfer state (usually at higher energies). Absorption is followed by redistribution of the photon energy into vibrational energy along the normal modes of the molecular system, determining a downhill energy path which can result in locating a minimum (Figure 1.4, on the locally excited-state), or a surface intersection (Figure 1.4, between charge transfer and locally excited-states). The accessibility of the intersection from the locally excited-state depends on the vibrational energy excess required to overcome the eventual energy barrier; also the topology of the crossing (see section 3.3.3) will determine the "*fate*" of the chemical reaction. After charge transfer state/locally excited-state crossing (usually an avoided crossing), the reaction proceeds downhill in energy up to a final cross with the ground-state (usually a conical intersection), which permits ultrafast formation of the photoproduct ($(A–H)^+\cdots B^-$, $A^-\cdots(H–B)^+$, A···H–B) or reactant restoration through back ET and/or PT. Eventually, the photoproduct can revert back to the reactant via a transition ground-state. In case ET is followed by PT (or PT followed by ET), the corresponding photoinduced mechanism describes how both transfer processes are coupled, therefore determining up to which extent the mechanism is stepwise or concerted.

Different photoinduced charge transfer mechanisms were described in polypeptides and bioinspired systems (*Serrano-Andres and*

Fülscher 1998; Serrano-Andres and Fülscher 2001; Vullev and Jones 2002), leading eventually to PCET processes (*Douhal 2004; Kobori and Norris 2006; Moore et al. 2008*).

The scheme shown in Figure 1.4 is a general description of ultrafast photoinduced processes in a hydrogen bonded moiety, where radiationless deactivation is possible. Even though they correspond to high-efficiency processes, we should also mention radiative (and therefore non-ultrafast) photoinduced processes, by which the same products can be reached, but ultrafast reactant restoration is not possible (Figure 1.5).

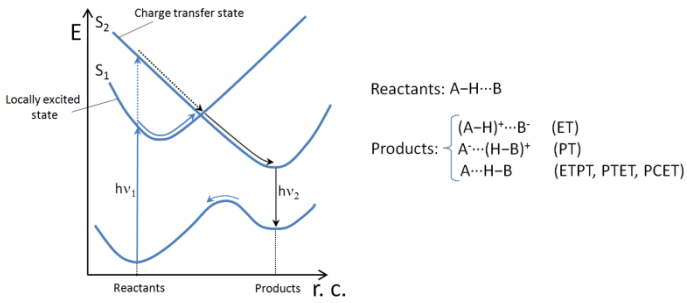

Figure 1.5 Schematic representation of electron and proton transfer photoinduced radiative processes in hydrogen bonded molecules (A–H···B). Formation of products via vertical excitation ($h\nu_1$) to the locally excited-state (S_1) or charge transfer state (S_2) is shown (black path), involving in any case fluorescence ($h\nu_2$). The eventual path back to reactants is possible only by a transition ground-state.

As shown in Figure 1.5, the charge transfer state can be populated through direct vertical excitation, or mediated by a locally excited-state. Differently from non-radiative photoinduced processes (Figure 1.4), the charge transfer state does not cross with the ground-state, instead reaching an excited-state minimum, from where only fluorescence is possible ($h\nu_2$), therefore slowing down the overall mechanism, and not admitting ultrafast reactant restoration. Indeed, reactants restoration is possible only by eventual thermal activation of final products (*Fores et al. 1998; Fores and Scheiner 1999; Fores et al. 2000; Paterson et al. 2005*).

In all mentioned photoinduced processes (radiative and non-radiative), singlet states are discussed. More generally, we should consider

also triplet states, eventually leading to singlet/singlet, triplet/triplet or singlet/triplet intersections. If singlet/singlet and triplet/triplet intersections can both provide radiationless deactivation of the excitation energy from a higher to a lower potential energy surface without changing the molecular spin state (*i.e.* internal conversion), singlet/triplet crossings do imply radiationless deactivation coupled to spin change (*i.e.* intersystem crossing). In the latter case, the probability of the event to happen is determined by the magnitude of the spin-orbit coupling.

Additionally, intermolecular ground-state and excited-state double proton transfer (DPT) were proposed as possible mechanisms in DNA (*Florian et al. 1994; Florian and Leszczynski 1996; Matsui et al. 2009*). More in detail, a hydrogen bonded base pair can exchange two protons by a stepwise or concerted mechanism: in stepwise DPT, a single PT occurs from the normal conformation to an intermediate zwitterionic form, followed by a second single PT, establishing the tautomeric form. In concerted DPT, the mechanism does not proceed through any intermediate, being both protons simultaneously transferred to form the tautomer (*Douhal et al. 1995*). The eventual catalytic role of water in DPT processes between base pairs was also considered (*Ceron-Carrasco et al. 2009; Ceron-Carrasco et al. 2009*), being anyway the controversy between stepwise and concerted mechanism still under debate (*Sekiya and Sakota 2008*).

Nevertheless, we should highlight that DPT requires always a dimer forming at least two hydrogen bonds between the monomers. This necessary condition is always fulfilled by face-to-face nucleobases, but in a more general biological environment (*e.g.* amino acids, proteins, polysaccharides, lipids) the presence of doubly hydrogen bonded dimers is rather the exception than the rule. Therefore, even though DPT mechanisms are eventually relevant for DNA photostability (see section 1.4), they cannot be considered general biochemical mechanisms.

1.3.2 Energy Transfer Processes

Energy transfer can take place between an electronically excited donor (D*) and a ground-state species (A) without emission of a photon while transferring energy, where D and A can be two molecules (intermolecular process) or two parts of the same molecule (intramolecular process). Energy transfer processes can be divided into two main classes, both of increasing importance in chemistry and biochemistry: Förster resonant energy transfer (FRET) and Dexter-type energy transfer. For state-of-the-art applications see: (*Muñoz-Losa et al. 2009; Langhals et al. 2010*) (FRET) and (*Monguzzi et al. 2008; Reineke et al. 2009*) (Dexter-type).

The Förster model is based on the idea that a Coulomb interaction stands between D* and A, by which the energy released by D* can simultaneously excite A, finally resulting in D and A* species (Figure 1.6a) (*Forster 1946; 1949*). David L. Dexter proposed a different energy transfer mechanism, based on a bilateral exchange of electrons between D* and A (Figure 1.6b,c). Dexter-type energy transfer implies a relevant overlap between the orbitals involved in the electronic exchange, therefore requiring D* and A to be close enough in order that exchange can occur (*Dexter 1953*). In case of an intramolecular process, D* and A could come close by a conformational rearrangement of the molecule, while for an intermolecular process a collision between D* and A can produce the energy transfer (*e.g.* in case of reactants in a solvent medium).

In order to elucidate the distance range dependence of FRET and Dexter-type energy transfer processes, the rate constants (k_{FRET}, k_{Dexter}) are given:

$$k_{\mathrm{FRET}} = K_{\mathrm{FRET}} \frac{c^2 J_{\mathrm{DA}} \Phi_{\mathrm{D}}}{\tau_{\mathrm{D}} |\boldsymbol{R}_{\mathrm{DA}}|^6} \qquad \text{Eq. 1.2}$$

$$k_{\mathrm{Dexter}} = K_{\mathrm{Dexter}} J_{\mathrm{DA}} U^2 \exp\left(\frac{-2R_{\mathrm{DA}}}{L}\right) \qquad \text{Eq. 1.3}$$

where K_{FRET} and K_{Dexter} are constants, J_{DA} is the overlap integral between the normalized emission spectrum of the donor (D*→D) and the

normalized absorption spectrum of the acceptor (A→A*), Φ_D is the fluorescence quantum yield of the donor, τ_D is the fluorescence lifetime of the donor, L is the sum of D and A van der Waals radius, R_{DA} is the distance between donor and acceptor, $\boldsymbol{\mu}_{D,}$ and $\boldsymbol{\mu}_A$ are the electronic transition dipole moments, taken into account by the factor c in case of FRET, which describes the influence of their orientation:

$$c = (\hat{\boldsymbol{\mu}}_D \cdot \hat{\boldsymbol{\mu}}_A) - 3(\hat{\boldsymbol{\mu}}_D \cdot \hat{\boldsymbol{R}}_{DA}) \cdot (\hat{\boldsymbol{R}}_{DA} \cdot \hat{\boldsymbol{\mu}}_A) \qquad \text{Eq. 1.4}$$

In Dexter-type energy transfer processes the U^2 term represents the electron exchange coupling, which depends only on the electronic configuration of the initial and final transfer states, resulting in an exchange integral between donor and acceptor wavefunctions (Ψ):

$$U = \langle \Psi_{D^*} \Psi_A \left| \frac{e^2}{|\boldsymbol{R}_{DA}|} \right| \Psi_D \Psi_{A^*} \rangle \qquad \text{Eq. 1.5}$$

which mainly depends on the overlap of donor and acceptor molecular orbitals, while the last term of eq. 1.3 gives rise to an exponential decay of the rate constant with $\boldsymbol{R}_{DA}$ increase. Therefore, we can refer to FRET and Dexter-type energy transfer processes as long-range and short-range processes, respectively.

In this Thesis, we will focus mainly on Dexter-type processes. Especially, singlet-singlet (hydrogen bonded mediated) and triplet-triplet Dexter-type energy transfer (Figure 1.6b,c) processes are studied.

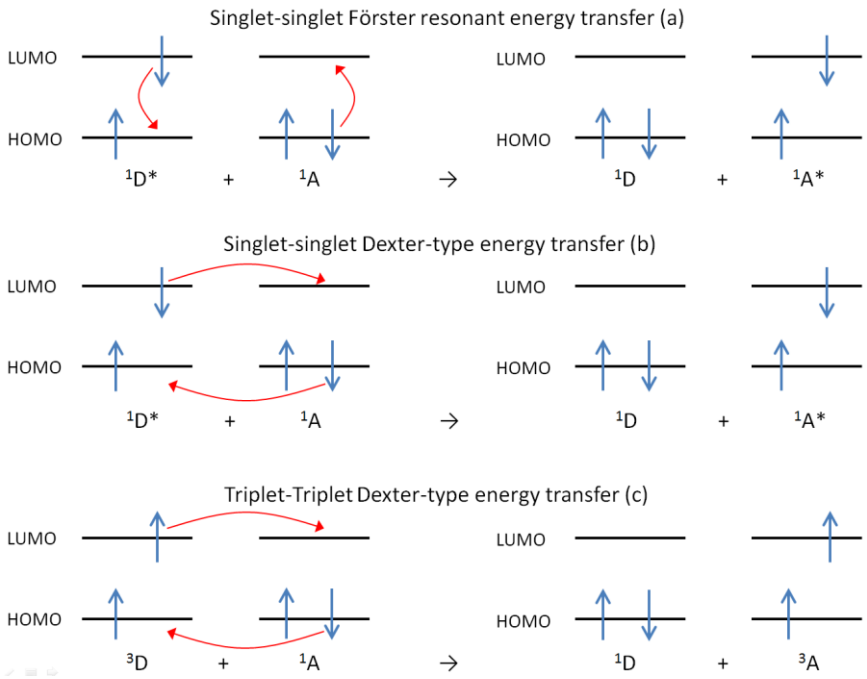

Figure 1.6 Singlet-singlet Förster energy transfer (**a**), singlet-singlet Dexter-type energy transfer (**b**) and triplet-triplet Dexter-type energy transfer (**c**). For simplicity, the processes are shown to occur between HOMO and LUMO of donor (D) and acceptor (A).

1.4 Photostability Mechanisms

Upon absorption of a photon, a molecule is promoted to an electronically excited-state, from which relaxation back to the ground-state is possible through two main pathways: radiatively (by fluorescence or phosphorescence) or non-radiatively (*i.e.* dissipating the vibrational energy by emitting heat). On the one side, if high fluorescence or phosphorescence quantum yield is recorded accompanied by long excited-state lifetimes, there is a high probability that important chemical rearrangements occur, eventually leading to dangerous photoinduced reactions. On the other side, if ultrafast non-radiative processes take place, the excited-state lifetime is minimized, resulting in efficient fluorescence or phosphorescence

quenching, since the energy of the incoming photon is rapidly dissipated into heat (*i.e.* vibrational relaxation) before irreversible electronic or structural rearrangements occur. Therefore, we can define photostability as the *property of molecular systems to dissipate efficiently the incoming energy of a photon, finally recovering the initial ground-state structure*.

Photostability is a fundamental property of biological systems: different mechanisms may have been especially important for the development of life on the surface of primitive Earth under UV extreme exposure, and still now UV irradiation constitutes a potential danger (Figure 1.4). Molecular structures responsible for transmission of the genetic information or for harvesting of the solar energy have to be photostable or at least minimize the damages provoked by photoinduced chemical changes to them or the surrounding environment. But how? Which are such mechanisms and processes? In other words, how does photostability works at the atomic level?

To answer these questions, a deep understanding of the mechanisms including vibrational relaxation and energy dissipation upon optical excitation is required. Especially, excited-state crossings (*i.e.* conical intersections and avoided crossings) were proved to be the funnels by which non-radiative efficient deactivation can take place: when the PESs approach each other, nonadiabatic transitions are facilitated by their close proximity and the rate of radiationless transition increases (see chapter 3).

Hydrogen bonds have been proposed as features conferring photostability through PCET mechanisms, as indicated in Figure 1.4 (*Sobolewski et al. 2005; Sobolewski and Domcke 2007*). This process has been described as a two-step mechanism: as first the proton in the hydrogen bond is transferred, promoted by photoinduced electron transfer (forward step). Then a second electron transfer process is followed by proton transfer (backward step), in order to restore the system to its initial hydrogen bond configuration in picoseconds *(Schultz et al. 2004*). This forward-backward PCET mechanism was already proposed in DNA base pair models (*Frutos et al. 2007; Zhang et al. 2009*), being possible experimental observation by electron and mass spectroscopy in the 2-aminopyridine dimer (*Samoylova et al. 2009*). However, few attempts were performed for the elucidation of this mechanism in proteins (*Shemesh et al. 2009; Shemesh et al. 2009; Shemesh et al. 2010*).

In this Thesis, after studying possible energy, electron and proton transfer processes, we focus on PCET mechanims, finding out a possible general photostability mechanism within hydrogen-bonded protein backbone strands (*Marazzi et al. 2010; Marazzi et al. 2011*). A closer insight into the photoreactivity of human γB-crystallin was then considered, in order to elucidate the first photoinduced events which can occur in one of the main structural proteins of the eye lens (*Marazzi et al. 2012*).

1.5 Molecular Switches

The design and construction of molecular machines by the bottom-up strategy (*i.e.* from atoms to molecular devices) is a major goal of nanotechnology. Molecular switches and motors are essential parts of molecular machines, and full understanding of its mechanisms and dynamical properties is of fundamental importance. These devices convert energy supply into mechanical energy, leading to a controlled motion (*Feringa 2007*). Among different possible stimuli, we focus on photoinduced processes, since they provide several advantages and improvements compared to other possible stimuli (*Balzani et al. 2004*).

Especially in the biochemical field, we know that protein activity can be controlled by light. Perhaps one of the most known examples is rhodopsin, which is responsible for vision in mammalians through *cis-trans* photoisomerization of its cofactor retinal (Figure 1.6a) (*Kandori et al. 2001; Andruniow et al. 2004; Frutos et al. 2007; Nakamichi et al. 2007; Smitienko et al. 2010; Schapiro et al. 2011*). Therefore, we can consider the retinal chromophore as a two-state molecular photoswitch, to which light can be applied in order to move from state 1 (*cis* initial conformation) to state 2 (*trans* final conformation). For many biological applications, the capability to selectively switch the activity of a protein on and off in a similar manner would be highly desirable (*Sampedro et al. 2004; Gorostiza and Isacoff 2008; Sinicropi et al. 2009*). This was successfully accomplished by the introduction of a photosensitive compound into the protein of interest: molecules like azobenzene and derived from rhodopsin can reversibly undergo excited-state isomerization of the central carbon-carbon double

bond (C=C), switching between *cis* and *trans* forms (Figure 1.6b) (*Kumita et al. 2000; Flint et al. 2002; Blanco-Lomas et al. 2012*). Especially, azobenzene undergoes *trans*-to-*cis* isomerization by UV irradiation and *cis*-to-*trans* isomerization by blue-light irradiation or just thermal conversion (*Renner and Moroder 2006; Sadovski et al. 2009; Schierling et al. 2010*). Such applications require the photoswitch to be covalently bound at both ends to different parts of the same protein, provoking a reversible interchange between an active and an inactive conformation of the protein. This was performed by different approaches: chemical modification of peptides and proteins (*Woolley 2005; Mayer and Heckel 2006; Renner and Moroder 2006*), azobenzene modified ligands (*Westmark et al. 1993; Pearson et al. 2008*), incorporation during peptide synthesis (*Liu et al. 1997; James et al. 2001; Dong et al. 2006*), incorporation in vitro (*Muranaka et al. 2002; Nakayama et al. 2004*) and in vivo (*Bose et al. 2006*), being chemical modification the most widely applied.

Therefore once incorporated into the protein, the photoswitch will be subject to external forces acted by the protein environment, most probably leading to changes in the ground-state minimum energy structure and to a different redistribution of the vibrational energy when compared to the unbounded photoswitch. Also, the absorption energy needed for electronic transition to the optically bright state could undergo a bathochromic or hypsochromic shift, as a consequence of energy stabilization (or destabilization) of the electronic-states of interest.

In this Thesis we try to elucidate the effects of a couple of external force vectors acting on *cis*- and *trans*-azobenzene, therefore attempting to mimic a simplified protein environment surrounding the photoswitch.

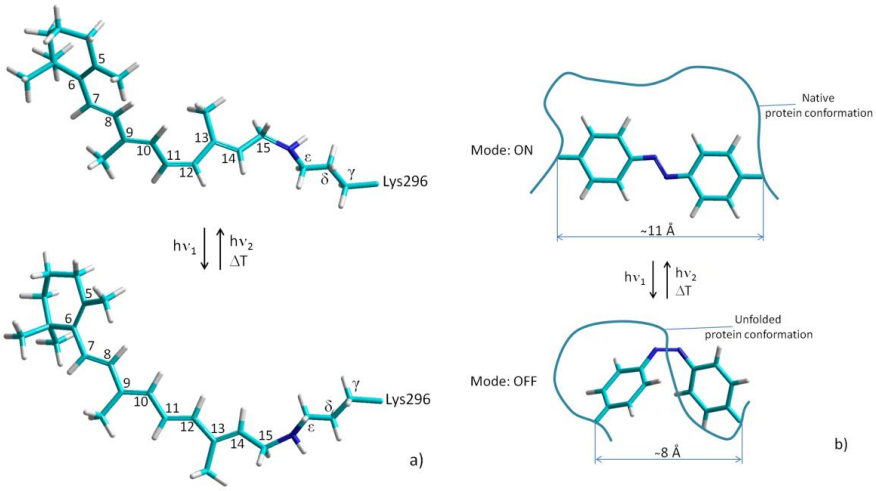

Figure 1.7 *Cis-trans* photoisomerization of retinal chromophore in bovine rhodopsin (PDB code: 1U19), implying torsion around the C_{11}=C_{12} bond. The chromophore is covalently bound to the opsin through residue Lys296 (**a**). Switching on and off a peptide (or protein) by light, through azobenzene photoisomerization (**b**). Atom colors: blue=nitrogen; cyan=carbon; white=hydrogen.

2. Aims

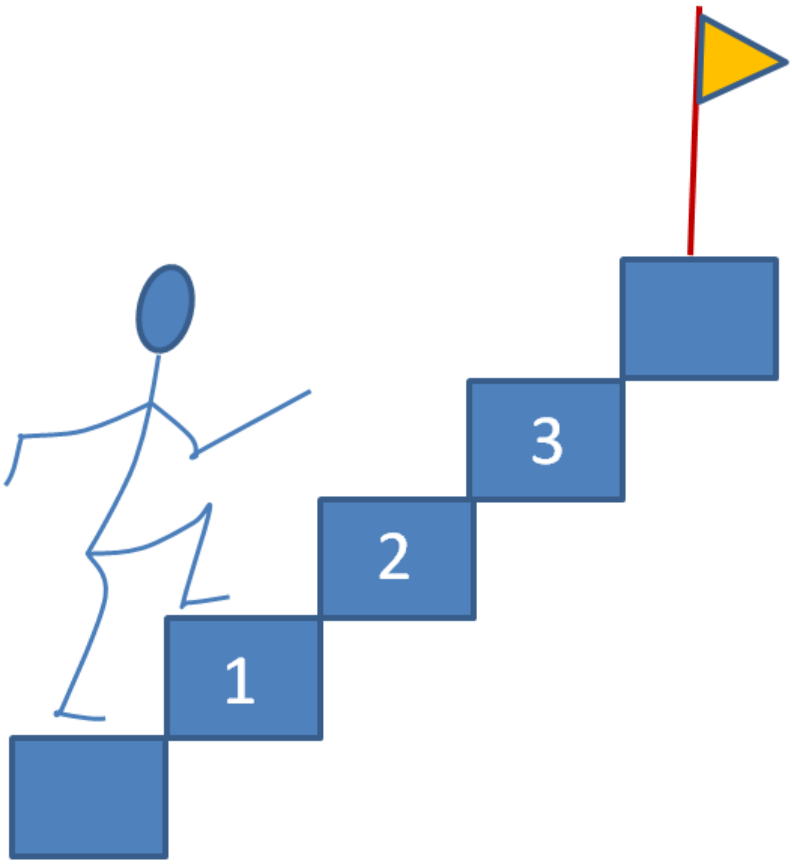

"Some things are easy, they are only hard to do"

Albert Einstein to Joseph O. Hirschfelder

The project presented in this Ph. D. Thesis concerns the application and development of theoretical and computational methods to the description of the photochemistry and photophysics of chemical and biologically relevant molecular systems.

Specifically, the overall project can be divided into two sections:

A first section includes the application of multiconfigurational *ab initio* methods to the qualitative and quantitative description of photoinduced energy, electron and proton transfer processes. Especially, the study was oriented towards hydrogen-bonded moieties, proposing them as characteristic features to provide (or at least enhance) photostability against UV irradiation within amino acids, peptides and proteins.

The second section results from the understanding of the limits and/or computational expenses required to perform reliable calculations of excited-state properties. Therefore, different methods were proposed in order to overcome these limits, including its mathematical definition, implementation and application to different sets of molecules.

More in detail, the following goals were achieved:

i. The CASPT2//CASSCF methodology was applied to study a β-turn minimal model composed by two hydrogen-bonded glycines, elucidating the minimum energy paths which follow UV irradiation, finally dissipating the excitation energy into vibrational energy.

ii. The CASPT2//CASSCF/AMBER methodology was applied to study photostability mechanisms in human γB-crystallin, one of the main protein forming the vertebrate eye lens, focusing on the role of the tyrosine corner element.

iii. A definition of the reaction coordinate for Dexter-type (electronic exchange) energy transfer processes between a donor and an acceptor molecule was proposed within the weak electronic

coupling limit. The method was applied to the long debated case of *nonvertical* triplet-triplet energy transfer in *cis*-stilbene as acceptor molecule.

iv. In order to overcome the limits imposed by numerical CASPT2 energy gradient calculation, and to improve CASPT2//CASSCF methodology, a scheme for scaling the CASSCF energy gradient was proposed and applied to retinal models (*i.e.* models of the visual pigment chromophore), resulting in the implementation of a program for performing excited-state dynamics.

v. A method to determine quantitatively the excitation energy of a chromophore when structurally affected by chemical substitution was developed, being valid within the limit of a chemical substitution which does not modify the nature of the electronic excited-state considered.

vi. The concept of *structural substituent excitation energy effect* aforementioned was applied to a wide series of S-nitrosothiols, in order to predict their ability to release nitric oxide. The final results suggest a clear tendency in favor of an absorption spectra modulation.

vii. The effects of the environment on a photoswitch were treated as external forces acting at two ends of the chromophore. In the case of azobenzene (one of the most commonly applied photoswitches), *cis* and *trans* isomers show considerable photosensitivity to the applied forces, resulting in possible modulation of the maximum absorption wavelength.

3. Methods

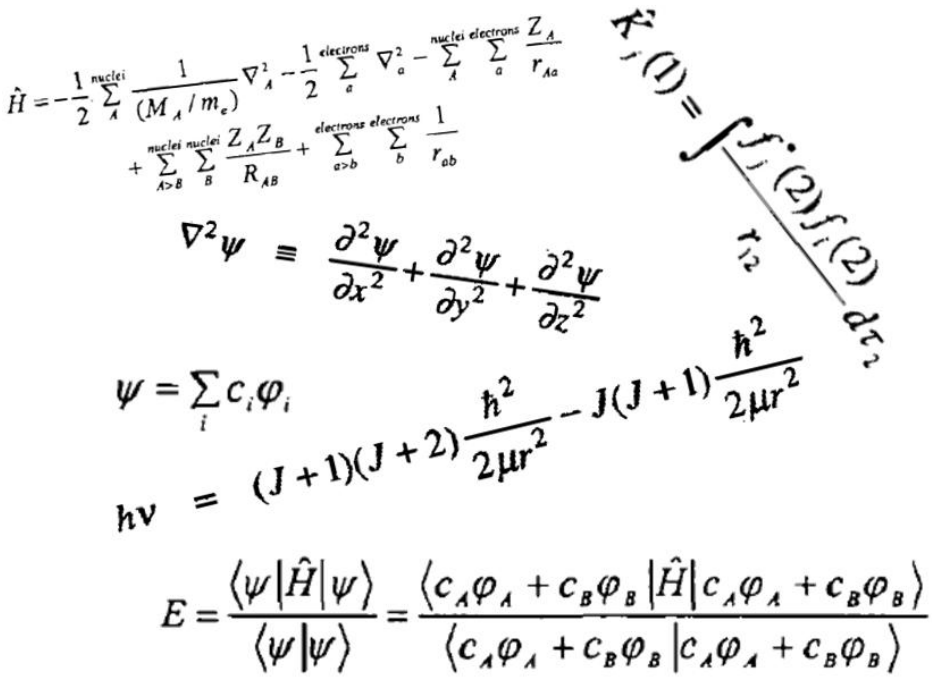

"We are reaching the stage where the problems we must solve are going to become insoluble without computers. I do not fear computers. I fear the lack of them"

Isaac Asimov

3.1 From the Born–Oppenheimer approximation to Multiconfigurational *ab initio* Methods

As mentioned in the introduction, the Born–Oppenheimer approximation is a fundamental concept for the development of theoretical chemistry, since it permits decoupling of nuclear and electronic motions, due to the fact that nuclei are heavier than electrons while their momenta are similar, corresponding to much lower velocities of the nuclei. This leads to the approximation that the total wavefunction describing the molecule can be factorized in a pure electronic and a pure nuclear wavefunction (eq. 1.1). Indeed, the correlated motion of nuclei and electrons is the bottleneck when analytically solving the time-dependent Schrödinger equation which, in its general formulation, can be expressed as follows:

$$i\hbar\frac{\partial}{\partial t}\Psi(\boldsymbol{r},t) = \hat{H}\Psi(\boldsymbol{r},t) \qquad \text{Eq. 3.1}$$

where i is the imaginary unit, $\hbar$ is the reduced Planck constant, Ψ is the wavefunction of the quantum system as a function of space $\boldsymbol{r}$ and time t, and $\hat{H}$ is the Hamiltonian operator. When considering the case of a single particle moving in an electric field, the time-dependent Schrödinger equation can be expressed in non-relativistic terms:

$$i\hbar\frac{\partial}{\partial t}\Psi(\boldsymbol{r},t) = \left[\frac{-\hbar^2}{2m}\nabla^2 + V(\boldsymbol{r},t)\right]\Psi(\boldsymbol{r},t) \qquad \text{Eq. 3.2}$$

where m is the particle's mass, ∇^2 is the Laplacian, and V is the particle's potential energy. By applying the time-dependent Schrödinger equation, it can be predicted that wavefunctions form stationary states (*i.e.* atomic or molecular orbitals). It follows that the time-independent Schrödinger equation describes such stationary states:

$$E\Psi(\boldsymbol{r}) = \left[\frac{-\hbar^2}{2m}\nabla^2 + V(\boldsymbol{r})\right]\Psi(\boldsymbol{r}) \qquad \text{Eq. 3.3}$$

where wavefunction and Hamiltonian are only dependent on the spatial coordinates $\boldsymbol{r}$.

For the purpose of describing molecular systems larger than H_2, a direct application of the Schrödinger equation is impractical. Therefore, here we briefly show how to apply the Born−Oppenheimer approximation to solve the Schrödinger equation. It consists of two consecutive steps: as first, the nuclear kinetic energy is subtracted from the total molecular Hamiltonian (because of instant electronic relaxation with respect to nuclear motion), while electron-nuclear interactions are still included. This allows the electronic Schrödinger equation to be solved having as parameters the nuclear positions $\boldsymbol{q}$:

$$\hat{H}_e \Psi(\boldsymbol{q}) = E_e \Psi(\boldsymbol{q}) \qquad \text{Eq. 3.4}$$

where

$$\hat{H}_e = \hat{H}_{total} - \hat{T}_n - \hat{H}_{pf};\ E_e = V_{ne} + V_{ee} + V_{nn} \qquad \text{Eq. 3.5}$$

being $\hat{H}_e$ the electronic Hamiltonian, E_e the electronic energy, $\hat{H}_{total}$ the total Hamiltonian, $\hat{T}_n$ the nuclear kinetic energy operator, $\hat{H}_{pf}$ the Hamiltonian of the particle field, V_{ne} the attraction energy between nuclei and electrons, V_{ee} the repulsion energy between electrons, and V_{nn} the repulsion energy between nuclei.

The second step of the approximation consists in introducing the nuclear kinetic energy operator and solving the resulting Schrödinger equation, finally calculating the energy of the molecule E:

$$\left[\hat{H}_e + \hat{T}_n\right]\Psi(\boldsymbol{q}) = E\Psi(\boldsymbol{q}) \qquad \text{Eq. 3.6}$$

In this Ph.D. Thesis, *ab initio* quantum chemistry methods are mainly applied. Among them, the Hartree−Fock (HF) theory can be considered the most fundamental, being all post-HF methods further developments of the same theory. By the HF method, the ground-state

wavefunction Ψ_0 is determined, being the molecular orbitals products of monoelectronic wavefunctions. Within this approximation, the electronic field is determined by a self-consistent field method, where every single electron is moving under the mean-potential created by the other electrons. The wavefunction is built from Slater determinants as an antisymmetrized product of spin orbitals (*i.e.* the product of a spatial orbital and a spin function):

$$|\Psi_0> = (N!)^{1/2}\begin{bmatrix}\varphi_1(1) & \varphi_2(1) & \cdots & \varphi_N(1)\\ \varphi_1(2) & \varphi_2(2) & \cdots & \varphi_N(2)\\ \cdots & \cdots & \ddots & \vdots\\ \varphi_1(n) & \varphi_2(n) & \cdots & \varphi_N(n)\end{bmatrix} = |\varphi_1\varphi_2 \cdots \varphi_a\chi_b \cdots \varphi_N>$$

Eq. 3.7

It follows the calculation of the energy:

$$E = \langle\Psi_0|\hat{H}|\Psi_0\rangle \qquad \text{Eq. 3.8}$$

where the Hamiltonian can be expressed as follows:

$$\hat{H} = -\frac{1}{2}\sum_{i=1}^{n}\nabla_i^2 - \sum_{\mu,j}\frac{Z_\mu}{q_{\mu j}} + \sum_{i,j}\frac{1}{q_{ij}} \qquad \text{Eq. 3.9}$$

The first, second and third term on the r.h.s. of eq. 3.9 are the electron kinetic energy operator, the nuclei-electron attraction potential operator and the electron-electron repulsion potential operator, respectively. This corresponds to the electronic Hamiltonian, since nuclei-nuclei repulsion potential energy and the nuclei kinetic energy can be omitted, thanks to the Born−Oppenheimer approximation. Now we have all the elements to determine the energy of the system, by replacing eq. 3.7 and 3.9 in eq. 3.8:

$$\mathrm{E} = 2\sum_{i=1}^{n}H_{ii} + \sum_{i=1}^{n}\sum_{j=1}^{n}(2J_{ij} - K_{ij}) \qquad \text{Eq. 3.10}$$

where H_{ii} is the electronic energy of a single electron moving under the attraction of a nuclear "core"; J_{ij} is the so-called Coulomb integral, representing electrostatic repulsion between the electrons in χ_i and χ_j; K_{ij} is an exchange integral which includes different terms differing only in exchange of electrons. The terms J_{ij} and K_{ij} take into account for the average electrostatic repulsion between electrons. The energy is finally calculated by applying the variational principle.

The main drawback of the HF method is the lack of electron correlation treatment (each electron is moving in an average non-local potential, generated by the rest of electrons), which causes large deviations when compared to experimental data. Therefore, different post-HF methods were developed to overcome such drawback. Among them, the Complete Active-Space Self-Consistent Field (CASSCF) method and its perturbation to the second order (CASPT2) − multiconfigurational post-HF methods − were found to succeed in the description of electronic excited-states, and will be presented in the next sections.

3.1.1 The Complete Active-Space Self-Consistent Field Method

The principle of all Multiconfigurational Self-Consistent Field (MCSCF) methods is the expansion of a monoconfigurational HF wavefunction as a linear combination of Slater determinants. Among all MCSCF methods, the CASSCF method results in a MCSCF wavefunction generated by linear combination of configurations Φ_K, considering that each configuration corresponds to a different occupation of the molecular orbitals φ_i included in the so-called active space (*Roos 1987*), where each molecular orbital is a linear combination of atomic orbitals χ_μ:

$$|\Psi_{CASSCF}\rangle = \sum_K A_K \, |\Phi_K\rangle \qquad \text{Eq. 3.11}$$

$$\Phi_K = A\{\prod_{i \subset K} \varphi_i\} \qquad \text{Eq. 3.12}$$

$$\varphi_i = \sum_\mu C_{\mu i}\, \chi_\mu \qquad \text{Eq. 3.13}$$

The optimization of Ψ_{CASSCF} is based, therefore, on the simultaneous variation of orbital coefficients $C_{\mu i}$ and configuration coefficients A_K, until reaching self-consistency. Once Ψ_{CASSCF} is optimized, the energy of the system is calculated as follows:

$$E = \langle \Psi | \hat{H} | \Psi \rangle = \sum_{i,j} h_{ij}\, D_{ij} + \sum_{i,j,k,l} g_{ijkl}\, P_{ijkl} \qquad \text{Eq. 3.14}$$

where h_{ij} and g_{ijkl} are the monoelectronic and bielectronic integrals, respectively:

$$h_{ij} = \langle \chi_i(1) | \hat{h} | \chi_j(1) \rangle \qquad \text{Eq. 3.15}$$

$$g_{ijkl} = \iint \varphi_i^*(\boldsymbol{q}_1)\varphi_j(\boldsymbol{q}_1) r_{12}^{-1} \varphi_k^*(\boldsymbol{q}_2)\varphi_l(\boldsymbol{q}_2)\, d\boldsymbol{q}_1 d\boldsymbol{q}_2 \qquad \text{Eq. 3.16}$$

where $\boldsymbol{r}$ is the position vector. $\boldsymbol{D}$ is the first order reduced density matrix, which is defined as a function of the expansion coefficients given in eq. 3.11:

$$D_{ij} = \langle \Psi | \hat{E}_{ij} | \Psi \rangle = \sum_{K,L} A_K^* A_L D_{ij}^{KL} = \sum_{K,L} A_K^* A_L \langle \Phi_K | \hat{E}_{ij} | \Phi_L \rangle \qquad \text{Eq. 3.17}$$

P is the second order reduced density matrix, with elements:

$$P_{ijkl} = \frac{1}{2} \sum_{K,L} A_K^* A_L \langle \Phi_K | \hat{E}_{ij}\hat{E}_{kl} - \delta_{kj}\hat{E}_{il} | \Phi_L \rangle \equiv \sum_{K,L} A_K^* A_L\, P_{ijkl}^{K,L} \qquad \text{Eq. 3.18}$$

where $P_{ijkl}^{K,L}$ are defined as the bielectronic coupling coefficients. One of the characteristics of the CASSCF method is the selection of the configurations (*i.e.* the orbitals) to be included in the wavefunction. In principle, the active space could include all the orbitals, leading to a so-called full CI (Configuration Interaction) treatment. Unfortunately, a full CI requires an unfeasibly high computational cost even for small size molecules, and therefore a limited number of orbitals has to be selected. The number and type of orbitals will depend on the chemical nature of the problem to be studied, in any case being necessary that all chemically relevant orbitals are part of the active space (*e.g.*, for a conjugated hydrocarbon the active space should include all π and π* orbitals). Therefore, when applying the CASSCF method all orbitals will be divided into three groups: (*i*) inactive orbitals, which remain doubly occupied; (*ii*) virtual orbitals, which stay unoccupied; (*iii*) active orbitals, where all possible electronic excitations are allowed, resulting in a total number N of configuration state functions which form Ψ_{CASSCF}, given by the following formula (for a defined state multiplicity) (*Cramer 2004*):

$$N = \frac{n!(n+1)!}{\left(\frac{m}{2}\right)!\left(\frac{m}{2}+1\right)!\left(n-\frac{m}{2}\right)!\left(n-\frac{m}{2}+1\right)!} \qquad \text{Eq. 3.19}$$

where m is the number of electrons and n the number of orbitals, usually indicated as CASSCF(m,n). With state-of-the-art computational resources, a CASSCF(4,4) is a straightforward task, being N=20, while a CASSCF(14,12) is highly demanding, being N=169884. Considering that the computational feasibility depends also on the basis set applied, we can nowadays set the upper limit to the size of the active space as a CASSCF(20,20).

3.1.2 The CASPT2 Method

One of the most convenient ways to include dynamical electron correlation effects in molecules is to apply a second order perturbation approach. In the CASPT2 method, a multiconfigurational CASSCF wavefunction $|\Psi_0\rangle$ is considered as zeroth order wavefunction for a second order perturbation approach to the correlation problem. The formulation presented was shown to be valid for any reference state built as a full CI wavefunction in a certain orbital subspace (*Andersson et al. 1990*).

$|\Psi_0\rangle$ is expanded in a configuration space which, for convenience, is divided into four subspaces: V_0 is the one dimensional space spanned by $|\Psi_0\rangle$ for the electronic state calculated; V_K is the orthogonal space to $|\Psi_0\rangle$ within the restricted full CI subspace used to generate the CASSCF wavefunction; V_{SD} is the space related to single and double excitation states generated from V_0; $V_{TQ..}$ is the space containing all higher order excitations not included in V_0, V_K and V_{SD}. It has to be noted that only the functions defined in the V_{SD} subspace interact with $|\Psi_0\rangle$ via the total Hamiltonian, and therefore it has to be considered that only V_{SD} contributes to the expansion of the first order wavefunction when formulating the zeroth order Hamiltonian.

Since the total dimension of the first order space corresponds to the dimension of V_{SD} (Andersson et al. 1990), the first order wavefunction can be expanded into a set of functions $|\Psi_j\rangle$ from V_{SD}:

$$|\Psi_1\rangle = \sum_{j=1}^{M} C_j |\Psi_j\rangle \qquad \text{Eq. 3.20}$$

where $M \geq V_{SD}$ dimension and the coefficients C_j are calculated by solving the following system of linear equations:

$$\sum_{j=1}^{M} C_j \langle \Psi_i | \hat{H}_0 - E_0 | \Psi_j \rangle = -\langle \Psi_i | \hat{H} | \Psi_0 \rangle, \; i = 1, \ldots, M \qquad \text{Eq. 3.21}$$

where the zeroth order energy E_0 can be readily calculated as:

$$E_0 = \langle \Psi_0 | \hat{H}_0 | \Psi_0 \rangle \qquad \text{Eq. 3.22}$$

It is reasonable to assume that , in the majority of cases, $M > V_{SD}$ dimension and therefore the double excitation states will be linearly dependent. Such linear (and near linear) dependence can be removed by diagonalizing the overlap matrix $\boldsymbol{S}$

$$S_{ij} = \langle \Psi_i | \Psi_j \rangle \qquad \text{Eq. 3.23}$$

and removing the eigenvectors corresponding to zero (or close to zero) eigevalues. Eq. 3.21 can then be solved by transforming the CI space into a orthonormalized form, and the second order energy can be finally obtained. The resulting CASPT2 energy takes into account a weighted sum over all active orbitals, being this formulation valid for all types of electronic excitations.

Usually, the inclusion of dynamical electron correlation effects brings to quantitative results in photochemistry and photophysics, when compared to experimental data. The main drawbacks are a considerably larger computational time than CASSCF calculations and the lack of an analytical energy gradient for medium and large size active spaces. Therefore, in this Ph.D. Thesis the CASPT2//CASSCF methodology is applied in all the cases that a CASPT2 treatment is not feasible, being a compromise between accuracy of results and computational expense: the CASSCF method is used to determine minimum energy paths by computing analytical gradients (see section 3.3.2), while the CASPT2 method was employed to compute single-point corrections to the energy.

An attempt to go beyond the CASPT2//CASSCF methodology, by scaling the CASSCF energy gradient in order to reproduce an approximate CASPT2 energy gradient, is shown in chapter 5.

3.1.3 Other methods

Apart from multiconfigurational *ab initio* methods, other quantum chemical methods were used when necessary. For ground-state electronic structure calculations, the Møller–Plesset second order perturbation method (MP2) was applied as a reliable (and computationally affordable) approximation of the CASPT2 wavefunction in any case that the ground-state could be correctly described by a closed shell single electronic configuration. The MP2 method uses a HF wavefunction as reference, by applying a second order perturbation. This concept corresponds to the explained CASPT2 method where, instead of a HF wavefunction, the reference is a CASSCF wavefunction (see section 3.2.2).

In other minor cases, density functional theory methods for ground-state optimization followed by time dependent-density functional theory methods (DFT and TD-DFT, respectively) were applied to study the absorption properties of that chromophores which CAS cannot be currently treated at the multiconfigurational level, in any case only after careful calibration with CASPT2//CASSCF methodology (by calculations on minimal chromophores) and/or available experimental data.

As a quantum chemical methodology, DFT is based on two theorems proved by Hohenberg and Kohn in 1964. The Hohenberg–Kohn existence theorem states that the energy of a molecular system depends on the ground-state electron density $\rho(\boldsymbol{q})$, since this density determines the Hamiltonian operator. Integration of the ground-state density gives the number of electrons, that interact one with each other and within an external potential (*i.e.* the attraction to the nuclei). The Hohenberg–Kohn existence theorem proves that the ground-state electron density determines the external potential, and therefore the Hamiltonian (*Hohenberg and Kohn 1964; Cramer 2004*).

By this formulation, the energy depends on the electron density, *i.e.* it is a density functional $E[\rho]$:

$$E[\rho] = T_e[\rho] + \int \rho(\boldsymbol{r})v(\boldsymbol{r})\, d\boldsymbol{r} + \frac{1}{2}\iint \frac{\rho(\boldsymbol{q}_1) - \rho(\boldsymbol{q}_2)}{|\boldsymbol{q}_1 - \boldsymbol{q}_2|} d\boldsymbol{q}_1 d\boldsymbol{q}_2 + E_{CE}[\rho]$$

Eq. 3.24

where $T_e[\rho]$ is the electron kinetic energy, the second and third term on the r.h.s. are related to the classical electrostatic interaction between electrons, while $E_{CE}[\rho]$ is the correlation and exchange energy term, containing all non-classical electronic interactions. This last term is the only one which exact formulation is not known, therefore requiring approximate expressions giving rise to different possible types of density functional.

The existence of electron density as a fundamental quantity is thus a first step, which is followed by demonstration that electron density obeys to a variational principle, and therefore it can be optimized. The Hohenberg–Kohn variational theorem assumes that a guess ground-state electron density is provided (thanks to the existence theorem), by which the proper number of electrons can be integrated. As a consequence, such electron density determines a guess wavefunction (Ψ_{guess}) and Hamiltonian (H_{guess}), permitting the evaluation of the expected energy (E_{guess}), being greater than or equal to the ground-state true energy (E_0):

$$\langle \Psi_{guess} | H_{guess} | \Psi_{guess} \rangle = E_{guess} \geq E_0 \qquad \text{Eq. 3.25}$$

By this procedure, it can be avoided to solve the Schrödinger equation to compute the energy, nevertheless leaving unsolved which criteria should be followed in order to choose different possible electron densities which could lead to more and more reliable ground-state energy ($E_{guess} \approx E_0$). Especially, a different approximation of $E_{CE}[\rho]$ can lead to a different final energy value, being necessary a careful decision of the density functional to be applied (*i.e.* a suitable density functional has to be calibrated for each set of molecules). That is why, in this Ph.D. Thesis, DFT calculations are always compared to experimental data and/or calibrated with multiconfigurational *ab initio* methods.

3.2 Quantum Mechanics/Molecular Mechanics Method

A hybrid Quantum Mechanics/Molecular Mechanics (QM/MM) model is composed by two subsystems: a QM region is focused on the description of a chemical reaction and the surrounding MM region is treated classically. Therefore, QM/MM methods are suitable to describe the effect of the environment on a particular molecular system, *e.g.* surrounding it by explicit solvent molecules, or considering the actual biomolecule where it is included (a base pair in DNA, an amino acid in a protein, etc.).

Different QM/MM schemes were designed and developed (Lin and Truhlar 2007). In this Ph.D. Thesis, we adopted an approach already implemented (see section 3.4) by which the Hamiltonian of the QM/MM model (H_{tot}) is a sum of three components:

$$H_{tot} = H_{QM} + H_{MM} + H_{QM/MM} \qquad \text{Eq. 3.26}$$

H_{QM} is the Hamiltonian of the QM system as treated in vacuum, while H_{MM} refers to the MM region treated with a classical force field. The interaction between QM and MM regions is described by the term $H_{QM/MM}$:

$$H_{QM/MM} = V_{QM/MM}^{elec} + V_{QM/MM}^{nucl} + V_{QM/MM}^{vdW} + V_{QM/MM}^{bond} \qquad \text{Eq. 3.27}$$

by which electrostatic, nuclear, van der Waals and bonding interactions are taken into account, respectively. Especially, the electrostatic and nuclear terms are given by the following relations:

$$V_{QM/MM}^{elec} = -\sum_i^n \sum_{B \in MM} \frac{q_B}{|\boldsymbol{q}_B - \boldsymbol{q}_i|} \qquad \text{Eq. 3.28}$$

$$V_{QM/MM}^{nucl} = \sum_A^M \sum_{B \in MM} \frac{Z_A q_B}{|\boldsymbol{q}_B - \boldsymbol{q}_A|} \qquad \text{Eq. 3.29}$$

$V_{QM/MM}^{elec}$ describes the interaction between the n electrons of the QM region with the B point charges (q_B) in the MM region; while $V_{QM/MM}^{nucl}$ is responsible for the interaction between the M nuclei of the QM region

(with Z_A being the proton number of nucleus A) and the B point charges of the MM region. For both electrostatic and nuclear terms the Electro-Static Potential Fitted (ESPF) method is applied (*Ferré and Angyan 2002*): one-electron operators are added to H_{QM} in order to calculate the interaction between the QM charges distribution and the MM electrostatic potential field, considered as an external field, resulting in the following interaction energy:

$$\Delta E = \sum_a \sum_{\mu\varepsilon} P_{\mu\varepsilon} Q^a_{\mu\varepsilon} V^a \qquad \text{Eq. 3.30}$$

where $P_{\mu\varepsilon}$ and $Q^a_{\mu\varepsilon}$ are the density matrix and multipole-like matrix elements interacting with the electrostatic potential V^a calculated at the point-center a.

Van der Waals interactions are taken into account by a short-range Lennard-Jones term, assigning parameters to both QM and MM atoms:

$$V^{vdW}_{QM/MM} = \sum_{A>B} 4\varepsilon_{AB} \left[\left(\frac{\sigma_{AB}}{d_{AB}}\right)^{12} - \left(\frac{\sigma_{AB}}{d_{AB}}\right)^{6} \right] \qquad \text{Eq. 3.31}$$

where, for every AB couple, ε is the depth of the potential well, σ is the finite distance at which the potential between A and B is zero, and d_{AB} is the distance between A and B.

If the frontier between QM and MM regions involves covalent bonds, an additional term ($V^{bond}_{QM/MM}$) is added to H_{tot}, by including some empirical bonded terms. The scheme used to treat frontier bonds is the Link Atom (LA) scheme, where a monovalent atom (usually hydrogen) is used to saturate the QM system. Applying the Morokuma's scheme for LA positioning, the distance between LA and the first linked QM atom (d_{QM_1-LA}) is modified with respect to the frontier QM and MM atoms ($d_{QM_1-MM_1}$) while optimizing, thanks to a scaling factor (s_{LA}):

$$d_{QM_1-LA} = s_{LA} d_{QM_1-MM_1} \qquad \text{Eq. 3.32}$$

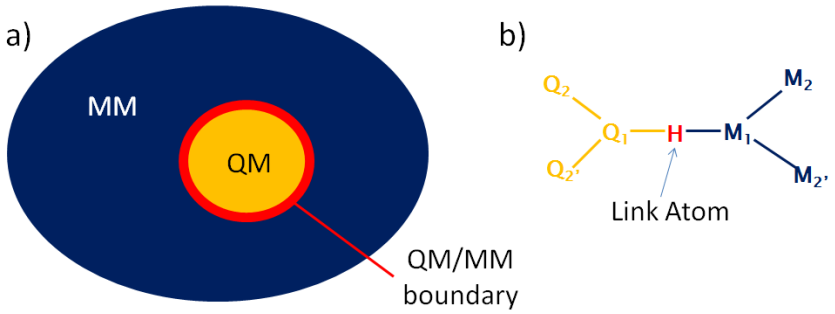

Figure 3.1 General scheme of a QM/MM model (**a**) and of the QM/MM boundary treatment with hydrogen as Link Atom (**b**).

3.3 Modeling Photochemical Reaction Pathways

The potential energy surface (PES) can be considered the key concept by which modeling of chemical reactions is possible. A PES is a multidimensional surface where each point corresponds to the potential energy of a molecular structure. Especially, a PES has a number of dimensions equal to the number of degrees of freedom within the molecule, *i.e.* 3*N*-6 dimensions, where *N* is the number of atoms. The definition and application of PESs to describe mechanisms and dynamics in chemistry are a direct consequence of the Born–Oppenheimer approximation, by which the motion of nuclei and electrons can be separated (see section 3.1): reactants, products and intermediates (*i.e.* equilibrium structures) correspond to minima on the PES, while transitions states are saddle points.

More in detail, first and second derivatives of the potential energy with respect to each of the variables (3*N*-6) define mathematically the different local topological elements that can be found on a PES (*Levine 1991; Cramer 2002*): the first derivative of the potential energy is the gradient vector; the second derivative of the potential energy is the Hessian matrix. In physical terms, the negative of the gradient vector corresponds to the force vector acting on the molecule, while the Hessian matrix elements correspond to force-constant elements. When the first derivative with respect to each of the variables is zero, gradient and force vectors have zero length, defining a stationary point. In order to determine which kind of stationary point is, the second derivative has to be calculated: if all the eigenvalues of the Hessian matrix are positive, that point on the PES is a minimum (local or global) in all 3*N*-6 dimensions. On the contrary, if all the eigenvalues of the Hessian matrix are negative, the point is a PES maximum. A saddle point of *n*-th order corresponds to *n* negative eigenvalues and all but *n* positive eigenvalues: the point is a maximum in *n* mutually perpendicular directions, and a minimum in all but *n* perpendicular directions. The case of first-order saddle point is of special interest in chemistry, since it defines a transition state structure.

In the following sections we will describe how to calculate spectroscopic properties (3.3.1), the different techniques to define relaxation pathways (3.3.2), how to characterize a crossing between

electronic states (3.3.3), a brief introduction to semiclassical dynamics (3.3.4) and finally, the computer programs used (3.3.5).

3.3.1 Spectroscopic Properties

In electronic spectroscopy, two quantities are fundamental in order to reproduce absorption and emission spectra: the energy difference between distinct electronic states and the oscillator strength. Indeed, an experimental UV/visible spectrum is characterized by absorption or emission wavelengths (corresponding to the energies of the electronic transitions) and absorption or emission intensities (which depend on oscillator strengths and indicate the transition probabilities). In this Ph.D. Thesis, both quantities are preferably calculated at the CASPT2 level of theory. We have already shown how to calculate the CASPT2 energy (see section 3.1.2), therefore here we will focus on the determination of transition dipole moment μ and oscillator strength f.

An electronic transition is intended from an initial state i to a final state f, being usually (but not necessarily) i the ground-state and f one of the excited-states for absorption, while i is one of the excited-states and f the ground-state for emission. More in general $i < f$ for absorption, while $i > f$ for emission. The transition dipole moment couples the wavefunctions of initial and final states (Ψ_i and Ψ_f), resulting in a vector $\boldsymbol{\mu}_{\mathrm{if}}$ which expresses the redistribution of electrons in the molecular system after the transition (*Sakurai 1967*):

$$\boldsymbol{\mu}_{if} = \int_{\boldsymbol{q}} \Psi_i^*(\boldsymbol{q}) \hat{\mu} \Psi_f(\boldsymbol{q}) d\boldsymbol{q} \qquad \text{Eq. 3.33}$$

being $\boldsymbol{q}$ the position vector. It may be shown that the square of $\boldsymbol{\mu}_{if}$ module is, in case of emission:

$$\mu_{if}^2 = A_{if} \frac{3\varepsilon_0 hc^3}{2\omega_{if}^3} \qquad \text{Eq. 3.34}$$

where ε_0 is the dielectric constant in vacuum, h the Planck's constant, c the speed of light, ω_{if} the resonance frequency of the transition, and A_{if} is the Einstein coefficient to describe the total rate of spontaneous emission. The emission oscillator strength f_{if}^{em} can be then defined by the relation (*Hilborn 1982*):

$$f_{if}^{em} = -\frac{1}{3}\frac{A_{if}}{\gamma_{cl}} \quad \text{Eq. 3.35}$$

where

$$\gamma_{cl} = \frac{e^2\omega_{if}^2}{6\pi\varepsilon_0 m_e c^3} \quad \text{Eq. 3.36}$$

where e and m_e are charge and mass of the electron. γ_{cl} determines the classical radiative decay rate of the single-electron oscillator at frequency ω_{if}. The absorption oscillator strength f_{if}^{abs} is then defined by:

$$g_{down} f_{if}^{abs} \equiv -g_{up} f_{if}^{em} \equiv gf \quad \text{Eq. 3.37}$$

where g_{down} and g_{up} are the degeneracy factors of the two electronic states (upper and lower in energy). The f values have been defined in order that if (*i*) $g_{down} = 1$ (*i.e.* the angular momentum of the lower state in energy $J_{down} = 0$, (*ii*) $g_{up} = 3$ (*i.e.* $J_{\mathrm{up}} = 1$), and (*iii*) $A_{if} = \gamma_{cl}$, then $f_{if}^{abs} = 1$ and $f_{if}^{em} = -\frac{1}{3}$. Tables of gf values can be found in literature (Hilborn 1982).

The absorption oscillator strength can be finally related to A_{if}:

$$f_{if}^{abs} = \frac{g_{up}}{g_{down}}\frac{2\pi\varepsilon_0 m_e c^3 A_{if}}{e^2\omega_{if}^2} \quad \text{Eq. 3.38}$$

As alternative procedure, f_{if}^{abs} can be determined by comparing the absorption cross section of a classical oscillator with that determined by the

Einstein B coefficients (which are defined in terms of transition rates for induced absorption and stimulated emission).

3.3.2 Relaxation Pathways

After absorption to an excited-state, or after locating minima and saddle points, a Minimum Energy Path (MEP) connecting these distinct points on the PES can be determined. Especially, a MEP can be defined in terms of the Intrinsic Reaction Coordinate (IRC). The IRC is the path that a classical particle follows when proceeding with infinitesimal velocity (*i.e.* infinitesimal kinetic energy) on a PES, and mathematically corresponds to a steepest-descent path in mass-weighted Cartesian coordinates. Different algorithms have been proposed for the IRC calculation. Here, we will use the one proposed by Schlegel: a constrained optimization is performed on the surface of a hypersphere centered at a defined step size along the energy gradient vector calculated for the previous IRC point. Therefore, the two consecutive points of the IRC are connected by an arc of a circle tangent to the energy gradient vectors of both points. This method allows for large step sizes to be applied (*e.g.* 15-40 Bohr·amu$^{1/2}$), being able to reproduce accurately the PES curvature, especially when including predictor-corrector methods (*Hratchian and Schlegel 2004; 2005*).

Every minimum or saddle point was characterized by calculating the force constants and the resulting vibrational frequencies. This is possible by determining the second derivatives of the energy with respect to the Cartesian coordinates, followed by transformation to mass-weighted coordinates.

3.3.3 Crossings Between Electronic States

In the vicinity of electronic state crossings the Born–Oppenheimer approximation (see section 3.1) is not anymore valid, being necessary to take into account non-adiabatic coupling effects for a correct description of

the photochemical reaction path. The study of molecular systems is often based on the Born−Oppenheimer approximation, which differentiates between fast moving electrons and slow moving nuclei, and therefore leads to the generation of electronic (adiabatic) eigenstates and the corresponding non-adiabatic coupling terms. Mechanistic and dynamical treatments are usually carried out by applying the Born–Oppenheimer approximation, which assumes the existence of single decoupled adiabatic states, therefore ignoring the non-adiabatic coupling between the electronic states. The main justification resides in the fact that non-adiabatic coupling terms are proportional to $(m_e/m_p)^{1/2}$ (where m_e and m_p are electron and proton mass, respectively), being two orders of magnitude smaller than other characteristic terms of the nuclear Schrödinger equation. However, when electronic states become degenerate in energy, non-adiabatic coupling terms become, in principle, infinitely large and can explain the topological effects observed for the corresponding molecular structures (*Zener 1932; Baer 2006*).

For diatomic molecules, two electronic states can intersect only if they belong to a different (spatial or spin) symmetry. However, in polyatomic molecules two (or more) electronic states can be degenerate in energy (E) even if they have the same symmetry (*Herzberg and Longuet-Higgins 1963*). If two PESs (1 and 2) intersect for a certain molecular structure described by the internal coordinates $\boldsymbol{q}$, this leads easily to the condition:

$$E_1(\boldsymbol{q}) = E_2(\boldsymbol{q}) \qquad \text{Eq. 3.39}$$

and we should expect an intersection subspace of *M*-1 dimensions (where *M*=3*N*-6 and *N* is the number of atoms in the system). However, E_1 and E_2 are two solutions of the same eigenvalue problem given by a single Hamiltonian H, and therefore they are not independent of each other, leading to an additional condition (*von Neumann and Wigner 1929; Teller 1937*).

The two intersecting adiabatic states Ψ_1 and Ψ_2 can be expressed as linear combinations of two diabatic orthogonal states Φ_1 and Φ_2 in the complementary hyperspace to the one spanned by all other eigenstates Ψ_n

($n \geq 3$), for which the energies E_n ($n \geq 3$) are non-degenerate with E_1 and E_2:

$$\Psi_1 = c_{11}\Phi_1 + c_{21}\Phi_2;\ \Psi_2 = c_{12}\Phi_1 + c_{22}\Phi_2 \qquad \text{Eq. 3.40}$$

By solving the eigenvalue problem given by the 2×2 matrix $H_{ij} = \langle \varphi_i | \hat{H} | \varphi_j \rangle$, the expansion coefficients c_{ij} and the corresponding energies (E_1 and E_2) can be determined. The matrix elements are therefore:

$$H_{11} = \langle \Phi_1 | \hat{H} | \Phi_1 \rangle$$

$$H_{22} = \langle \Phi_2 | \hat{H} | \Phi_2 \rangle \qquad \text{Eq. 3.41}$$

$$H_{12} = \langle \Phi_1 | \hat{H} | \Phi_2 \rangle = H_{21}$$

It can be demonstrated that E_1 and E_2 have the following expressions (*Schlegel 1987*):

$$E_{1,2} = \frac{(H_{11}+H_{22}) \pm \sqrt{(H_{11}-H_{22})^2 + 4{H_{12}}^2}}{2} \qquad \text{Eq. 3.42}$$

Therefore, in order to fulfill that $E_1 = E_2$, two independent conditions have to be satisfied:

$$H_{11} = H_{22};\ H_{12} = H_{21} = 0 \qquad \text{Eq. 3.43}$$

leading to the existence of at least two independent coordinates, $\boldsymbol{q}_1$ and $\boldsymbol{q}_2$.

In a diatomic molecule, H_{12} is always zero for states of different symmetry, thus only $H_{11} = H_{22}$ has to be satisfied. This is coherent with the existence of only one internal coordinate (the interatomic distance), being

necessary a suitable value to satisfy the condition. If the two states belong to the same symmetry, an intersection is therefore not possible.

In a polyatomic (three or more atoms) molecule, the increased number of degrees of freedom allows both conditions of eq. 3.43 to be satisfied simultaneously (even for the same symmetry) for suitable values of $\boldsymbol{q}_1$ and $\boldsymbol{q}_2$. This means that a branching plane spanned by $\boldsymbol{q}_1$ and $\boldsymbol{q}_2$ vectors can be defined (with the origin at the point where both conditions of eq. 3.43 are satisfied), where energy degeneracy is left. On the other hand, the *M*-2 (*M*=3*N*-6) hyperspace defined by all degrees of freedom but $\boldsymbol{q}_1$ and $\boldsymbol{q}_2$ determines the coordinates which can be varied remaining in the crossing region (*i.e.* energy degeneracy holds true).

Imposing the conditions of eq. 3.43 two eigenvalues are found, resulting in the equation of a double cone with vertex at the origin. This is why crossing points between electronic states are called conical intersections (*CI*s). A schematic picture is given in Figure 3.2.

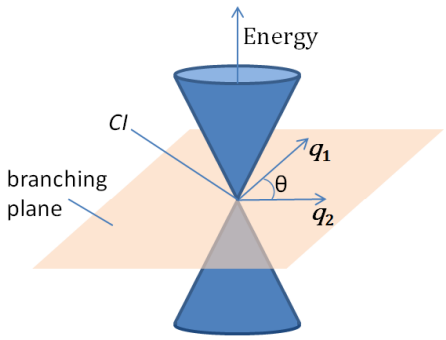

Figure 3.2 Scheme of a conical intersection between two electronic states: the upper cone constitutes a funnel to proceed on the lower PES. $\boldsymbol{q_1}$ and $\boldsymbol{q_2}$ vectors define a branching plane centered at the vertex (*CI*), determining the only two independent coordinates where energy degeneracy is left.

The crossing can be real or avoided: considering the two diabatic orthogonal states φ_1 and φ_2 which form the two adiabatic states Ψ_1 and Ψ_2 (eq. 3.40), the crossing condition is fulfilled when φ_1 and φ_2 cross each other, *i.e.* when $H_{11} = H_{22}$. At this point the energies of the adiabatic functions are $E_1 = H_{11} - H_{12}$ and $E_2 = H_{11} + H_{12}$. The energy gap is therefore $E_2 - E_1 = 2H_{12}$. If $H_{12} = 0$ the crossing is real (*i.e.* a *CI*), while if $H_{12} \neq 0$ the crossing is avoided (*i.e.* an avoided crossing, *AC*: upper and

lower PESs become near in energy but, instead of crossing, they repel each other).

In the adiabatic basis, $\boldsymbol{q}_1$ and $\boldsymbol{q}_2$ are defined as follows:

$$\boldsymbol{q}_1 = \frac{\partial(E_1 - E_2)}{\partial \boldsymbol{q}} \qquad \text{Eq. 3.44}$$

$$\boldsymbol{q}_2 = \left\langle \Psi_1 \middle| \frac{\partial H}{\partial \boldsymbol{q}} \middle| \Psi_2 \right\rangle \qquad \text{Eq. 3.44}$$

$\boldsymbol{q}_1$ corresponds to the gradient difference (**GD**) vector, while $\boldsymbol{q}_2$ is parallel to the direction of the derivative coupling (**DC**) vector:

$$\mathbf{DC} = \left\langle \Psi_1 \middle| \frac{\partial}{\partial \boldsymbol{q}} \Psi_2 \right\rangle \qquad \text{Eq. 3.46}$$

Apart from their mathematical description, **GD** and **DC** vectors have a physical meaning: the **GD** vector measures the distortion of the system leading to the largest variation of the energy difference between the two electronic states involved in the crossing. The **DC** vector measures the distortion of the system providing the maximum coupling between the two electronic states involved in the crossing. A brief analysis of **GD** and **DC** directions is crucial in characterizing the crossing: as we can see in Figure 3.2 through eq. 3.44 and 3.45, **GD** and **DC** vectors have the same origin and need to form a certain angle $\theta > 0^o$ between them in order to define a two-dimensional branching plane, and thus a *CI*. Otherwise, if **GD** and **DC** vectors are parallel ($\theta = 0^o$) and the former is non-vanishing, a branching plane does not exist. Instead, only a one-dimensional hyperline can be defined, being the case of an *AC*.

The characterization of the branching plane in the vicinity of a *CI* defines the topology of the real crossing. This is possible by calculating a circle contained in the branching plane of evenly distributed points at a certain radius around the *CI* (*i.e.* a scan around the *CI*), and analyzing energy and wavefunction of the two electronic states along the circle. Especially,

three different crossing topologies can be found (*Atchity et al. 1991*), as shown in Figure 3.3.

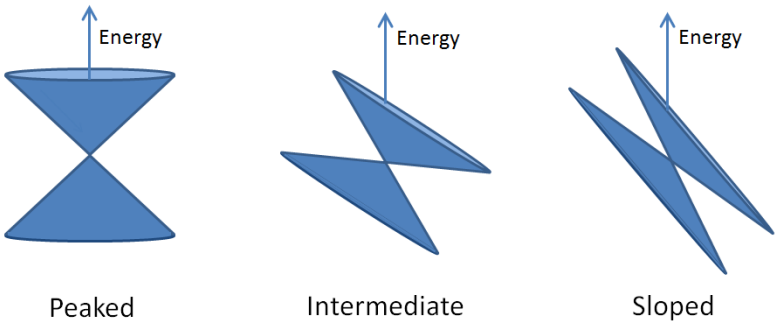

Figure 3.3 Topologies of electronic state crossings: peaked, intermediate and sloped.

The importance of the topology is usually connected to the efficiency of the crossing: a peaked crossing is expected to be more efficient than a sloped crossing, because of the sudden change in the character of the wavefunctions once decay to the lower PES happens, coupled to a larger energy difference. Moreover, the topology of the lower PES in the vicinity of a *CI* gives important information about the evolution of the system: in principle, two or more reaction pathways are accessible from a *CI*, corresponding to two or more products if the intersection is between an excited-state and the ground-state. Therefore, it is crucial to determine the initial relaxation directions (IRDs) just after decay to the lower PES. This can be accomplished by examining the scan around the *CI* as a plot of the lower PES energy: every energy minimum along the scan determines a geometry from where a relaxation pathway departs, and therefore the vector connecting the *CI* to a scan minimum defines an IRD (Figure 3.4). The MEP calculated along each IRD results in a possible relaxation pathway, being necessary to run dynamics in order to know which relaxation pathway will be interested by a certain trajectory (see next section). The branching plane formed by $\boldsymbol{q}_1$ and $\boldsymbol{q}_2$ (**GD** and **DC** vectors) is just a linear approximation in internal coordinates of the energy difference between both states. Therefore the reaction paths departing from a *CI* can be found by geometry optimization on a hypersphere (*Celani et al. 1995*).

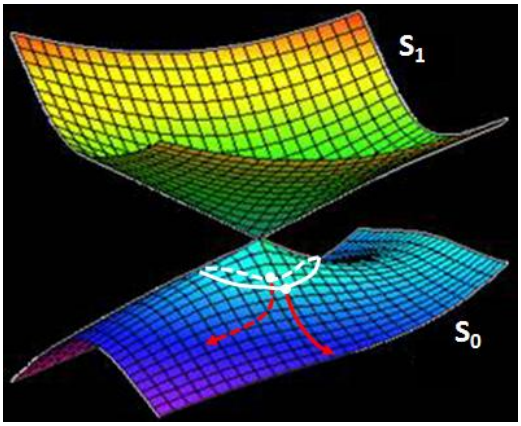

Figure 3.4 Scheme of the MEPs (red arrows) departing from the two minima resulting from the scan around the *CI* on the lower energy PES (S_0 in this example).

3.3.4 Semiclassical Dynamics

The computational techniques presented above are necessary in order to determine the reaction pathways, giving a mechanistic description of the photochemistry involved. However, a dynamical study is also important, since it defines the time scale of the reaction, and it helps clarifying whether the minimum energy path is really representative, or if additional parts of the potential energy surface are explored by the dynamics trajectories, because of vibrational energy. Moreover, a mechanistic study of ultrafast photochemical processes usually focuses on the localization of the minimum energy crossings between electronic states, being in principle possible that a hop event from a higher energy surface to a lower energy surface does happen before the minimum energy crossing point, when the two surfaces are just close enough in energy. Therefore, it is important to define with enough accuracy a trajectory surface hopping method, considering that the topology of the intersection space determines the final fate of the photoproducts formation.

During this Thesis, classical trajectories were calculated in the S_1 excited-state of a retinal chromophore model (2-*cis*-α-Me-$C_5H_6NH_2^+$), in

order to determine the differences between a CASSCF (qualitative) and a CASPT2 (quantitative) description. Moreover, an attempt to approximate "on the fly" the CASPT2 energy gradient by projecting the CASSCF energy gradient is described, being applied to excited-state dynamics (see chapter 5). For this reason, different trajectory surface hopping methods will not be treated here, since only a single potential energy surface was studied for the presented trajectories, in the framework of a methodological development. Nevertheless, we should mention two trajectory surface hopping methods: the Landau–Zener model (*Landau 1932; Zener 1932; Wittig 2005*) and, more recently, the Tully's "fewest switch" surface hopping technique (*Tully 1990; Granucci and Persico 2007*).

3.3.5 Software and Packages

All calculations were performed with Gaussian 03, Gaussian 09, MOLCAS 6, MOLCAS 7 and Tinker 4.2 suite of programs.

More in detail, the absorption spectrum oscillator strength and the CASPT2 calculations were performed with the MOLCAS program (*Aquilante et al. 2010*). The calculation of the relaxation pathways, including optimization, IRCs, MEPs, localization of minima and transitions states, were performed with either Gaussian (*Frisch et al. 2004*) or MOLCAS. The characterization of the crossings between electronic states was possible through the calculation of non-adiabatic coupling vectors (by Gaussian) and subsequent scanning of the branching plane (by a program developed in the group).

QM/MM calculations were performed by the available MOLCAS/Tinker interface (Molcas/Tinker QM/MM 2012), being the setup of the MM model carried out with the Tinker program (*Tinker Molecular Modeling 2012*).

4. Energy, Electron and Proton Transfer Processes

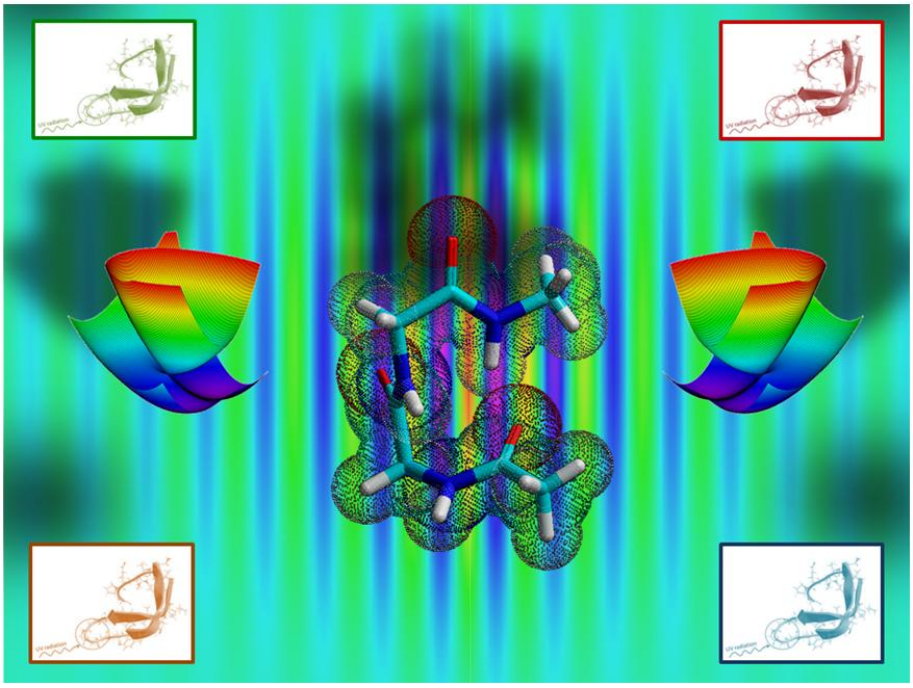

"First Principles Study of Photostability within

Hydrogen-bonded Amino Acids"

Marco Marazzi, Unai Sancho, Obis Castaño and Luis Manuel Frutos

Physical Chemistry Chemical Physics **2011**, *13*, 7805-7811

Issue 17 cover artwork

4.1 UV Irradiation of Amino Acids and Proteins

By means of ab initio multiconfigurational quantum chemistry (CASPT2//CASSCF methodology) coupled to molecular mechanics when necessary (hybrid QM/MM method), we studied photoinduced energy, electron and proton transfer processes within selected amino acids and protein systems. The main results are summarized here, showing the related publications in the next sections.

We present evidences for a possible mechanism of photoinduced proton transfer in a β-turn motif composed by three glycines, being a secondary structure commonly found in proteins (section 4.1.1, 4.1.2). Special attention is posed on the hydrogen bond formed between CO and NH groups of two facing glycines on the ground-state, by which a β-turn motif is able to reverse the direction of the protein backbone, often promoting the formation of antiparallel β-sheets (see, for example, the backbone strand Thr170-Gly193 of the protease B peptide chain).

We focused on photoinduced proton transfer as a general mechanism to provide (or at least enhance) photostability in proteins: we describe the mechanism by which the incoming UV irradiation is dissipated as thermal energy through vibrational modes (*i.e.* non-radiative decay), reducing the yield of photodegradation and therefore protecting from eventual damages (*Sekhar and Plapp 1988; Warshel et al. 1989; Dobson and Hore 1998; Li et al. 1998; Lu and Voth 1998; Lyon et al. 2002; Pal and Zewail 2004; Callegari and Kelly 2006; Schreier et al. 2007*). This implies the activation of electronic state crossings as highly efficient funnels to allow ultrafast (sub-picosecond) recovery of the initial bioactive structure on the ground-state.

Our quantitative results show the following mechanism: after vertical excitation (*i.e.* absorption) to the lowest optically bright state, intrapeptide electron transfer is expected by population of a charge transfer state via an avoided crossing. The unbalanced electrostatics of the two glycines involved in electron transfer promotes proton transfer, leading to net transfer of a hydrogen atom (CO···HN → CO-H···N). Finally, a conical intersection between charge transfer and ground-state corresponds to back electron transfer, which drives back proton transfer, permitting to reform

the initial closed shell configuration (CO-H···N → CO···HN). A metastable CO-H···N photoproduct was also found, being expected to evolve rapidly towards the formation of the initial CO···HN structure because of the energetic and structural proximity with the charge transfer/ground-state conical intersection aforementioned.

Summarizing, forward-backward Photoinduced Proton coupled electron Transfer (PPT) was found to be a highly efficient excited-state deactivation pathway between two hydrogen-bonded backbone moieties. This mechanism was already proposed experimentally (*Nir et al. 2000; Crespo-Hernandez et al. 2004; Samoylova et al. 2009*) and computationally (*Hammes-Schiffer 2001; Sobolewski and Domcke 2004; Frutos et al. 2007; Lan et al. 2008*) in DNA base pairs, but it is still largely unexplored in proteins (*Sobolewski and Domcke 2006; Shemesh et al. 2009*), being a challenge even with state-of-the art techniques (*e.g.* femtosecond laser spectroscopy). Therefore, a theoretical approach can help in elucidating the processes involved and their eventual feasibility.

The key step of the overall mechanism was found to be the population of the charge transfer state from the lowest optically bright state, which requires to overcome a small energy barrier of only ca. 2 kcal·mol^{-1}, resulting in a feasible process thanks to a vibrational excess energy of 14.2 kcal·mol^{-1}.

An additional photoinduced mechanism was also found to be potentially relevant in providing UV photostability to hydrogen-bonded peptides and proteins: singlet-singlet Dexter-type photoinduced energy transfer between the two hydrogen-bonded amino acids (section 4.1.2). By this mechanism ultrafast population of a low-energy optically dark state is possible: after absorption to the lowest optically bright state (a $^1(\pi,\pi^*)$ locally excited-state, confined in a single amino acid, **A**), a barrierless minimum energy path indicates decrease in energy until an avoided crossing with an optically dark state (a $^1(n,\pi^*)$ excited-state located on the hydrogen-bonded amino acid, **B**) is found. This electronic state crossing permits non-radiative population of the low-energy dark state, transferring energy across the hydrogen-bond from one amino acid to the facing one (**A** → **B**). An analysis of the geometrical structure at the avoided crossing and of its topology clarifies the necessary molecular characteristics which allow this process: the parallel non-adiabatic coupling vectors indicate coupling of

both C=O stretching modes, promoted by pyramidalization centered on the carbonyl carbon atom of **A** and on the nitrogen atom of **B**, resulting in a final alignment of the C=O···H-N moiety.

Photoinduced singlet-singlet energy transfer was therefore proven to be in competition with forward-backward photoinduced proton coupled electron transfer. Especially, the first step in PPT (*i.e.* electron transfer) is a high probability event, thanks to possible population of two charge transfer states, both leading to energy stabilization coupled to proton transfer, finally allowing the net transfer of a hydrogen atom along the intrapeptide hydrogen bond.

After studying photoinduced energy, electron and proton transfer processes in peptide minimal models (section 4.1.1, 4.1.2), the attention was focused on understanding the influence of protein environment on photostability mechanisms. Especially, the tyrosine corner is proposed as a featured element to enhance photostability in human γB-crystallin, one of the main structural proteins forming the vertebrate eye lens (section 4.1.3) (*Oyster 1999*). In α-, β- and γ-crystallins, photostability mechanisms are of fundamental importance, since these proteins are not subject to turnover during a whole lifetime. Therefore the long-term transparency of the eye lens is guaranteed by high stability against UV/visible irradiation. If the crystallin structure undergoes changes or damages, protein aggregates could be formed in the lens cells, blocking partially or completely the light, which is not able anymore to reach the retina (*Benedek 1997*). In the medical point of view, this phenomenon corresponds to a cataract, one of the major cause of blindness worldwide (*Clark 1994*). In spite of several biochemical, molecular biology and medical oriented studies, the molecular causes of cataract are still not completely understood (*Horwitz 1992; Merck et al. 1993; van Boekel et al. 1996; Bloemendal et al. 2004*).

We proposed efficient ultrafast non-radiative pathways by which the incoming UV irradiation could be dissipated in γB-crystallin. Especially, the tyrosine corner is a highly conserved motif found in all β- and γ-crystallins (*i.e.* the structural proteins of the eye lens), characterized by a tyrosine side chain hydrogen-bonded to the backbone. In order to elucidate the effects of the protein environment on the tyrosine corner, two systems are studied: a quantum mechanics model of the tyrosine corner in vacuo and a QM/MM model of the tyrosine corner surrounded by γB-crystallin. In

both models we found and described two competing mechanisms: photoinduced Dexter-type singlet-singlet energy transfer to an originally dark $^1(n,\pi^*)$ state, and forward-backward proton coupled electron transfer.

Among them, PPT provides a mechanism for feasible ultrafast internal conversion, fulfilling the requirements for efficient UV photostability. The key structural element is found to be the hydrogen bond between tyrosine side chain and the backbone, which permits population and further energy stabilization of a charge transfer state. In absence of the hydrogen bond, only photoinduced energy transfer mechanisms would be eventually possible, leading in any case to fluorescence (or phosphorescence) from $^1(n,\pi^*)$ or $^1(\pi,\pi^*)$ states minima.

When compared to tyrosine corner in vacuo, the protein environment contributes to the following processes:

- The energy barrier of 5.49 kcal·mol^{-1} determined in vacuo for populating the charge transfer state is not found in the QM/MM protein model, leading to a barrierless PPT mechanism, and therefore crucially increasing its efficiency.
- Förster resonance energy transfer can be additionally proposed to Dexter-type energy transfer, as a mechanism to quench fluorescence, as suggested by available experimental data.

Considering the high stability of the tyrosine corner conformation in both β- and γ-crystallins (confirmed experimentally), our results describe general mechanisms acting in the eye lens, by which UV-photostability could be enhanced and cataract formation avoided.

As possible future perspectives, tyrosine corner could be introduced as a molecular framework in different proteins, in order to provide (or increase) the photostability of the overall protein against UV irradiation around 260 nm, being necessary only the formation of a hydrogen bond between the tyrosine side chain and the backbone.

4.1.1 Photoinduced Proton Transfer as a Possible Mechanism for Highly Efficient Excited-State Deactivation in Proteins

THE JOURNAL OF PHYSICAL CHEMISTRY Letters

pubs.acs.org/JPCL

Photoinduced Proton Transfer as a Possible Mechanism for Highly Efficient Excited-State Deactivation in Proteins

Marco Marazzi,[†] Unai Sancho,[†] Obis Castaño,[†] Wolfgang Domcke,[‡] and Luis Manuel Frutos*[,†]

[†]Departamento de Química Física, Universidad de Alcalá, 28871 Alcalá de Henares (Madrid), Spain and [‡]Department of Chemistry, Technische Universität München, D-85747 Garching, Germany

ABSTRACT CASSCF//CASPT2 pathways for a two-glycine minimal model system show that photoinduced electron-driven forward and backward proton transfer could play an important role for the stability of proteins against damage by UV radiation, when a hydrogen bond is located between the two amino acids. The overall photoinduced process involves two electron and proton transfer processes (forward and backward) and results in the reformation of the initial closed-shell electronic structure of the system.

SECTION Molecular Structure, Quantum Chemistry, General Theory

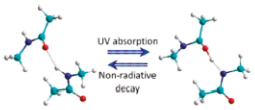

Exposure to UV-radiation represents a serious risk for living matter, since it can cause changes in the structure of proteins and DNA, provoking photodamage in nucleic acids,[1,2] or loss of protein functionality in fundamental enzymatic processes (e.g., substrate recognition,[3−5] or catalysis of chemical reactions[6−9]). It has been proposed experimentally[10−12] and computationally[13−18] that photoinduced proton transfer (PPT) could be a process providing efficient stability against UV radiation for hydrogen-bonded biomolecules, reducing the yield of photodegradation.

In proteins, secondary structure (α-helix, β-sheet, etc.) is crucial in determining their overall structure, with the CO and NH groups of the backbone being primarily important in the formation of hydrogen bonds between different peptides of the same chain.[19,20] These hydrogen bonds have been pointed out to be key structures enabling PPT, where a mechanism involving forward−backward proton transfer along the C═O···H−N hydrogen bond coordinate could be responsible for the photostability of proteins, converting the absorbed energy of the photon into vibrational energy, which is then dissipated by the environment.[17,18]

Multiconfigurational self-consistent-field methods have been demonstrated to be very useful in qualitatively describing the properties of excited-state potential-energy surfaces. Nevertheless, the inclusion of dynamic correlation is crucial in order to quantitatively describe the features of excited states. For this reason, the CASSCF//CASPT2 methodology[21] has been used to study the mechanism of the PPT process in a β-turn model system (see Figure 1). Indeed, the complete optimized reaction pathways have been determined, including the characterization of the electronic crossings involved in the process. The studied model system consists of two amino acids that are properly constrained to mimic two alternate glycines within a β-turn secondary structure. This secondary structure is commonly present in proteins for reversing the direction of the peptide chain, often promoting the formation of antiparallel β-sheets (Figure 1).

By restraining the relative position of the C1 and C2 methyl moieties,[22] the conformation and the corresponding hydrogen bond of the β-turn are correctly described within a minimal model of two hydrogen-bonded amino acids (**A** and **B**) (Figure 1).

Our results show that after excitation to the lowest optically bright state, a charge transfer (CT) state can be efficiently populated via an avoided crossing, giving rise to an intrapeptide electron transfer process. The electron transfer from **B** to **A** promotes the forward proton transfer from the NH group to the CO moiety. Finally, a conical intersection, i.e., a crossing between electronic states of the same spin multiplicity, between CT and ground state (GS) provides the funnel for efficient population of the GS, recovering the initial structure of the system by a second (backward) proton transfer. The overall process provides an efficient photochemical pathway for photostability.

Two locally excited bright states have been identified: one of them localized in the glycine **A**, corresponding to a $^1(\pi_A,\pi_A^*)$ state, and a second one, $^1(\pi_B,\pi_B^*)$, localized on the glycine **B**, the vertical excitation energies of which are 6.85 and 7.16 eV, respectively. We will focus on the evolution of the $^1(\pi_A,\pi_A^*)$ state, i.e., the lowest excited state corresponding to the most feasible excitation. In the following, the $^1(\pi_A,\pi_A^*)$ state will be referred to as the locally excited (LE) state. The $^1(n_A,\pi_A^*)$ and $^1(n_B,\pi_B^*)$ locally excited dark states of both amino acids lie below in energy (5.72 and 6.06 eV for glycine **A** and **B**, respectively). Finally, a $^1(\pi_B\rightarrow\pi_A^*)$ CT state appears at 8.48 eV, involving an electron transfer from glycine **B** to **A**. The vertical excitation to the LE state yields a vibrational excess energy of 14.2 kcal/mol (the 0−0 transition is located at 6.23 eV). These results for the absorption spectrum are in

Received Date: November 12, 2009
Accepted Date: December 10, 2009
Published on Web Date: December 15, 2009

DOI: 10.1021/jz900262w | J. Phys. Chem. Lett. 2010, 1, 425–428

THE JOURNAL OF PHYSICAL CHEMISTRY Letters
pubs.acs.org/JPCL

agreement with previous CASPT2 calculation on other polyglycine systems.[23]

After excitation of the peptide **A** to the LE state, the CT state can be populated via an avoided crossing between the LE and CT energy curves. This avoided crossing acts as a transition state for the electron transfer from glycine **B** to **A**. In order to reach the LE/CT crossing, the O···H distance of the hydrogen bond has to be shortened to ca. 1.3 Å (see Figure 2).

The efficiency of the LE/CT crossing depends mainly on the activation energy and the electronic coupling between the two states. On the one hand, the electronic coupling (ca. 230 cm^{-1}) is large enough for the electron transfer to occur efficiently. It is related mainly to the movement of the proton along the hydrogen-bond coordinate, as can be deduced from the graphical representation of derivative coupling (DC) and gradient difference (GD) vectors[24] (Figure 2). Moreover, the excitation to the $^1(\pi_A,\pi_A^*)$ state provokes the pyramidalization of the carbonyl group of the peptide **A**, giving rise to the shortening of the O···H distance, which in turn, effectively drives the system to the avoided crossing after Franck–Condon excitation.

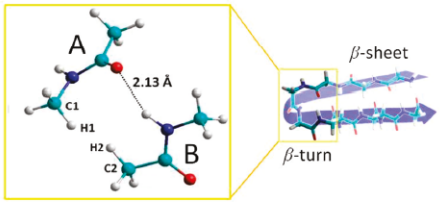

Figure 1. GS optimized structure of the polyglycine model. The relative position of the C1 and C2 methyl groups has been restrained in order to mimic a β-turn structure. The CO hydrogen-bonded glycine is labeled as A, while the NH bonded glycine is referred as B.

On the other hand, this crossing is estimated to be located only ca. 2 kcal/mol above the minimum of the $^1(\pi,\pi^*)_A$ state. Therefore, the crossing should be accessible from the LE state, permitting the population of the CT state on a time-scale of a few tens of femtoseconds.

The sudden charge separation taking place in the system due to the electron transfer process from glycine **B** to **A** triggers the proton transfer process, in which the proton involved in the hydrogen bond moves to the peptide **A** in order to compensate the charge separation. This proton motion in the CT state does not encounter an energetic barrier, and two more crossings are reached along the minimum energy path. The first, with the $^1(n,\pi^*)_A$ state, may not be efficient in populating this state, since the crossing is avoided and visited only once during the vibrational relaxation process in the CT state. A second crossing (conical intersection) with the GS, on the other hand, provides a funnel for population of the electronic GS (Figure 2).

This CT/GS conical intersection allows the system to decay to S_0. The DC and GD vectors (see Figure 2) of the conical intersection describe the nuclear motion in the relaxation process after the crossing. Therefore, these vectors determine to some extent the formed photoproducts. It should be noted

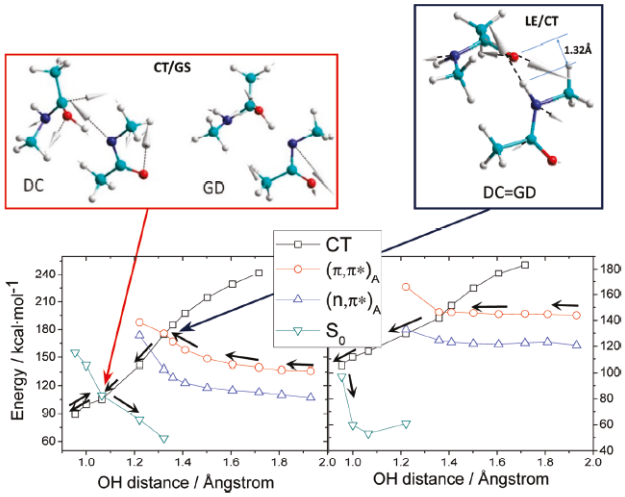

Figure 2. Global view of PPT minimum-energy paths computed at the CASSCF level, as a function of the O···H distance. Both CASSCF (left) and CASPT2 (right) profiles are shown. Note the steepness of the energy profile of the CT state, guiding the proton transfer to B after LE/CT crossing leading to the CT/GS conical intersection. The GD and DC vectors are shown for the two most important crossings.

DOI: 10.1021/jz900262w | J. Phys. Chem. Lett. 2010, 1, 425–428

THE JOURNAL OF PHYSICAL CHEMISTRY Letters

pubs.acs.org/JPCL

that both vectors for the two crossings have a large component in proton transfer, indicating the efficient proton motion after crossings. Two photoproducts can be formed from this electronic state crossing. For the most stable product, the closed-shell electronic configuration is recovered via a second (backward) electron transfer, in this case from **A** to **B**. This electron transfer drives the proton to its initial position, linked to the nitrogen atom of glycine **B** in the GS, recovering the GS minimum-energy structure. A second high-energy species with CT character can be reached from the CT/GS conical intersection. The corresponding minimum on the potential energy surface lies very close to the conical intersection, with the proton linked to the CO group of peptide **A**. Because of the energetic and structural proximity of this CT intermediate to the CT/GS conical intersection, this CT metastable state is expected to evolve rapidly toward the electronic GS, leading to the formation of the initial minimum-energy structure.

In conclusion, the computed CASSCF//CASPT2 pathways for the photoinduced electron-driven forward and backward proton transfers in a minimal β-turn protein model support the energetic feasibility of this process between hydrogen-bonded amino acids. The overall mechanism provides an efficient way of recovering the initial closed-shell structure after electronic excitation to the lowest bright electronic state. This mechanism could play a significant role in nature, providing to hydrogen-bonded peptides stability against damage by UV radiation. This mechanism may have been especially important for the development of life on the surface of the primitive earth under extreme UV exposure providing to proteins a possible mechanism for photostability.

SUPPORTING INFORMATION AVAILABLE Complete citation of ref 21. Computational details. Cartesian coordinates for optimized structures. Minimum energy paths. This material is available free of charge via the Internet at http://pubs.acs.org.

AUTHOR INFORMATION

Corresponding Author:

*To whom correspondence should be addressed. Tel: +34-91885-2512. Fax: +34-91885-4763. E-mail: luisma.frutos@uah.es.

ACKNOWLEDGMENT This research has been supported by the projects CTQ2006-07643 and CTQ2009-07120 of the Spanish MEC, and CGO8-UAH/PPQ-3790 of UAH/CAM. M.M. is grateful to the UAH for a doctoral fellowship. U.S. acknowledges receipt of a doctoral fellowship from the CAM and ESF. L.M.F acknowledges a grant from the Alexander von Humboldt Foundation and a "Ramón y Cajal" contract from the MEC.

REFERENCES

(1) Schreier, W. J.; Schrader, T. E.; F. O. Koller, F. O.; Gilch, P.; Crespo-Hernández, C. E.; Swaminathan, V. N.; Carell, T.; Zinth, W.; Kohler, B. Thymine Dimerization in DNA is an Ultrafast Photoreaction. *Science* **2007**, *315*, 625–629.

(2) Callegari, A. J.; Kelly, T. J. UV Irradiation Induces a Postreplication DNA Damage Checkpoint. *Proc. Natl. Acad. Sci. U.S.A.* **2006**, *103*, 15877–15882.

(3) Dobson, C. M.; Hore, P. J. Kinetic Studies of Protein Folding Using NMR Spectroscopy. *Nat. Struct. Biol.* **1998**, *5*, 504–507.

(4) Lyon, C. E.; Suh, E. S.; Dobson, C. M.; Hore, P. J. Probing the Exposure of Tyrosine and Tryptophan Residues in Partially Folded Proteins and Folding Intermediates by CIDNP Pulse-Labeling. *J. Am. Chem. Soc.* **2002**, *124*, 13018–13024.

(5) Pal, S. K.; Zewail, A. H. Dynamics of Water in Biological Recognition. *Chem. Rev.* **2004**, *104*, 2099–2123.

(6) Lu, D.; Voth, G. A. Proton Transfer in the Enzyme Carbonic Anhydrase: An Ab Initio Study. *J. Am. Chem. Soc.* **1998**, *120*, 4006–4014.

(7) Li, G.-S.; Maigret, D.; Rinaldi, D.; Ruiz-López, F. Influence of the Environment on Proton Transfer Mechanisms in Model Triads from Theoretical Calculations. *J. Comput. Chem.* **1998**, *19*, 1675–1688.

(8) Warshel, A.; Naray-Szabo, G.; Sussman, F.; Hwang, J.-K. How Do Serine Proteases Really Work? *Biochemistry* 1989, *28*, 3629−3637.

(9) Sekhar, V. C.; Plapp, B. V. Mechanism of Binding of Horse Liver Alcohol Dehydrogenase and Nicotinamide Adenine Dinucleotide. *Biochemistry* **1988**, *27*, 5082–5088.

(10) Crespo-Hernández, C. E.; Cohen, B.; Hare, P. M.; Kohler, B. Ultrafast Excited-State Dynamics in Nucleic Acids. *Chem. Rev.* **2004**, *104*, 1977–2019.

(11) Nir, E.; Kleinermanns, K.; de Vries, M. S. Pairing of Isolated Nucleic-Acid Bases in the Absence of the DNA Backbone. *Nature* **2000**, *408*, 949–951.

(12) Kobori, Y.; Norris, J. R. 1D Radical Motion in Protein Pocket: Proton-Coupled Electron Transfer in Human Serum Albumin. *J. Am. Chem. Soc.* **2006**, *128*, 4–5.

(13) Hammes-Schiffer, S. Theoretical Perspectives on Proton-Coupled Electron Transfer Reactions. *Acc. Chem. Res.* **2001**, *34*, 273–281.

(14) Sobolewski, A. L.; Domcke, W. Ab Initio Studies on the Photophysics of the Guanine−Cytosine Base Pair. *Phys. Chem. Chem. Phys.* **2004**, *6*, 2763–2771.

(15) Lan, Z.; Frutos, L. M.; Domcke, W. Chemical Dynamics Special Feature: Photochemistry of Hydrogen-Bonded Aromatic Pairs: Quantum Dynamical Calculations for the Pyrrole−Pyridine Complex. *Proc. Natl. Acad. Sci. U.S.A.* **2008**, *105*, 12707–12712.

(16) Frutos, L. M.; Markmann, A.; Sobolewski, A. L.; Domcke, W. Photoinduced Electron and Proton Transfer in the Hydrogen-Bonded Pyridine−Pyrrole System. *J. Phys. Chem. B* **2007**, *111*, 6110–6112.

(17) Shemesh, D.; Sobolewski, A. L.; Domcke, W. Efficient Excited-State Deactivation of the Gly-Phe-Ala Tripeptide via an Electron-Driven Proton-Transfer Process. *J. Am. Chem. Soc.* **2009**, *131*, 1374–1375.

(18) Sobolewski, A. L.; Domcke, W. Relevance of Electron-Driven Proton-Transfer Processes for the Photostability of Proteins. *ChemPhysChem* **2006**, *7*, 561–564.

(19) Cantor, C. R.; Schimmel, P. R. *Biophysical Chemistry: The Behavior of Biological Macromolecules*; W. H. Freeman & Co.: San Francisco, CA, 1980.

(20) Jeffrey, G. A. *Saenger Hydrogen Bonding in Biological Structures*; Springer-Verlag: Berlin, 1991.

(21) Complete Active Space Self Consistent Field (CASSCF) was used to determine minimum energy paths by computing analytical gradients, while Complete Active Space Perturbation Theory to Second Order (CASPT2) was employed to compute single-point correction to energy. CASSCF calculations were performed using Gaussian 03 (see http://www.gaussian.com/), while CASPT2 calculations were performed with MOLCAS, version 6.0 (see http://www.teokem.lu.se/molcas/). See Supporting Information for complete references.

DOI: 10.1021/jz900262w | *J. Phys. Chem. Lett.* **2010**, *1*, 425–428

THE JOURNAL OF PHYSICAL CHEMISTRY Letters
pubs.acs.org/JPCL

(22) A $(Gly)_5$ structure was previously modelled in a β-turn conformation. After CASSCF geometry optimization, the glycine residue in the middle of the tripeptide was removed, and the remaining two residues were saturated, each one with a hydrogen atom pointing in the direction of the removed glycine backbone (H1 and H2 in Figure 1). The mentioned constraints are set during every geometry optimization. The complete active space was selected in order to include for each peptide unit all π orbitals (2π and $1\pi^*$) and one n orbital on the oxygen, with six corresponding electrons, resulting in a CAS(12,8) (12 electrons in 8 orbitals). See Supporting Information for computational details.

(23) Serrano-Andrés, L.; Fülscher, M. P. Theoretical Study of the Electronic Spectroscopy of Peptides. III. Charge-Transfer Transitions in Polypeptides. *J. Am. Chem. Soc.* **1998**, *120*, 10912–10920.

(24) The DC vector measures the distortion of the system providing the maximum coupling between the electronic states involved in the crossing. The GD vector measures the distortion of the system leading to the largest variation of the energy difference between the two electronic states involved in the crossing.

DOI: 10.1021/jz900262w | *J. Phys. Chem. Lett.* **2010**, *1*, 425–428

4.1.2 First Principles Study of Photostability within Hydrogen-Bonded Amino Acids

www.rsc.org/pccp **PAPER**

First principles study of photostability within hydrogen-bonded amino acids†‡

Marco Marazzi,* Unai Sancho, Obis Castaño and Luis Manuel Frutos*

Received 16th November 2010, Accepted 20th January 2011
DOI: 10.1039/c0cp02554b

The photochemistry and photophysics of a two-glycine minimal model is studied at the CASPT2//CASSCF level of theory. Different photoinduced processes are discussed, on the basis of the calculated minimum energy paths and the characterization of the electronic state crossings. Two main processes could provide UV-photostability to the hydrogen-bonded peptide system: (i) forward–backward photoinduced electron/proton transfer involving the H in the hydrogen bond, (ii) singlet–singlet energy transfer between two amino acids, providing ultrafast population of the low-energy n,π^* state.

Introduction

Hydrogen bonds are known to be crucial in determining the conformation and the biological function of proteins.[1,2] In particular, the CO and NH groups of the backbone, which can form hydrogen bonds between different amino acids of the same polypeptide chain, mainly determine the type of secondary structure within the proteins (α-helix, β-sheet, *etc.*); additionally, they are crucial in the enzymatic activity *via* recognition of substrates in the binding region of protein complexes,[3–5] and in the catalysis of chemical reactions (*e.g.* carbonic anhydrase,[6] serine protease,[7,8] alcohol dehydrogenase[9]).

Hydrogen bonds not only provide the main structural and functional properties of proteins and DNA, but they have also been proposed as features conferring photostability *via* photoinduced proton transfer (PPT) reactions.[10,11] This process has been described as a two-step mechanism, where the proton in the hydrogen bond is transferred, promoted by photoinduced electron transfer. A second electron (backward) transfer process followed by proton transfer can restore the system to its initial hydrogen bond configuration in picoseconds.[12]

With the aim of clarifying and providing further insight into these mechanisms, different computational methodologies were successfully applied to chemical and biological systems.[13,14] In particular, when adopting *ab initio* multiconfigurational quantum chemistry methods, the PPT was shown to play an important role under the following conditions: an excited electronic state with charge transfer character can be efficiently populated, and its stabilization in energy allows the efficient crossing of one or more electronic states (*i.e.* through conical intersections), resulting in a radiationless decay providing an ultrafast internal conversion, or an ultrafast photoproduct formation (see Scheme 1). As a confirmation of these theoretical studies, experiments on macromolecular systems with biological relevance (*e.g.* bi-imidazoline iron complexes[15] and human serum albumin[16]) showed mechanistic evidence of PPT.

A major risk for all photoactivated biological processes is UV-radiation exposure, which can cause structural and conformational changes, resulting in a loss in the system function or activity. A forward–backward PPT can be proposed as a mechanism to provide photostability, since the absorbed energy of the photon can be converted into vibrational energy dissipated by the environment, finally recovering the initial structure.[17–19]

This mechanism was already proposed in DNA base pair models,[20,21] and experimentally the PPT was recently observed

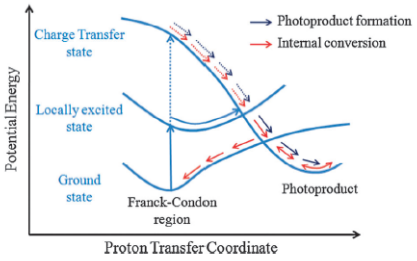

Scheme 1 Mechanisms expected for ultrafast internal conversion and photoproduct formation.

Departamento de Química Física, Universidad de Alcalá, 28871 Alcalá de Henares (Madrid), Spain.
E-mail: luisma.frutos@uah.es, marco.marazzi@uah.es;
Fax: +34 918854763; Tel: +34 918852512

† Electronic supplementary information (ESI) available: Complete ref. 31 and 32; computational details; absorption spectrum parameters; details of pathways and inter-state crossings mentioned in the main text; Cartesian coordinates of the most representative structures. See DOI: 10.1039/c0cp02554b/

‡ This work is dedicated to the memory of Prof. Luis Serrano-Andrés.

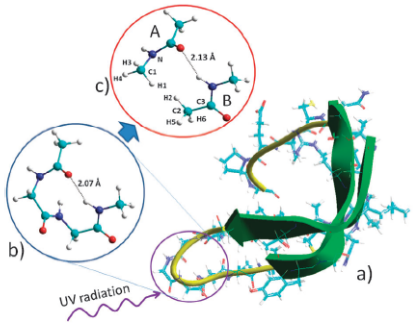

Fig. 1 Structure of a β-hairpin motif in protease B (SGPB)[33] (a), containing a $(Gly)_3$ β-turn (b). The system studied is composed by the glycines A and B properly constrained to model the removed middle glycine (c).

in the 2-aminopyridine dimer by electron and mass spectroscopy.[22] However, few attempts were performed for the eventual elucidation of this mechanism in proteins,[23,24] where a clear picture was given only about the electron transfer.[25–27] Actually, to get experimental data concerning PPT in proteins represents a challenge even with the most modern state-of-the-art techniques (*e.g.* femtosecond laser spectroscopy). Thus, a theoretical approach can be helpful in elucidating what could happen to a protein when exposed to UV-radiation.

Here, we present a computational study of a minimal two-glycine hydrogen-bonded model (see Fig. 1) at the CASPT2//CASSCF level of theory, with the intention of describing the properties of a β-turn structural element, commonly found in several proteins. The evolution of the first seven singlet electronic states (from S_0 to S_6) is investigated from the Franck–Condon region (*i.e.* UV-radiation absorption) by calculating all related minimum energy paths (MEPs), including the characterization of the excited-state crossings by means of multiconfigurational CASPT2//CASSCF methodology. The resulting potential energy surfaces (PESs) show three different types of photoinduced processes: energy transfer, electron transfer, and proton transfer. Among them, a forward–backward PPT along the C═O···H–N hydrogen bond coordinate was found to be a possible mechanism for highly efficient excited-state deactivation in proteins,[28] but also ultrafast singlet–singlet energy transfer could provide an efficient way to populate the low energy n,π^* state. In this article we aim to give a detailed explanation of all the competitive processes activated by exposure to UV-radiation in a two-glycine minimal model, discussing their relative feasibility through the calculated MEPs and characterized excited-state decay channels.

2. Theoretical methods and computational setup

The calculation of electronic excited-state properties require the application of *ab initio* multiconfigurational methods. Among them, the CASPT2//CASSCF methodology provides, in many systems, quantitative results for excited states, and has been shown to correctly describe the electronic structure of molecular systems studied in the present work.[28,29] This method is a combination of the Complete Active Space Self-Consistent Field (CASSCF) energy derivatives with single-point corrections to the energy at the Complete Active Space Perturbation Theory to Second Order (CASPT2) method (see supplementary information for a description of the methods†).

Employing a 6-31G(d) basis set, optimized ground-state and excited-state geometries have been determined at the CASSCF level by computing analytical gradients and numerical frequencies (*i.e.* first and second derivatives of the energy, respectively). MEPs were calculated by applying the steepest descent algorithm in redundant internal coordinates.[30] When the electronic state crossings (energy degeneracy between two different singlet states) were located, the gradient difference (GD) and derivative coupling (DC) vectors (*i.e.* the non-adiabatic coupling vectors) were calculated to characterize the branching space for both types of crossings found: avoided crossings (AC) or conical intersections (CI). Additionally, the branching space was explored by evaluating the energy, charge and dipole moment along a closed loop generated around each CI.

The dynamic correlation effect has been introduced by calculating CASPT2 single-point energies of the most relevant structures previously determined at the CASSCF level: the optimized ground-state and excited-state geometries, the electronic state crossings, as well as representative structures along the MEPs.

In order to consider all the necessary orbitals for a full description of the electronic excited-states, all π orbitals (4π and $2\pi^*$) and $2n$ orbitals on the respective oxygens of the model were included in the active space, corresponding to 12 electrons in 8 orbitals. In this way, the π,π^* and n,π^* electronic states are being described.

All CASSCF calculations were carried out using the Gaussian 03 software,[31] while CASPT2 calculations were performed using the MOLCAS-6 software.[32]

It has to be noted that both processes, photoinduced electron/proton and energy transfer, studied in this work involve some of the above mentioned crossings between electronic states, *i.e.* CI or AC, which are key features in rationalizing the mechanisms. CIs are intersections of N-2 dimensionality (with N being the number of internal degrees of freedom of the system) with the two remaining degrees of freedom defining the branching space (expanded by GD and DC vectors). On the contrary, the ACs found for photoinduced electron and energy transfer processes present a small and almost constant electronic coupling, making the crossing slightly avoided along N-1 dimensions with the branching space defined by one single vector: the GD vector. Therefore this vector provides the initial direction of the reaction coordinate of the process.

When the system is in the upper surface, CI provides an extremely efficient funnel to populate the lower state (see A in the "CI case", Scheme 2). On the contrary, depending on the energy gap, ACs provide a less efficient way of populating the lower state, where some trajectories are not able to hop to the lower state (see A in the "AC case", Scheme 2). When the system is initially in the lower surface, the transformation of reactants "R" to products "P" does not involve the CI itself

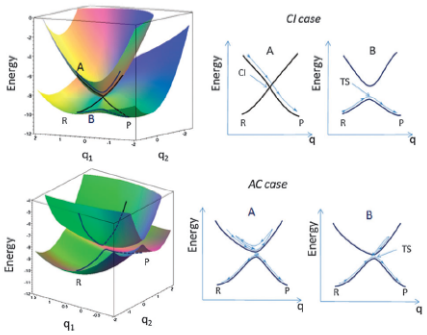

Scheme 2 Potential energy surfaces along a set of internal coordinates (q_1 and q_2) as well as energy profiles along reaction coordinate (q) for: (i) conical intersection crossings (CI case, top) and (ii) avoided crossing with constant electronic coupling (AC case, bottom). "R" and "P" designate reactants and products, respectively.

(see B in the "CI case", Scheme 2), which does not play a chemical role since the system remains in the lower surface and the reaction takes place adiabatically through a transition state (TS in B in the "CI case", Scheme 2). On the contrary, for the AC patterns found in this work, the conversion of reactants to products (see B in the "AC case", Scheme 2) proceeds also through a TS, but in this case the TS structure corresponds to the lowest avoided crossing structure, and also, depending on the energy gap, some of the trajectories will be unable to reach products. The TS vector in this case has the same direction of the GD vector. It has to be noted that, for the AC case, the internal coordinates mix more efficiently both electronic states *via* the energy gradient difference vector, since it defines the coordinate for which the coupling between both states changes more efficiently, whilst for the remaining internal coordinates the coupling essentially remains constant. Therefore, parallel GD and DC vectors indicate, for the above mentioned processes, this potential energy surface pattern.

3. Results and discussion

3.1 Ground-state (GS) structure

In order to study PPT in proteins with multiconfigurational methods, a rational model presenting the essential features of hydrogen-bonded peptides, which is computationally affordable is necessary. Among all possible hydrogen-bonded peptides, we have selected a β-turn element composed of three glycines, for the following reasons:

1. A β-turn element is able to fold stable antiparallel β-strands, leading to the formation of structural motifs as β-hairpin, commonly found in proteins (see Fig. 1a);

2. $(Gly)_3$ is the easiest possible sequence that can be shaped in a β-turn conformation, resulting in a system affordable for an *ab initio* multiconfigurational approach.

After geometry optimization of the tripeptide (shown in Fig. 1b), the middle glycine was removed and substituted with a set of constraints (detailed in the supplementary information section†) between the two remaining glycines, **A** and **B**, which are hydrogen-bonded along the C═O···H–N coordinate. These constraints are imposed in order to mimic the effect of the middle glycine. Glycines **A** and **B** were saturated by inserting the hydrogen atoms H1 and H2, respectively (see Fig. 1), in the direction of the backbone of the removed glycine. The final optimized ground-state structure (Fig. 1c) keeps a β-turn conformation showing only smooth changes, *e.g.* in the hydrogen bond length (from 2.07 Å to 2.13 Å).

3.2 The absorption spectrum

The Franck–Condon (FC) vertical excitation energies, oscillator strengths (f) and orbital transitions of the six lowest singlet excited-states are shown in Table 1. Four locally excited (LE) and two charge transfer (CT) states are found. On one hand, a direct population of a CT state is expected to be unfavorable, because of the very low f values. Moreover, the energy for the transition (8.5 eV) corresponds to high energy UV-irradiation. On the other hand, among LE states, LE_1 and LE_2 (both $^1(n,\pi^*)$ states) are dark states ($f \approx 0$), while LE_3 and LE_4 (both $^1(\pi,\pi^*)$ states) correspond to the optically brightest states, with a higher probability of population when absorbing UV-irradiation.

The CASPT2 excitation energies (ΔE_{CASPT2}) correspond to a quantitative description of the absorption spectrum since it includes the dynamic correlation effect *via* perturbational theory applied to CASSCF (ΔE_{CASSCF}) wavefunction: the LE $^1(\pi,\pi^*)$ states are the most stabilized by perturbation treatment, followed by CT states, while the LE $^1(n,\pi^*)$ states are the less affected, consistently with the method.

In previous CASPT2 calculations (supported by experiments) of $(Gly)_2$ and $(Gly)_3$ peptides in α-helix and β-sheet conformations, LE (n,π^*) and (π,π^*) states were located at 5.6 eV and 6.5 eV respectively, and a CT (π,π^*) state was found at around 7.5 eV, being attributed to CT between neighboring peptides.[25] Compared to the ΔE_{CASPT2} values of our model, we can conclude that the same overall picture of the FC-region is depicted, with all excited electronic states being more stable in energy than the corresponding values found in this study (especially in the case of CT).

3.3 Singlet–singlet energy transfer processes

One of the possible photophysical processes after excitation of one glycine (*e.g.* glycine **A**, presenting the lowest bright state) is the singlet excitation energy transfer. Singlet energy transfer

Table 1 FC-vertical excitation energies at CASPT2 and CASSCF levels (ΔE_{CASSCF}, ΔE_{CASPT2}) for the first six electronic excited-states (LE or CT states). S_0 corresponds to the ground-state and is considered as a reference: $\Delta E = E(S_n) - E(S_0)$. Oscillator strengths ($f$) and orbital transitions are also indicated

State	ΔE_{CASSCF}	ΔE_{CASPT2}	f	Transition
S_6 (CT_2)	10.26	8.87	0.023	$^1(n_B \rightarrow \pi_A^*)$
S_5 (CT_1)	9.76	8.48	0.008	$^1(\pi_B \rightarrow \pi_A^*)$
S_4 (LE_4)	9.59	7.16	0.558	$^1(\pi,\pi^*)_B$
S_3 (LE_3)	8.93	6.85	0.457	$^1(\pi,\pi^*)_A$
S_2 (LE_2)	6.00	6.06	0.001	$^1(n,\pi^*)_B$
S_1 (LE_1)	5.90	5.72	0.001	$^1(n,\pi^*)_A$

is verified when crossing and coupling between locally excited states of **A** and **B** takes place.

After irradiation to the lowest optically bright excited-state (LE_3, $^1(\pi,\pi^*)_A$), the MEP indicates a decrease in energy until an avoided crossing with the LE_2 $^1(n,\pi^*)_B$ state is reached (Fig. 2). The corresponding structure shows how both glycines tend to distort from their ground-state geometry: the carbonyl carbon atom of glycine **A** pyramidalizes, resulting in a reorientation of the CO group towards the NH group of glycine **B**, which undergoes a complementary distortion to favor the O···H alignment.

As indicated by the gradient difference and derivative coupling vectors (which are parallel), the mechanism implies coupling of the CO stretching modes, resulting in energy transfer from glycine **A** to **B**. This excitation energy transfer implies the migration of the energy from the originally excited chromophore **A** (LE_3, $^1(\pi,\pi^*)_A$) to **B** (LE_2, $^1(n,\pi^*)_B$).[34]

On one hand, the difference in energy between LE_3 and LE_2 states at the AC (0.2 kcal mol^{-1}) suggests an estimation of the inter-state coupling of around 35 cm^{-1}, a non negligible value. This small but non-vanishing coupling is due to the mixing of the two wavefunctions (LE_3 and LE_2 states) close to the crossing along the GD vector, as is apparent from the analysis of the CASSCF wavefunctions in the crossing region, which ultimately allows for the energy transfer process to take place.[35]

On the other hand, the low coupling between these states (energy difference at the crossing *ca.* 0.2 kcal mol^{-1}) indicates that most of the wave packets passing through the LE_3/LE_2 AC are expected to remain on the $(\pi,\pi^*)_A$ state, leading to a minimum located 0.4 eV lower than the FC-LE_3 energy, where the C═O···H–N bond is shortened from 2.13 Å (FC-region) to 2.09 Å. In this way, the low populated $^1(n,\pi^*)_B$ state could decay radiatively to S_0 as an accessible pathway for further deactivation or evolution of this state was not found. Nevertheless, many other processes like intersystem crossing with triplet states cannot be excluded.[36]

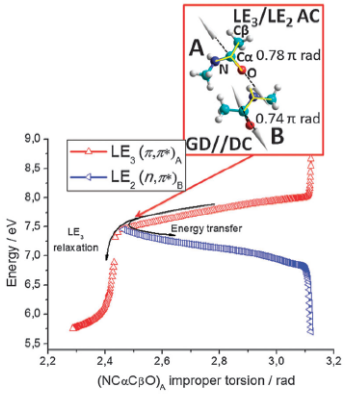

Fig. 2 Mechanism of the most relevant energy transfer process: from glycine **A** to **B** through an LE_3/LE_2 AC.

Other possible energy transfer processes could involve the $(n,\pi^*)_B$ and $(n,\pi^*)_A$ states, since a LE_2/LE_1 AC was found on the LE_2 MEP (Fig. 2S in supplementary information†). In principle, this crossing would allow energy transfer from glycine **B** to **A**, and is accessible by means of two different pathways:

1. decreasing in energy from the LE_3/LE_2 AC mentioned above, implying an overall **A** → **B** → **A** energy transfer mechanism;

2. from the FC-region, in case the $(n,\pi^*)_B$ is directly populated, resulting in **B** → **A** energy transfer.

Considering the weak coupling between the (n,π^*) states and the low oscillator strength of the S_0 → LE_2 FC-transition (required for pathway 2), it can be concluded that both **B** → **A** processes are highly unlikely events.

3.4 Electron and proton transfer processes

Photoinduced electron/proton transfer has been proposed as an efficient process for photodeactivation in proteins.[23,24,28] Basically, the mechanism of the process consists of two electron–proton coupled transfer steps taking place between the two hydrogen-bonded moieties (see Scheme 3).

An overall picture of the photoinduced electron/proton transfer CASPT2 PES for the model system under investigation is given in Fig. 3.

As shown, both CT states are stabilized in energy along the proton transfer (O···H distance in RCO···HNR) coordinate, becoming more stabilized as the proton is transferred (the OH distance decreases), and in turn crossing the LE states. At the same time, the H–N bond in glycine **B** weakens and finally breaks. Every LE_n/CT_n crossing corresponds to a potential electron transfer process (LE → CT transition) from glycine **B** to **A**, giving rise to a charge separation state ($^-$RC═O···H–NR$^+$). The eventual population of a CT state promotes a proton transfer process, stabilizing the system (see Fig. 3) and recovering the neutral charge of the two glycine residues (C–O–H···N). This proton transferred bond pattern is not stable on the CT states. In fact, the CT states cross with the closed-shell (CS) electronic state (CT_1/CS and CT_2/CS CI crossings in Fig. 4 and 6a), permitting to populate the CS and giving rise to a second electron transfer, in this case from glycine **A** to **B**. Again, vibrational relaxation on CS is mediated by a second proton transfer, providing the pathways for an internal conversion mechanism (C═O···H–N).

It follows a description of the calculated LE paths:

The LE_1 and LE_2 states are both (n,π^*) dark states and their pathways, leading to a crossing with the CT_1 state, are not energy barrierless, therefore it is not expected that these states would play a significant role for electron transfer processes.

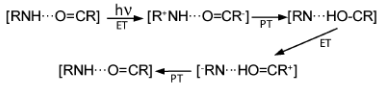

Scheme 3 Photoinduced electron transfer (ET) and coupled proton transfer (PT) as a mechanism for photostability in hydrogen-bonded amino acids.

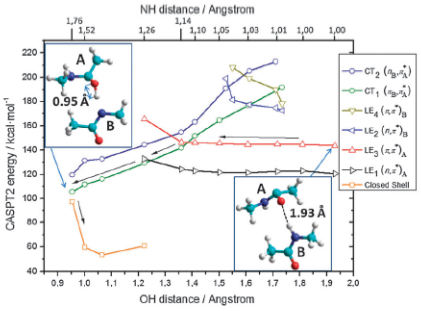

Fig. 3 CASPT2 energy profiles as a function of the CO···HN distance (N–H distance in the upper scale) for the reaction coordinate in LE_3 and CT_1. both CT states are stabilized in energy along the proton transfer coordinate, crossing the LE states and finally allowing population of the ground state. The PPT path indicated by arrows is proposed as an ultrafast highly efficient process.

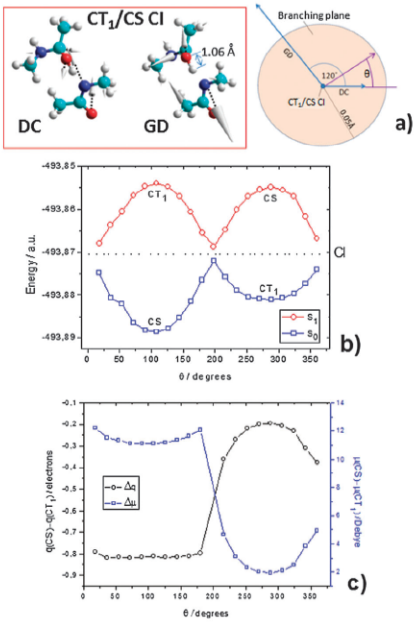

Fig. 4 (a) Non-adiabatic coupling vectors (|GD| ≈ 3 |DC|), (b) energy profile, (c) Mulliken charge and dipole moment differences, at the CT_1/CS CI, along a loop generated around the degeneracy point of radius 0.05 Å (θ is the angle for the branching space). The Mulliken charges are calculated for glycine B without contribution of the hydrogen atom which is transferred to glycine A.

On the contrary, the LE_3 and LE_4 (π,π^*) states can be populated directly by UV-irradiation from the FC-region since they are bright states (see Table 1). On one hand, the LE_4 $(\pi,\pi^*)_B$ MEP leads to a minimum, where the OH distance is 1.73 Å. From this minimum, *ca.* 10 kcal mol^{-1} are required to reach the LE_4/CT_1 CI, demanding a considerable vibrational excess. On the other hand, the minimum energy structure in the LE_3 $(\pi,\pi^*)_A$ state is only *ca.* 2 kcal mol^{-1} lower than the LE_3/CT_1 AC, which could efficiently act as a transition state to populate the CT_1 state.

Once the CT_1 state is populated, the CT_1/CS (or equivalently S_1/S_0) CI is the funnel which permits the system to decay to S_0. An analysis of the branching space vectors[37] for this crossing (Fig. 4a) indicates a large contribution of the glycine **B** nitrogen atom to different possible paths: the DC vector shows the nitrogen pointing towards the detached hydrogen (now on glycine **A**), with a concerted geometric rearrangement in favor of the hydrogen back transfer (note the contribution of both oxygen atoms), while the GD vector tends to stabilize the C–O–H···N structure corresponding to an eventual photoproduct. A topological study of the hyperspace around the CI supports this conclusion (Fig. 4b): two minima are located on the S_0 PES, one corresponding to population of the GS initial structure, and the other to formation of the hydrogen-transferred species on the CT_1 state.

The difference in charge (Δq) and dipole moment ($\Delta\mu$) between CS and CT_1 was also evaluated (Fig. 4c): in the CT_1 minimum region (200–360 degrees) both Δq and $\Delta\mu$ are minimized, not allowing electron transfer processes, while in the CS minimum region (0–200 degrees) $\Delta q \approx 1$ electron, which is back transferred from glycine **A** to **B**, with a consequential increase of μ up to 12 Debye.

The two possible pathways on the S_0 PES are shown in Fig. 5: a high energy species is located 8 kcal mol^{-1} below the CT_1/CS CI, at the CASPT2 level of theory (OH distance = 0.95 Å, NH distance = 2.04 Å), corresponding to the hydrogen-transferred structure. Meanwhile, the initial GS structure can be fully recovered by a backward proton transfer that follows the backward electron transfer (*i.e.* a backward PPT mechanism).

Due to its metastability, the high energy H-transferred species can easily evolve recovering the system its initial structure, as has been also found in similar processes.[20] Therefore, the CT_1/CS CI provides the funnel for the efficient recovery of the GS initial structure.

3.5 Alternative electron transfer migrations

In spite of the equivalent covalent bond pattern of glycines **A** and **B**, charge transfer states do not have the same, or even similar energy for both possible types (**A** to **B** and **B** to **A**). In fact, the two lowest CT states are ($\pi_B \rightarrow \pi_A^*$) and ($n_B \rightarrow \pi_A^*$), *i.e.* an electron transfer from moiety **B** to **A**, which corresponds to ($^-$RC=O···H–NR$^+$) situation. This is due to the slight charge transfer character of the GS: (δ^-)RC=O···H–NR(δ^+) pattern, which in turn stabilizes the above mentioned **B** to **A** electron transfer states.

In this way, the lowest CT state is CT_1 ($\pi_B \rightarrow \pi_A^*$) followed by CT_2 ($n_B \rightarrow \pi_A^*$). Since both CT_1 and CT_2 have similar

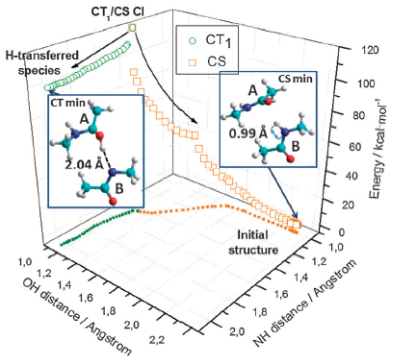

Fig. 5 The CT_1/CS (*i.e.* S_1/S_0) CI is a funnel to decay on the S_0 surface. Two possible photoproducts are found: formation of a metastable hydrogen-transferred species (CT_1 character), or recovery of the initial structure (FC-region).

electronic structure, their behavior along the proton transfer coordinate is similar (see Fig. 3).

The energy profile of the CT_2 state shows that a charge transfer processes involving this state is less probable than that involving the CT_1 state. This is because the LE_n/CT_2 crossings are located higher in energy than the LE_n/CT_1 crossings, resulting in an increase in the energy barrier for every possible mechanism. Nevertheless, the stabilization of the CT_2 state along the proton transfer coordinate leads to a LE_3/CT_2 crossing (Fig. 3, below 1.4 Å OH distance), which could be reached from the LE_3 state with the available vibrational excess, being to some extent a competitive pathway with the more efficient LE_3/CT_1 CI discussed above. A dynamic study (*e.g.* semiclassical dynamics) could provide information about the feasibility of the LE_3/CT_2 crossing.

Descending in energy, a CT_2/CS (S_2/S_1) CI can be the funnel to populate the CS state after population of the CT_2, with a backward electron transfer (as at CT_1/CS CI), which would initiate the backward proton transfer process, finally recovering the FC-initial structure (Fig. 6a, 5S in supplementary information†).

Unlike CT_1, CT_2/CS crossing is not the energy lowest crossing. In fact, there is a second crossing (between CT_2 and CT_1) which could provide another path for the population of CT_1 (Fig. 6c). Exploring the topology of this CI only one minimum in the energy profile around the CT_2/CT_1 CI is found (Fig. 6b), and corresponds to population of CT_1. A further relaxation of the system (*ca.* 10 kcal mol^{-1}) on the CT_1 state leads to the same minimum (a metastable hydrogen-transferred structure) located when descending from the CT_1/CS CI (Fig. 5). The metastable species is expected to evolve towards the closed-shell ground-state minimum structure passing through the CT_1/CS CI, because of the following considerations:

1. the energy required to overcome the *ca.* 8 kcal mol^{-1} barrier should be furnished by the vibrational excess, as suggested by the steepness of the CT_2 and CT_1 profiles;

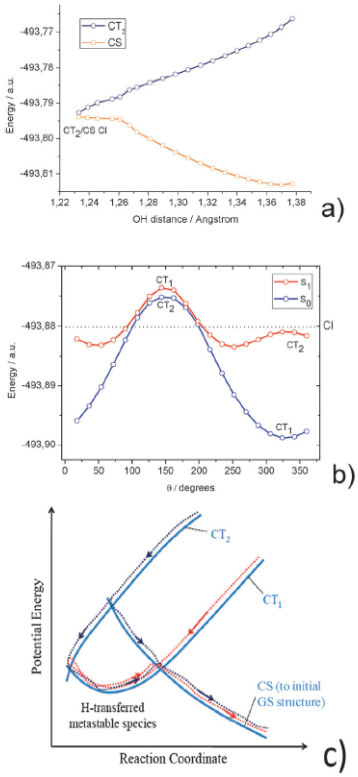

Fig. 6 (a) MEP on the CT_2 state, reaching a CI with the CS state. (b) Energy profile of the CT_2/CT_1 CI (loop radius: 0.05 Å). (c) Schematic view of the possible dynamic behavior, on the basis of the calculated paths.

2. by vibrational excess the system could evolve back to the CT_2/CT_1 CI, but the topology of the crossing assumes that the system will stay on the CT_1 state, again leading to internal conversion;

3. the geometrical similarity between the hydrogen-transferred metastable structure and the CT_1/CS CI corresponding structure.

The scheme of Fig. 6c clarifies these considerations.

Conclusions

Different processes can be photoinduced in a β-turn minimal structure, including electron, proton and energy transfer, but only feasible reaction paths are likely to play a significant role after UV-irradiation.

Activation energy is always required to populate the CT states, where an electron transfer from glycine **B** to **A** would be possible. Especially, population of the CT_1 state can be a highly

efficient process through a LE_3/CT_1 CI, located only *ca.* 2 kcal mol^{-1} higher than the LE_3 minimum. Crossings with the CT_2 state were also found, but considered of less importance because of the higher activation energy required. All the possible electron transfer processes are followed by further stabilization of the CT states along the C=O···H–N coordinate, until the proton detaches from glycine **B** and forms a C–O–H···N structure (*i.e.* charge separation induced proton transfer). The CT_1/CS CI is proposed as a highly efficient excited-state deactivation funnel to restore the ground-state closed-shell minimum energy structure, *via* a second (back) electron and proton transfer. This mechanism could enhance photostability in proteins against UV-irradiation.

A metastable species with hydrogen transfer character was located on the CT_1 state, between the CT_1/CS CI and the CT_2/CT_1 CI. The topology of the related PES region suggests a fast evolution towards S_0, which permits the recover of the FC-initial structure, contributing to photostability.

Singlet energy transfer processes were also proposed from glycine **A** to **B**, and *vice versa*, being energy barrierless processes: the **A** → **B** excitation energy migration could be relevant and should be considered in competition with the photoinduced proton transfer, while the **B** → **A** mechanisms do imply a crossing between weakly coupled states, resulting in low probability events.

It has been proven that the calculation of the MEPs and a full characterization of the electronic state crossings is an essential first step to validate the proposed photoinduced processes and mechanisms. A further understanding of the feasibility of the forward–backward PPT in proteins should include molecular dynamic studies and eventually QM/MM (Quantum Mechanics/Molecular Mechanics) methodologies.

Acknowledgements

This research has been supported by the project CTQ2009-07120 of the Spanish MICINN. M.M. acknowledges the UAH for a doctoral fellowship. US is grateful for a doctoral fellowship from CAM and ESF. L.M.F. acknowledges receipt of a "Ramon y Cajal" contract from MEC.

Notes and references

1 C. R. Cantor and P. R. Schimmel, *Biophysical Chemistry: The Behavior of Biological Macromolecules*, W. H. Freeman & Co., San Francisco, 1980.
2 G. A. Jeffrey and W. Saenger, *Hydrogen Bonding in Biological Structures*, Springer-Verlag Berlin, 1991.
3 C. M. Dobson and P. Hore, *Nat. Struct. Biol.*, 1998, **5**, 504.
4 C. E. Lyon, E. S. Suh, C. M. Dobson and P. J. Hore, *J. Am. Chem. Soc.*, 2002, **124**, 13018.
5 S. K. Pal and A. H. Zewail, *Chem. Rev.*, 2004, **104**, 2099.
6 D. Lu and G. A. Voth, *J. Am. Chem. Soc.*, 1998, **120**, 4006.
7 G.-S. Li, D. Maigret, D. Rinaldi and F. Ruiz-López, *J. Comput. Chem.*, 1998, **19**, 1675.
8 A. Warshel, G. Naray-Szabo, F. Sussman and J.-K. Hwang, *Biochemistry*, 1989, **28**, 3629.
9 V. C. Sekhar and B. V. Plapp, *Biochemistry*, 1988, **27**, 5082.
10 A. L. Sobolewski and W. Domcke, *J. Phys. Chem. A*, 2007, **111**, 11725.
11 A. L. Sobolewski, W. Domcke and C. Hättig, *Proc. Natl. Acad. Sci. U. S. A.*, 2005, **102**, 17903.
12 T. Schultz, E. Samoylova, W. Radloff, I. V. Hertel, A. L. Sobolewski and W. Domcke, *Science*, 2004, **306**, 1765.
13 S. Hammes-Schiffer, *J. Phys. Chem. A*, 1998, **102**, 10443.
14 S. Hammes-Schiffer, *Acc. Chem. Res.*, 2001, **34**, 273.
15 J. P. Roth, S. Lovel and J. M. Mayer, *J. Am. Chem. Soc.*, 2000, **122**, 5486.
16 Y. Kobori and J. R. Norris, *J. Am. Chem. Soc.*, 2006, **128**, 4.
17 S. Perun, A. L. Sobolewski and W. Domcke, *J. Phys. Chem. A*, 2006, **110**, 9031.
18 A. L. Sobolewski and W. Domcke, *ChemPhysChem*, 2006, **7**, 561.
19 Z. Lan, L. M. Frutos and W. Domcke, *Proc. Natl. Acad. Sci. U. S. A.*, 2008, **105**, 12707.
20 L. M. Frutos, A. Markmann, A. L. Sobolewski and W. Domcke, *J. Phys. Chem. B*, 2007, **111**, 6110.
21 F. Zhang, Y.-J. Ai, Y. Luo and W.-H. Fang, *J. Chem. Phys.*, 2009, **130**, 144315.
22 E. Samoylova, W. Radloff, H.-H. Ritze and T. Schultz, *J. Phys. Chem. A*, 2009, **113**, 8195.
23 D. Shemesh, A. L. Sobolewski and W. Domcke, *J. Am. Chem. Soc.*, 2009, **131**, 1374.
24 D. Shemesh, C. Hättig and W. Domcke, *Chem. Phys. Lett.*, 2009, **482**, 38.
25 L. Serrano-Andrés and M. P. Fülscher, *J. Am. Chem. Soc.*, 1998, **120**, 10912.
26 L. Serrano-Andrés and M. P. Fülscher, *J. Phys. Chem. B*, 2001, **105**, 9323.
27 T. Herz, P. Gedeck and T. Clark, *J. Am. Chem. Soc.*, 1999, **121**, 1379.
28 M. Marazzi, U. Sancho, O. Castaño, W. Domcke and L. M. Frutos, *J. Phys. Chem. Lett.*, 2010, **1**, 425.
29 M. Merchán, L. Serrano-Andrés, M. P. Fülscher and B. O. Roos, *Recent Advances in Multireference Theory*, ed. K. H. U., World Scientific Publishing Co., Singapore, 1999, vol. IV, pp. 161–195.
30 H. B. Schlegel, *J. Comput. Chem.*, 1982, **3**, 214.
31 See http://www.gaussian.com/.
32 See http://www.teokem.lu.se/molcas/.
33 Thr170-Gly193 selected residues of the protease B peptide chain (see http://www.rcsb.org/; DOI: 10.2210/pdb3sgb/pdb).
34 Similar crossings have been theoretically described for electron transfer: (*a*) L. Blancafort, F. Jolibois, M. Olivucci and M. A. Robb, *J. Am. Chem. Soc.*, 2001, **123**, 722; (*b*) E. Fernández, L. Blancafort, M. Olivucci and M. A. Robb, *J. Am. Chem. Soc.*, 2000, **122**, 7528; and triplet energy transfer: (*c*) L. M. Frutos, U. Sancho and O. Castaño, *J. Phys. Chem. A*, 2005, **109**, 2993.
35 This value, determined as the lowest energy separation between both states at CASPT2 level of theory falls in the range of previously described coupling for energy transfer reactions. See for example C.-P. Hsu, *Acc. Chem. Res.*, 2009, **42**, 509 and references therein.
36 The population of the triplet state from $^1n,\pi^*$ state in single peptide seems to be possible: E. Muchova, P. Slavíček, A. L. Sobolewski and P. Hobza, *J. Phys. Chem. A*, 2007, **111**, 5259, therefore it is not excluded the triplet state population after singlet formation.
37 (*a*) A. Migani and M. Olivucci, Conical intersections and organic reaction mechanisms, in *Conical intersections: Electronic structure, dynamics and spectroscopy*, ed. W. Domcke, D. R. Yarkony and H. Köppel, World Scientific, Singapore, 2004, pp. 271–320; (*b*) A. Sinicropi, R. Pogni, R. Basosi, M. A. Robb, G. Gramlich, W. M. Nau and M. Olivucci, *Angew. Chem., Int. Ed.*, 2001, **40**, 4185.

4.1.3 Photostability Mechanisms in Human γB-Crystallin: Role of the Tyrosine Corner Unveiled by Quantum Mechanics/Molecular Mechanics Methodologies

JCTC Journal of Chemical Theory and Computation
Article
pubs.acs.org/JCTC

Photostability Mechanisms in Human γB-Crystallin: Role of the Tyrosine Corner Unveiled by Quantum Mechanics and Hybrid Quantum Mechanics/Molecular Mechanics Methodologies

Marco Marazzi,*[,†] Isabelle Navizet,[‡] Roland Lindh,[§] and Luis Manuel Frutos*[,†]

[†]Departamento de Química Física, Universidad de Alcalá, E-28871 Alcalá de Henares (Madrid), Spain
[‡]School of Chemistry, University of the Witwatersrand, ZA-2050 Johannesburg, South Africa
[§]Department of Chemistry, Ångström, The Theoretical Chemistry Programme, Uppsala University, SE-75120 Uppsala, Sweden

Supporting Information

ABSTRACT: The tyrosine corner is proposed as a featured element to enhance photostability in human γB-crystallin when exposed to UV irradiation. Different ultrafast processes were studied by multiconfigurational quantum chemistry coupled to molecular mechanics: photoinduced singlet−singlet energy, electron and proton transfer, as well as population and evolution of triplet states. The minimum energy paths indicate two possible UV photoinduced events: forward−backward proton-coupled electron transfer providing to the system a mechanism for ultrafast internal conversion, and energy transfer, leading to fluorescence or phosphorescence. The obtained results are in agreement with the available experimental data, being in line with the proposed photoinduced processes for the different tyrosine environments within γB-crystallin.

INTRODUCTION

Crystallins are the main proteins forming the vertebrate eye lens, reaching 90% of the total protein content in the human eye lens.[1] Light passes through the cornea, the barrier between the external environment and the inside of the eye, and is focused by the lens on the retina, which contains the necessary photoreceptors to initiate the transmission of the optic information to the brain via nerve cells.[2,3]

α-, β-, and γ-crystallins (the three main types of crystallin) are not subject to protein turnover during a whole lifetime. Thereby the high stability showed against UV/vis irradiation is responsible for the long-term transparency of the eye lens. Changes in the crystallin structure can cause precipitation of protein aggregates in the lens cells.[4] As a result, light is largely blocked by the lens and the optical information does not reach the retina anymore. This phenomenon is known as a cataract, the major cause of blindness worldwide.[5]

Therefore a major challenge is to understand which chemical mechanisms can be considered responsible for a stable transparency of the crystallin. In other words, what kind of molecular or atomistic processes can prevent the eye lens from being damaged from the UV irradiation present in sunlight? In order to attempt possible answers to this question, all UV photostability mechanisms should be taken into account, since they could play a prominent role. Here we focus attention on the structural proteins of the eye lens, i.e., β- and γ-crystallins, characterized by high similarity: they are both formed by domains consisting of two Greek-key motifs (Figure 2). Different photostability mechanisms were already proposed: as a biological mechanism, α-crystallin was shown to bind in vitro partially unfolded proteins preventing aggregation,[6−8] therefore suggesting that α-crystallin can prevent aggregation of partially damaged or unfolded β- and γ-crystallins (i.e., prevent cataract formation).[9]

Evidently, other photostability mechanisms would be more efficient if β- and γ-crystallins could maintain their structures without undergoing partial unfolding. Especially, ultrafast internal conversion could allow conversion of the excitation energy into vibrational energy. The dissipation of the extra energy by the environment could permit the system to finally reach the ground state (GS), restoring the initial electronic structure of the system. β- and γ-crystallins contain tryptophan (Trp) and tyrosine (Tyr) residues that can act as UV filters, protecting the retina by absorbing at wavelengths $\lambda < 315$ nm (energy > 3.94 eV) in the case of Trp, and $\lambda < 300$ nm (energy > 4.13 eV) in the case of Tyr (Figure 1). Trp has shown intrinsic fluorescence in different proteins.[10,11] In human γD- and γS-crystallins, Trp fluorescence is quenched in the native state, but small changes in the protein conformation around Trp could result in a loss of efficiency of the fluorescence quenching mechanism.[12−15] The fluorescence quenching results from ultrafast mechanisms acting on Trp and its environment, such as fast electron transfer mechanisms, as has been shown by experiments and computations,[14−16] and it may protect the lens proteins from ultraviolet photodamage. The much wider match between γB-crystallin[17] and Tyr fluorescence emission spectra, instead of γB-crystallin and Trp fluorescence emission spectra,[18] is an indication that Trp fluorescence quenching is a relevant process. Moreover, Tyr residues can cause phosphorescence of γ-crystallins, although the presence of specific quenchers can decrease it.[19]

Nevertheless, additional mechanisms for ultrafast internal conversion could act on Tyr residues, furnishing additional pathways to enhance photostability. Especially the Tyr corner is a highly conserved conformational element in all β- and γ-crystallin domains,[21,22] where a Tyr side chain is hydrogen bonded to the

Received: February 8, 2012
Published: February 28, 2012

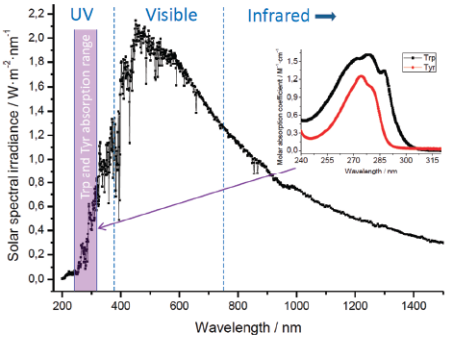

Figure 1. Solar spectrum subdivided into UV, visible, and infrared regions.[20] Tryptophan and tyrosine UV absorption spectra are shown as an inset.[18]

protein backbone (see Figures 2 and 3). Hydrogen bonds between amino acids were proposed as featuring elements to

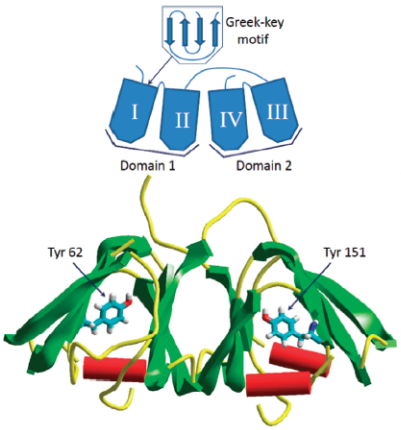

Figure 2. Schematic view of the γ-crystallin tertiary structure, with Greek-key motif I depicted (top). Human γB-crystallin structure and its Tyr corners (bottom). PDB code: 2JDF.

confer photostability to proteins via a photoinduced proton transfer (PPT) mechanism:[23−26] in a first (forward) step photoinduced electron transfer promotes the proton transfer along the hydrogen bond coordinate, resulting in a net transfer of a hydrogen atom. A second (backward) step permits reforming the initial hydrogen bond pattern in picoseconds, via a back electron transfer which promotes a back proton transfer.[27,28]

Especially proton-coupled electron transfer from Tyr and phenol (the Tyr chromophore) systems was proposed by theoretical studies[29] and observed experimentally,[30−33] including different possible mechanisms: stepwise electron transfer followed by proton transfer (PPT), stepwise proton transfer

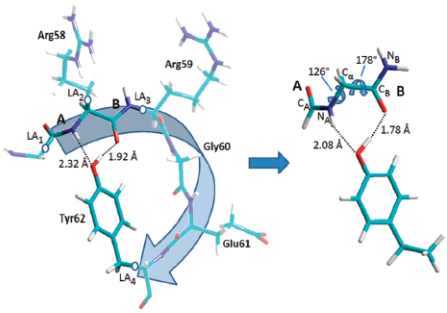

Figure 3. GS optimized structures at the CASSCF level (12 electrons in 10 orbitals). In both QM/MM (left) and QM (right) models the C_A−N_A−C_α−C_B and N_A−C_α−C_B−N_B dihedrals were kept constant at 126 and 178°, respectively (crystallographic structure).

followed by electron transfer, and a concerted mechanism where the hydrogen atom is transferred in a single step.

The aim of this study is to evaluate the role of the Tyr corner as a conformational element enhancing photostability. In order to understand how (and to what extent) the protein environment affects each photoinduced mechanism, we performed quantum mechanics (QM) and quantum mechanics/molecular mechanics (QM/MM) calculations on a Tyr-corner model as a self-assembling unit and as a model taking into account the surrounding human γB-crystallin (see Figure 3). The possible photoinduced pathways in the Tyr corner indicate PPT and energy transfer as possible competitive mechanisms conferring photostability to the eye lens.

METHODS

The study is focused on the calculation of the excited states of the Tyr-corner structure, a conformational element present in all structural crystallins, characterized by stable hydrogen bonds which could give rise to ultrafast internal conversion as a possible deactivation process of the incoming UV irradiation on earth (see Figure 1). In order to obtain a mechanistic description of the relevant photophysical processes, ab initio multiconfigurational methods were applied to a QM model of the hydrogen-bonded moiety within the Tyr corner as a standalone system and as a QM region of a QM/MM model including the whole human γB-crystallin (Figure 3). More in detail, considering its successful results in describing quantitatively the energies and electronic structure of several molecular systems, the MS-CASPT2//SA-CASSCF[34] methodology was applied to the system studied in this work.[35,36] (see Supporting Information for computational details).

Minimum energy paths (MEPs) were calculated at the SA-CASSCF level, permitting location of the energy minima on the potential energy surfaces (PESs) under study.

When two different singlet states were found to be degenerate in energy, the resulting crossing was characterized by calculating the nonadiabatic coupling vectors (i.e., derivative coupling (DC) and gradient difference (GD) vectors), in order to determine the crossing topology: for avoided crossings (ACs), GD and DC vectors are parallel, thus providing the initial direction of the reaction coordinate of the process, while for conical intersections (CIs), GD and DC vectors generate a

two-dimensional branching space where the energy degeneracy is left.

An active space of 12 electrons in 10 orbitals was selected, including four orbitals on the Tyr side chain (two π and two π^* on the aromatic ring) and three orbitals on each of the two peptide bonds of the backbone (one π, one π^*, and one n orbital on the C═O). In order to validate the employed active space, a more extended study was performed to determine the absorption spectrum, by considering additionally two larger active spaces: 14 electrons in 12 orbitals, adding one π and one π^* orbital on the aromatic ring of the Tyr side chain, and 16 electrons in 13 orbitals, adding also one n orbital on the oxygen atom of the Tyr side chain (see Supporting Information for parameter details and main orbitals involved). For all atoms a 6-31G(d) basis set was adopted.

After the study of the QM model was performed by CASPT2//CASSCF methodology, the role of the protein environment and surrounding water molecules was considered by setting up a QM/MM model at the CASPT2//CASSCF/AMBER level, applying the AMBER99SB force field (see Supporting Information for a description of the methodology and model details).[37,38]

More in detail, the backbone strand selected for a quantum chemical treatment in the QM/MM model includes the two peptide bonds, A and B, directly involved (by the hydrogen bonds with the Tyr side chain) in a description of the possible photoinduced mechanisms. Three hydrogen link atoms (LA_1 to LA_3) were needed to define the QM/MM frontier for the selected backbone, while LA_4 permits including the Tyr62 side chain in the QM region. This results in a QM region of the size appropriate for a CASPT2//CASSCF treatment.

The QM model, properly constrained to mimic the Tyr-corner conformation (see Supporting Information), includes all the features described for the QM region of the QM/MM model, allowing for a comparison of the photoinduced processes feasibility in vacuo and within the native protein environment (see Figure 3).

All calculations for the QM model were performed with Molcas 7[39] and Gaussian 03[40] packages. The setup of the MM model was carried out with the Tinker 4.2 software.[41] The QM/MM calculations were performed with the Molcas 7.6/Tinker 4.2 interface.

■ RESULTS AND DISCUSSION

Ground-State Structure. The Tyr corner is a conformational element which usually acts as a β-arch connecting two consecutive β-strands: in β- and γ-crystallins the Tyr corner connects two Greek-key motifs (see Figure 2). The Tyr corner is commonly formed by a short sequence of four, five, or six residues having always Tyr as the C-terminal amino acid. The Tyr-corner element is usually stabilized by a hydrogen bond placed between the OH group of the Tyr side chain and the backbone CO group of the first residue of the corner sequence (i.e., a Tyr—OH···O═C pattern). Additionally, a second hydrogen bond can be formed between the oxygen of the Tyr side chain and the backbone NH group of the first residue of the corner structure (i.e., a Tyr—O···H—N pattern).

All β- and γ-crystallins contain two almost identical Tyr-corner elements. Especially in human γB-crystallin the two Tyr-corner sequences (Arg58-Arg59-Gly60-Glu61-Tyr62 and Arg147-Pro148-Gly149-Glu150-Tyr151) differ only in the second residue of the sequence, favoring in both cases the formation of two hydrogen bonds between Tyr and the first residue of the corner (Tyr62···Arg58 and Tyr151···Arg147, respectively).

In this study attention is focused on the description of the interaction between the Tyr62 side chain and the backbone, via a QM minimal model of the Tyr corner and a hybrid QM/MM model where the Tyr62 corner is the QM center surrounded by the rest of human γB-crystallin, treated at the MM level (see Figure 3).

Absorption Spectra. The Franck−Condon (FC) main electronic transitions, CASPT2 vertical excitation energies (ΔE), and oscillator strengths (f) of the singlet excited states up to 8 eV are shown in Table 1. As expected, UV absorption

Table 1. CASPT2 (16 Electrons in 13 Orbitals) Absorption Spectra of the QM and QM/MM Models[a]

state	transition	ΔE_{QM}/eV	$\Delta E_{QM/MM}$/eV	$f_{QM} \times 10$	$f_{QM/MM} \times 10$
S_6 (CT)	$^1(\pi_{Ph} \rightarrow \pi^*_B)$	7.11	7.21	12.834	16.038
S_5 (LE_5)	$^1(\pi,\pi^*)_{Ph}$	7.06	7.08	0.218	0.766
S_4 (LE_4)	$^1(\pi,\pi^*)_{Ph}$	6.04	6.54	0.141	0.177
S_3 (LE_3)	$^1(n,\pi^*)_B$	6.03	6.49	0.007	0.010
S_2 (LE_2)	$^1(n,\pi^*)_A$	5.89	6.17	0.006	0.010
S_1 (LE_1)	$^1(\pi,\pi^*)_{Ph}$	4.84	4.81	0.357	0.245

[a] S_0, corresponding to the GS at the Franck−Condon point, is the energy reference: $\Delta E = E(S_n) - E(S_0)$.

by the phenol group (Ph) of the Tyr side chain ($S_0 \rightarrow S_1$) is the highest probability transition, within the biologically relevant middle-UV region (from ca. 4.1 to 6.2 eV), which could initiate any photophysical process: the f value of the $^1(\pi,\pi^*)_{Ph}$ transition corresponding to a single excitation to the lowest locally excited state (LE_1) is from 1 to 2 orders of magnitude larger than the f values of the $^1(n,\pi^*)_A$ and $^1(n,\pi^*)_B$ dark states.

Higher in energy, both QM and QM/MM absorption spectra show LE states associated with the $^1(\pi,\pi^*)_{Ph}$ transition (LE_4 and LE_5), and a charge transfer (CT) state corresponding to a $^1(\pi_{Ph} \rightarrow \pi^*_B)$ transition. Direct population of the CT state is favored by a high f value and would lead to electron transfer from the Tyr side chain to the backbone, but the high energy required for the transition (ΔE_{QM} = 7.11 eV, $\Delta E_{QM/MM}$ = 7.21 eV) makes the event not likely to happen in the FC region.

In the following sections, the possible excited-state relaxation pathways are investigated and the resulting processes are organized as follows: first all singlet−singlet energy, electron, and proton transfer processes are detailed for the QM model, followed by a section dedicated to the role of triplet states. Once all possible mechanisms are shown in vacuo, a comparison with the photoinduced processes in the QM/MM model is made, in order to elucidate the effect of the protein environment on the Tyr-corner element.

Energy Transfer Processes. After vertical transition to the first excited state corresponding to the Tyr side chain (LE_1, $^1(\pi,\pi^*)_{Ph}$), the first photophysical process which could take place is energy transfer to the crystallin backbone: an LE_2/LE_1 singlet−singlet state crossing is found between the lowest bright $^1(\pi,\pi^*)_{Ph}$ state and the dark $^1(n,\pi^*)_A$ state, corresponding to a conical intersection (CI). Two different pathways are possible after the crossing: on one side, the eventual population of the LE_2 state could allow ultrafast energy transfer from Tyr to peptide bond A, finally reaching a minimum where the O_{Tyr}···HN_A hydrogen bond is increased from 2.08 to 2.28 Å (see Figure 4). The DC vector at

dx.doi.org/10.1021/ct300114w | J. Chem. Theory Comput. 2012, 8, 1351−1359

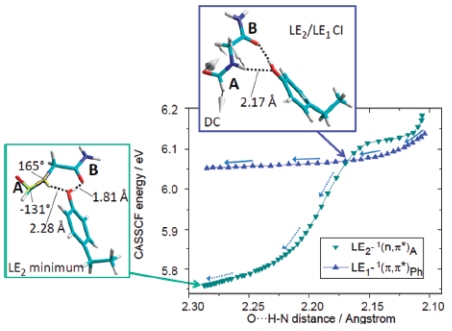

Figure 4. CASSCF MEPs of LE_1 and LE_2 states in the QM model after FC-vertical excitation, corresponding to LE_1 energy stabilization (solid arrows) or ultrafast energy transfer at LE_2/LE_1 CI ($O_{Tyr}\cdots HN_A$ distance = 2.17 Å), followed by LE_2 minimization (dashed arrows). The corresponding DC vector is shown.

the LE_2/LE_1 CI and the LE_2 minimum structure show clearly the driving force in the relaxation process: while the B moiety keeps the H−N−C−O planarity, the A moiety undergoes pyramidalization over the carbon and nitrogen atoms of the peptide bond.

The topology of the PESs near the CI suggests that the coupling between LE_1 and LE_2 states should be not strong enough to make efficient the population of LE_2, thus favoring LE_1 energy stabilization instead of LE_2 population. Both electronic states energies are in fact slightly avoided in the branching space close to the CI, indicating the low efficiency of the crossing.

On the other hand, if the system is further stabilized in the LE_1 state, an excited-state intermediate is reached which evolves giving rise to a second process where the O_{Tyr}—H···O=C_B hydrogen bond is the main reaction coordinate: after the LE_2/LE_1 CI, LE_1 decreases in energy reaching a minimum at an O_{Tyr}—H···O=C_B distance around 1.55 Å. From this minimum, a transition state is found at 5.49 kcal·mol^{-1}, at the CASPT2 level (see Figure 5). The vibrational excess on LE_1 (more than 37 kcal·mol^{-1})[42] can be considered reasonably large to overcome this excited-state energy barrier, thereby leading to a second crossing between LE_1 and LE_2 (O_{Tyr}—H···O=C_B distance = 1.16 Å), corresponding to an AC in which the proton is almost transferred. Again both events (i.e., LE_1 further stabilization and energy transfer from Tyr to A, through LE_2 population) are possible competitive processes, in this case implying coupling of the C_A=O and in-plane aromatic ring stretching modes, as indicated by the parallel nonadiabatic coupling vectors (Figure 5, LE_1/LE_2 AC). If the dark $^1(n,\pi^*)_A$ state is populated, a minimum is then found on LE_2, corresponding to the same geometry found by the first described energy transfer process. A similar geometric change of the peptide bond was already found by the authors in a hydrogen-bonded two-glycine model, where the same mechanism proposed here (an AC between a $^1(\pi,\pi^*)$ and a $^1(n,\pi^*)$ state) could permit ultrafast energy transfer.[35]

Further evolution of the $^1(n,\pi^*)_A$ state could involve radiative decay to S_0, or a transition to the first triplet state (T_1, see Role of Triplet States).

Energy transfer processes from the Tyr side chain to B or between A and B were not found. The only possibility of populating the dark $^1(n,\pi^*)_B$ state (LE_3) is directly by absorption in the FC region, an unlikely event considering the low f value and the high energy required (see Table 1 and Supporting Information for details of the LE_3 evolution).

Electron and Proton Transfer Processes. Electron transfer processes are possible if the CT state can be populated, leading to transfer of negative charge from the aromatic ring to the B moiety. Especially the CT state is stabilized in energy along the O_{Tyr}—H···O=C_B proton transfer coordinate, crossing in turn with LE_2 and LE_1 states (Figure 5).

Therefore, electron transfer enhances the proton transfer already initiated in the LE_1 state, permitting ultimately the complete transfer in the CT state: once the CT state is populated, further stabilization in energy along the proton transfer coordinate allows an ultimate crossing with GS, where a backward electron transfer is followed by a backward proton transfer, reestablishing the initial electronic configuration (see Scheme 1).

Since the CT state cannot be populated by absorption in the FC region, efficient crossing with LE states constitute the bottleneck of any electron transfer process in the Tyr corner. A second requirement which should be fulfilled is a low energy barrier on the LE states, in order to increase the feasibility of the process.

An analysis of the nonadiabatic coupling vectors of the CT/LE_1 CI (Figure 5) clarifies that the proton on the Tyr side chain tends to detach from the phenol moiety and attach to the

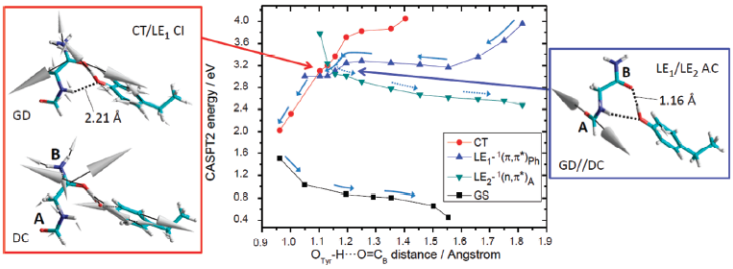

Figure 5. CASPT2 energy profile as a function of the O_{Tyr}—H···O=C_B hydrogen bond distance (QM model), starting from the LE_2 minimum (O_{Tyr}—H···O=C_B distance = 1.81 Å). Two UV-induced ultrafast processes are proposed: proton transfer (solid arrows) and energy transfer (dashed arrows). The nonadiabatic coupling vectors of CT/LE_1 CI (|GD| ≈ 18 |DC|) and LE_1/LE_2 AC (parallel vectors) are shown.

Scheme 1. Photoinduced Forward–Backward (f–b) Electron Transfer (ET) and Proton Transfer (PT) Mechanism, Suggested To Provide Photostability to the Tyr Corner of Human γB-Crystallin

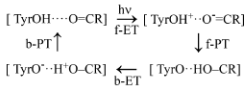

oxygen of the negatively charged B moiety, minimizing the charge separation. This causes rearrangements on the aromatic ring (which tends to adopt the configuration of a semiquinone) and on the B peptide bond (where CO and CN bonds tend to become single bonds).

An alternative pathway for electron and proton transfer implies population of the LE_2 state, which in turn could cross the CT state (CT/LE_2 AC, Figure 6). Even though the non-

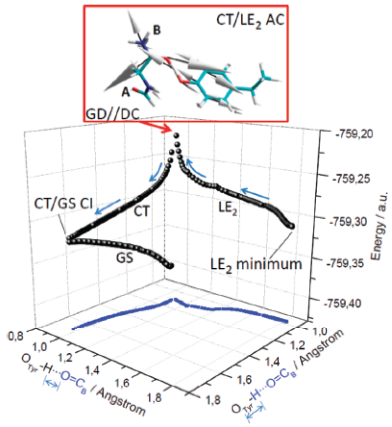

Figure 6. CASSCF MEPs calculated for CT and LE_2 states indicating electron and proton transfer (solid arrows) through a CT/LE_2 AC (GD parallel to DC). The potential energy is plotted as a function of O_{Tyr}—H···O=C_B hydrogen bond and O_{Tyr}–H bond distances.

adiabatic coupling vectors are similar to those found at the CT/LE_1 CI, the high energy barrier on the LE_2 state (ca. 36 kcal·mol^{-1}) makes the process not likely to happen.

Once the CT state is populated, the system undergoes vibrational relaxation, minimizing its energy and completing the proton transfer to the B moiety, ultimately reaching a CI with the GS state, corresponding to an S_1/S_0 CI (Figure 7). As indicated by the energy profile of CT and GS states around the CI, on the branching plane where energy degeneracy is left, two possibilities are given to the system when decaying to the GS state, corresponding to the energy minima along the loop (at ca. 70° for GS and 235° for CT): on one side, the GS state can be populated, transferring one electron from the B moiety to the Tyr side chain (as indicated by the Mulliken charges calculated around the CI). On the other side, the CT state can further decrease in energy, stabilizing the hydrogen-transferred electronic configuration. The nonadiabatic coupling vectors confirm this description and give the initial relaxation directions

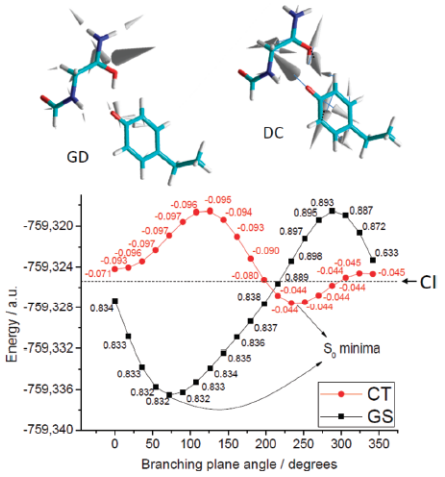

Figure 7. Energy of CT and GS states along a loop generated around the CT/GS CI (radius 0.05 Å) on the branching plane defined by the nonadiabatic coupling vectors (|GDI ≈ 53 |DCI). Mulliken charges, determined for the B moiety with contribution of the transferred hydrogen atom, are shown for both states at each point of the loop.

on S_0, with the transferred hydrogen on B pointing back to the Tyr side chain (GD vector) or being stabilized on the B moiety (DC vector).

The MEPs calculated from the CT/GS CI are shown in Figure 8: if the GS state is directly populated, the proton just

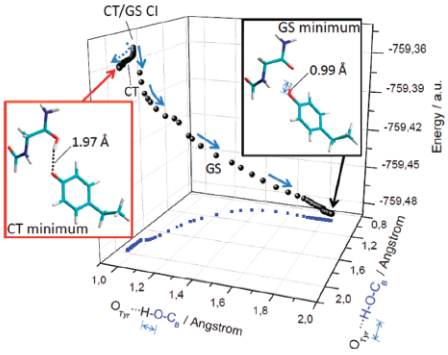

Figure 8. MEPs on S_0 after CT/GS CI, indicating back proton transfer from B to the Tyr side chain, reforming the initial FC structure (solid arrows), or formation of a metastable hydrogen-transferred photoproduct (dashed arrows).

formed on B migrates back to the Tyr side chain, reestablishing the initial Tyr-corner structure, therefore providing photostability. As an additional pathway, a minimum on the CT state is found ca. 6 kcal·mol^{-1} lower than the CT/GS CI, where the

dx.doi.org/10.1021/ct300114w | J. Chem. Theory Comput. 2012, 8, 1351–1359

OH hydrogen bond between semiquinone and B moieties enlarges to 1.97 Å. This hydrogen-transferred species should correspond to a metastable photoproduct, since the high vibrational excess on the CT state (see at Figure 5 the steepness of the CT energy profile) can be sufficient to overcome the low energy barrier between the CT minimum and the CT/GS CI, allowing for population of the GS state which promotes back electron and proton transfer.

Role of Triplet States. Triplet states also play a role for the photostability of the Tyr-corner structure: when irradiating the system (FC region), the low spin−orbit coupling between GS and triplet states excludes direct excitation to a triplet state and suggests that an excited singlet state will be populated, most probably corresponding to LE_1 (see Table 1). Therefore, a triplet state can be formed only by a transition from an excited singlet state (i.e., by intersystem crossing). As previously discussed, the LE_1/LE_2 AC involves an energy transfer process, where the initially excited molecule (LE_1 state) has some probability of populating the $^1(n,\pi^*)_A$ state (LE_2), reaching a minimum at an O_{Tyr}—H···O═C_B distance around 1.8 Å (Figure 5). From this stationary point an alternative pathway to radiative decay (i.e., fluorescence) is given by a possible transition to the $^3(n,\pi^*)_A$ state (T_1), where the minimum energy structure in this state is located as close as 5 kcal·mol^{-1} below the LE_2 state. The structural and energy proximity of LE_2 and T_1 minima as well as the nonvanishing spin−orbit coupling (0.15 cm^{-1})[43] ensures that the $^3(n,\pi^*)_A$ state can be populated. Once the $^3(n,\pi^*)_A$ state is populated, two different mechanisms can be proposed: phosphorescence from the T_1 minimum and evolution along the triplet states.

The energy profile shown in Figure 9 suggests that, in principle, the triplet states can undergo the same forward−backward proton-coupled electron transfer process: a $^3(n,\pi^*)_A/^3(\pi,\pi^*)_{Ph}$ crossing between triplet LE states permits reaching a second $^3(\pi,\pi^*)_{Ph}/^3(\pi_{Ph} \rightarrow \pi^*_B)$ crossing, where a triplet CT state can be populated, corresponding to electron transfer from the Tyr side chain to B (as for the singlet CT). The charge separation is stabilized by proton transfer to B, by which an ultimate $^3(\pi_{Ph} \rightarrow \pi^*_B)$/GS crossing is reached, allowing for ultrafast internal conversion.

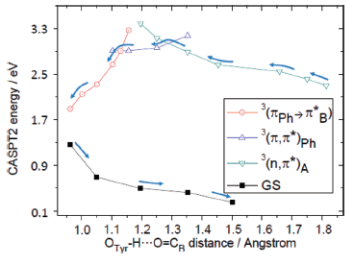

Figure 9. QM model CASPT2 energy profile of the triplet states possibly involved in PPT (mechanism showed by arrows). The proposed pathway implies population of the $^3(n,\pi^*)_A$ state at O_{Tyr}—H···O═C_B distance around 1.8 Å, a $^3(n,\pi^*)_A/^3(\pi,\pi^*)_{Ph}$ crossing, population of a triplet CT state through a $^3(\pi,\pi^*)_{Ph}/^3(\pi_{Ph} \rightarrow \pi^*_B)$ crossing, and finally decay to the GS state.

The factor limiting the feasibility of PPT by triplet states is the energy barrier on the $^3(n,\pi^*)_A$ state (from the $^3(n,\pi^*)_A$ minimum to the $^3(n,\pi^*)_A/^3(\pi,\pi^*)_{Ph}$ crossing), which was estimated to be 29 kcal·mol^{-1}.

Effect of the Protein Environment. Excited-state deactivation pathways were calculated for a QM/MM model, where the active center, which corresponds to the QM model studied in vacuo, is now surrounded by the protein and water molecules (Figure 10).

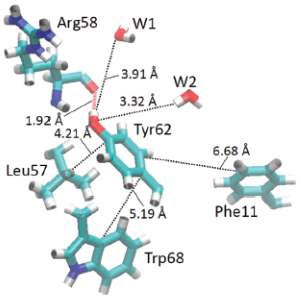

Figure 10. Side chains (Phe11, Leu57, Arg58, and Trp68) and the water molecules (W1 and W2) surrounding Tyr62, as defined by the ground-state optimized QM/MM geometry.

The photoinduced energy, electron, and proton transfer processes depicted for the QM model were found also in the QM/MM model, with differences in energy and structure which affect the efficiency of the mechanism of photostability (the most relevant structures are given in the Supporting Information).

Both possibilities described in the QM model to populate the dark $^1(n,\pi^*)_A$ state after irradiation to the bright $^1(\pi,\pi^*)_{Ph}$ state (through crossings between LE_1 and LE_2) were found also in the QM/MM model. Especially two LE_1/LE_2 crossings could imply migration of energy from the initially excited Tyr side chain to peptide bond A (see Figure 11). Just after vertical excitation from GS to LE_1, a first LE_1/LE_2 crossing is found,

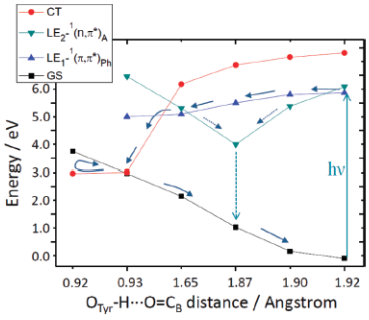

Figure 11. Energy profile of the possible UV photoinduced mechanisms in a human γB-crystallin QM/MM model, as a nonlinear function of the O_{Tyr}—H···O═C_B distance: forward−backward proton-coupled electron transfer (solid arrows) and energy transfer followed by fluorescence (dashed arrows).

while a second possibility to populate LE_2 is located at an O_{Tyr}—H···O═C_B distance around 1.65 Å. For the first crossing (lower vibrational excess), the probability of non-adiabatic transition was estimated to be 0.12, while for the second crossing (higher vibrational excess), the probability decreases to 3.60×10^{-5}, as indicated by Landau−Zener theory (see Supporting Information).

This means that the originally populated $^1(\pi,\pi^*)_{Ph}$ state (LE_1) first crosses with the $^1(n,\pi^*)_A$ state (LE_2) with a minor but still relevant probability of transferring energy to LE_2, and preferentially continuing to descend in energy up to the second cross with LE_2, where the population of the $^1(n,\pi^*)_A$ state is a much less likely event, leading to electron transfer via a CT state population.

Comparing QM and QM/MM models, two main differences were found:

1. No intermediate was found in the QM/MM model for the LE_1 state after vertical excitation. Therefore, no energy barrier is present in this state, making more efficient the subsequent photophysical processes predicted for this state. On the contrary, an energy barrier of 5.49 kcal·mol^{-1} was found for the QM model (see Figures 5 and 11).
2. The crossing between LE_1 and LE_2 states corresponds to different structures for QM and QM/MM models: in the QM model, considering the O_{Tyr}—H···O═C_B hydrogen bond coordinate, the hydrogen atom is almost transferred to peptide bond B (Figure 5, at 1.16 Å), while in the QM/MM model the same hydrogen atom is still distant from peptide bond B: 1.92 and 1.65 Å for the first and second crossings, respectively (see Figure 11). This suggests that Dexter-type singlet−singlet energy transfer is a competitive process when the protein environment is included, while proton-coupled electron transfer is highly preferred in the Tyr corner as a standalone moiety.

In the QM/MM model, the population of the CT state through a CT/LE_1 crossing corresponds to migration of one electron from the Tyr side chain to peptide bond B, followed by transfer of a proton to minimize the charge separation. This corresponds to stabilization of the CT state up to crossing with the GS. At the CT/GS crossing two processes can occur: a back proton-coupled electron transfer from peptide bond B to the Tyr side chain, restoring the initial GS geometry (FC region), or further stabilization of the CT state, where a metastable photoproduct, corresponding to net transfer of a hydrogen atom from the Tyr side chain to peptide bond B (CT minimum), was found ca. 4.5 kcal·mol^{-1} lower in energy than the CT/GS crossing. Since the same kind of hydrogen-transferred photoproduct was found in the QM model ca. 6 kcal·mol^{-1} lower in energy than the CT/GS crossing (see Figure 8), it can be concluded that a lower vibrational excess on the CT state is required for the QM/MM model to overcome the energy barrier between the CT minimum and the CT/GS crossing, therefore populating the GS and enhancing ultrafast internal conversion.

Singlet−singlet energy transfer leads to a $^1(n,\pi^*)_A$ minimum, characterized by pyramidalization over the carbon and nitrogen atoms of peptide bond A (−149 and 171°, respectively), as in the QM model (−131 and 165° respectively; see Figure 4, LE_2 minimum), but indicating lower deviation from the peptide bond planarity. Also in the QM/MM model, the eventual population of a triplet state from the $^1(n,\pi^*)_A$ minimum was considered as a possible alternative to fluorescence: a $^3(n,\pi^*)_A$ state is located ca. 9 kcal·mol^{-1} higher in energy, suggesting a possible but not prominent role of the triplet states eventually leading to phosphorescence (as indicated by experimental studies)[19] and therefore indicating fluorescence as the most important photophysical process after energy transfer. Especially fluorescence is calculated to take place at 4 eV (310 nm), mostly corresponding to the expected value for Tyr fluorescence in water (303 nm).[18] Considering the protein environment around the Tyr corner (see Figure 10), the proximity of Trp68 to Tyr62 suggests a possible fluorescence quenching mechanism through Förster resonance energy transfer between the two chromophores, a common event in proteins. Once the energy is transferred to Trp68, fluorescence quenching can follow, as suggested by theoretical and experimental studies showing the efficiency of Trp fluorescence quenching within γ-crystallin.[14−17]

Nevertheless, singlet−singlet energy transfer was estimated to be not prominent, as the highest probability for the process to happen was calculated to be 0.12 (LE_2/LE_1 crossing associated with low vibrational excess). Therefore, proton-coupled electron transfer is the most probable process within the Tyr-corner element of γB-crystallin (Figure 11 and Scheme 2, left), a process

Scheme 2. Energy Profiles of the UV Photoinduced Processes within the Tyr Residues of γB-Crystallin, Indicating by Arrows the Most Probable Mechanism: Ultrafast Radiationless Deactivation for Hydrogen-Bonded Tyr-Corner Elements (Left) and Fluorescence Radiative Decay for Tyr Residues Not Involved in Hydrogen Bonds (Right)

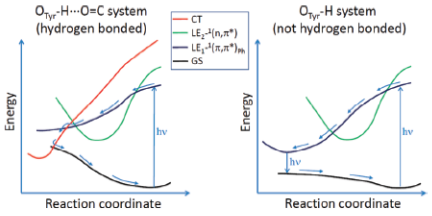

which can be proposed on the basis of theoretical and experimental findings.[29−33] This ultimately suggests that both Tyr-corner elements present in γB-crystallin can enhance the photostability of the human eye lens. Anyway, other Tyr residues are present in γB-crystallin not arranged as Tyr corners, therefore are not involved in hydrogen bonds with the protein backbone, and finally leading to photochemical pathways not including CT states (Scheme 2, right): proton-coupled electron transfer is not possible, while the most probable UV photoinduced event is fluorescence from the LE_1 minimum. This can explain fluorescence spectra recorded in γB-crystallin, where Tyr fluorescence quenching does not have a prominent role:[17] non-hydrogen-bonded Tyr residues produce fluorescence, while Tyr-corner elements provide the necessary conformation to release the UV irradiation energy by ultrafast radiationless deactivation.

■ CONCLUSIONS

The absorption spectrum and excited-state deactivation pathways of a Tyr-corner model in vacuo and as part of human γB-crystallin were studied by means of quantum mechanics (CASPT2//CASSCF level) and hybrid quantum mechanics/

dx.doi.org/10.1021/ct300114w | J. Chem. Theory Comput. 2012, 8, 1351−1359

molecular mechanics (CASPT2//CASSCF/AMBER level) methodologies, respectively. Different photoinduced processes were described, including energy, electron, and proton transfer for both models. Among them, energy transfer and especially forward−backward photoinduced proton transfer were found to play relevant roles in enhancing UV photostability. More in detail, Dexter-type singlet−singlet energy transfer was shown to possibly play a significant role when considering the Tyr corner within the protein environment, finally leading to fluorescence from an originally dark $^1(n,\pi^*)$ state, or Förster resonance energy transfer to a Trp residue, followed by Trp fluorescence quenching. Energy transfer processes compete with radiationless forward−backward proton-coupled electron transfer, which was shown to be the prominent UV photoinduced process within the human γB-crystallin environment of the Tyr corner. When looking at the Tyr corner as a standalone system, energy transfer mechanisms are even less significant, although fluorescence from a $^1(n,\pi^*)$ state or phosphorescence from a $^3(n,\pi^*)$ state is still possible, and therefore favoring the competing mechanism: radiationless forward−backward proton-coupled electron transfer. Ultimately, both energy transfer and forward−backward proton-coupled electron transfer mechanisms could provide (at least partially) an explanation for the characteristic photostability of the eye lens when exposed to UV irradiation. A transition state on the locally excited $^1(\pi,\pi^*)$ state, initially activated by irradiation, defines a ca. 5.5 kcal·mol^{-1} barrier as the only limiting factor for photostability when in vacuo. Including the protein environment, no energy barriers were found on the potential energy surfaces involved in proton transfer (LE_1, CT, GS), thereby allowing ultrafast internal conversion. Apart from direct recovery of the initial structure (through a conical intersection with the ground state, CT/GS CI), a hydrogen-transferred species was found in both models as a metastable photoproduct of charge transfer character. A small vibrational excess (ca. 4.5 kcal·mol^{-1} in the case of the biologically relevant model) permits reaching again the CT/GS CI where back electron transfer is followed by back proton transfer, restoring the Franck−Condon geometry.

From the biological point of view, the description of the above-mentioned photoinduced processes suggests, when compared to available experimental studies, that the Tyr corner is a conformational element which can induce or enhance photostability against UV irradiation, therefore indicating the possibility of modifying an existing protein by including one or more Tyr-corner elements, in order to avoid UV photodamage. The residues surrounding the Tyr corner will be critical in enhancing energy transfer mechanisms toward proton-coupled electron transfer mechanisms, or vice versa.

In the eye lens, the presence of two mostly identical Tyr-corner elements in all γ-crystallins and the similarity of all β- and γ-crystallins (grouped together as βγ-crystallins superfamily) raises the probability that this structural moiety can play an effective role. Semiclassical trajectories of the studied QM/MM system could be proposed in order to provide additional information, especially related to the time scale and quantum yield of the different possible mechanisms.

■ ASSOCIATED CONTENT

Supporting Information

CASPT2//CASSCF methodology and computational details. QM/MM methodology and model details. Absorption spectra additional parameters. Description of the $^1(n,\pi^*)_B$ state evolution. Description of the energy transfer probability calculation. Cartesian coordinates of the most relevant structures. This material is available free of charge via the Internet at http://pubs.acs.org.

■ AUTHOR INFORMATION

Corresponding Author

*E-mail: marco.marazzi@uah.es (M.M.); luisma.frutos@uah.es (L.M.F.). Tel.: +34 91 885 2512. Fax: +34 918854763.

Notes

The authors declare no competing financial interest.

■ ACKNOWLEDGMENTS

This research was supported by the Spanish MICINN Grant CTQ2009-07120. M.M. is grateful to the UAH for a doctoral fellowship and a short-term scholarship spent in the Uppsala University. I.N. thanks Prof H. M. Marques for funding through the DST/NRF SARChI initiative. L.M.F. acknowledges receipt of a "Ramon y Cajal" contract from MEC. We thank Alexandra Ryazanova from Lomonosov Moscow State University for helpful discussions on biological aspects of the system studied.

■ REFERENCES

(1) Oyster, C. W. *The Human Eye: Structure and Function*; Sinauer Associates: Sunderland, MA, 1999; pp 595−647.
(2) Davson, H. *Physiology of the Eye*, 5th ed.; The Macmillan Press Ltd.: London, U.K., 1990; pp 105−138.
(3) Bermann, E. R. *Biochemistry of the Eye*, 1st ed.; Plenum Press: New York, 1991; pp 201−290.
(4) Benedek, G. *Invest. Ophthalmol. Vis. Sci.* **1997**, *38*, 1911−1921.
(5) Clark, J. I. *Principle and Practice of Ophthalmology*; Saunders College Publishing: Philadelphia, PA, 1994; pp 114−123.
(6) Horwitz, J. *Proc. Natl. Acad. Sci. U.S.A.* **1992**, *89*, 10449−10453.
(7) Merck, K. B.; Groenen, P. J.; Voorter, C. F.; de Haard-Hoekman, W. A.; Horwitz, J.; Bloemendal, H.; de Jong, W. W. *J. Biol. Chem.* **1993**, *268*, 1046−1052.
(8) van Boekel, M. A.; Hoogakker, S. E.; Harding, J. J.; de Jong, W. W. *Ophthalmic Res.* **1996**, *28S*, 32−38.
(9) Bloemendal, H.; de Jong, W.; Jaenicke, R.; Lubsen, N. H.; Slingsby, C.; Tardieu, A. *Prog. Biophys. Mol. Biol.* **2004**, *86*, 407−485.
(10) Eftink, M. R. *Methods Biochem. Anal.* **1991**, *35*, 127−205.
(11) Callis, P. R.; Liu, T. *J. Phys. Chem. B* **2004**, *108*, 4248−4259.
(12) Phillips, S. R.; Borkman, R. F. *Curr. Eye Res.* **1988**, *7*, 55−59.
(13) Kosinski-Collins, M. S.; Flaugh, S. L.; King, J. *Protein Sci.* **2004**, *13*, 2223−2235.
(14) Chen, J.; Flaugh, S. L.; Callis, P. R.; King, J. *Biochemistry* **2006**, *45*, 11552−11563.
(15) Chen, J.; Callis, P. R.; King, J. *Biochemistry* **2009**, *48*, 3708−3716.
(16) Chen, J.; Toptygin, D.; Brand, L.; King, J. *Biochemistry* **2008**, *47*, 10705−10721.
(17) Mayr, E.-M.; Jaenicke, R.; Glockshuber, R. *J. Mol. Biol.* **1997**, *269*, 260−269.
(18) Du, H.; Fuh, R. A.; Li, J.; Corkan, A.; Lindsey, J. S. *Photochem. Photobiol.* **1998**, *68*, 141−142.
(19) Mandal, K.; Chakrabarti, B. *Biochemistry* **1988**, *27*, 4564−4571.
(20) ASTM G173-03(2008). *Standard Tables for Reference Solar Spectral Irradiances: Direct Normal and Hemispherical on 37° Tilted Surface*; ASTM International: West Conshohocken, PA, 2008.
(21) Hemmingsen, J. M.; Gernert, K. M.; Richardson, J. S.; Richardson, D. C. *Protein Sci.* **1994**, *3*, 1927−1937.
(22) Hamill, S. J.; Cota, E.; Chothia, C.; Clarke, J. *J. Mol. Biol.* **2000**, *295*, 641−649.
(23) Frutos, L. M.; Markmann, A.; Sobolewski, A. L.; Domcke, W. *J. Phys. Chem. B* **2007**, *111*, 6110−6112.
(24) Sobolewski, A. L.; Domcke, W. *J. Phys. Chem. A* **2007**, *111*, 11725−11735.

(25) Shemesh, D.; Sobolewski, A. L.; Domcke, W. *J. Am. Chem. Soc.* **2009**, *131*, 1374−1375.
(26) Marazzi, M.; Sancho, U.; Castaño, O.; Domcke, W.; Frutos, L. M. *J. Phys. Chem. Lett.* **2010**, *1*, 425−428.
(27) Schultz, T.; Samoylova, E.; Radloff, W.; Hertel, I. V.; Sobolewski, A. L.; Domcke, W. *Science* **2004**, *306*, 1765−1768.
(28) Lan, Z.; Frutos, L. M.; Sobolewski, A. L.; Domcke, W. *Proc. Natl. Acad. Sci. U.S.A.* **2008**, *105*, 12707−12712.
(29) Sobolewski, A. L.; Domcke, W. *J. Phys. Chem. A* **2001**, *105*, 9275−9283.
(30) Sjödin, M.; Styring, S.; Wolpher, H.; Xu, Y.; Sun, L.; Hammarström, L. *J. Am. Chem. Soc.* **2005**, *127*, 3855−3863.
(31) Görner, H.; Khanra, S.; Weyhermüller, T.; Chaudhuri, P. *J. Phys. Chem. A* **2006**, *110*, 2587−2594.
(32) Malval, J.-P.; Diemer, V.; Morlet-Savary, F.; Jacques, P.; Chaumeil, H.; Defoin, A.; Carré, C.; Poizat, O. *J. Phys. Chem. A* **2010**, *114*, 2401−2411.
(33) Swarnalatha, K.; Rajkumar, E.; Rajagopal, S.; Ramaraj, R.; Banu, I. S.; Ramamurthy, P. *J. Phys. Org. Chem.* **2011**, *24*, 14−21.
(34) Finley, J.; Malmqvist, P.-Å; Roos, B. O.; Serrano-Andres, L. *Chem. Phys. Lett.* **1998**, *288*, 299−306.
(35) Marazzi, M.; Sancho, U.; Castaño, O.; Frutos, L. M. *Phys. Chem. Chem. Phys.* **2011**, *13*, 7805−7811.
(36) Merchán, M.; Serrano-Andrés, L.; Fülscher, M. P.; Roos, B. O. *Recent Advances in Multireference Methods*; Hirao, K., Ed.; Recent Advances in Computational Chemistry 4; World Scientific Publishing Co.: Singapore, 1999; pp 161−195.
(37) Dapprich, S.; Komárino, I.; Byun, K. S.; Morokuma, K.; Frich, M. J. *J. Mol. Struct. (THEOCHEM)* **1999**, *461*, 1−21.
(38) Humbel, S.; Sieber, S.; Morokuma, K. *J. Chem. Phys.* **1996**, *105*, 1959−1967.
(39) Aquilante, F.; De Vico, L.; Ferré, N.; Ghigo, G.; Malmqvist, P.-Å.; Neogrády, P.; Pedersen, T. B.; Pitoňák, M.; Reiher, M.; Roos, B. O.; Serrano-Andrés, L.; Urban, M.; Veryazov, V.; Lindh, R. *J. Comput. Chem.* **2010**, *31*, 224−247.
(40) Frisch, M. J.; Trucks, G. W.; Schlegel, H. B.; Scuseria, G. E.; Robb, M. A.; Cheeseman, J. R.; Montgomery, J. A., Jr.; Vreven, T.; Kudin, K. N.; Burant, J. C.; Millam, J. M.; Iyengar, S. S.; Tomasi, J.; Barone, V.; Mennucci, B.; Cossi, M.; Scalmani, G.; Rega, N.; Petersson, G. A.; Nakatsuji, H.; Hada, M.; Ehara, M.; Toyota, K.; Fukuda, R.; Hasegawa, J.; Ishida, M.; Nakajima, T.; Honda, Y.; Kitao, O.; Nakai, H.; Klene, M.; Li, X.; Knox, J. E.; Hratchian, H. P.; Cross, J. B.; Adamo, C.; Jaramillo, J.; Gomperts, R.; Stratmann, R. E.; Yazyev, O.; Austin, A. J.; Cammi, R.; Pomelli, C.; Ochterski, J. W.; Ayala, P. Y.; Morokuma, K.; Voth, G. A.; Salvador, P.; Dannenberg, J. J.; Zakrzewski, V. G.; Dapprich, S.; Daniels, A. D.; Strain, M. C.; Farkas, O.; Malick, D. K.; Rabuck, A. D.; Raghavachari, K.; Foresman, J. B.; Ortiz, J. V.; Cui, Q.; Baboul, A. G.; Clifford, S.; Cioslowski, J.; Stefanov, B. B.; Liu, G.; Liashenko, A.; Piskorz, P.; Komaromi, I.; Martin, R. L.; Fox, D. J.; Keith, T.; Al-Laham, M. A.; Peng, C. Y.; Nanayakkara, A.; Challacombe, M.; Gill, P. M. W.; Johnson, B.; Chen, W.; Wong, M. W.; Gonzalez, C.; Pople, J. A. *Gaussian 03*, revision C.02; Gaussian, Inc.: Wallingford, CT, 2004.
(41) Tinker Molecular Modeling, version 4.2; http://dasher.wustl.edu/tinker/ (accessed Feb 27, 2012).
(42) The vibrational excess is calculated as the energy difference from the LE_1 $^1(\pi,\pi^*)_{Ph}$ vertical absorption (FC region) to the LE_1 minimum (O_{Tyr}—H··O═C_B hydrogen bond distance around 1.55 Å).
(43) The spin−orbit coupling (i.e., $\langle T_1|H|S_1\rangle$) was calculated considering the CASPT2 energy difference between T_1 and S_1 states at the LE_2 minimum and applying atomic mean-field integrals.

4.2 Donor-Acceptor Energy Transfer Reaction Coordinate

A theoretical formalism was developed in order to identify the molecular reaction coordinate involved in any electronic non-radiative energy transfer reaction mediated by an electron exchange mechanism (Dexter-type), within the weak electronic coupling limit. The formalism allows the separation of donor and acceptor contributions to the reaction coordinate, enabling the identification of the intrinsic role of each molecule in the energy transfer process. Indeed, within the weak coupling limit the transfer process can be correctly separated in two individual electronic transitions: donor deactivation ($^3D \rightarrow {}^1D$ or $^1D^* \rightarrow {}^1D$) and acceptor excitation ($^1A \rightarrow {}^3A$ or $^1A \rightarrow {}^1A^*$). Therefore, an energy transfer reaction coordinate can be defined for each individual transition, being additionally possible to identify the most relevant internal coordinates involved in the energy transfer process, by splitting the molecular reaction coordinate into different contributions of each individual internal coordinate. In this way, the role of each bond, angle and dihedral to accomplish the required molecular distortion is elucidated.

The developed formalism was applied to the debated case of Triplet-triplet Energy Transfer (TET) where *cis*-stilbene is an acceptor molecule (*Caldwell et al. 1992; Brennan et al. 1994; Saltiel et al. 2003; Lalevee et al. 2005*), determining the effect of each molecular internal coordinate on the transfer rate. Considering the nonvertical character of *cis*-stilbene and of other molecules (*e.g.* cyclooctatetraene) involved as acceptors in triplet-triplet energy transfer processes (*Frutos et al. 2004; Frutos and Castaño 2005*), a generalized geometrical distortion parameter is proposed, in order to quantify the nonvertical character of any given donor or acceptor molecule.

TET is an elementary radiationless process (*Turro et al. 2009*) taking place in natural photochemical reactions, *e.g.* in photosynthesis (*Moore et al. 1982; Gust and Moore 1989; Gust et al. 2009; Vura-Weis et al. 2010*), as well as in many photoinduced reactions with photochemical or technical relevance (*Nicholson 1993*). In the case of intermolecular TET, donor molecules excited to the lowest electronic triplet state (^3D) exchange energy and spin with ground-state singlet acceptor molecules (^1A), to yield

triplet-excited acceptor molecules (^{3}A). The energy balance of the transfer process can be expressed from the respective singlet-triplet transition energies as $\Delta E_T = E_T^D - E_T^A$, where $E_T^D = E(^3D \rightarrow {}^1D)$ and $E_T^A = E(^3A \leftarrow {}^1A)$ are the vertical transition energies from ^{3}D and ^{1}A equilibrium geometries respectively. In solution, when $\Delta E_T \geq 0$ (the so-called exothermic case) the transfer efficiency is nearly diffusion-controlled (*Forster 1949; Dexter 1953; Naqvi and Steel 1970*), indicating that close approach of donor and acceptor molecules (< 1 nm) is required, while in biological systems the transfer is usually limited by the donor-acceptor distance as well as their relative spatial orientation. In the so-called endothermic case ($\Delta E_T \leq 0$), energy transfer generally takes place through an Arrhenius-type thermally activated process, decreasing the transfer efficiency very rapidly with the energy deficit (*Forster 1949*). In solution, TET can be modelled as a bimolecular rate process in which diffusive (k_d, k_{-d}) and transfer (k_e, k_{-e}) steps are separated (*Saltiel and Atwater 1988*) and the transfer process takes place within the encounter complex [D···A] (a kind of "supermolecule") in which donor and acceptor partners are at collision distance. In some biological and condensed systems, direct-contact single-step or long distance multi-step hopping are also possible (*Moore et al. 1982; Gust and Moore 1989; Nicholson 1993; Gust et al. 2009; Vura-Weis et al. 2010*). The total spin of the [D···A] couple is conserved for both cases, and the electronic mechanism of energy transfer process is explained by a Dexter-type two-electron exchange (see section 1.3.2) through overlapping donor and acceptor molecular orbitals (*Saltiel and Atwater 1988*), especially between the respective frontier orbitals.

The nonvertical term was established analyzing anomalous cases regarding some highly endothermic TET reactions where the experimental value of the rate constant was much larger than that expected from the unfavourable energy balance (*Saltiel and Hammond 1963; Saltiel et al. 1984*), computed using singlet-triplet optical transition energies. These cases had in common acceptor compounds with flexible molecular structure for which nonvertical $^3A \leftarrow {}^1A$ excitation processes were initially postulated. It was later shown that excitation transitions in these cases do not depart from the classical vertical behaviour, and the apparent deviations from classical TET are now explained by a thermally-activated

population of acceptor molecules for which the energy of the lowest triplet state is decreased due to geometrical changes (*Ramamurthy and Liu 1976*).

4.2.1 Potential Energy Surfaces in Triplet-Triplet Energy Transfer

As shown above, the transfer process in condensed phase can be analyzed as proceeding from a reactant supermolecule [^{3}D···^{1}A] to the product one [^{1}D···^{3}A].

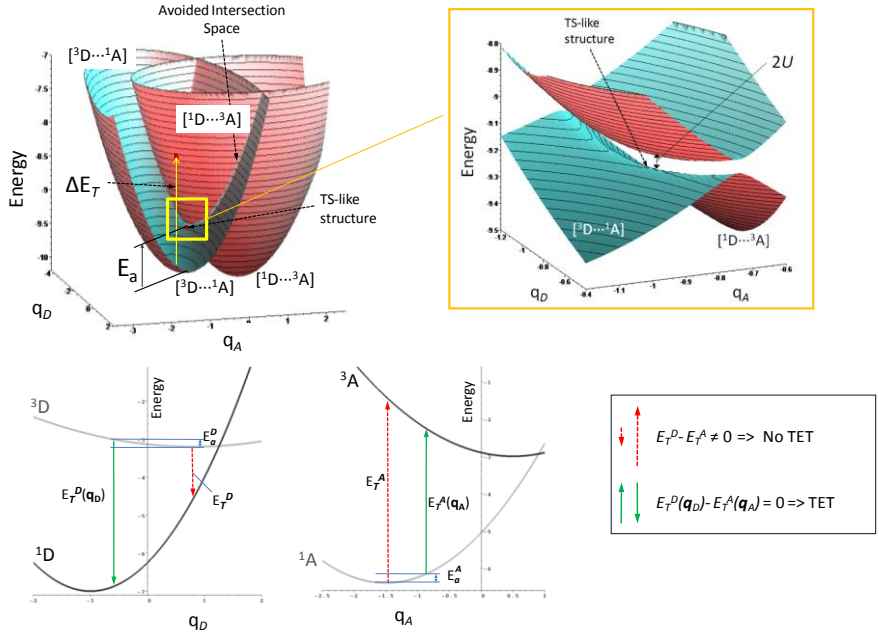

Figure 4.1 Top panel: Complete potential energy surfaces of the model supermolecules [^{3}D···^{1}A] and [^{1}D···^{3}A] in a TET process, with a magnified view of the avoided crossing between surfaces (2U). Lower panel: decomposition of the TET process in individual singlet-triplet transitions of donor and acceptor. The activation energy (E_a) shown in the complete PES representation corresponds to a minimum-energy, transition-state like configuration (TS), of the avoided intersection space. The energy of donor deactivation, E_T^D (^{3}D→^{1}D transition), and acceptor excitation, E_T^A (^{3}A←^{1}A transition), for the respective equilibrium conformations are indicated with red arrows in the lower panel. These values give rise to highly endothermic energy balance and therefore TET would not be possible for the ^{3}D and ^{1}A equilibrium conformation. However, D-A energy resonance can be attained by geometrical changes requiring modest activation energies (green arrows), which correspond to the transition-state configuration of the upper diagram.

Since the absolute value of the electronic coupling term is very low compared with other energies involved in the transfer step, the PES of the

supermolecule can be separated in two uncoupled PESs for the donor and acceptor partners. Therefore, considering a negligible value of electronic coupling and taking into account the resonance condition $E[^3D\cdots^1A] = E[^1D\cdots^3A]$, the TET process may be analyzed in terms of the individual transitions $^3D\rightarrow{}^1D$ and $^3A\leftarrow{}^1A$. In Figure 4.1 it is shown model PESs for a donor/acceptor couple in a TET process, as well as the potential energy curves of the singlet-triplet individual transitions as a function of internal coordinates $\mathbf{q}_A$ and $\mathbf{q}_D$ defining the molecular structure for acceptor and donor respectively. Because of the non-vanishing coupling, the adiabatic potential energy surfaces of both electronic states (*i.e.* before and after the transfer) do not present real crossings (*i.e.* conical intersections), showing slightly avoided crossings in the intersection space defined by the diabatic states as a result of the weak coupling. Note that the ground- and excited-state geometry in each transfer couple differs substantially. The available energy from the donor deactivation transition $^3D\rightarrow{}^1D$ at the equilibrium conformation (E_T^D Figure 4.1, lower panel) is insufficient for excitation of acceptor from its equilibrium conformation (E_T^A corresponding to $^3A\leftarrow{}^1A$ transition. Figure 4.1, lower panel) and TET is not possible. However, small changes in the conformation of both partners ($\mathbf{q}_A$ for acceptor and $\mathbf{q}_D$ for donnor) yield singlet-triplet transition energies very different from the equilibrium values, achieving energy resonance $E_T^D(\mathbf{q}_D) - E_T^A(\mathbf{q}_A) \approx 0$ for a given donor and acceptor structures: $\mathbf{q}_D$ and $\mathbf{q}_A$) and, therefore, leading to efficient transfer. These molecular distortions would take place at room temperature depending on the value of the corresponding activation energies E_a^D and E_a^A. In summary, TET would be most favourable for D/A couples in which the resonance condition $E_T^D(\mathbf{q}_D) - E_T^A(\mathbf{q}_A) \approx 0$ can be reached by changes in molecular geometry ($\mathbf{q}_A$ and $\mathbf{q}_D$) that are very efficient in altering (tuning) the singlet-triplet gap with the lowest possible energy demand. In general, each geometrical distortion would influence to a different extent the singlet-triplet energy gap, and it is very likely that some displacements along specific internal coordinates would leave unchanged the energy of this transition. This is illustrated in the simplified potential energy curves of Figure 4.2. On the other hand, the conformational changes which are very efficient in modifying the singlet-triplet energy gap of donor and acceptor molecules would be likely a

combination of multiple internal coordinates, characterized also for low values of activation energy as noted above.

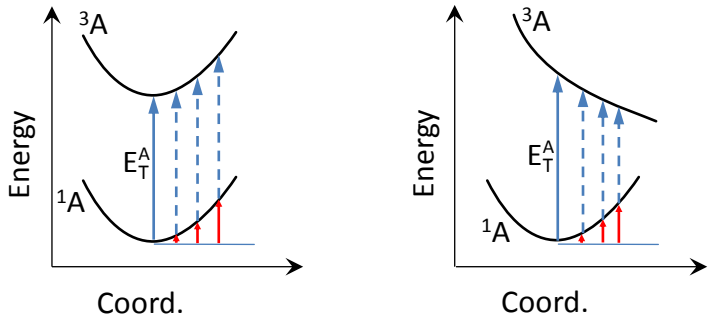

Figure 4.2 Energy profiles for singlet ^{1}A and triplet ^{3}A states of an acceptor molecule. Left: Structural changes along inactive coordinates do not modify significatively the ^{1}A - ^{3}A energy gap. Right: In the case of active coordinates, these changes modulate efficiently (blue arrows) the singlet-triplet energy gap (E_T^A for the ^{1}A equilibrium structure). All these geometrical changes require an activation energy E_a^A indicated by red arrows.

Therefore, the correct description of a TET reaction coordinate requires the simultaneous analysis of both, the singlet-triplet (triplet-singlet) energy gap variation along all internal coordinates and the activation energy associated to the geometrical change defined by each coordinate.

4.2.2 Triplet-Triplet Energy Transfer Reaction Coordinate

The internal coordinates that are able to modulate the singlet-triplet energy gap are involved in the reaction coordinate, but the relative contribution of these coordinates to the triplet energy transfer reaction coordinate (TET-RC) depends also on their role in yielding low activation energies in the initial states (^{1}A in the case of acceptor and ^{3}D in the case of donor). Therefore, TET-RC should include those coordinates providing a maximum variation of the singlet-triplet energy gap with a minimum energy of activation. As a result of that, the TET-RC is defined by the set of minimum energy configurations providing a given singlet-triplet energy gap.

This definition is consistent with a minimum energy principle: the energy transfer reaction will take place with the lowest possible activation energy. Moreover, the analysis of the TET process in terms of individual donor and acceptor transitions, as discussed above, allows the definition of a TET-RC for each individual process $^3D \rightarrow {}^1D$ and $^3A \leftarrow {}^1A$.

In summary, the construction of the TET-RC entails the identification of those molecular distortions that change the singlet-triplet energy gap in the donor and acceptor molecules with the lowest energy demand. This can be exemplified by the analysis of the TET-RC for a generic acceptor molecule which is promoted to the triplet state $^3A \leftarrow {}^1A$ as a result of the transfer (the same reasoning may be applied to donor quenching). According to a minimum energy principle, the energy transfer reaction coordinate for an acceptor molecule is determined by the set of singlet ground-state minimum-energy structures that present a given singlet-triplet energy gap, *i.e.* among all the points of the PES presenting a given singlet-triplet energy gap, only that of minimum energy in the ground-state is a point of the reaction coordinate. This situation is illustrated on Figure 4.3: the PES of the singlet (S_0) and triplet (T_1) states of the generic acceptor molecule have been pictured (left), as a function of nuclear displacements described by internal nuclear coordinates q_1 and q_2 . A series of nuclear configurations for which the singlet-triplet energy gap is constant are shown here by combining pairs of the blue curves drawn on the T_1 and S_0 surfaces, for energy values of 2, 5 and 7 relative units. For example, all the configurations defined by the pair of blue curves joined by the red arrow correspond to a singlet-triplet energy gap of 7 relative units. Thus, it can be seen that there are many different ways of changing the equilibrium geometry to get a reduction of the singlet-triplet excitation energy, as was proposed before[13]. However, among all these possible molecular distortions yielding a given reduction of the singlet-triplet gap, only a single structure has minimum energy on the initial (in this case S_0) state. Joining all of these points on the PES would define the TET reaction coordinate.

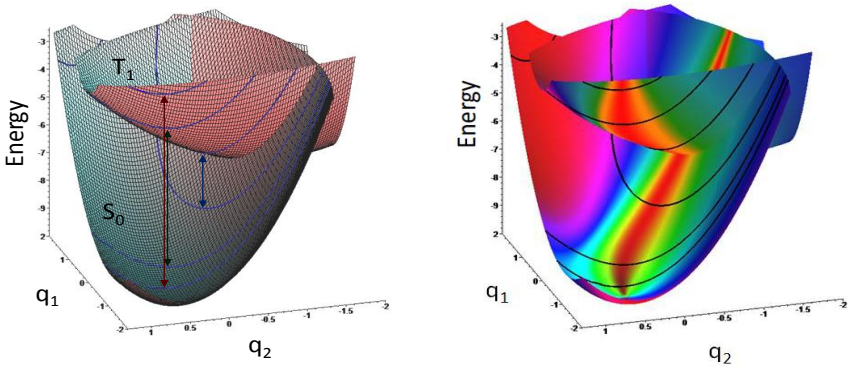

Figure 4.3. Schematic representation of the PES of singlet S_0 and triplet T_1 electronic states of a generic acceptor molecule as a function of internal nuclear coordinates q_1 and q_2. Left: The arrows joining pairs of the blue curves highlighted over each surface mark sets of configurations with a constant S_0-T_1 energy gap (three different gap values have been represented for three different energy values: 2, 5 and 7 relative units). Right: the same PESs color-mapped to show the value of cosine of the angle between S_0 and T_1 energy gradient vectors. Red color corresponds to cosine values ≈ ±1, *i.e.* parallel gradient vectors.

The minimum-energy configurations on the S_0 with a given singlet-triplet energy gap can be located by constraining the energy gradient vectors on both singlet and triplet states to be parallel (*Frutos et al. 2004*). Therefore, if $E_{S0}(\boldsymbol{q})$ and $E_{T1}(\boldsymbol{q})$ represent the S_0 and T_1 potential energy surfaces as a function of nuclear internal coordinates $\boldsymbol{q}$, a molecular geometry corresponding with a minimum activation energy in the initial state (S_0 in this case) must satisfy the following condition:

$$\frac{\left(\nabla E_{\mathrm{T}_1}(\boldsymbol{q}^{RC})\right)^{\mathrm{T}} \cdot \nabla E_{\mathrm{S}_0}(\boldsymbol{q}^{RC})}{\|\nabla E_{\mathrm{T}_1}(\boldsymbol{q}^{RC})\| \cdot \|\nabla E_{\mathrm{S}_0}(\boldsymbol{q}^{RC})\|} = \pm 1 \qquad \text{Eq. 4.1}$$

where ∇E represents the first derivatives of the energy (energy gradient) for each electronic state. The reaction coordinate for triplet energy transfer is defined by the set of geometries ($\boldsymbol{q}^{RC}$) which are solutions of eq. 4.1, in mass-weighted Cartesian coordinates. In Figure 4.3 (right) the PESs of the generic acceptor have been mapped with a color scale representing the value of the cosine of the angle formed by gradient vectors ∇E_{S0} and ∇E_{T1}, where red color corresponds to absolute values of

the cosine close to unit. The molecular configurations that satisfy this condition define the triplet energy transfer coordinate for this specific acceptor.

Since the TET-RC is defined in terms of local properties of both potential energy surfaces, $\boldsymbol{q}^{RC}$ will be, in general, a complex combination of internal coordinates. Therefore, it would be unlikely to find a TET-RC determined only by a single molecular deformation, *e.g.* a bond torsion or a stretching.

4.2.3 A Quantitative Determination of Nonvertical Transfer Properties

In acceptor molecules giving rise to nonvertical energy transfer, a large reduction of the equilibrium singlet-triplet energy gap E_T^A takes place with low activation energy E_a^A. These two factors are correlated along the TET-RC: maximum variation of the singlet-triplet energy gap with minimum activation energy on the ground-state. Therefore, the TET-RC makes it possible to attach a quantitative meaning to nonvertical deviation from classical transfer for a given acceptor/donor couple. As noted above, a geometrical distorsion parameter γ was derived (*Frutos et al. 2004*), which is a function of the ratio of the above two factors: the new reduced acceptor singlet-triplet energy gap, and the corresponding activation energy, both of them depending on the acceptor internal coordinates ($\boldsymbol{q}_A$). This parameter was originally derived from local quadratic expansion of acceptor singlet and triplet PES, but its definition is completely general and can be computed for any molecular configuration along the TET-RC without any approximation in the PESs. The γ value measures the extent to which geometrical changes in the acceptor molecule modulate its singlet-triplet gap: large γ values correspond to large changes in singlet-triplet energy gap with low activation energy (*nonvertical* transfer), while low γ values correspond to the opposite situation (classical transfer).This applies also to donor molecules. Therefore, it is possible to extend the application of this parameter by determining a γ value for each individual point of the reaction

coordinate ($\boldsymbol{q}^{RC}$), yielding in this way the *generalized geometrical distortion parameter* for an specific acceptor:

$$\gamma_{\boldsymbol{q}^{RC}} = \left[\frac{\left(\Delta E_{\mathrm{T}}^{\mathrm{A}}(\boldsymbol{q}^{RC})\right)^2}{E_{\mathrm{a}}(\boldsymbol{q}^{RC})}\right]^{\frac{1}{2}} \qquad \text{Eq. 4.2}$$

where $\Delta E_T^A(\boldsymbol{q}^{RC}) = E_T^A(\boldsymbol{q}^{RC}) - E_T^A$ is the singlet-triplet energy gap variation relative to that of the equilibrium structure of the acceptor molecule for a specific point of the reaction coordinate ($\boldsymbol{q}^{RC}$), and $E_a(\boldsymbol{q}^{RC})$ is the corresponding activation energy. Note that nonvertical deviation from classical transfer for a given acceptor molecule should be also a function of the donor triplet energy, because the extent of the geometrical changes that would take place in the acceptor molecule to approach energy resonance depends on the available energy of the donor to be exchanged, *i.e.* $E_T^D(\boldsymbol{q}^{RC}) - E_T^A(\boldsymbol{q}^{RC}) = 0$.

4.2.4 Determination of the Internal Coordinates Weight in TET

As shown above for the case of an acceptor molecule, the optimum molecular structure to match a given triplet excitation energy is defined by the reaction coordinate ($\boldsymbol{q}^{RC}$), corresponding to a collection of molecular structures showing a complex combination of internal coordinates. Nevertheless, the extent (*i.e.* magnitude) of the internal coordinate variations along the reaction coordinate is not strictly related to the relevance or "weight" of the specific coordinate in the reaction coordinate ($\boldsymbol{q}^{RC}$) definition. This is due mainly to two possibilities: first, a coupling between efficient and inefficient vibrational displacements which would provoke significant variations along the inefficient coordinate, and second, large amplitude, ground-state low-frequency vibrational modes which do not contribute efficiently to the energy gap variation, in spite that may result in large geometrical distortions.

The weight of an specific internal coordinate for a given point of the TET-RC depends on its contribution to the variation of the singlet-triplet energy gap, as well as to the change of the energy of activation, in such a way that a coordinate with a large contribution or weight in the TET process should provide a large variation of the energy gap with low activation energy. It is possible to measure the weight of each coordinate along the TET-RC according to these conditions and within a second order approximation for the PESs. Under this approximation, the variation of the singlet-triplet energy gap for an acceptor or donor, $\Delta E_{\mathrm{T}}^{\mathrm{A(D)}}$, and the corresponding activation energy on the initial state, $E_{\mathrm{a}}^{\mathrm{A(D)}}$, for a transition between two electronic states (denoted as initial "0" and final "1" states) are given by:

$$\Delta E_{\mathrm{T}}^{\mathrm{A(D)}}(\boldsymbol{q}^{RC}) = (\boldsymbol{q}^{RC})^{\mathrm{T}}\boldsymbol{g}_1 + \frac{1}{2}\,(\boldsymbol{q}^{RC})^{\mathrm{T}}(\boldsymbol{H}_1 - \boldsymbol{H}_0)(\boldsymbol{q}^{RC}) \qquad \text{Eq. 4.3}$$

$$\Delta E_{\mathrm{a}}^{\mathrm{A(D)}}(\boldsymbol{q}^{RC}) = \frac{1}{2}\,(\boldsymbol{q}^{RC})^{\mathrm{T}}\,\boldsymbol{H}_0\boldsymbol{q}^{RC} \qquad \text{Eq. 4.4}$$

where $\boldsymbol{q}^{RC}$ are the molecular internal coordinates displacements relative to the minimum energy structure on the "0" state, $\boldsymbol{g}_1$ is the energy gradient vector on the final state for the "0" state equilibrium geometry, and $\boldsymbol{H}_0$ and $\boldsymbol{H}_1$ are the Hessian matrices for the initial and final state, respectively, determined also at the equilibrium structure for "0" state. Each coordinate contributes to the singlet-triplet energy gap variation, $\Delta E_{\mathrm{T}}^{\mathrm{A(D)}}$, linearly in the energy gradient term and quadratically through the Hessian matrices. Therefore, for a specific "i" internal coordinate q_i^{RC}, eq. 4.3 and eq. 4.4 can be split in terms of the "*N*" internal coordinates of the molecule:

$$\Delta E_{\mathrm{T}}^{\mathrm{A(D)}}(\boldsymbol{q}^{RC}) = \sum_{i=1}^{N}\left[q_i^{RC}(\boldsymbol{g}_1)_i + \frac{1}{2}\sum_{j=1}^{N} q_i^{RC}\,q_j^{RC}(\boldsymbol{H}_1 - \boldsymbol{H}_0)_{ij}\right] \qquad \text{Eq. 4.5}$$

$$\Delta E_{\mathrm{a}}^{\mathrm{A(D)}}(\boldsymbol{q}^{RC}) = \sum_{i=1}^{N}\left[\frac{1}{2}\sum_{j=1}^{N} q_i^{RC}\,q_j^{RC}(\boldsymbol{H}_0)_{ij}\right] \qquad \text{Eq. 4.6}$$

where the expressions in brackets are the individual contribution of each component q_i to the global singlet-triplet energy gap variation (eq. 4.5) and the global activation energy (eq. 4.6).

According to eq. 4.2 it is possible to assign a γ value for each individual coordinate following exactly the same definition, determining in this way the relevance of each internal coordinate in the global reaction coordinate. The following generalized definition of the γ parameter for each internal coordinate of donor (or acceptor) molecule, results:

$$\gamma_{\boldsymbol{q}_i^{RC}} = \left[\frac{\left((\boldsymbol{q}_i^{RC})^{\mathrm{T}} \boldsymbol{g}_1 + \frac{1}{2} (\boldsymbol{q}_i^{RC})^{\mathrm{T}} (\boldsymbol{H}_1 - \boldsymbol{H}_0)(\boldsymbol{q}_i^{RC}) \right)^2}{\frac{1}{2} (\boldsymbol{q}_i^{RC})^{\mathrm{T}} \boldsymbol{H}_0 \boldsymbol{q}_i^{RC}} \right]^{\frac{1}{2}} \qquad \text{Eq. 4.7}$$

where $\boldsymbol{q}_i^{RC}$=(0,0,…,q_i^{RC},..,0,0) is a vector in which all the terms are zero except the "*i*" term that is equal to the value of the coordinate "*i*" in the specific point of the TET-RC, q_i^{RC}. Each $\gamma_{\boldsymbol{q}_i^{RC}}$ parameter yields the contribution to nonvertical transfer for each "*i*" coordinate, permitting the determination of the role of each coordinate in the TET process in terms of energy effects instead of amplitude changes.

4.2.5 Nonvertical TET in *cis*-Stilbene

Hammond and Saltiel introduced the nonvertical concept from the study of TET reactions in which *cis*-stilbene (c-Stb) was the triplet-energy acceptor *(Saltiel and Hammond 1963; Hammond et al. 1964*). This outstanding work ignited a great interest on the process and give rise to a substantial amount of related investigations (*Saltiel et al. 1984; Catalan and Saltiel 2001*). However, in spite of the elapsed 50 years from the initial discovery, there is not yet consensus on the nature of c-Stb structural changes responsible for the nonvertical effect (*Saltiel et al. 2003; Lalevee et al. 2005*). In this regard, a description of the reaction coordinate of the triplet energy transfer to this prototype acceptor that incorporates the

ideas discussed above may provide a well-founded interpretation of the changes that make possible triplet excitation. Therefore, we present below the TET-RC for the transfer process in which c-Stb is the acceptor compound.

The TET-RC was constructed by computing c-Stb molecular and electronic structure properties with Density Functional Theory by using hybrid B3LYP functional with a 6-31+G* basis set as implemented in Gaussian 03. In addition, a novel algorithm detailed elsewhere (*Frutos and Castaño 2005*) was applied using mass-weighted cartesian coordinates and including a second-order local expansion of the PES. Figure 4.4A presents the c-Stb ground-state activation energy as a function of the singlet-triplet energy gap along the TET-RC computed following the definition in eq. 4.1. It can be seen that modest changes in ground-state energy give rise to a large reduction in the S_0-T_1 energy gap and, consequently, in the required triplet excitation energy. Thus, for example, an increase of only ca. 4 kcal·mol^{-1} of S_0 energy gives rise to the reduction of ca. 20 kcal·mol^{-1} in the S_0-T_1 energy gap, which stands on the origin of the *nonvertical* transfer properties. Figure 4.4A also shows that variations in the ground-state relative energy may also produce a much larger *increase* of the singlet-triplet energy gap; for instance, the same 4 kcal·mol^{-1} of S_0 energy gives rise an increase of more than 40 kcal·mol^{-1} in the S_0-T_1 energy gap. Therefore, vibrational activation of ground-state in c-Stb can facilitate accepting triplet excitation from low-energy donors, although the contrary effect (transfer from high-energy donors) would be also favored by thermal activation, presenting an even more pronounced nonvertical transfer for the latter case.

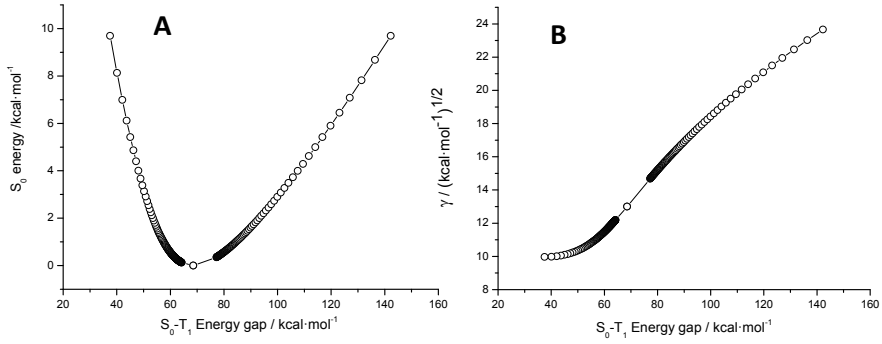

Figure 4.4. (**A**) Relative S_0 energy vs. S_0-T_1 energy gap for c-Stb along triplet energy transfer reaction coordinate, and (**B**) the relationship between the *geometrical distortion parameter* $\boldsymbol{\gamma}$ and the S_0-T_1 energy gap, for the same computed reaction coordinate of *c*-Stb.

As mentioned above, a quantitative meaning can be attached to nonvertical transfer through γ, the *generalized geometrical distortion parameter* as defined in eq. 4.2. Thus, Figure 4.4B shows the relationship between γ and the S_0-T_1 energy gap for c-Stb along the TET-RC. This parameter takes a value of ca.13 $(\text{kcal·mol}^{-1})^{1/2}$ for the S_0-T_1 energy gap corresponding to ground-state equilibrium geometry (E_0^{A} about 67 kcal/mol), decreasing slowly for lower values of the energy gap, and increasing rapidly for augmented singlet-triplet energy gaps. The c-Stb triplet energy in solution, estimated from the onset of the optical $T_1 \leftarrow S_0$ absorption by oxygen perturbation techniques, is ca. 58 kcal mol^{-1} (*Bylina and Grabowski 1969; Ni et al. 1989*). Since the main properties of the c-Stb TET reaction coordinate do not depend on the absolute value of this energy, we used here the value computed by DFT techniques (67 kcal mol^{-1}) for internal consistency, which is also consistent with the high-level CASPT2 theoretical calculations (*Molina et al. 1999*),where vertical excitation of c-Stb is predicted to be ca. 70 kcal·mol^{-1}. The CASPT2 method provides quantitative excitation energy predictions (usually within 4-5 kcal·mol^{-1} deviation from experimental results in organic chromophores).

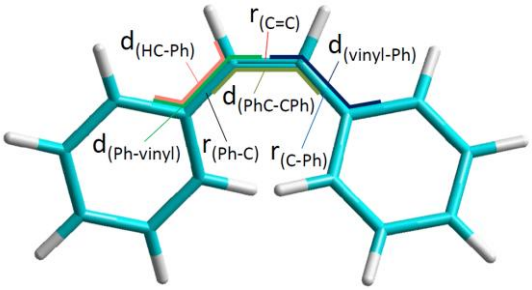

Figure 4.5 Ground-state equilibrium geometry of *cis*-stilbene and internal coordinates r_i (bond stretching) and d_i (bond torsion). Ph = phenyl ring.

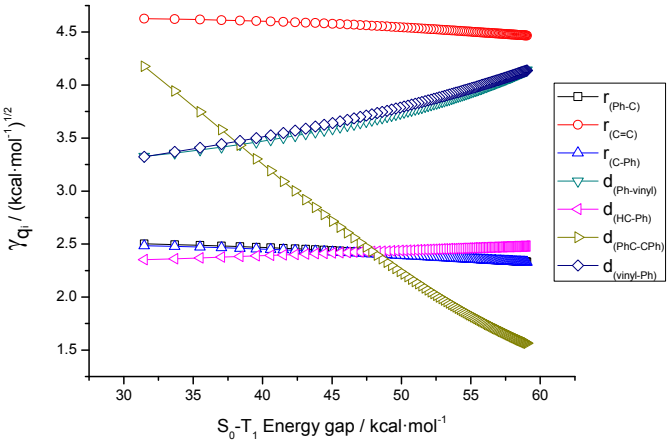

Figure 4.6 The γ_{q_i} values computed for each effective internal coordinate of *cis*-stilbene for triplet energies in the 30-60 kcal·mol^{-1} range along the TET-RC. Since the singlet-triplet energy gap of this compound for the equilibrium configuration is ca. 67 kcal·mol^{-1}, efficient TET from low triplet-energy donors would be only possible if the energy mismatch is eliminated by activated geometrical distortions of the phenylpolyene. Large γ_{q_i} values correspond to geometrical distortions that are very effective in attaining energy resonance for the indicated singlet-triplet energy exchange.

The key internal coordinates controlling the nonvertical character of TET to c-Stb, as well as the relative weight of each motion in diminishing the triplet excitation energy, have been obtained by computing the respective γ_{q_i} values. The c-Stb equilibrium geometry, together with the relevant internal coordinates, $\boldsymbol{r}_i$ (bond stretching) and $\boldsymbol{d}_i$ (bond torsion) are

presented in Figure 4.5, while Figure 4.6 shows the weight of each internal coordinate in tuning the singlet-triplet energy gap, expressed by its γ_{q_i} value. As discussed above, a large γ_{q_i} value indicates that this specific internal coordinate is very effective in matching (decreasing) the c-Stb singlet-triplet excitation energy to that available from the donor. In this regard, the central double-bond stretching vibration $r_{(C=C)}$ appears as the most important geometrical change in minimizing the singlet-triplet excitation energy of the acceptor, with a weight which is virtually independent of the energy deficit. The group of stretching vibrations localized along the two carbon-phenyl bonds $r_{(Ph-C)}$ and $r_{(C-Ph)}$ produce a much lower effect in altering the triplet energy gap. This prediction departs from the ideas advanced before on the way bond torsions account for nonvertical transfer in this compound (*Caldwell et al. 1992; Brennan et al. 1994; Catalan and Saltiel 2001*). In fact, the effect of bond torsional modes is quite surprising. Thus, the two phenyl-vinyl torsions $d_{(Ph-vinyl)}$ and $d_{(vinyl-Ph)}$ show a contribution to nonvertical effects which is very important for a small triplet energy deficit, but declines when the energy mismatch increases. In contrast, the central double-bond torsion $d_{(PhC-CPh)}$ shows a very small contribution in the energy range close to resonance, but this contribution rapidly becomes much more important for large values of energy mismatch. Finally, the torsion including the vinyl hydrogen atom $d_{(HC-Ph)}$ shows a modest effect, similar to that of the carbon-phenyl stretching.

The effects of the different internal motions shown above were determined by considering all the degrees of freedom of the c-Stb molecule. However, if restrictions are introduced in any of them, as for example is the case in the stiff-stilbenes (*Saltiel et al. 2003*), the relative contribution of each nuclear motion would be different. This prevents a direct comparison of the results obtained here with those of some sets of experimental data.

4.2.6 Conclusions

We presented a definition of the reaction coordinate for the triplet-triplet energy transfer elementary process (TET-RC), based on the minimum energy principle for modulating the singlet-triplet energy gap. It is shown that the transfer process, in the weak electronic coupling limit, can be properly analyzed in terms of the two intervening individual electronic transitions for donor deactivation $^3D \rightarrow {}^1D$ and acceptor excitation $^3A \leftarrow {}^1A$. In this way a reaction coordinate ($\boldsymbol{q}^{RC}$) for each individual transition was defined according to the condition of parallel energy gradient vectors for both electronic states. Based on this definition it was obtained a generalized geometrical distortion parameter ($\gamma_{\boldsymbol{q}_i^{RC}}$) that yields a quantitative measurement of the nonvertical character of a given donor or acceptor molecule in the TET process. Moreover, according to this quantitative description of the nonvertical character, it was also developed a formalism to split the contribution of each individual internal coordinate to the TET-RC, permitting the identification of the crucial coordinates in the excitation transfer reaction.

This formalism was applied by computing the TET-RC for the anomalous and conflicting case of energy transfer using c-Stb as acceptor compound, the first example of large nonvertical transfer. It is shown that geometrical molecular distortions due to the C=C bond stretching vibration and phenyl-vinyl torsions are the important coordinates in explaining the nonvertical transfer. In contrast, the central double bond torsion presents a variable effect, being very important for large donor-acceptor energy discrepancies but of lesser relevance near energy resonance conditions.

The TET-RC formulation developed here is completely general and, therefore, may be of utility for the detailed characterization of the TET process involving a wide range of donor and acceptor molecular partners at the required level of theory. Finally, since this formalism was developed for a Dexter-type energy transfer process under weak electronic coupling, it can be used in the study of any energy transfer process mediated by electron exhange mechanism, and therefore not limited to triplet-triplet energy transfer.

5. Beyond CASPT2//CASSCF Methodology: "On The Fly" Scaling of the CASSCF Forces for Excited-state Dynamics of a Retinal Model

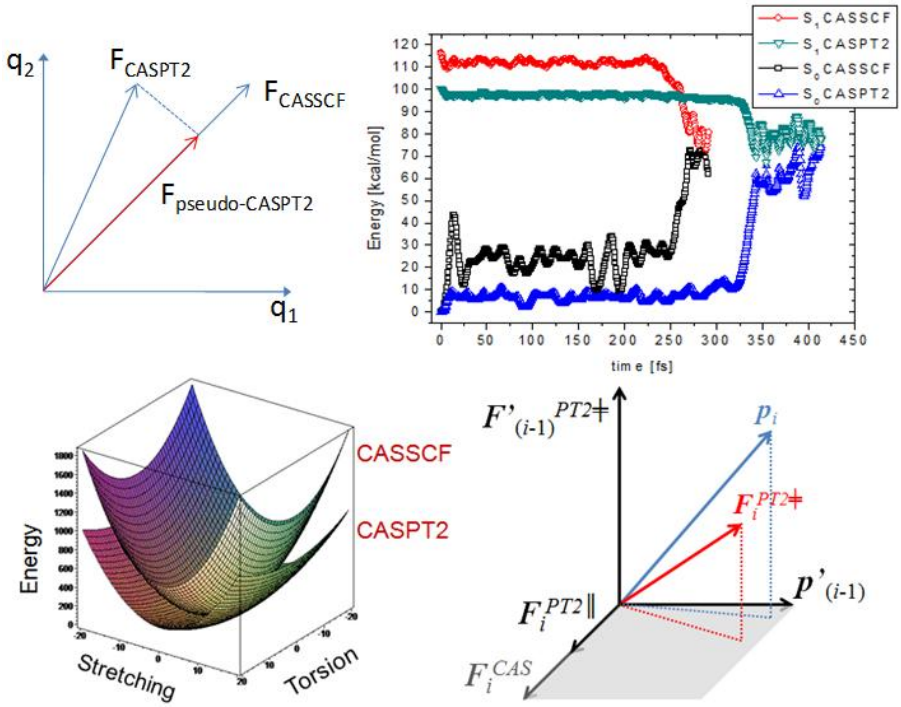

"Imagination will often carry us to worlds that never were.

But without it we go nowhere"

Carl Sagan

The CASPT2//CASSCF methodology (*i.e.* calculation of the CASSCF forces while performing minimum energy paths, with CASPT2 single point corrections to the energy) is widely applied to the high level (quantitative) prediction of excited-state electronic structures, resulting in a balanced compromise between quality of the results and affordable computational time.

In order to improve the description of photophysical and photochemical processes, alternatives to the CASPT2//CASSCF methodology were proposed:

- Application of CASPT2 analytical forces.
- Global scaling of the CASSCF forces.

The implementation of CASPT2 analytical forces was recently carried out, but the algorithm for its calculation was shown to be reasonably efficient only for small active spaces, therefore being not computationally feasible its application to medium or large size chromophores (*Celani and Werner 2003*). Especially, biological chromophores usually require large active spaces for a correct description of the biochemical reactivity, and a possible solution to the problem is to approximate the CASPT2 forces as the CASSCF forces times a global scaling factor, α (*Frutos et al. 2007*). The value of α can be calculated as a proportionality factor between CASSCF and CASPT2 minimum energy paths, therefore assuming a constant proportionality between both energy gradients (where the energy gradient is the opposite of the force):

$$\vec{\nabla} E_{CASPT2} = \alpha \vec{\nabla} E_{CASSCF} \qquad \text{Eq. 5.1}$$

Nevertheless this assumption is not of general validity, but requires to be tested for each system to be studied. Moreover, even if it is valid for any specific system, in the framework of a dynamics study not all trajectories have necessarily to explore only the regions close to the minimum energy path, eventually reaching parts of the potential energy surface where constant proportionality between CASPT2 and CASSCF forces does not hold true.

Considering these premises, we developed a novel method to perform quantitative excited-state dynamics, by applying a so called local scaling factor: α is not anymore constant, but it is calculated for each new geometry along the trajectory ($\alpha(\boldsymbol{q})$).

$$\vec{\nabla}E_{CASPT2} = \alpha(\boldsymbol{q})\vec{\nabla}E_{CASSCF} \qquad \text{Eq. 5.2}$$

After a formal description, the locally scaled gradient method was applied to calculate "on the fly" excited-state dynamics of the protonated Schiff base 2-*cis*-α-methyl-pentadieniminium cation (2-*cis*-α-Me-$C_5H_6NH_2^+$), selected as minimal model of the retinal chromophore (*Garavelli et al. 1997; Sampedro et al. 2004; Szymczak et al. 2008; Send et al. 2009*). Especially, planar and pre-twisted conformations were selected (Figure 5.1), in order to mimic the behavior of the retinal chromophore in solution and surrounded by opsin in Rhodopsin, respectively (*Wanko et al. 2004; Blomgren and Larsson 2005; Cembran et al. 2005; Wanko et al. 2005; Aquino et al. 2006; Cembran et al. 2007; Send and Sundholm 2007; 2007; 2007; Weingart 2007; Schapiro et al. 2009; Szymczak et al. 2009; Zaari and Wong 2009*).

Finally potentialities, limits and future perspectives of the proposed method are discussed.

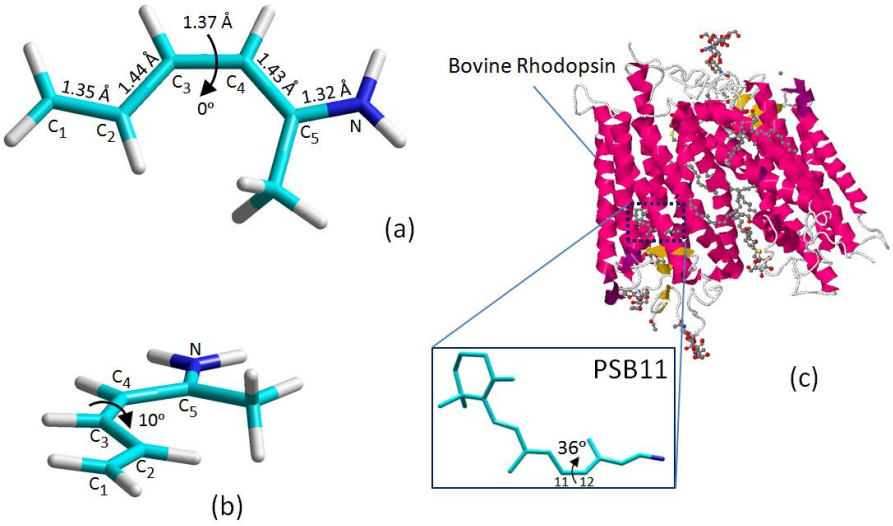

Figure 5.1 The *locally* scaled gradient method was applied to 2-*cis*-α-Me-$C_5H_6NH_2^+$ in planar (**a**) and 10 degrees pre-twisted (*i.e.* the C_2-C_3-C_4-C_5 dihedral angle is constrained at 10 degrees) (**b**) initial conformation, as minimal models of PSB11 in solution or within rhodopsin, respectively. By 2.2 Å resolution X-rays, torsion around the C_{11}-C_{12} bond in bovine rhodopsin is 36 degrees (PDB code: 1U19) (**c**). Geometrical bond length parameters are given for fully optimized structures at the MP2/6-31G(d) level, being almost equivalent for the two conformations.

5.1 Theoretical Method

The developed method of CASSCF *local* gradient scaling (meant to reproduce an approximated CASPT2 gradient) is shown by its mathematical description and insights into the algorithm and numerical implementation required for application to chemical problems.

In molecular dynamics, a numerical method is used to integrate Newton's equation of motion, in order to calculate the trajectory of the molecule by applying forces which (in this case) are computed at the quantum mechanical level. In this work, the Velocity Verlet integrator is used, propagating the trajectory through CASSCF forces scaled at each step.

Given the position $\boldsymbol{q}$, linear momentum $\boldsymbol{p}$, force $\boldsymbol{F}$, mass m and time step t, the Velocity Verlet algorithm can be expressed as follows:

$$\boldsymbol{p}_i = \boldsymbol{p}_{(i-1)} + \frac{1}{2}\boldsymbol{F}_{(i-1)}\Delta t + \frac{1}{2}\boldsymbol{F}_i\Delta t \qquad \text{Eq. 5.1}$$

$$\boldsymbol{q}_i = \boldsymbol{q}_{(i-1)} + \frac{1}{m}\boldsymbol{p}_{(i-1)}\Delta t + \frac{1}{2m}\boldsymbol{F}_{(i-1)}\Delta t^2 \qquad \text{Eq. 5.2}$$

As shown in Figure 5.2, the *locally* scaled gradient method is based on the projection of the CASPT2 gradient vector ($-\boldsymbol{F}^{PT2}$) along the CASSCF gradient vector ($-\boldsymbol{F}^{CAS}$), generating a pseudo-CASPT2 gradient vector ($-\boldsymbol{F}_{\mathbf{ps}}^{PT2}$).

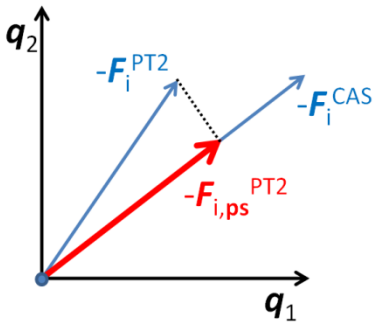

Figure 5.2 Two-dimensional ($\boldsymbol{q}_1$, $\boldsymbol{q}_2$) scheme of the *locally* scaled gradient method for a single geometry (q_i) along the trajectory: the CASPT2 gradient vector ($-\boldsymbol{F}_i^{PT2}$) is projected along the CASSCF gradient vector ($-\boldsymbol{F}_i^{CAS}$), obtaining a pseudo-CASPT2 gradient vector ($-\boldsymbol{F}_{i,ps}^{PT2}$).

Replacing $\boldsymbol{F}$ in Eq. 5.1 by $\boldsymbol{F}_{i,\mathbf{ps}}^{PT2}$ we obtain $\boldsymbol{p}_i$, by which the next geometry of the trajectory ($\boldsymbol{q}_{i+1}$) can be readily calculated:

$$\boldsymbol{q}_{(i+1)} = \boldsymbol{q}_i + \frac{1}{m}\boldsymbol{p}_i\Delta t + \frac{1}{2m}\boldsymbol{F}_{i,\boldsymbol{ps}}^{PT2}\Delta t^2 \qquad \text{Eq. 5.3}$$

When applying the *locally* scaled gradient method, a pseudo-CASPT2 force field is generated, defining a new potential energy surface, formally different from CASSCF and CASPT2 potential energy surfaces (E^{CAS}, E^{PT2}). Since the molecule will explore the new (pseudo-CASPT2) potential energy surface, it has to be noted that the original energy is not in general conserved.

For an *n*-D space, with *n*=3*N*-6 where *N* is the number of atoms and *n* is the number of *q* internal coordinates, the CASSCF and CASPT2 energies of a potential energy surface can be expressed as a generic function *f*:

$$E^{CAS} = f^{CAS}(\boldsymbol{q})\ ;\ E^{PT2} = f^{PT2}(\boldsymbol{q}) \qquad \text{Eq. 5.4}$$

Therefore the force vectors can be defined as:

$$\boldsymbol{F}^{CAS}(q_j) = -\sum_{j=1}^{n} \frac{\partial f^{CAS}(\boldsymbol{q})}{\partial q_j};\ \boldsymbol{F}^{PT2}(q_j) = -\sum_{j=1}^{n} \frac{\partial f^{PT2}(\boldsymbol{q})}{\partial q_j} \qquad \text{Eq. 5.5}$$

$\boldsymbol{F}_{\mathbf{ps}}^{PT2}$ is obtained by projection of $\boldsymbol{F}^{PT2}$ along $\boldsymbol{F}^{CAS}$:

$$\boldsymbol{F}_{\boldsymbol{ps}}^{PT2} = \sum_{j=1}^{n} \boldsymbol{F}^{PT2}(q_j) \cdot \boldsymbol{F}^{CAS}(q_j) \cdot \widehat{\boldsymbol{F}}^{CAS}(q_j) \qquad \text{Eq. 5.6}$$

being $\widehat{\boldsymbol{F}}^{CAS}$ the unit vector. Finally, the new potential energy surface (E_{ps}^{PT2}) can be calculated by integration, taking an arbitrary zero-energy reference:

$$E_{ps}^{PT2} = -\int \boldsymbol{F}_{\boldsymbol{ps}}^{PT2}\, \mathrm{d}q_1 \mathrm{d}q_2 \mathrm{d}q_n \qquad \text{Eq. 5.7}$$

The approximation of $\boldsymbol{F}^{PT2}$ calculated by the *locally* scaled gradient method ($\boldsymbol{F}_{\mathbf{ps}}^{PT2}$) can be considered reasonable in all cases when $\boldsymbol{F}^{PT2}$ and $\boldsymbol{F}^{CAS}$ are nearly parallel, since the method scales the module of $\boldsymbol{F}^{CAS}$ to resemble the one of $\boldsymbol{F}^{PT2}$, maintaining the direction indicated by $\boldsymbol{F}^{CAS}$ (see Figure 5.2).

In order to calculate $\boldsymbol{F}_{\mathbf{ps}}^{PT2}$, two displacements along $\boldsymbol{F}^{CAS}$ (forward and backward: +Δ**d**, -Δ**d**) are required for each geometry of the trajectory, $\boldsymbol{q}_i$ (Figure 5.3), *i.e.* a numerical gradient is performed.

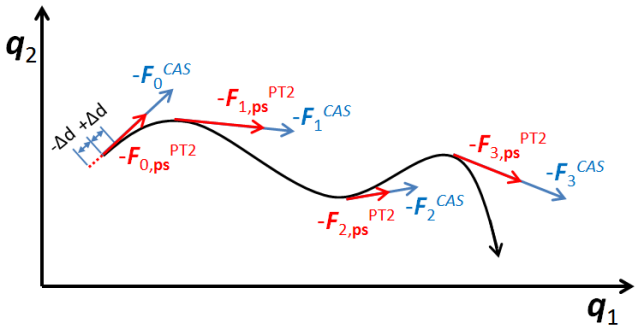

Figure 5.3 Scheme of a trajectory performed with the *locally* scaled gradient method in the space defined by two arbitrary coordinates ($\boldsymbol{q}_1$, $\boldsymbol{q}_2$): at each step the CASSCF gradient ($-F_i^{CAS}$) is scaled to approximate the CASPT2 gradient. $-F_{i,ps}^{PT2}$ is calculated by generating two geometries at +Δd and -Δd along $-F_i^{CAS}$.

$\boldsymbol{F}_{i,ps}^{PT2}$ is therefore calculated as follows:

$$\boldsymbol{F}_{i,\boldsymbol{ps}}^{PT2} = \frac{E_{i,(+\Delta d)}^{PT2} - E_{i,(-\Delta d)}^{PT2}}{2\|\Delta \boldsymbol{d}\|} \cdot \widehat{\boldsymbol{F}}_i^{CAS} \qquad \text{Eq. 5.8}$$

In order to correct the energy as well, a CASPT2 single-point energy calculation is performed for each geometry of the trajectory.

The main advantage of the method is a consistent reduction in the number of single-point CASPT2 energy calculations needed: the numerical CASPT2 energy gradient requires 6*N* single-point CASPT2 energy calculations (where *N* is the number of atoms), while only three single-point CASPT2 energy calculations are required to approximate the CASPT2 energy gradient by the *locally* scaled gradient method. Moreover, by our method the number of single-point CASPT2 energy calculations does not depend on the molecular size (*i.e. N*), being feasible the application to large polyatomic molecules, if the active space considered is within state-of-the-art multiconfigurational limits.

5.2 Results and Discussion

The *locally* scaled gradient method was applied to describe the excited-state dynamics of planar and pre-twisted 2-*cis*-α-Me-$C_5H_6NH_2^+$ (Figure 5.1a,b). Topologies and dynamics of planar 2-*cis*-α-Me-$C_5H_6NH_2^+$ are firstly compared, in order to highlight differences and similarities between CASSCF and CASPT2 description of a minimum retinal model.

5.2.1 2-*cis*-α-Me-$C_5H_6NH_2^+$ Excited-State Topology

2-*cis*-α-Me-$C_5H_6NH_2^+$ was optimized on the ground-state at the MP2 level without imposing any symmetry, with a 6-31G(d) basis set applied to all atoms (Figure 5.1a). MP2 was selected since it can be considered a good approximation of the CASPT2 wavefunction for a single closed-shell configuration (as the ground-state of 2-*cis*-α-Me-$C_5H_6NH_2^+$ is), at the same time lowering the necessary computational cost. It was previously shown that a correct study of 2-*cis*-α-Me-$C_5H_6NH_2^+$ photoisomerization requires two electronic states: the ground-state (S_0) and the energetically lowest singlet excited-state (S_1), being S_2 always well above in energy and not influencing S_1 trajectories (Garavelli et al. 1997; Sampedro et al. 2004; Valsson and Filippi 2010). Therefore, State-Average CASSCF (SA-CASSCF) calculations were performed with equal weights over S_0 and S_1. A complete active space of six electrons in six orbitals (CAS(6,6)) was selected, in order to include all π and π* orbitals with corresponding electrons, being required for a correct description of the conjugated molecule.

Full Multi-State CASPT2 (MS-CASPT2) and MS-CASPT2//SA-CASSCF S_1 MEPs for 2-*cis*-α-Me-$C_5H_6NH_2^+$ were previously reported by Valsson and Filippi, reaching the conclusion that CASPT2 topology is somehow different from the CASSCF one: on one side, after excitation to S_1 in the Franck–Condon region, the CASSCF path leads to bond-length alternation (*i.e.* single bonds become double, and double bonds become single) up to a transition state corresponding to a planar structure; this transition state is followed by rotation around the central C_3-C_4 bond up to reach a S_1/S_0 conical intersection, which is the funnel to populate efficiently the ground-

state and eventually produce 2-*trans*-α-Me-$C_5H_6NH_2^+$ (*Garavelli et al. 1997*). The CASSCF path is barrierless, while the CASPT2//CASSCF path shows a really small energy barrier of about 0.8 kcal·mol^{-1} (Figure 5.4a, minimum at 0.1 a.u.). On the other side, the CASPT2 MEP following absorption to S_1 leads to a flat planar minimum characterized by only partial bond-length alternation, resulting in almost equal length of the three middle bonds (C_2-C_3 ,C_3-C_4 ,C_4-C_5). Then, as for CASSCF, torsion around the C_3-C_4 bond leads to a conical intersection geometry similar to the CASSCF one. Therefore, in spite of a similar photoisomerization process, CASSCF and CASPT2 S_1 topologies differ especially from the Franck−Condon region to the planar minimum/transition state structure (Figure 5.4a, from 0 to 0.5 a.u. for CASSCF, and from 0 to 0.9 a.u. for CASPT2).

This is a case when *global* scaling of the CASSCF energy gradient to mimic the CASPT2 energy gradient is not enough accurate during the entire MEP. In order to demonstrate it, we calculated CASSCF, CASPT2//CASSCF (and CASPT2) MEPs for 2-*cis*-α-Me-$C_5H_6NH_2^+$, by which we show that CASSCF and CASPT2//CASSCF (as well as CASSCF and CASPT2) topologies are different in the in-plane region (scaling factor $\alpha_{\text{in-plane}} = 0.094$), while they are similar in the out-of-plane region ($\alpha_{\text{out-of-plane}} = 0.919$). Moreover, a non acceptable correlation is found in the in-plane region, while a good correlation applies to the out-of-plane region (Figure 5.4b). By calculating and applying a different α value at each step of the dynamics (*local* scaling method), we will try to correctly scale the CASSCF energy gradient also in the in-plane region, reproducing an approximate CASPT2 energy gradient.

S_1 corresponds to a $^1(\pi,\pi^*)$ state with charge transfer character (Figure 5.4c), as previously reported (*Garavelli et al. 1997*). More in detail, the MEP along S_1 shows how the positive charge (q), localized on the nitrogen atom while in the ground-state minimum (Franck−Condon region), is partially displaced along the conjugated backbone, finally moving towards the non-methylated half moiety when the S_1/S_0 conical intersection is reached. Especially, a decrease in $\Delta q(=q(S_1)-q(S_0))$ is associated with breaking of the double C_3-C_4 middle bond, becoming a single bond (from ca. 0.3 to 0.15 electrons): at CASSCF and CASPT2//CASSCF level such a Δq decrease is found immediately after irradiation, while at CASPT2 level it happens at the end of the in-plane region (MEP around 1.1 a.u.), when torsion around the C_3-C_4 bond is initiated.

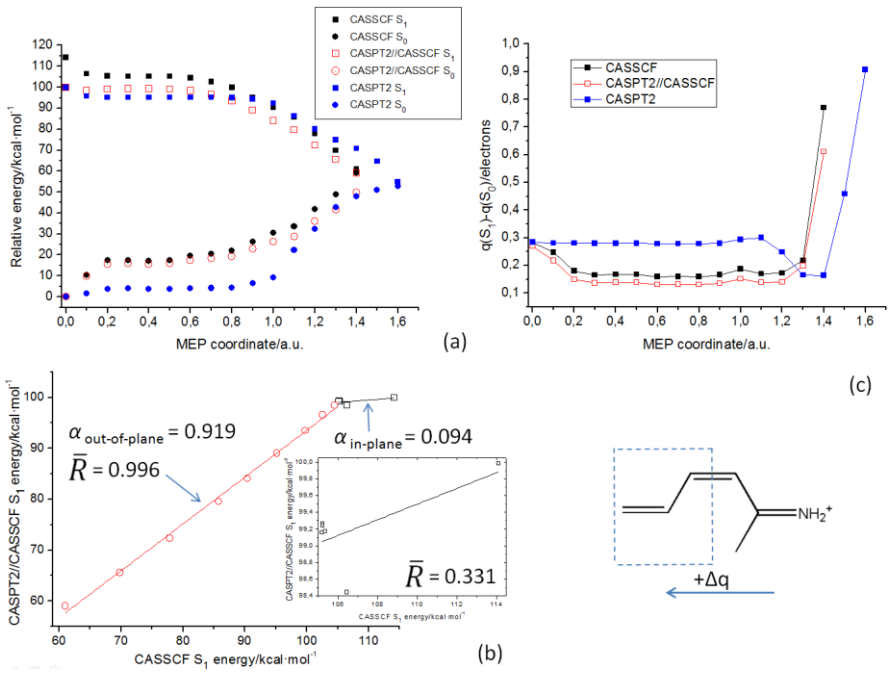

Figure 5.4 S_1 minimum energy paths (MEPs) of 2-*cis*-α-Me-$C_5H_6NH_2^+$ at CASSCF, CASPT2//CASSCF and CASPT2 level (**a**), by which $\alpha_{\text{in-plane}}$ and $\alpha_{\text{out-of-plane}}$ were calculated (**b**). The charge transfer character was evaluated along the MEPs as $\Delta q = q(S_1) - q(S_0)$, where the charge q is calculated for the non-methylated half moiety (**c**).

5.2.2 Comparison of 2-*cis*-α-Me-$C_5H_6NH_2^+$ Excited-State CASSCF and CASPT2 Trajectories

In order to have a valid reference to test the *local* scaling method, one SA-CASSCF(6,6)/6-31G(d) trajectory and one full MS-CASPT2(6,6)/6-31G(d) trajectory were calculated in the excited-state (S_1) applying the same conditions: $S_0 \rightarrow S_1$ vertical excitation of the ground-state optimized planar geometry with initial velocities (*i.e.* initial linear momentum) set to zero, therefore not including any kinetic energy initial contribution. A time step of 0.5 fs was applied.

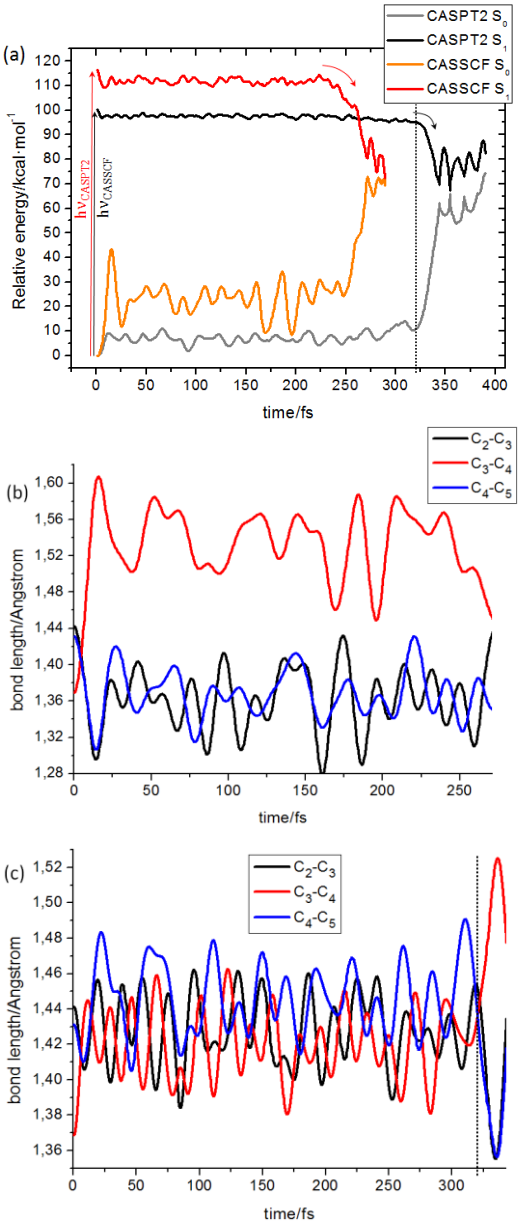

Figure 5.5 Energy profiles of 2-*cis*-α-Me-$C_5H_6NH_2^+$ S_1 trajectories: CASSCF and CASPT2 entire trajectories (**a**). Dynamical behavior of the three middle bonds at CASSCF (**b**) and CASPT2 (**c**) level. The dashed vertical line in **a** and **c** sets the time when isomerization starts, at the CASPT2 level of theory.

CASSCF and CASPT2 S_1 trajectories are rather different (Figure 5.5):

1. The Franck–Condon $^1(\pi,\pi^*)$ vertical excitation to S_1 is ca. 16 kcal·mol^{-1} lower at the CASPT2 level, due to an expected stabilization of the CASSCF energy when including dynamic electron correlation.

2. CASPT2 energy gradient vectors have usually a smaller module than CASSCF energy gradient vectors, resulting in CASPT2 less pronounced energy changes along the trajectory (on S_1 and S_0), *i.e.* the peak-to-peak amplitude is shorter than the CASSCF one. Therefore, the CASPT2 S_1 trajectory remains for a longer time (ca. 100 fs more than CASSCF) in the region corresponding to in-plane vibrational redistribution of the irradiation energy, preceding out-of-plane activation of different normal modes. Indeed, when comparing CASSCF and CASPT2 topologies, the in-plane region is predicted to be more flat at the CASPT2 level (Figure 5.4a,b).

3. Moreover, the bond-length profile in the in-plane region is distinctively different: the CASSCF trajectory is clearly characterized by bond-length alternation, which is only partial at the CASPT2 level. More in detail, at the CASSCF level the first photoinduced event (between 12 and 15 fs) is lengthening of double bonds and contraction of single bonds, followed by oscillations which maintain such inverted bond pattern (Figure 5.5b). At the CASPT2 level (Figure 5.5c), the period of bond-length oscillation is usually shorter than the CASSCF one, as well as the peak-to-peak amplitude, resulting in three almost equal middle bonds (C_2-C_3 ,C_3-C_4 ,C_4-C_5) oscillating around 1.43 Å, and two shorter side bonds oscillating around 1.39 Å (C_1-C_2) and 1.36 Å (C_5-N_6), consistently with the results found by Valsson and Filippi for the CASPT2 S_1 minimum structure.

4. In spite of the different behaviour observed in the in-plane region, both CASSCF and CASPT2 trajectories lead to a S_1/S_0 conical intersection. At the CASSCF level, after 217 fs the S_1 energy decreases and correspondingly the S_0 energy increases, reaching a peaked conical intersection at 271 fs, around 80 kcal·mol^{-1}. Then the dynamics is continued on S_1 (instead of letting the system hop on the lower potential energy surface), in order to demonstrate that excited-state oscillations maintain the molecule in this crossing region dominated by a single conical intersection, which is found again at 281 and 290 fs. At the CASPT2 level, a steeper decrease of the S_1 energy is initiated at 317 fs, also reaching a S_1/S_0 peaked conical intersection at 343 fs, around 70 kcal·mol^{-1}, therefore with a

time delay of ca. 70 fs respect to the CASSCF trajectory and 10 kcal·mol^{-1} lower in energy. Structurally, we confirm at the CASPT2 level what was recently reported at the CASPT2//CASSCF level for PSB11 in rhodopsin (*Schapiro et al. 2011*): hydrogen out-of-plane (HOOP) modes drive the excited-state torsion around the middle (C_3-C_4) bond, being responsible of the S_1 energy decrease up to the conical intersection. Even more than the CASSCF description (where bond-length alternation promotes formation of a single middle bond free to rotate), CASPT2 dynamics highlights that HOOP activation is the fundamental event responsible to initiate rotation around the middle C_3-C_4 bond, since this bond is only partially lengthened, maintaining a partial double bond character (Scheme 5.1). Indeed, at CASPT2 level the formal C_3-C_4 double bond finally becomes a single bond only after torsion around the same bond starts, demonstrating the most important difference between CASSCF and CASPT2 description of $^1(\pi,\pi^*)$ states with charge transfer character in protonated Schiff bases: by CASSCF, bond-length alternation happens first, followed by HOOP activation; by CASPT2, the conjugated moiety reaches a flat region where formal single and double bonds are almost equivalent, followed by a HOOP-coupled bond-length alternation mechanism, initiated by HOOP activation (Figure 5.6).

Considering the planarity of the conjugated backbone in the Franck–Condon region and the initial condition of zero kinetic energy, we can assume that all other possible CASSCF and CASPT2 S_1 trajectories of 2-*cis*-α-Me-$C_5H_6NH_2^+$ (with initial geometry out of global minimum, as expected in a ground-state dynamic environment) should be able to leave the in-plane region and evolve towards the ground-state, even though a higher flexibility of the backbone is expected at the CASPT2 level.

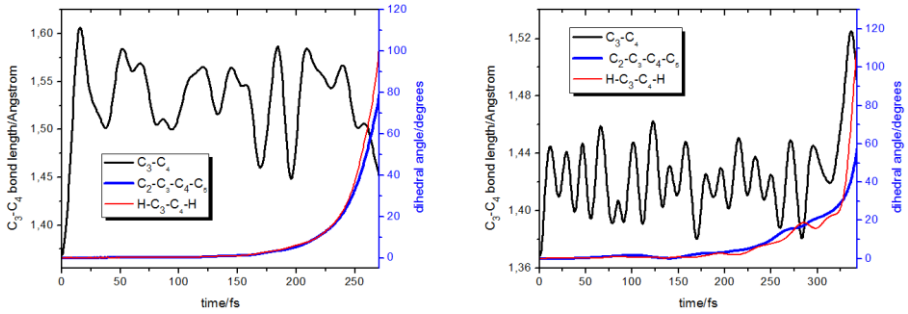

Figure 5.6 Main parameters involved in torsion of the 2-*cis*-α-Me-$C_5H_6NH_2^+$ middle bond during CASSCF (left) and CASPT2 (right) dynamics: C_3-C_4 bond length, HOOP (H-C_3-C_4-H) and C_2-C_3-C_4-C_5 dihedral angles.

5. The S_1/S_0 conical intersections reached by CASSCF and CASPT2 trajectories correspond to similar qualitative structures, showing differences in some coordinates (Figure 5.7) More in detail, the H-C_3-C_4-H dihedral angle involved in HOOP activation is 115 degrees (100 degrees) at CASPT2 (CASSCF) level, displacing the two hydrogen atoms respectively up and down of the backbone moiety, and therefore allowing rotation around the middle C-C bond: the C_2-C_3-C_4-C_5 dihedral angle is 56 degrees at CASPT2 level and 78 degrees at CASSCF level. This result is consistent (within the limit of a dynamic study involving only one trajectory per level of theory) with the geometries located by minimum energy path and reported in literature (*De Vico et al. 2002; Page and Olivucci 2003; Serrano-Andres et al. 2005; Valsson and Filippi 2010*).

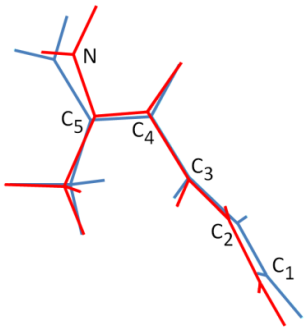

Figure 5.7 CASPT2 (red) and CASSCF (blue) superimposed structures at the corresponding S_1/S_0 conical intersection.

The photoinduced S_1 reactivity of initially planar 2-*cis*-α-Me-$C_5H_6NH_2^+$ is summarized in Scheme 5.1, showing differences and similarities between CASSCF and CASPT2 descriptions.

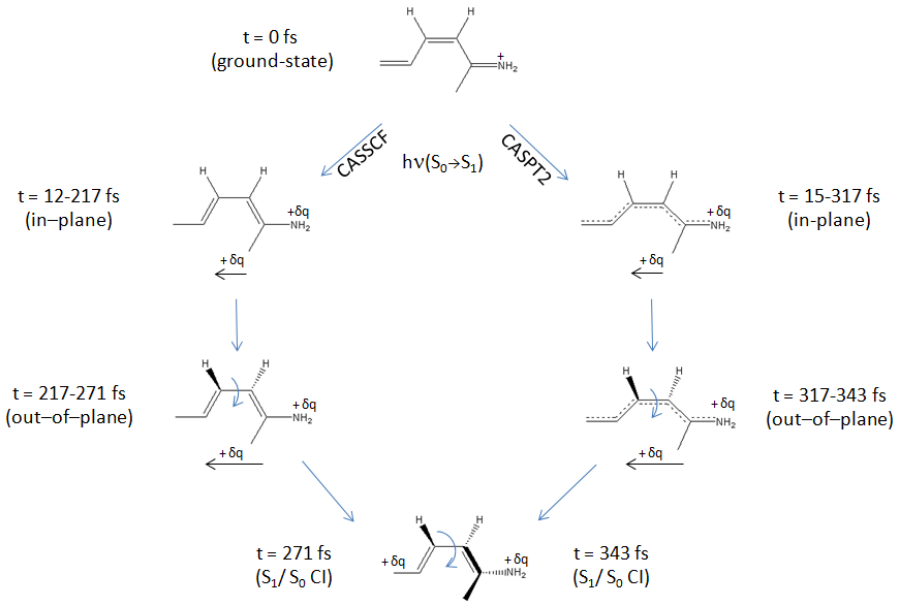

Scheme 5.1 Comparison between CASSCF and CASPT2 photoisomerization mechanisms of initially planar 2-*cis*-**α**-Me-$C_5H_6NH_2^+$, from vertical excitation ($S_0 \rightarrow S_1$) to the conical intersection (S_1/S_0 CI).

5.2.3 Locally Scaled Trajectories of initially planar 2-*cis*-α-Me-$C_5H_6NH_2^+$

The CASSCF and CASPT2 S_1 trajectories of 2-*cis*-α-Me-$C_5H_6NH_2^+$ were considered as a reference to test the validity of the proposed *locally* scaled gradient method: by *local* scaling of the CASSCF forces, the scaled trajectory is meant to mimic the CASPT2 trajectory. Therefore, the same initial conditions were applied: MP2 optimized geometry (Figure 5.1a), zero kinetic energy and a time step of 0.5 fs. The displacement along the CASSCF gradient (Δd) to generate the pseudo-CASPT2 gradient was set to 0.05 Å.

The CASSCF locally scaled trajectory is able to resemble the CASPT2 trajectory up to 217 fs (Figure 5.8), which corresponds to the time when the CASSCF in-plane region terminates (*i.e.* torsion around the C_3-C_4 bond is initiated at the CASSCF level), while the CASPT2 trajectory continues to describe vibrational planar relaxation (Figure 5.5). From this point on, CASSCF and CASPT2 topologies are strikingly different, and therefore a projection of the CASPT2 energy gradient along the CASSCF energy gradient (Figure 5.2) is not enough to approximate the CASPT2 dynamics, since the two gradient vectors are not nearly parallel, and therefore additional coordinates are required to continue following the CASPT2 path *(Marazzi et al. 2012*).

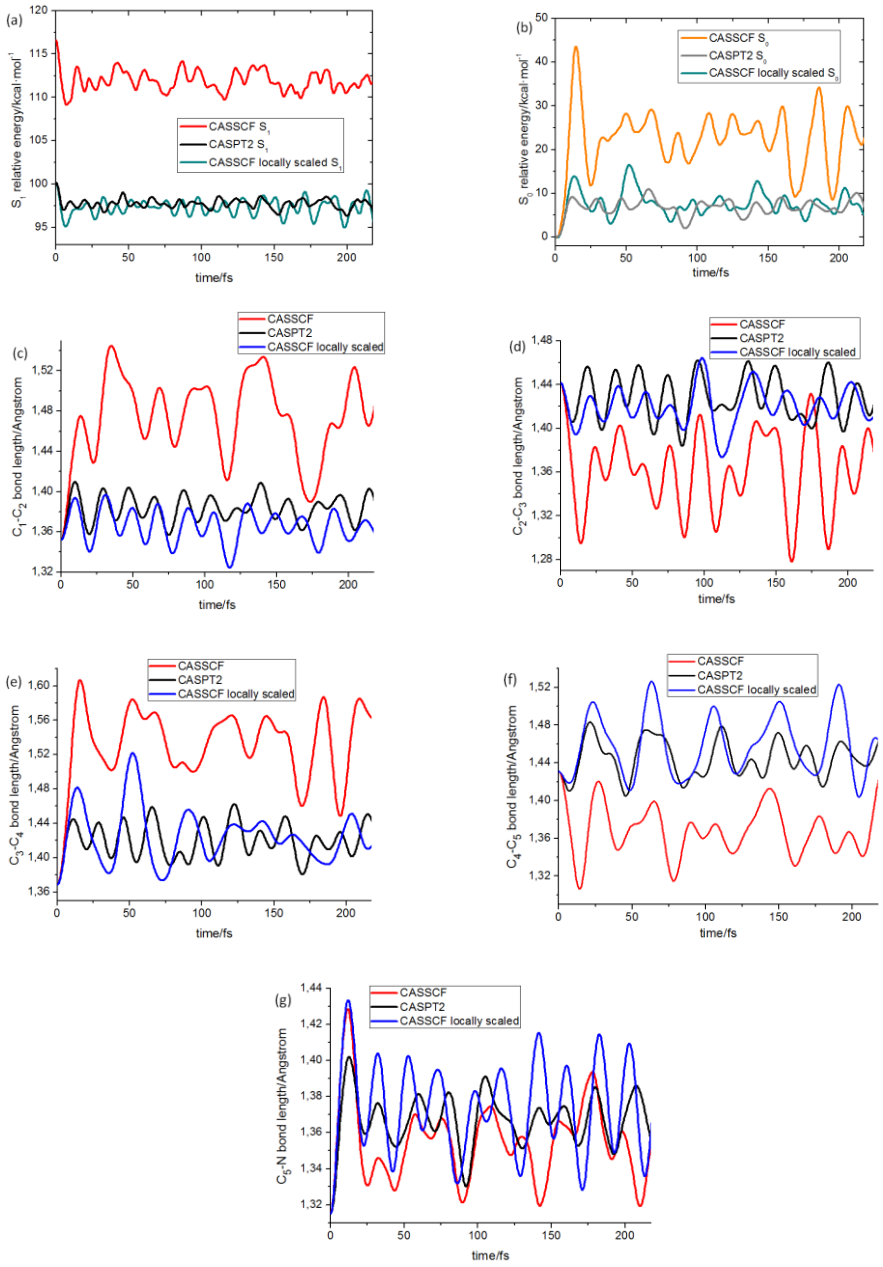

Figure 5.8 Comparison between CASSCF, CASPT2 and CASSCF locally scaled trajectories: S_1 and S_0 energies (**a**,**b**), and backbone bonds (**c**-**g**) in the in-plane region (up to 217 fs).

5.2.4 Locally Scaled Trajectories of pre-twisted 2-*cis*-α-Me-$C_5H_6NH_2^+$

In order to mimic (at first glance) the opsin environment around the retinal, the C_2-C_3-C_4-C_5 dihedral angle of 2-*cis*-α-Me-$C_5H_6NH_2^+$ was constrained at 10 degrees while optimizing the ground-state structure at the MP2/6-31G(d) level of theory. The optimized structure results in a backbone pattern almost equivalent to planar 2-*cis*-α-Me-$C_5H_6NH_2^+$ (Figure 5.1b).

Considering the aforementioned topological study, the S_1 MEP (and therefore the S_1 dynamics) of pre-twisted 2-*cis*-α-Me-$C_5H_6NH_2^+$ is expected to start directly in the out-of-plane region, where the application of a *global* scaling factor can be justified by the good correlation shown in Figure 5.4b, indicating high similarity between CASSCF, CASPT2//CASSCF and CASPT2 profiles up to the S_1/S_0 conical intersection ($\alpha_{\text{out-of-plane}}$ = 0.919). This allowed us to compare a CASSCF globally scaled trajectory with a CASSCF locally scaled trajectory (Δd = 0.05 Å). The initial conditions of each dynamics were the same applied to planar 2-*cis*-α-Me-$C_5H_6NH_2^+$: zero kinetic energy and a time step of 0.5 fs.

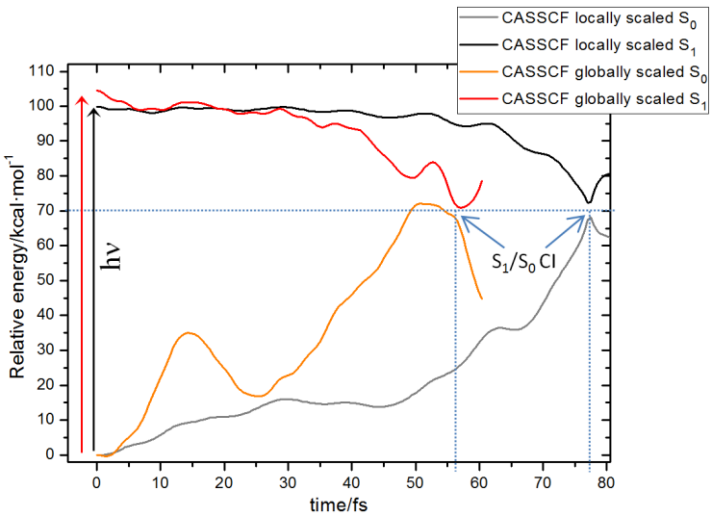

Figure 5.9 CASSCF globally and locally scaled energies of the S_1 photoisomerization trajectories of a 10 degrees pre-twisted 2-*cis*-α-Me-$C_5H_6NH_2^+$ model. The S_1/S_0 conical intersection (CI) energy and time is highlighted.

As shown in Figure 5.9, the *local* scaling method ensures a less steep out-of-plane region than the *global* scaling method, therefore resulting in 21 fs delay to reach the S_1/S_0 conical intersection (56 fs for CASSCF globally scaled; 77 fs for CASSCF locally scaled). As expected, both methods almost coincide in the value of relative energy at which the conical intersection is found, at about 70 kcal·mol^{-1}.

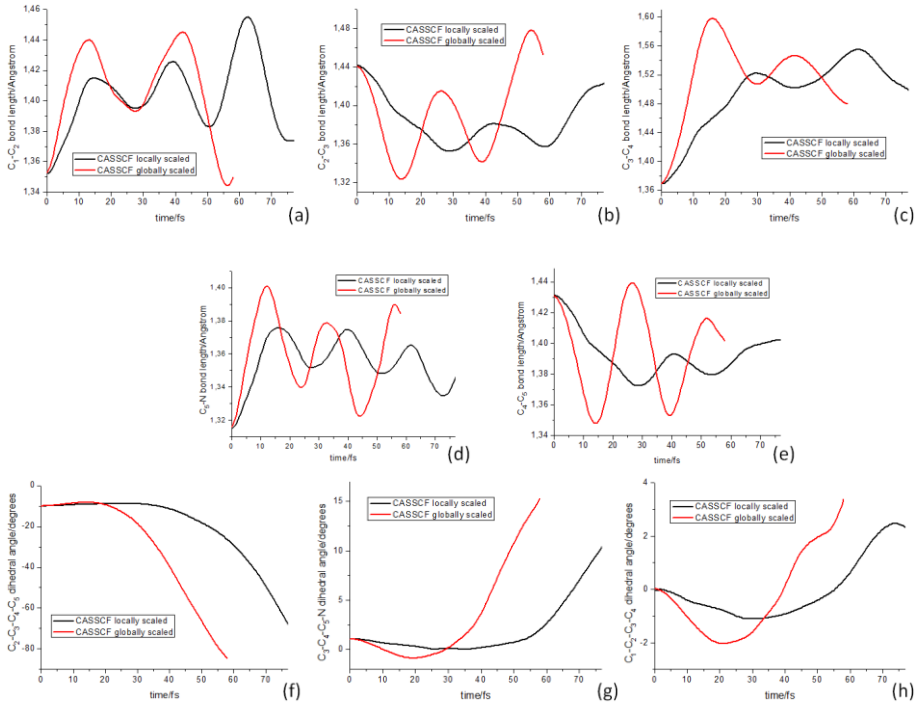

Figure 5.10 Comparison between backbone bonds (**a**-**e**) and dihedral angles (**f**-**h**) of 10 degrees pre-twisted 2-*cis*-α-Me-$C_5H_6NH_2^+$ CASSCF globally and locally scaled trajectories.

In the geometrical point of view, CASSCF *global* and *local* scaling methods give the same qualitative description of the photoisomerization process: as first bond length inversion takes place, accompanied by slight negative torsion of the backbone dihedral angles. Once bond length alternation is completed, it follows positive torsion, especially around the C_3-C_4 bond, finally reaching the S_1/S_0 conical intersection. Nevertheless, the CASSCF locally scaled trajectory describes, as well as for initially planar 2-

cis-α-Me-$C_5H_6NH_2^+$ dynamics, CASPT2-like properties: the energy gradient has a lower module than in CASSCF dynamics, therefore requiring more time for initial bond length inversion, which anyway does not reach the typical CASSCF amplitude.

5.3 Summary, Conclusions and Perspectives

A novel method to scale the CASSCF energy gradient (*i.e.* the CASSCF force) is presented and implemented for application in excited-state molecular dynamics. Especially, the definition of a *locally* scaled gradient method is mathematically formulated, where the CASSCF energy gradient is scaled at each step of the trajectory, in order to provide the approximate CASPT2 energy gradient, if the two gradient vectors are nearly parallel. This *local* approach is intended to improve the previously developed *globally* scaled gradient method, which assumes appreciable correlation between CASSCF and CASPT2//CASSCF minimum energy paths, a condition not necessarily fulfilled.

This novel method was applied to the excited-state *cis-trans* photoisomerization process of a minimum retinal model (2-*cis*-α-Me-$C_5H_6NH_2^+$), considering two different initial conformations: planar and 10 degrees twisted around the middle carbon-carbon bond. In order to validate the method and understand its limits, CASSCF, CASPT2//CASSCF and CASPT2 minimum energy paths were calculated, showing differences especially in the bond alternation path of the in-plane region. Therefore, CASSCF and CASPT2 trajectories were compared for the initially planar 2-*cis*-α-Me-$C_5H_6NH_2^+$, highlighting such difference in bond length profile, but confirming hydrogen-out-of-plane normal modes as responsible for photoisomerization.

The *locally* scaled gradient method applied to initially planar 2-*cis*-α-Me-$C_5H_6NH_2^+$ is able to reproduce CASPT2 typical characteristics of the in-plane region, reaching the limits of its validity (*i.e.* not nearly parallel energy gradient vectors) when the CASSCF trajectory initiates torsion, while the CASPT2 trajectory continues to describe in-plane vibrational relaxation. In

order to overcome such validity limits, different scaling schemes are actually being evaluated by the authors.

The *locally* scaled gradient method was tested also on 10 degrees twisted retinal model, where the *globally* scaled gradient method is in principle valid. We show that, in spite of a qualitatively similar excited-state mechanism, the novel method is able to properly scale the energy gradient vectors, resulting in a different time scale for initial bond length alternation, later torsion, and finally reaching the S_1/S_0 conical intersection.

We should note that, in principle, the *locally* scaled gradient method is not limited by the multiconfigurational approach, since it can be applied to whatever couple of levels of theory where nearly parallel energy gradient vectors are expected. Indeed, energy gradient vectors starting to diverge indicate that we reached the validity limits of the proposed method.

Moreover, this novel method could be applied also to optimization schemes (*i.e.* not only for dynamics), therefore showing its general purpose, conserving its main computational advantage: at each step, only three single-point CASPT2 energy calculations are required to generate a pseudo-CASPT2 energy gradient, instead of the 6*N* CASPT2 energy calculations needed for a numerical CASPT2 energy gradient, at the same time being not limited by the size number of atoms *N* of the molecule.

6. Tuning Spectroscopical Properties

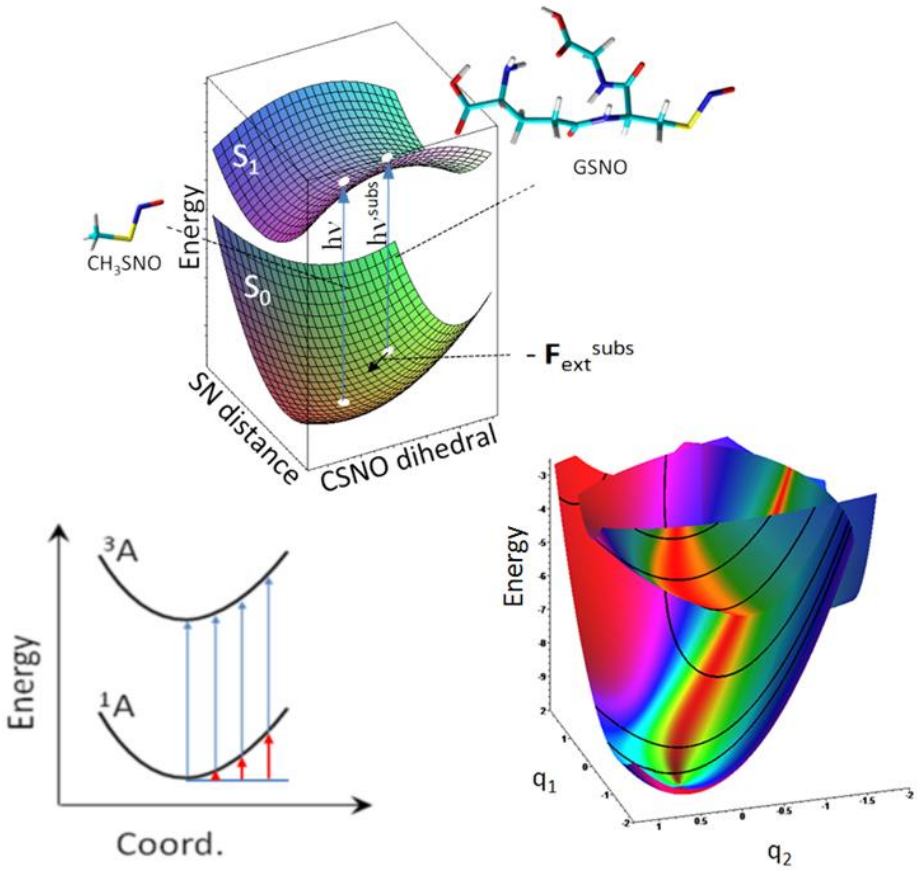

"Nature uses only the longest threads to weave her patterns,

so that each small piece of her fabric reveals

the organization of the entire tapestry"

Richard P. Feynman

Modulation of spectroscopical properties is a relevant aim in chemistry and biochemistry. Especially, fine tuning of the absorption wavelength determines a selected control over photoactivation (*Wanko et al. 2005*), while the possibility to modulate fluorescence (or phosphorescence) energies is highly attractive for tracking cellular processes (*Shaner et al. 2007; Nienhaus 2008*) and propose technological developments in optical nanoscopy (*Hofmann et al. 2005; Betzig et al. 2006; Hess et al. 2006*) and data storage (*Sauer 2005*).

The modulation of spectroscopical properties can be accomplished by applying different approaches, based on chemical substitution of the chromophore, influence of the solvent (pH, permittivity of the media) or, in case of biomolecules, effect of the environment (steric hindrance, selected mutations). Several experimental studies can be found throughout the literature, where the so-called chemical intuition is used to attempt different modifications to the chromophore which could induce a certain bathochromic or hypsochromic shift. Nevertheless, considering the almost infinite number of possible modifications, a predictive study of the distinctive effects is highly desirable, in order to determine which kind of modification is most likely to determine the effect we are interested in.

In this Ph.D. Thesis, we focus on prediction of the absorption energy, in order to determine if modulation is eventually possible, and up to which extent. Especially, the effects of chemical substitution on a chromophore (of the S-nitrosothiols family) are investigated by systematic and methodological approaches. Moreover, the mechanical external forces acting on a chromophore (*e.g.* in the case of a switch in a protein environment, or of a monomer as part of a polymer chain subject to stretching or compression) will be considered by a dynamical study on the ground-state potential energy surface, leading to an estimation of the absorption spectrum modulation for one of the most commonly applied photoswitches: azobenzene. The results are shown and discussed in the following sections.

6.1 Substituent Effect in the Excitation Energy of a Chromophore

During the past decades, the substituent effect has become one of the major research topics in physical organic chemistry. Especially, different methodologies were developed in order to systematically describe the relationships between substituent groups and chemical (or physical) properties in the ground-state, all of them based on the Hammett equation:

$$\log \frac{k}{k_0} = \rho\sigma \qquad \text{Eq. 6.1}$$

where k_0 and k are the unsubstituted and substituted aryl reaction rate constants, respectively, ρ is a term which depends on the specific reaction and σ is a term which depends on the specific substituent (*Hammett 1937*).

Applying eq. 6.1, Hammett introduced a Linear Free Energy Relationship (LFER) by which the change in Gibbs activation energy for any two reactions with two aromatic reactants only differing in the type of substituent (meta or para position) is proportional to the change in Gibbs energy. Subsequent modifications to the Hammett equation were proposed, leading to appropriate LFERs to describe and interpret the mechanism of organic reactions in the ground-state: the Swain–Lupton equation(*Swain and Lupton 1968*), the Taft equation (*Taft 1952; 1952; 1953*) and the Yukawa–Tsuno equation (*Yukawa and Tsuno 1959*).

In spite of the successful application to ground-state reactivity (including synthetic, mechanistic and catalytic properties), the attempt to describe excited-state processes by the Hammett equation was shown to be somehow controversial: in some cases, an acceptable correlation was found between the rate of a reaction in the excited-state (including molecules differently substituted) and the Hammett constants of the same substituents derived from ground-state reactivity. In other cases, the effect of the substituent on the excited-state reactivity differs from that found in the ground-state (*Sadlej-Sosnowska and Kijak 2012*). Therefore, additional parameters were introduced with the aim of describing photochemical substituent effects (σ^{hv} (*McEwen and Yates 1991*), σ_{ex} (*Wehry and Rogers*

1965), σ^* (*Shim et al. 1982; Shim et al. 1983*), $\sigma^{\bullet h\nu}$ (*Fleming and Jensen 1996*), $\sigma_{cc}^{h\nu}$ (*Cao et al. 2008*)), keeping the mathematical expression defined by Hammett (eq. 6.1). Furthermore, a reformulation of the Hammett equation was proposed in order to correlate the substituent effect with the absorption frequency (*Charton 1981*), nevertheless leaving the application of the Hammett equation to the description of excited-state properties as a non-prominent trial and error methodology.

As an attempt to rationalize substituent effects in organic chromophores, Woodward developed empirical rules by which it is possible to demonstrate a correlation between the wavelength of the absorption maximum in UV spectra and the extent of carbon-carbon double bond substitution in conjugated systems (*Woodward 1941*). The Woodward rules were successfully applied to carbonyl compounds, mono- and di-substituted benzene derivatives, benzoyl derivatives, and later improved by the introduction of a considerable amount of experimental data (*Fieser et al. 1948*). A complementation of the Woodward–Fieser rules, applicable only to molecules with one to four conjugated double bonds, is the Fieser–Kuhn rule, by which wavelengths of the absorption maxima and extinction coefficients can be estimated for whatever conjugated molecule (*Kuhn 1948*).

In this Ph.D. Thesis, we present a general methodology to predict excitation energies in substituted chromophores, by determining the structural modifications that a substituent causes to a reference unsubstituted chromophore (section 6.1.2). Especially, we show that the concept of "structural substituent excitation energy effect" can be formally introduced, in order to rationally predict and quantify the substituent effect in the excitation energy of a chromophore to an excited electronic state. Therefore, the developed methodology can be successfully applied only if the structural change of the chromophore induced by the substituent does not affect the electronic nature of the absorption process.

More in detail, each molecule under study can be formally divided into chromophore and substituent fragments, leading to the following definition of ground-state (E_{GS}) and excited-state (E_{ES}) electronic energy:

$$E_{\mathrm{GS}} = E_{\mathrm{GS}}^{chrom} + E_{\mathrm{GS}}^{subs} + E_{\mathrm{GS}}^{chrom/subs} \qquad \text{Eq. 6.2}$$

$$E_{\mathrm{ES}} = E_{\mathrm{ES}}^{chrom} + E_{\mathrm{ES}}^{subs} + E_{\mathrm{ES}}^{chrom/subs} \qquad \text{Eq. 6.3}$$

where E_{GS}^{chrom}, E_{GS}^{subs} and $E_{\mathrm{GS}}^{chrom/subs}$ are the electronic energies of chromophore, substituent and interaction between both parts in the ground-state, respectively, while E_{ES}^{chrom}, E_{ES}^{subs} and $E_{\mathrm{ES}}^{chrom/subs}$ are the counterparts in the excited-state. Indeed, by assuming that the substituent is not participating in the electronic excitation (*i.e.* only the chromophore is involved), the eventual energy stabilization or destabilization caused by the substituent is the same for ground and excited-state, leading to $E_{\mathrm{GS}}^{subs} = E_{\mathrm{ES}}^{subs}$ and $E_{\mathrm{GS}}^{chrom/subs} = E_{\mathrm{ES}}^{chrom/subs}$. Therefore, it is straightforward to obtain eq. 6.4:

$$E_{\mathrm{ES}} = E_{\mathrm{ES}}^{chrom} + E_{\mathrm{GS}}^{subs} + E_{\mathrm{GS}}^{chrom/subs} \qquad \text{Eq. 6.4}$$

Finally, the excitation energy (E_{exc}) can be obtained by subtracting eq. 6.2 from 6.4:

$$E_{\mathrm{exc}} = E_{\mathrm{ES}} - E_{\mathrm{GS}} = E_{\mathrm{ES}}^{chrom} - E_{\mathrm{GS}}^{chrom} \qquad \text{Eq. 6.5}$$

Within the limits of validity aforementioned, only the chromophore structure is responsible for the excitation energy, and its eventual deformations caused by the attached substituent can be interpreted as forces acting on the chromophore itself, finally leading to shifts of the absorption wavelengths. By the developed methodology, it is possible to determine which internal coordinates contribute to the chromophore deformation and therefore to the excitation energy of the substituted chromophore, avoiding direct calculation. Especially, the following data are required: (*i*) the ground-state structure of the substituted chromophore and (*ii*) the ground and excited-state potential energy surfaces of the unsubstituted chromophore. Both tasks have to be performed with a consistent level of theory, depending on the molecular system under study. Among the possible approaches which can be used to calculate ground and excited-state potential energy surfaces of the unsubstituted chromophore, we employed a quadratic approximation, resulting in the following expressions:

$$E_{\mathrm{GS}}(\Delta \boldsymbol{q}) = E_{\mathrm{GS}}\left(\boldsymbol{q}_{\mathrm{C}}^{eq}\right) + \frac{1}{2}\Delta \boldsymbol{q}^{T}\boldsymbol{H}_{\mathrm{GS}}\Delta \boldsymbol{q} \qquad \text{Eq. 6.6}$$

$$E_{\mathrm{ES}}(\Delta \boldsymbol{q}) = E_{\mathrm{ES}}\left(\boldsymbol{q}_{\mathrm{C}}^{eq}\right) + \Delta \boldsymbol{q}^{T}\boldsymbol{g}_{\mathrm{ES}} + \frac{1}{2}\Delta \boldsymbol{q}^{T}\boldsymbol{H}_{\mathrm{ES}}\Delta \boldsymbol{q} \qquad \text{Eq. 6.7}$$

where $\Delta \boldsymbol{q} = \boldsymbol{q} - \boldsymbol{q}_{\mathrm{C}}^{eq}$ is the vector which takes into account of the displacement from the ground-state equilibrium geometry ($\boldsymbol{q}_{\mathrm{C}}^{eq}$), $\boldsymbol{g}_{\mathrm{ES}}$ is the excited-state energy gradient vector, $\boldsymbol{H}_{\mathrm{GS}}$ and $\boldsymbol{H}_{\mathrm{ES}}$ are the Hessian matrices for the two electronic states.

The excitation energy can be obtained by subtracting eq. 6.6 from eq. 6.7. Therefore, by calculating ground and excited-state potential energy surfaces for the unsubstituted chromophore, the vertical excitation energy of any given substituted chromophore (fulfilling the requirements of a chemical substitution which does not affect the nature of the electronic excitation) can be predicted.

As aforementioned, apart from such prediction, also the internal coordinates controlling the excitation energy gap can be determined. Especially, the contribution of the distortions along the energy gradient vector and of the ones orthogonal to it (*i.e.* first-order and second-order energy gap variation respectively, according to eq. 6.6 and 6.7) were considered.

The developed methodology was applied to S-nitrosothiols (RSNOs), a family of compounds which has been shown to store, transport and release nitric oxide (NO) within the mammalian body (*Stamler et al. 1992*). In spite of their intrinsic instability at room temperature, attention has been focused on possible phototherapies based on RSNO photochemical decomposition to give the corresponding disulfide and NO (*Bartberger et al. 2001; de Oliveira et al. 2002; Grossi and Montevecchi 2002*). As part of this Ph.D. Thesis, the photocleavage mechanism of the model compound CH_3SNO to release CH3S· and ·NO was studied at the CASPT2 level resulting in a barrierless process when irradiating in the visible region (S_1), in the near UV region (S_2) and for photosensitized (T_1) reactions (*i.e.* RSNO photocleavage is expected to be an ultrafast process without involving any side reaction). Therefore, an eventual control of the photocleavage mechanism is possible only by modulation of the RSNOs vertical excitation

energies. After accurate calibration of the appropriate TD-DFT method to be used by CASPT2 calculations over model compounds, the electronic absorption spectra of a series of differently substituted RSNOs was calculated for the lowest-energy $^1(n,\pi^*)$ and $^1(\pi,\pi^*)$ transitions, finding acceptable correlations with the corresponding σ_p Hammett constants of the substituents for a series of aryl derivatives. Therefore, these results (see section 6.1.1) provide basic understanding of RSNO photophysical and photochemical processes.

In order to understand up to which extent the developed methodology can be considered a predictive tool for designing substituents with desired absorption wavelength sensitivity, it was applied on the same set of RSNOs, considering CH_3SNO as the unsubstituted reference. The results show a remarkable agreement between calculated and predicted values (see section 6.2.2)

6.1.1 Modulating Nitric Oxide Release by S-Nitrosothiol Photocleavage: Mechanism and Substituent Effects

THE JOURNAL OF PHYSICAL CHEMISTRY A
Article
pubs.acs.org/JPCA

Modulating Nitric Oxide Release by *S*-Nitrosothiol Photocleavage: Mechanism and Substituent Effects

Marco Marazzi, Alberto López-Delgado, Miguel Angel Fernández-González, Obis Castaño, Luis Manuel Frutos,* and Manuel Temprado*

Departamento de Química Física, Universidad de Alcalá, E-28871 Alcalá de Henares, Madrid, Spain

Supporting Information

ABSTRACT: The photochemistry and photophysics of a series of *S*-nitrosothiols (RSNOs) have been studied computationally. The photocleavage mechanism of the model compound CH_3SNO to release $CH_3S\cdot$ and ·NO was studied at the CASPT2 level resulting in a barrierless process when irradiating in the visible region (S_1), in the near UV region (S_2) and for photosensitized (T_1) reaction. The absorption energy required to initiate photocleavage was calculated at the CASPT2 and B3P86 levels showing the possibility of the modulation of NO release by RSNO photoactivation as a function of the substituent R. Good correlations between the wavelengths of the lowest energy $^1(n,\pi^*)$ and $^1(\pi,\pi^*)$ transitions of aryl *S*-nitrosothiols and the corresponding Hammett constants of the substituents have been obtained.

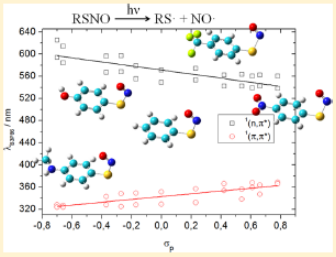

INTRODUCTION

Nitric oxide (NO) has emerged as a fundamental molecule in biology and medicine since its identification in 1986 as endothelium-derived relaxing factor[1] and further in 1996 as a signaling molecule in cells and tissues.[2] Since then, this simple stable radical has been proven to be implicated in a growing number of physiological processes[3] such as relaxation of vascular muscle tone,[4] immune stimulation,[5] and neurotransmission.[6] Furthermore, NO has many functions in the skin, including the mediation of inflammation and antimicrobial defense, wound healing, regulation of keratinocyte homeostasis, and apoptosis.[7] Thus, a large number of diseases are associated to NO overproduction, and considerable effort has being spent in developing enzyme inhibitors to compensate this overproduction. There are also medical conditions causing NO deficiency, due to a misfunction of the arginine−NO synthase cycle. In vivo NO is generated via enzymatic metabolism of L-arginine[8] or via compounds able to release NO.[9] Therefore, the creation of synthetic NO donors for research and therapeutic applications has received increased interest.[3b,10]

Different families of compounds are capable of generating NO in situ: organic nitrates ($RONO_2$) and nitrites (RONO), metal nitrosyl complexes, *N*-nitrosamines (RN(NO)R′), *S*-nitrosothiols (RSNO), etc.[9] Among them, RSNOs have been shown to store, transport, and release NO within the mammalian body.[11] NO is transported around the body (as RSNO) mostly as *S*-nitrosoalbumin and *S*-nitrosohemoglobin,[11,12] and it has been suggested that the formation and decay of low molecular weight RSNOs, such as *S*-nitrosoglutathione and *S*-nitrosocysteine, also represent a mechanism for the storage or transport of NO.[13] Recently, several studies have been devoted to try to understand the mechanism of cellular nitrosothiol formation.[14] Moreover, *S*-nitrosylation has shown to regulate protein function in many proteins.[15] In addition, NO can be converted into RSNOs that are stable until cleaved by UV irradiation to release NO.

RSNOs, as free NO, can be used as potent vasodilators, antiplatelet agents, and for the treatment of a variety of diseases including hypertension, atherosclerosis, or as anticancer agents.[16] Specifically, *S*-nitrosoglutathione has been tested as a therapeutic agent for clinical use in several human investigations with good results.[17] Furthermore, photolysis of some RSNOs results in an enhanced cytotoxic effect on some leukemia cells,[18] and there is considerable potential for the use of these species in phototherapy.

The main drawback of most RSNOs is their instability at room temperature, followed by thermal or photochemical decomposition to give the corresponding disulfide and NO.[19] More in detail, it was proposed that RSNO decomposition is a two-step process: the first step corresponds to homolytic dissociation of the S−N bond to form ·NO and RS· radicals (Scheme 1a, reaction A), followed by dimerization of RS· to form the disulfide RSSR (Scheme 1a, reaction B). The general instability of RSNOs has made them difficult to study. The most efficient synthetic approach to make more stable RSNO species has been focused on tertiary[20] or aromatic derivatives bearing bulky groups in the 2 and 6 positions.[21] Generally, these RSNOs are more stable than aliphatic secondary or primary RSNOs because of the increase in steric interactions associated with the dimerization of the thiyl radical that forms

Received: May 15, 2012
Revised: June 4, 2012
Published: June 5, 2012

dx.doi.org/10.1021/jp304707n | J. Phys. Chem. A 2012, 116, 7039−7049

Scheme 1. Proposed Two-Step Process (A and B) for RSNO Decomposition (a) and Resonant Structures Corresponding to *syn* and *anti* Conformers (b)

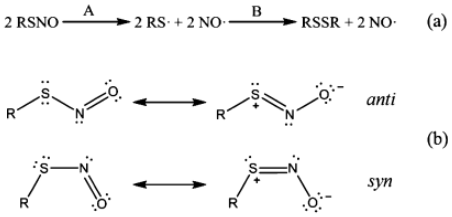

upon homolytic cleavage of the S−N bond.[19a] In addition, the S−N bond has a partial double bond character, due to delocalization of the sulfur lone pairs in the nitroso group. Therefore, RSNOs can exist as *syn* and *anti* conformers (Scheme 1b).[19b]

Different computational studies were carried out with the goal of a better understanding of RSNOs instability on the basis of structural and energy parameters (e.g., bond dissociation energy),[19a,b,20a,22] therefore not studying explicitly the photochemical aspects of NO releasing, and usually focusing only on model compounds (i.e., HSNO and CH_3SNO).[22b−i]

In this study, the attention is focused on the photochemistry and photophysics of a series of RSNOs, including primary, secondary, tertiary, vinyl, and phenyl substituted RSNOs (Figure 1). CH_3CH_2SNO, $(CH_3)_2CHSNO$, $(CH_3)_3CSNO$, CF_3SNO, $(C_6H_5)_3CSNO$, and $(CH_3)_2N(CH_2)SNO$ can be considered as derivatives of CH_3SNO, while vinyl (CH_2CHSNO) and several phenyl substituted RSNOs are meant to expand the conjugation of the −SNO chromophore. Furthermore, the substituent effect of electron withdrawing and donating groups was investigated. Specifically, the photochemical rupture of the S−N bond was explored from a computational point of view in a model compound (i.e., CH_3SNO), followed by a study of the substituent effect in a series of RSNOs, in order to modulate the energy needed for the electronic excitation and later cleavage of the S−N bond.

■ COMPUTATIONAL METHODS

Different computational methods were applied, depending on the size of the molecular system. Particularly, Møller−Plesset perturbation theory to the second order (MP2) with a 6-311+G(2df) basis set was applied to CH_3SNO, CH_3CH_2SNO, $(CH_3)_2CHSNO$, $(CH_3)_3CSNO$, CF_3SNO, $(CH_3)_2N(CH_2)$-SNO, and CH_2CHSNO in order to find all ground-state minima (*syn* and *anti* conformers), followed by multiconfigurational Multi-State Complete-Active-Space perturbation theory to the second order (MS-CASPT2) with a 6-31G(d) basis set for calculation of vertical excitation energies (i.e., absorption spectra). In order to evaluate the effect of the basis set reduction, the absorption spectrum of CH_3SNO was also calculated at the MS-CASPT2/ANO-L level of theory and compared to MS-CASPT2/6-31G(d).

The photochemical minimum energy paths leading from CH_3SNO photon absorption to release of nitric oxide were calculated by MS-CASPT2//SA-CASSCF methodology[23] (6-31G(d) basis set): State-Average Complete-Active-Space Self-Consistent Field (SA-CASSCF) theory was applied to calculate energy and force at each step of the minimum energy path, followed by MS-CASPT2 single-point energy corrections along the minimum energy path (see Supporting Information for details). When two electronic states were found to be degenerate in energy, the crossing was characterized by calculating the nonadiabatic coupling vectors: derivative coupling (DC) and gradient difference (GD) vectors.[24]

The selected active space includes 16 electrons in 11 orbitals for CH_3SNO, CH_3CH_2SNO, $(CH_3)_2CHSNO$, $(CH_3)_3CSNO$, CF_3SNO, and $(CH_3)_2N(CH_2)SNO$ models: 2σ and $2\sigma^*$ orbitals (C−S and S−N bonds), 1π and $1\pi^*$ orbitals (N=O bond), $5n$ orbitals (lone pairs on sulfur, nitrogen, and oxygen), and the corresponding electrons. The π and π^* orbitals of the vinyl moiety were additionally included in the active space of the CH_2CHSNO model, leading to 18 electrons in 13 orbitals.

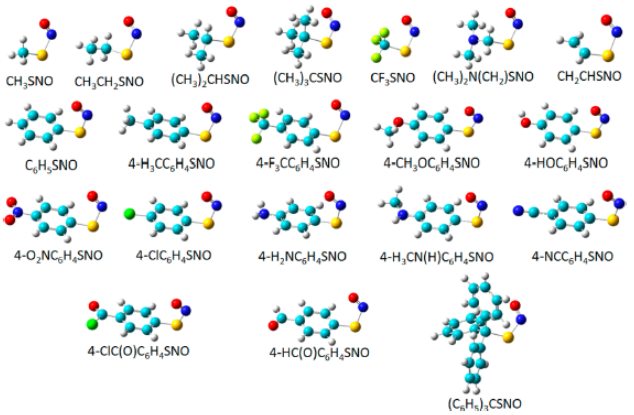

Figure 1. *S*-Nitrosothiol (RSNO) models under study in their *syn* conformation.

dx.doi.org/10.1021/jp304707n | *J. Phys. Chem. A* 2012, 116, 7039−7049

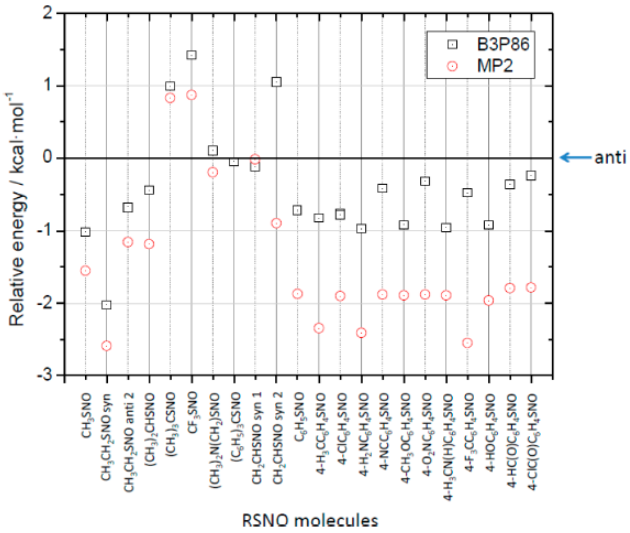

Figure 2. B3P86/6-311+G(2df) and MP2/6-311+G(2df) optimized ground-state energies of *syn* conformers relative to the *anti* conformers: a positive relative energy indicates that the *anti* conformer is more stable. For CH_3CH_2SNO, *syn* and *anti*2 conformers are compared to *anti*1. For CH_2CHSNO, both *syn*1 and *syn*2 conformers are compared to the *anti* conformer.

In order to test the validity of time dependent density functional theory (TD-DFT) in reproducing excited state properties of RSNOs, different DFT functionals (BLYP, B3LYP, CAM-B3LYP, BP86, LC-BP86, B3P86, and M05-2X) were applied and compared to available experimental data and CASPT2 results obtained for molecules of suitable size for a multiconfigurational approach, suggesting that the Becke's three-parameter hybrid exchange functional[25] with the Lee–Yang–Parr correlation functional[26] (B3LYP) and with Perdew's nonlocal correlation functionals[27] (B3P86) are the most suitable (see Supporting Information for details). However, it has been shown that the B3LYP method consistently overestimates the S–N bond length and increasingly underestimates the bond dissociation energy (BDE) with increasing RSNO size.[22j] In contrast, the B3P86/6-311+G(2df,p) method was found to perform the best of the methods considered in an assessment of theoretical methods study[22j] for obtaining optimized structures and S–N BDE of RSNOs. Thus, B3P86 (with a 6-311+G(2df) basis set) was chosen in the current study for ground-state optimizations and excited-state calculations of those RSNOs, where size is a limiting factor for CASPT2 treatment ($(C_6H_5)_3CSNO$ and all phenyl derivatives) because of the prohibitive computational cost.

Gaussian09[28] (for DFT, MP2, and CASSCF minimum energy paths) and Molcas 7[29] (for CASPT2) are the computer packages by which all calculations were performed.

■ RESULTS AND DISCUSSION

Ground-State Structures. The relative energy of *syn* and *anti* conformers in their ground-state minima is shown in Figure 2, being optimized at B3P86/6-311+G(2df) and MP2/6-311+G(2df) levels of theory. CH_3CH_2SNO has two different *anti* conformations (*anti*1 and *anti*2), while CH_2CHSNO has two different *syn* conformations (*syn*1 and *syn*2). In both cases, the almost planar *anti*1 CH_3CH_2SNO and *syn*1 CH_2CHSNO conformers can undergo a partial torsion around the C–S bond, resulting in *anti*2 CH_3CH_2SNO and *syn*2 CH_2CHSNO conformers. For all the other RSNO models, single *syn* and *anti* conformations were found, corresponding to an almost planar CSNO moiety.

Interestingly, while the vinyl moiety contributes to enlarge the chromophore conjugation by the almost planar *syn*1 and *anti* CH_2CHSNO, all aryl substituents form a dihedral angle ranging from 49° to 89° with the SNO moiety, indicating that the conjugation between the phenyl ring and the SNO fragment is less effective (see Table 4). This structural feature has been observed previously in the X-ray structures of several aryl RSNOs.[21] In fact, completely planar *syn* and *anti* C_6H_5SNO geometries correspond to transition states connecting stable equivalent conformers (see Supporting Information).

In all cases, the difference in energy between *syn* and *anti* conformers is lower than 3 kcal·mol^{-1}. Moreover, the transition state connecting the conformers was evaluated at the MP2/6-311+G(2df) and B3P86/6-311+G(2df) levels for CH_3SNO, $(CH_3)_3CSNO$, CF_3SNO, $(CH_3)_2N(CH_2)SNO$, and CH_2CHSNO: the activation energy required for the conformational change ranges from 4.6 to 12.7 kcal·mol^{-1} at the MP2 level, and from 8.0 to 15.3 kcal·mol^{-1} at the B3P86 level, considering that B3P86 transition state geometries tend to shorten the S–N distance (from 1.0% to 5.2%) and to enlarge the C–S–N angle (from 1.8% to 6.4%) with respect to MP2 transition state geometries.[30] These data suggest the establishment of a conformational equilibrium in all proposed RSNOs at room temperature, as supported by theoretical and experimental studies.[20a,22b] Thus, both *syn* and *anti* conformers are

expected to affect the spectroscopic behavior of a certain RSNO molecule. Nevertheless, the conformational equilibrium is expected to favor one specific conformation, and this should be taken into account when evaluating its spectroscopic properties.

As previously observed,[21,22b,c] all aryl derivatives, CH_3SNO, CH_3CH_2SNO, and $(CH_3)_2CHSNO$, are more stable in their *syn* conformation, while tertiary substituted RSNOs such as $(CH_3)_3CSNO$ and CF_3SNO preferentially assume the *anti* conformation. $(C_6H_5)_3CSNO$ and *syn*1 CH_2CHSNO almost do not show any conformational preference, while when looking at $(CH_3)_2N(CH_2)SNO$ and *syn*2 CH_2CHSNO, the conformational equilibrium is sensitive to the level of theory, suggesting a B3P86 destabilization of the *syn* conformation with respect to MP2 prediction. This result could be envisaged by the fact that MP2 theory includes electron correlation effects by means of the perturbation theory. More in detail, optimized MP2 and B3P86 structures are in good agreement (Tables 1S and 2S in Supporting Information). Nevertheless, it should be noted that the B3P86 optimized structures of some aryl RSNOs are more planar than the respective MP2 structures, highlighting that the higher difference in energy between the two levels of theory (2.1 kcal·mol^{-1} in 4-$F_3CC_6H_4SNO$) is associated to the higher difference in C−C−S−N dihedral angle (*syn* 4-$F_3CC_6H_4SNO$ has a C−C−S−N dihedral of 86° at the MP2 level and 69° at the B3P86 level).

Photochemistry of CH_3SNO. Several experimental studies by laser flash photolysis have proven that the photochemical decomposition of RSNO follows the mechanism depicted in Scheme 1a.[18,31] The formation of the thiyl radical was confirmed by ESR spectroscopy and the release of NO by its oxidation of oxyhemoglobin. However, to our knowledge, a detailed computational study of the photochemistry of RSNOs has not been previously conducted. Thus, in the current work, CH_3SNO was selected as a reference model to study the photochemistry of RSNOs. The absorption spectrum of *syn* and *anti* CH_3SNO was calculated at the MS-CASPT2/ANO-L level (Table 1). The effect of the basis set on the excitation energy was taken into account by calculating MS-CASPT2/6-31G(d) absorption spectra, observing the same qualitative description, with an expected stabilization in energy when including atomic natural orbitals (see Supporting Information).

Table 1. Absorption Spectra of *syn* and *anti* CH_3SNO at the MS-CASPT2/ANO-L Level of Theory[a]

		anti		*syn*	
state	transition	ΔE (nm)	$f \times 10^{-3}$	ΔE (nm)	$f \times 10^{-3}$
S_5	$^1(n,\pi^*)$	203	0.03	211	0.29
S_4	$^1(\pi,\sigma^*)$	224	0.54	215	14.75
S_3	$^1(\sigma,\pi^*)$	237	0.12	218	0.98
S_2	$^1(\pi,\pi^*)$	342	9.12	330	16.76
S_1	$^1(n,\pi^*)$	600	0.33	530	0.51

[a]The vertical excited-state energy (ΔE) is calculated as a reference to the ground-state at the Franck−Condon point (S_0): $\Delta E = E(S_n) - E(S_0)$. The oscillator strength f is given for each transition.

As shown in Table 1, the lowest energy excited-state (S_1) corresponds to a dark $^1(n,\pi^*)$ state, while S_2 is a bright $^1(\pi,\pi^*)$ state. Although CH_3SNO cannot be isolated because of its intrinsic instability, it shares the same chromophore (CSNO) with the synthesized tertiary RSNOs (like $(C_6H_5)_3CSNO$), therefore allowing for a quantitative comparison of the absorption spectra. The available experimental data show that, as well as for the calculated values, a weak band assigned to a $^1(n,\pi^*)$ state covers the spectrum in the region 520−590 nm, while a pronounced peak is found around 340 nm, being assigned to a $^1(\pi,\pi^*)$ state.[22b]

Higher in energy, the calculated excited-states for CH_3SNO (S_3, S_4, and S_5) correspond to $^1(\sigma,\pi^*)$, $^1(\pi,\sigma^*)$, and $^1(n,\pi^*)$ states, respectively. Looking at the absorption energy and oscillator strength, we can conclude that $S_0 \rightarrow S_1$ and $S_0 \rightarrow S_2$ vertical transitions are the initiating events of any photochemical pathway under visible and near-UV irradiation, respectively.

Since tertiary RSNOs usually show higher stability as *anti* conformers, therefore resulting as predominant conformation on the ground-state,[22b] *anti* CH_3SNO was selected as a reference model to study the photochemistry of tertiary substituted RSNOs (Figure 2). Nevertheless, our study shows that *syn* and *anti* conformers are divided only by a few kcal·mol^{-1} (see Figure 2), and therefore, the photochemistry of *syn* CH_3SNO was also studied, showing the same behavior as that described here for *anti* CH_3SNO (see Supporting Information).

An energy barrierless process was found for both $^1(n,\pi^*)$ and $^1(\pi,\pi^*)$ states. More in detail, after irradiation to the bright $^1(\pi,\pi^*)$ state (S_2), the system undergoes vibrational relaxation up to a nearly flat potential energy surface region where $^1(\pi,\sigma^*)$, $^1(\pi,\pi^*)$, and $^1(n,\pi^*)$ states are almost degenerate in energy. More in detail, the $^1(\pi,\pi^*)$ state crosses with the $^1(n,\pi^*)$ state when the S−N bond is almost broken (SN distance = 2.72 Å). The two crossing surfaces are almost not coupled ($|DC| \approx 0$), while the GD vector indicates S−N detachment as the most relevant process. The energy degeneracy between $^1(n,\pi^*)$ and $^1(\pi,\pi^*)$ states is conserved up to reaching the ground-state (S−N distance above 3.2 Å), where the derivative coupling is almost vanishing, determining a slightly avoided crossing region, with the GD vector defining the dissociation coordinate.[32] The GD vector depicts two possible pathways: formation of $CH_3S\cdot$ and ·NO radicals or radical recombination to form the starting CH_3SNO structure (i.e., internal conversion). In the presence of other CH_3SNO molecules, dimerization of two $CH_3S\cdot$ radicals to form the corresponding disulfide should be the driving force for the final release of NO. In case formation of $CH_3S\cdot$ and ·NO radicals is not followed by $CH_3S\cdot$ dimerization, the CH_3SNO structure will be recovered, without possibility to form any byproduct (at least when considering vertical excitation within 4 eV).

The same mechanism is valid if irradiating the $^1(n,\pi^*)$ state (S_1). The only possibility to follow a photochemical pathway different from S−N cleavage would be given by the conical intersection between $^1(\pi,\sigma^*)$ and $^1(\sigma,\pi^*)$ states, found above 5.5 eV, as shown by the nonadiabatic coupling vectors (Figure 3, S_4/S_3 CI): the GD vector favors S−N bond cleavage, while the DC vector indicates a possible torsion around the S−N bond, eventually leading to an *anti*-to-*syn* photoinduced conformational change. To reach the $^1(\pi,\sigma^*)/^1(\sigma,\pi^*)$ conical intersection, a vertical excitation to the $^1(\sigma,\pi^*)$ state at 5.52 eV or to the $^1(\pi,\sigma^*)$ state at 6.31 eV would be required when CH_3SNO is at the ground-state minimum, in both cases a too high absorption energy (middle-UV range), especially when considering a possible application of RSNOs in biology or medicine.

dx.doi.org/10.1021/jp304707n | J. Phys. Chem. A 2012, 116, 7039−7049

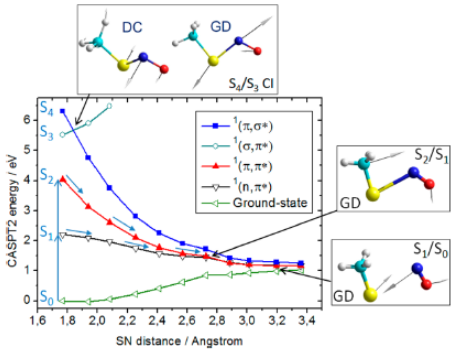

Figure 3. CASPT2 energy profile of *anti* CH_3SNO as a function of the S−N distance. The energetically feasible (i.e., vertical excitation within 4 eV) photoinduced processes are shown by arrows, both indicating barrierless photocleavage. The nonadiabatic coupling vectors are shown for S_4/S_3, S_2/S_1 and S_1/S_0 crossings (in the nearly planar region, the calculated DC vectors are almost zero).

In addition, the minimum energy path on T_1 (i.e., the triplet state at lower energy, located between S_0 and S_1 at the Franck−Condon point, corresponding to a $^3(n,\pi^*)$ state) was calculated in order to study an alternative mechanism to obtain NO; as suggested by experimental evidence, the population of T_1, mediated by a photosensitizer, is responsible of an increase in the reaction quantum yield of the S−N homolytic photocleavage.[33]

The minimum energy path on the $^3(n,\pi^*)$ state (Figure 4) shows how, also in this case, $CH_3S\cdot$ and ·NO can be formed by

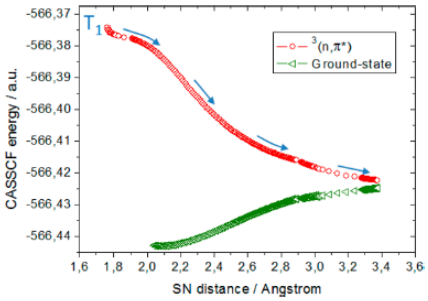

Figure 4. CASSCF minimum energy path on the $^3(n,\pi^*)$ state of *anti* CH_3SNO, corresponding to the lower energy triplet state (T_1).

a barrierless process, therefore furnishing an additional reaction pathway to the ones available by irradiation of the $^1(n,\pi^*)$ and $^1(\pi,\pi^*)$ states (S_1 and S_2, respectively).

Absorption Spectra. The comparison between experimental, CASPT2/6-31G(d), and B3P86/6-311+G(2df) absorption spectra for both *syn* and *anti* RSNOs, calculated for $S_0 \rightarrow S_1$ and $S_0 \rightarrow S_2$ transitions, is shown in Table 2.

For all proposed RSNOs, the lowest-energy vertical excitation ($S_0 \rightarrow S_1$) corresponds to a dark $^1(n,\pi^*)$ state, while more energy is required to obtain a bright $^1(\pi,\pi^*)$ transition ($S_0 \rightarrow S_2$). Experimental data are available for the weak $^1(n,\pi^*)$ transition (ϵ = 10 M^{-1} cm^{-1} ca.)[22b] of CH_3CH_2SNO, $(CH_3)_2CHSNO$, and $(CH_3)_3CSNO$, showing agreement with the calculated values: the maximum absorption wavelengths were measured to be 520 and 552 nm for *syn* and *anti* CH_3CH_2SNO, while 524 and 556 nm were recorded for *syn* and *anti* $(CH_3)_2CHSNO$, respectively, therefore defining an absorption range between 520 and 560 nm for the $S_0 \rightarrow S_1$ transition in primary and secondary derived RSNOs. However, the $^1(n,\pi^*)$ transition for $(CH_3)_3CSNO$ was detected at 550 nm (*syn*) and 596 nm (*anti*) showing a red shift in the maximum absorption as compared to primary and secondary derivatives.[20a]

In order to quantify the agreement between B3P86 and CASPT2 calculated absorption wavelengths, the correlation graphs related to the $^1(n,\pi^*)$ and $^1(\pi,\pi^*)$ transitions are shown in Figure 5.

The linear fit of E_{B3P86} versus E_{CASPT2} demonstrates that the B3P86 functional can be successfully applied especially to describe the bright $^1(\pi,\pi^*)$ transition ($S_0 \rightarrow S_2$), being the adjusted coefficient of determination (R^2) close to the unit. These results allowed us to apply the calibrated DFT functional to $(C_6H_5)_3CSNO$ and to all aryl derivatives. The computed $^1(n,\pi^*)$ and $^1(\pi,\pi^*)$ transitions for all aryl derivatives are shown in Table 3.

$(C_6H_5)_3CSNO$ was isolated and characterized experimentally,[20a] showing a broad and weak absorption band in the region 520−600 nm and a more pronounced peak around 340 nm, corresponding to $^1(n,\pi^*)$ and $^1(\pi,\pi^*)$ transitions, respectively. The calculated B3P86 absorption spectra reproduce the observed spectroscopic values, suggesting a shift of 18 nm between the maxima of *syn* and *anti* $^1(\pi,\pi^*)$ bands (Table 2). The $(C_6H_5)_3CSNO$ $^1(\pi,\pi^*)$ absorption wavelengths can be estimated at the CASPT2 level by the linear regression shown in Figure 5, resulting in a 15 nm shift between absorption maxima (353 nm (*anti*) and 338 nm (*syn*)). Moreover, a difference in oscillator strength of only 6.0×10^{-4} could explain the experimental difficulty in assigning $^1(\pi,\pi^*)$ peaks to each of the conformers in the experimental study.[20a]

Taking into account the data in Tables 2 and 3, we can therefore conclude that the $^1(n,\pi^*)$ transition corresponds to a weak band for both *syn* and *anti* conformers for all proposed derived RSNOs. However, large differences in the *f* values are found for the bright $^1(\pi,\pi^*)$ transition depending on the conformer type. *Syn* conformers have larger oscillator strengths than *anti* conformers for the $^1(\pi,\pi^*)$ transition, and therefore, they are expected to play a major role in determining the spectroscopic properties of the bright state.

In general, the *anti* conformers need a lower excitation energy (i.e., higher absorption wavelength) than *syn* conformers, for both $^1(n,\pi^*)$ and $^1(\pi,\pi^*)$ transitions, with the exceptions of CF_3SNO and CH_2CHSNO.

An analysis of the CF_3SNO conformers reveal that the S−N bond (expected to be 1.5−1.6 Å in length) is mostly broken already at the ground-state, as expected by the high electronegativity presented by the $-CF_3$ group, which attracts electron density toward itself and therefore weakens the S−N bond. Specifically, the absorption wavelength is highly sensitive to the S−N distance, which in turn is highly sensitive to the level of theory: at higher CASPT2 wavelengths of the *syn* conformer (with respect to the *anti* conformer) corresponds a higher S−N distance: 2.04 Å for *syn* CF_3SNO and 1.97 Å for

Table 2. CASPT2/6-31G(d), B3P86/6-311+G(2df) and Experimental (When Available) Absorption Spectra of All Primary, Secondary, Tertiary, and Vinyl RSNOs, Corresponding to the Two Singlet Lowest-Energy Vertical Excitations ($S_0 \rightarrow S_1$ and $S_0 \rightarrow S_2$)[a]

		$^1(n,\pi^*)$ transition (S_1)					$^1(\pi,\pi^*)$ transition (S_2)				
molecule	conformation	λ_{CASPT2}	λ_{B3P86}	λ_{exp}[b]	f_{CASPT2}	f_{B3P86}	λ_{CASPT2}	λ_{B3P86}	λ_{exp}[b]	f_{CASPT2}	f_{B3P86}
CH_3SNO	*anti*	571	545		0.00	0.00	323	315		8.52	8.80
	syn	502	506		0.10	0.10	313	302		16.40	17.50
CH_3CH_2SNO	*anti*1	571	573	552	0.10	0.10	323	317		8.14	8.80
	*anti*2	559	551		0.00	0.00	323	314		8.18	9.80
	syn	524	520	520	0.10	0.10	305	301		15.08	16.80
$(CH_3)_2CHSNO$	*anti*	546	549	556	0.00	0.00	325	315		8.72	10.40
	syn	528	520	524	0.10	0.10	304	303		16.37	18.30
$(CH_3)_3CSNO$	*anti*	579	584	596	0.10	0.10	319	310		10.70	10.00
	syn	551	564	550	0.20	0.20	297	291		24.20	13.60
CF_3SNO	*anti*	554	542		0.10	0.00	370	327		1.26	1.50
	syn	557	528		0.00	0.10	398	326		1.88	2.90
$(CH_3)_2N(CH_2)SNO$	*anti*	559	560		0.00	0.00	322	308		9.49	8.30
	syn	533	554		0.10	0.10	312	300		17.70	12.50
$(C_6H_5)_3CSNO$	*anti*		594	600		0.4		352	340		6.3
	syn		572			0.3		334			5.7
CH_2CHSNO	*anti*	541	543		0.41	0.10	358	367		30.10	33.90
	*syn*1	557	524		0.58	0.50	436	354		52.00	60.20
	*syn*2	515	522		0.24	0.20	349	351		4.30	4.90

[a]The absorption wavelength (λ) is given in nm, while the oscillator strength (f) is $\times 10^{-3}$. [b]$(C_6H_5)_3CSNO$ data can be found in ref 20a; CH_3CH_2SNO, $(CH_3)_2CHSNO$, and $(CH_3)_3CSNO$ data can be found in ref 22b.

anti CF_3SNO, at the MP2 level. However, the B3P86 functional predicts higher wavelengths for the *anti* conformer, being the S−N distance shortened with respect to MP2 optimized structures (1.90 Å for both *syn* and *anti* CF_3SNO).

Regarding CH_2CHSNO, the torsion around the C−S bond defines two possible *syn* conformers: if the vinyl moiety is coplanar with the CSNO moiety (*anti* and *syn*1, see Figure 1 and Supporting Information), the chromophore size increases, otherwise the effective conjugation is partially broken (a torsion of 60.6° around the C−S bond characterizes *syn*2), resulting in a lowering of absorption wavelengths and oscillator strengths for *syn*2 CH_2CHSNO.

Moreover, the energy required for vertical excitation to the $^1(\pi,\pi^*)$ state can be rationalized on the basis of the RSNO type: looking at B3P86 values, the spectroscopically more relevant *syn* conformers give similar excitation energies (300−303 nm) for primary and secondary derived RSNOs, while tertiary RSNOs show different behaviors: when compared to primary and secondary RSNOs, the $S_0 \rightarrow S_2$ vertical energy is blue-shifted for $(CH_3)_3CSNO$ (291 nm) and red-shifted for $(C_6H_5)_3CSNO$ (334 nm) and CF_3SNO (326 nm). Likewise, a lower energy is computed for this transition for the aryl derivatives (324−366 nm) and for CH_2CHSNO (354 nm). Analogously, a bathochromic shift in the $S_0 \rightarrow S_1$ vertical energy is computed for primary, secondary (520−554 nm), tertiary (528−572 nm), vinyl (524 nm), and aryl derivatives (538−594 nm) as compared to CH_3SNO (506 nm).

When comparing the absorption spectra of CH_2CHSNO with all aryl derivatives, it can be seen that the $^1(n,\pi^*)$ transition is lowered in energy when including an aryl substituent, while the $^1(\pi,\pi^*)$ transition shows a more complex behavior: it has higher energy requirements for C_6H_5SNO, 4-$H_3CC_6H_4SNO$, 4-ClC_6H_4SNO, 4-$CH_3OC_6H_4SNO$, 4-$H_2NC_6H_4hSNO$, 4-NCC_6H_4NSNO, 4-HOC_6H_4SNO, 4-$F_3CC_6H_4SNO$, and 4-$H_3CN(H)C_6H_4SNO$, while 4-$O_2NC_6H_4SNO$ and 4-$ClC(O)C_6H_4SNO$ are characterized by a lowering in energy requirements. 4-$HC(O)C_6H_4SNO$ almost does not show any shift in energy. This seems to be in contrast with the general idea that an increase of the conjugation length within the chromophore is always related to energy stabilization of $^1(\pi,\pi^*)$ states. This behavior can be related to the dihedral angle formed between the vinyl (or aryl) moiety and the SNO moiety: while the vinyl moiety is coplanar to the SNO moiety for *anti* and *syn*1 CH_2CHSNO, all *syn* and *anti* aryl derivatives are not planar and do form a dihedral angle ranging from 49 to 89° with the SNO moiety. Therefore, an increase in conjugation length stabilizes $^1(\pi,\pi^*)$ states only if the overall conjugated moiety is planar, while an eventual torsion between vinyl (or aryl) and SNO moieties lowers π-electron delocalization, usually resulting in destabilization of $^1(\pi,\pi^*)$ states (Table 4).

More in general, we observe that, in all aryl derivatives, the *anti* conformer requires a lower $^1(\pi,\pi^*)$ excitation energy than the *syn* conformer, showing that the *anti* conformer has a more effective conjugation related to a more planar structure (i.e., a lower C−C−S−N dihedral angle).

Substituent Effects. Classically, the substituent effects have been explained as a function of Hammett, Taft, or other empirical linear free energy relationships.[34] Among them, the Hammett relationship[34c] has been permanently utilized in the interpretation of reaction mechanisms and in the rationalization of the influence of substituents on a wide variety of reactions. Hammett constants reflect the electronic properties in the ground state of molecules, but recent studies support that correlations also hold in the excited state.[35] In this regard, it has been shown that Hammett analysis can also provide valuable information about electronic structure, molecular geometry, reactivity, electronic transition, and other properties of excited states of molecules.[36] Successful correlations of excitation energies with Hammett constants have been obtained for a wide variety of substrates[36l−r] in spite of the results of an old study showing the inapplicability of Hammett σ constants in

dx.doi.org/10.1021/jp304707n | J. Phys. Chem. A 2012, 116, 7039−7049

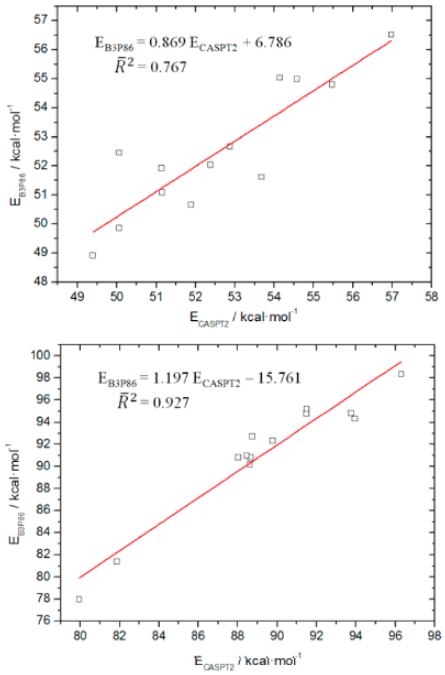

Figure 5. Correlation graphs including CH_3SNO, CH_3CH_2SNO, $(CH_3)_2CHSNO$, $(CH_3)_3CSNO$, $(CH_3)_2N(CH_2)SNO$, and *anti* and *syn*2 CH_2CHSNO: $^1(n,\pi^*)$ transition (up) and $^1(\pi,\pi^*)$ transition (down).

correlations of excitation energies.[37] Three different kind of σ scales have been applied to study the substituent effect on UV–vis spectra: (1) polar substituent parameters[34] such as Hammett constant σ_p (including resonance polar σ^+ or σ^-); (2) spin-delocalization substituent constants $(\sigma^{\cdot})$[38] since the excited state species possess radical character; and (3) excited-state constants (σ_{ex} σ^*, $\sigma^{h\nu}$, $\sigma^{h\psi}$, and σ_{CC}^{ex})[39,36m] derived from excited state data. Furthermore, dual parameter equations using two sets of σ scales have been employed in several studies giving improved correlations.[36r,38b,39c] However, a wide applicable scale has not been emerged, indicating that different scales can be appropriate for the description of different substrates, being necessary for a careful calibration depending on the case.

In order to evaluate how the substituent affects the electronic absorption in *S*-nitrosothiol species, several *para*-phenyl nitrosothiol derivatives, R = NO_2 (σ_p = 0.78), CN (σ_p = 0.66), COCl (σ_p = 0.61), CF_3 (σ_p = 0.54), CHO (σ_p = 0.42), Cl (σ_p = 0.23), CH_3 (σ_p = −0.17), OCH_3 (σ_p = −0.27), OH (σ_p = −0.37), NH_2 (σ_p = −0.66), and $NHCH_3$ (σ_p = −0.70), were chosen for a systematic variation in electron-withdrawing and -donating character as described by the Hammett parameter σ_p.[34a] Table 4 collects the shift in the calculated excitation energies between the proposed aryl derivatives and C_6H_5SNO. As it can be seen in Table 4, both $^1(n,\pi^*)$ and $^1(\pi,\pi^*)$ transitions exhibit significant substituent dependence reflecting the big sensitivity of the substrate to the electronic effects of the substituents.

Table 3. Absorption Spectra of All Phenyl Substituted RSNOs at B3P86/6-311+G(2df) Level of Theory[a]

		$^1(n,\pi^*)$ transition		$^1(\pi,\pi^*)$ transition	
molecule	conformation	λ_{B3P86}	f_{B3P86}	λ_{B3P86}	f_{B3P86}
C_6H_5SNO	*anti*	571	0.5	351	4.3
	syn	549	0.2	329	14.6
4-$H_3CC_6H_4SNO$	*anti*	579	0.5	349	2.9
	syn	555	0.2	328	18.6
4-ClC_6H_4SNO	*anti*	574	0.7	357	3.6
	syn	553	0.2	332	23.2
4-$CH_3OC_6H_4SNO$	*anti*	597	0.3	348	1.9
	syn	568, 334	0.2, 0.5	325	21.7
4-$O_2NC_6H_4SNO$	*anti*	560	1.2	369	1.4
	syn	538	0.6	366	79.2
4-$H_2NC_6H_4SNO$	*anti*	614, 366	0.2, 0.8	327	18.7
	syn	584, 360	0.2, 0.1	324	29.6
4-NCC_6H_4SNO	*anti*	562	1.1	364	3.8
	syn	542	0.6	347	30.3
4-$ClC(O)C_6H_4SNO$	*anti*	560	1.3	368	2.1
	syn	539	1.2	359	47.7
4-$HC(O)C_6H_4SNO$	*anti*	562	1.2	366	2.4
	syn	542, 356	1.0, 0.1	354	39.2
4-HOC_6H_4SNO	*anti*	596	0.3	343	2.2
	syn	567	0.2	328	5.9
4-$F_3CC_6H_4SNO$	*anti*	563	0.6	356	3.7
	syn	542	0.3	338	18.1
4-$H_3CN(H)C_6H_4SNO$	*anti*	625, 384	0.1, 0.3	328	26.5
	syn	594, 379	0.1, 0.1	324	42.1

[a]The absorption wavelenght (λ) is given in nm. The oscillator strength (f) is $\times 10^{-3}$. Two $^1(n,\pi^*)$ transitions are found for 4-$H_2NC_6H_4SNO$, 4-$H_3CN(H)C_6H_4SNO$, *syn* 4-$CH_3OC_6H_4SNO$, and *syn* 4-$HC(O)C_6H_4SNO$ corresponding to $S_0 \rightarrow S_1$ and $S_0 \rightarrow S_2$ vertical excitations ($S_0 \rightarrow S_3$ is a $^1(\pi,\pi^*)$ transition). For the rest of the molecules, $S_0 \rightarrow S_1$ is a $^1(n,\pi^*)$ transition, and $S_0 \rightarrow S_2$ is a $^1(\pi,\pi^*)$ transition.

Aryl derivatives bearing electron withdrawing substituents in *para* position are characterized by a blue-shift of the absorption maximum for the $^1(n,\pi^*)$ transition and a red-shift for the $^1(\pi,\pi^*)$ transition related to the parent unsubstituted compound C_6H_5SNO. However, the addition of electron donating groups decreases the excitation energy for the $^1(n,\pi^*)$ transition and increase it for the $^1(\pi,\pi^*)$ transition. Figure 6 shows a simple correlation graph between the wavelengths of both transitions for the *syn* and *anti* conformers of aryl *S*-nitrosothiols and the corresponding Hammett constants of the substituents. As it can be seen, there is a clear tendency although the correlation is not quantitative. Therefore, other factors such as the dihedral angle between the aryl and the SNO moieties and the S–N bond length may also play a role in determining the vertical excitation energies for this kind of species. In order to discern how such factors affect the spectroscopical properties of *S*-nitrosothiols, further studies are being conducted.[40] In addition, it has been proved that the correlation coefficients for the parameters in the excited states

dx.doi.org/10.1021/jp304707n | J. Phys. Chem. A 2012, 116, 7039–7049

Table 4. Shift in the Absorption Maxima between Aryl R-C_6H_4SNO and C_6H_5SNO, at B3P86/6-311+G(2df) Level of Theory[a]

		$^1(n,\pi^*)$ transition (S_1)		$^1(\pi,\pi^*)$ transition			
molecule	conformation	$\Delta\lambda_{B3P86}$ (nm)	ΔE_{B3P86} (kcal·mol^{-1})	$\Delta\lambda_{B3P86}$ (nm)	ΔE_{B3P86} (kcal·mol^{-1})	S−N distance (Å)	C−C−S−N dihedral (deg)
4-$O_2NC_6H_4SNO$	*anti*	−11	0.99	18	−3.98	1.86	50
4-NCC_6H_4SNO	*anti*	−9	0.80	13	−2.91	1.86	52
4-$ClC(O)C_6H_4SNO$	*anti*	−11	0.99	17	−3.77	1.86	49
4-$F_3CC_6H_4SNO$	*anti*	−8	0.71	5	−1.15	1.86	54
4-$HC(O)C_6H_4SNO$	*anti*	−9	0.80	15	−3.34	1.86	51
4-ClC_6H_4SNO	*anti*	3	−0.26	6	−1.37	1.85	62
C_6H_5SNO	*anti*	0	0	0	0	1.84	59
4-$H_3CC_6H_4SNO$	*anti*	8	−0.69	−2	0.46	1.84	66
4-$CH_3OC_6H_4SNO$	*anti*	26	−2.18	−3	0.70	1.84	78
4-HOC_6H_4SNO	*anti*	25	−2.10	−8	1.90	1.84	79
4-$H_2NC_6H_4SNO$	*anti*	43	−3.50	−24	5.98	1.84	84
4-$H_3CN(H)C_6H_4SNO$	*anti*	54	−4.32	−23	5.71	1.87	83
4-$O_2NC_6H_4SNO$	*syn*	−11	1.06	37	−8.78	1.88	78
4-NCC_6H_4SNO	*syn*	−7	0.67	18	−4.50	1.87	78
4-$ClC(O)C_6H_4SNO$	*syn*	−10	0.97	30	−7.26	1.88	73
4-$F_3CC_6H_4SNO$	*syn*	−7	0.67	9	−2.31	1.90	69
4-$HC(O)C_6H_4SNO$	*syn*	−7	0.67	25	−6.13	1.87	74
4-ClC_6H_4SNO	*syn*	4	−0.38	3	−0.78	1.86	88
C_6H_5SNO	*syn*	0	0	0	0	1.85	89
4-$H_3CC_6H_4SNO$	*syn*	6	−0.56	−1	0.27	1.85	89
4-$CH_3OC_6H_4SNO$	*syn*	19	−1.74	−4	1.07	1.85	88
4-HOC_6H_4SNO	*syn*	18	−1.65	−1	0.27	1.85	87
4-$H_2NC_6H_4SNO$	*syn*	35	−3.12	−5	1.35	1.85	88
4-$H_3CN(H)C_6H_4SNO$	*syn*	45	−3.95	−5	1.35	1.84	89

[a] $\Delta\lambda_{B3P86} = \lambda_{B3P86}(R\text{-}C_6H_4SNO) - \lambda_{B3P86}(C_6H_5SNO)$; $\Delta E_{B3P86} = E_{B3P86}(R\text{-}C_6H_4SNO) - E_{B3P86}(C_6H_5SNO)$. The S−N distance and C−C−S−N dihedral angle are also included.

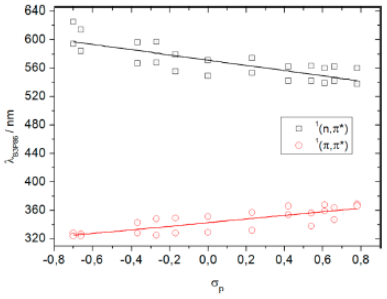

Figure 6. Correlation graph between the wavelengths of $^1(n,\pi^*)$ and $^1(\pi,\pi^*)$ transitions of aryl RSNOs and its Hammett constants.

are always lower than those for the ground state.[35] Likewise, errors in the DFT calculated excitation energies could be also responsible for the scatter of the data.

Figure 6 shows clearly that the absorption energy required to initiate photocleavage can be modulated by varying the substituent R in RSNOs. Moreover, a treatment more related to the classical Hammett relationship independently for the *syn* and *anti* conformers of substituted aryl RSNOs is given in Figure 7. Acceptable correlation of the vertical excitation energy of both $^1(n,\pi^*)$ and $^1(\pi,\pi^*)$ transitions for R-C_6H_4SNOs referred to C_6H_5SNO in energy units, and the corresponding σ_p Hammett constants for the corresponding R substituent are obtained. The excitation energy difference ($E_{R\text{-}C6H4SNO}$ − $E_{C6H5SNO}$) is expressed in RT units, where R is the gas constant and T is the room temperature (298.15 K). The slope of each linear regression (ρ) indicates the sensitivity of the vertical excitation energy to the substituent (i.e., the modulation of the vertical excitation energy on the basis of substituent electronic effects). It can be noted that the vertical excitation energy corresponding to the $^1(\pi,\pi^*)$ transition is almost twice as sensitive as the $^1(n,\pi^*)$ transition, therefore suggesting a more efficient modulation of the photocleavage mechanism when irradiating to the lowest-energy optically bright state, although a spectroscopical modulation is also possible for the lowest-energy optically dark state. Moreover, it can be noted the different sign of ρ (positive for $^1(n,\pi^*)$ transitions and negative for $^1(\pi,\pi^*)$ transitions), indicating two distinguished behaviors: electron-withdrawing substituents increase $^1(\pi,\pi^*)$ maximum wavelengths and decrease $^1(n,\pi^*)$ maximum wavelengths, while electron-donating substituents induce the opposite effect (see Figure 6). When comparing *syn* and *anti* ρ values of the same transition, $^1(n,\pi^*)$ or $^1(\pi,\pi^*)$, we can conclude that both conformers provide essentially the same sensitivity to the substituent.

Attempts to establish a correlation between the excitation energy and other σ scales such as σ_{CC}^{ex},[36m] $\sigma_{ij}^{\cdot}$,[38c] $\sigma_C^{\cdot}$,[38e] and σ_A[38a] gave worse correlations than those presented in Figure 7.

■ SUMMARY AND CONCLUSIONS

Computational calculations using multiconfigurational (CASSCF and CASPT2) and TD-DFT methods were employed to study the photocleavage mechanism and electronic absorption spectra of a series of *S*-nitrosothiols, a

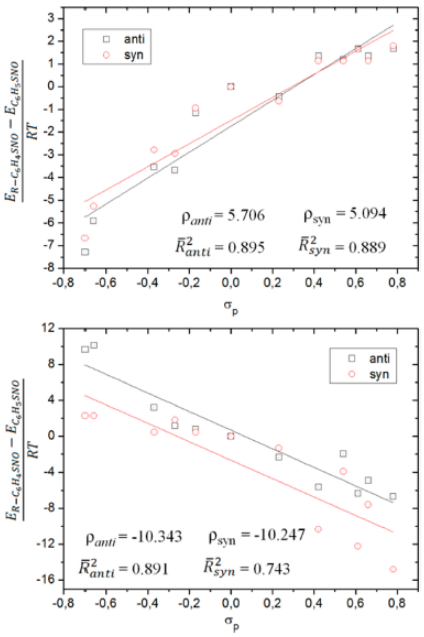

Figure 7. Graph showing the relationship between the vertical excitation energy of $^1(n,\pi^*)$ (up) and $^1(\pi,\pi^*)$ (down) transitions of R-C_6H_4SNOs (as referred to C_6H_5SNO) and its Hammett constants. All linear regression parameters are given in the Supporting Information.

family of compounds implicated in a wide variety of physiological processes.

The photocleavage mechanism of the model compound CH_3SNO to release $CH_3S\cdot$ and $\cdot NO$ results in a barrierless process when irradiating in the visible region (S_1), in the near UV region (S_2), and when using a photosensitizer to populate a triplet state (T_1). Therefore, RSNO photocleavage is expected to be an ultrafast process without involving any side reaction. Modulation of NO release by RSNO photoactivation is possible by tuning the absorption energy required to initiate photocleavage. The lowest-energy optically dark vertical excitation, $^1(n,\pi^*)$, corresponds to the $S_0 \rightarrow S_1$ transition, while the lowest-energy optically bright vertical excitation, $^1(\pi,\pi^*)$, corresponds to the $S_0 \rightarrow S_2$ or $S_0 \rightarrow S_3$ transition. Both types of transition exhibit significant substituent dependence being the calculated electronic transitions in the 505−625 nm (^{1}(n,π^*)) and 290−370 nm ($^1(\pi,\pi^*)$) ranges for the RSNOs studied. The wavelengths of both transitions correlate with the corresponding σ_p Hammett constants of the substituents for a series of aryl derivatives.

These results offer basic understanding of the photophysical and photochemical processes, and provide a predictive tool for designing *S*-nitrosothiol derivatives with desired wavelength sensitivity absorption spectra. Particularly, it has been proved that the addition of strong electron donating substituents shift the electronic $^1(n,\pi^*)$ transition to wavelengths around 600 nm, wavelengths at which radiation shows high penetration depth in skin tissues. In principle, this study could help in the design of chemical compounds that can be used in photo-therapy in the treatment of illnesses associated with a deficiency of nitric oxide.

■ ASSOCIATED CONTENT

Supporting Information

CASPT2 method and CASPT2//CASSCF methodology. Ground-state structural parameters. Calibration of DFT methods. Photochemistry of CH_3SNO. Excited-state transitions. Cartesian coordinates. This material is available free of charge via the Internet at http://pubs.acs.org.

■ AUTHOR INFORMATION

Corresponding Author

*Tel: +34 91 885 2512. Fax: +34 918854763. E-mail: manuel.temprado@uah.es (M.T.); luisma.frutos@uah.es (L.M.F.).

Notes

The authors declare no competing financial interest.

■ ACKNOWLEDGMENTS

This research was supported by the Spanish MICINN grant CTQ2009-07120 and by the CAM-UAH grant CCG10-UAH/PPQ-5927. M.M. and M.A.F.-G. are grateful to the UAH (Universidad de Alcalá) for a doctoral fellowship. A.L.D. acknowledges the UAH for a research grant. L.M.F. and M.T. acknowledge receipt of a "Ramon y Cajal" (L.M.F.) and a "Juan de la Cierva" (M.T.) contract from MICINN.

■ REFERENCES

(1) (a) Ignarro, L. J.; Byrns, R. E.; Buga, G. M.; Wood, K. S. *Circ. Res.* **1987**, *61*, 866. (b) Palmer, R. M.; Ferrige, A. G.; Moncada, S. *Nature* **1987**, *327*, 524.

(2) Ignarro, L. J. *Nitric Oxide* **1996**, 111.

(3) (a) Ignarro, L. J.; Murad, F., Eds. *Nitric Oxide: Biochemistry, Molecular Biology, and Therapeutic Implications*; Academic Press: New York, 1995; Vol. *34*, p 530. (b) Scatena, R.; Bottoni, P.; Pontoglio, A.; Giardina, B. *Curr. Med. Chem.* **2010**, *17*, 61. (c) Tennyson, A. G.; Lippard, S. J. *Chem. Biol.* **2011**, *18*, 1211.

(4) (a) Ignarro, L. J. *Pharmacol. Res.* **1989**, *6*, 651. (b) Moncada, S.; Palmer, R. M. J.; Gryglewski, R. J. *Proc. Natl. Acad. Sci. U.S.A.* **1986**, *83*, 9164. (c) Stamler, J. S.; Jia, L.; Eu, J. P.; McMahon, T. J.; Demchenko, I. T.; Bonaventura, J.; Gernert, K.; Piantadosi, C. A. *Science* **1997**, *276*, 2034.

(5) Hibbs, J. B., Jr. *Res. Immunol.* **1991**, *142*, 565.

(6) Garthwaite, J. *Trends Neurosci.* **1991**, *14*, 60.

(7) Mowbray, M.; McLintock, S.; Weerakoon, R.; Lomatschinsky, N.; Jones, S.; Rossi, A. G.; Weller, R. B. *J. Invest. Dermatol.* **2009**, *129*, 834.

(8) (a) Pfeiffer, S.; Mayer, B.; Hemmens, B. *Angew. Chem., Int. Ed.* **1999**, *38*, 1715. (b) Rosen, G. M.; Tsai, P.; Pou, S. *Chem. Rev.* **2002**, *102*, 1191.

(9) (a) Ignarro, L. J.; Napoli, C.; Loscalzo, J. *Circ. Res.* **2002**, *90*, 21. (b) Wang, P. G.; Xian, M.; Tang, X.; Wu, X.; Wen, Z.; Cai, T.; Jaczuk, A. J. *Chem. Rev.* **2002**, *102*, 1091.

(10) (a) Huang, J.; Kim-Shapiro, D. B.; King, S. B. *J. Med. Chem.* **2004**, *47*, 3495. (b) Lazzarato, L.; Rolando, B.; Lolli, M. L.; Tron, G. C.; Frutero, R.; Gasco, A.; Deleide, G.; Guenther, H. L. *J. Med. Chem.* **2005**, *48*, 1322. (c) Heikal, L.; Martin, G. P.; Dailey, L. A. *Nitric Oxide* **2009**, *20*, 157.

(11) Stamler, J. S.; Jaraki, O.; Osborne, J.; Simon, D. I.; Keaney, J.; Vita, J.; Singel, D.; Valeri, C. R.; Loscalzo, J. *Proc. Natl. Acad. Sci. U.S.A.* **1992**, *89*, 7674.

(12) Jia, L.; Bonaventura, C.; Bonaventura, J.; Stamler, J. S. *Nature* **1996**, *380*, 221.

(13) (a) Gaston, B.; Reilly, J.; Drazen, J. M.; Fackler, J.; Ramdev, P.; Arnelle, D.; Mullins, M. E.; Sugarbaker, D. J.; Chee, C.; Singel, D. J.; et al. *Proc. Natl. Acad. Sci. U.S.A.* **1993**, *90*, 10957. (b) Myers, P. R.; Minor, R. L., Jr.; Guerra, R., Jr.; Bates, J. N.; Harrison, D. G. *Nature* **1990**, *345*, 161.
(14) (a) Keszler, A.; Zhang, Y.; Hogg, N. *Free Radical Biol. Med.* **2010**, *48*, 55. (b) Basu, S.; Keszler, A.; Azarova, N. A.; Nwanze, N.; Perlegas, A.; Shiva, S.; Broniowska, K. A.; Hogg, N.; Kim-Shapiro, D. B. *Free Radical Biol. Med.* **2010**, *48*, 255. (c) Vasudevan, D.; Hickok, J. R.; Thomas, D. D. *Free Radical Biol. Med.* **2011**, *51*, S151.
(15) (a) Lipton, S. A.; Choi, Y. B.; Pan, Z. H.; Lei, S. Z.; Chen, H. S.; Sucher, N. J.; Loscalzo, J.; Singel, D. J.; Stamler, J. S. *Nature* **1993**, *364*, 626. (b) Foster, M. W.; Forrester, M. T.; Stamler, J. S. *Proc. Natl. Acad. Sci. U.S.A.* **2009**, *106*, 18948. (c) Lima, B.; Forrester, M. T.; Hess, D. T.; Stamler, J. S. *Circ. Res.* **2010**, *106*, 633. (d) Yun, B. W.; Feechan, A.; Yin, M.; Saidi, N. B. B.; Le Bihan, T.; Yu, M.; Moore, J. W.; Kang, J. G.; Kwon, E.; Spoel, S. H.; et al. *Nature* **2011**, *478*, 264.
(16) (a) Lefer, A. M.; Sedar, A. W. *Pharmacol. Res.* **1991**, *23*, 1. (b) Giles, G. I.; Billaud, E.; Giles, N. M. *Free Radical Biol. Med.* **2008**, *45* (Suppl. 1), S82. (c) Kevil, C. G.; Patel, R. P. *Curr. Opin. Invest. Drugs* **2010**, *11*, 1127. (d) Serafim, R. A. M.; Primi, M. C.; Trossini, G. H. G.; Ferreira, E. I. *Curr. Med. Chem.* **2012**, *19*, 386.
(17) Hornyak, I.; Pankotai, E.; Kiss, L.; Lacza, Z. *Curr. Pharm. Biotechnol.* **2011**, *12*, 1368.
(18) Wood, P. D.; Mutus, B.; Redmond, R. W. *Photochem. Photobiol.* **1996**, *64*, 518.
(19) (a) Lü, J. M.; Wittbrodt, J. M.; Wang, K.; Wen, Z.; Schlegel, H. B.; Wang, P. G.; Cheng, J. P. *J. Am. Chem. Soc.* **2001**, *123*, 2903. (b) Bartberger, M. D.; Mannion, J. D.; Powell, S. C.; Stamler, J. S.; Houk, K. N.; Toone, E. J. *J. Am. Chem. Soc.* **2001**, *123*, 8868. (c) de Oliveira, M. G.; Shishido, S. M.; Seabra, A. B.; Morgon, N. H. *J. Phys. Chem. A* **2002**, *106*, 8963. (d) Grossi, L.; Montevecchi, P. C. *Chem.—Eur. J.* **2002**, *8*, 380.
(20) (a) Arulsamy, N.; Bohle, D. S.; Butt, J. A.; Irvine, G. J.; Jordan, P. A.; Sagan, E. *J. Am. Chem. Soc.* **1999**, *121*, 7115. (b) Lin, C. E.; Richardson, S. K.; Wang, W.; Wang, T.; Garvey, D. S. *Tetrahedron* **2006**, *62*, 8410. (c) Spivey, A. C.; Colley, J.; Sprigens, L.; Hancock, S. M.; Cameron, D. S.; Chigboh, K. I.; Veitch, G.; Frampton, C. S.; Adams, H. *Org. Biomol. Chem.* **2005**, *3*, 1942.
(21) (a) Goto, K.; Hino, Y.; Takahashi, Y.; Kawashima, T.; Yamamoto, G.; Takagi, N.; Nagase, S. *Chem. Lett.* **2001**, 1204. (b) Itoh, M.; Takenaka, K.; Okazaki, R.; Takeda, N.; Tokitoh, N. *Chem. Lett.* **2001**, 1206.
(22) (a) Bainbrigge, N.; Butler, A. R.; Goerbitz, C. H. *J. Chem. Soc., Perkin Trans. 2* **1997**, 351. (b) Bartberger, M. D.; Houk, K. N.; Powell, S. C.; Mannion, J. D.; Lo, K. Y.; Stamler, J. S.; Toone, E. J. *J. Am. Chem. Soc.* **2000**, *122*, 5889. (c) Zhao, Y.-L.; McCarren, P. R.; Houk, K. N.; Choi, B. Y.; Toone, E. J. *J. Am. Chem. Soc.* **2005**, *127*, 10917. (d) Timerghazin, Q. K.; Peslherbe, G. H.; English, A. M. *Phys. Chem. Chem. Phys.* **2008**, *10*, 1532. (e) Timerghazin, Q. K.; Peslherbe, G. H.; English, A. M. *Org. Lett.* **2007**, *9*, 3049. (f) Lai, C. H.; Chou, P. T. *J. Mol. Model.* **2008**, *14*, 1. (g) Ruangpornvisuti, V. *Int. J. Quantum Chem.* **2009**, *109*, 275. (h) Bharatam, P. V.; Amita; Senthilkumar, P. *Tetrahedron* **2004**, *60*, 4801. (i) Bharatam, P. V.; Amita. *Tetrahedron Lett.* **2002**, *43*, 8289. (j) Baciu, C.; Gauld, J. W. *J. Phys. Chem. A* **2003**, *107*, 9946. (k) Li, X.-H.; Zhang, R.-Z.; Yang, X.-D. *J. Mol. Struct.* **2007**, *817*, 43.
(23) Finley, J.; Malmqvist, P.-Å.; Roos, B. O.; Serrano-Andres, J. L. *Chem. Phys. Lett.* **1998**, *288*, 299.
(24) The derivative coupling (DC) vector measures the distortion of the system providing the maximum coupling between the electronic states involved in the crossing. The gradient difference (GD) vector measures the distortion of the system leading to the largest variation of the energy difference between the two electronic states involved in the crossing. DC and GD vectors (i.e., the nonadiabatic coupling vectors) define the two-dimensional subspace where the energy degeneracy between two crossing states is broken.
(25) Becke, A. D. *J. Chem. Phys.* **1993**, *98*, 1372.
(26) Lee, C.; Yang, W.; Parr, R. G. *Phys. Rev. B* **1988**, *37*, 785.
(27) Perdew, J. P. *Phys. Rev. B* **1986**, *33*, 8822.
(28) Frisch, M. J.; Trucks, G. W.; Schlegel, H. B.; Scuseria, G. E.; Robb, M. A.; Cheeseman, J. R.; Scalmani, G.; Barone, V.; Mennucci, B.; Petersson, G. A.; Nakatsuji, H.; Caricato, M.; Li, X.; Hratchian, H. P.; Izmaylov, A. F.; Bloino, J.; Zheng, G.; Sonnenberg, J. L.; Hada, M.; Ehara, M.; Toyota, K.; Fukuda, R.; Hasegawa, J.; Ishida, M.; Nakajima, T.; Honda, Y.; Kitao, O.; Nakai, H.; Vreven, T.; Montgomery, J. A., Jr.; Peralta, J. E.; Ogliaro, F.; Bearpark, M.; Heyd, J. J.; Brothers, E.; Kudin, K. N.; Staroverov, V. N.; Kobayashi, R.; Normand, J.; Raghavachari, K.; Rendell, A.; Burant, J. C.; Iyengar, S. S.; Tomasi, J.; Cossi, M.; Rega, N.; Millam, J. M.; Klene, M.; Knox, J. E.; Cross, J. B.; Bakken, V.; Adamo, C.; Jaramillo, J.; Gomperts, R.; Stratmann, R. E.; Yazyev, O.; Austin, A. J.; Cammi, R.; Pomelli, C.; Ochterski, J. W.; Martin, R. L.; Morokuma, K.; Zakrzewski, V. G.; Voth, G. A.; Salvador, P.; Dannenberg, J. J.; Dapprich, S.; Daniels, A. D.; Farkas, O.; Foresman, J. B.; Ortiz, J. V.; Cioslowski, J.; Fox, D. J. *Gaussian 09*, revision B.01; Gaussian, Inc.: Wallingford, CT, 2009.
(29) Aquilante, F.; De Vico, L.; Ferré, N.; Ghigo, G.; Malmqvist, P.-Å.; Neogrády, P.; Pedersen, T. B.; Pitoňák, M.; Reiher, M.; Roos, B. O.; et al. *J. Comput. Chem.* **2010**, *31*, 224.
(30) Marazzi, M.; Lopez-Delgado, A.; Castaño, O.; Frutos, L. M.; Temprado, M. To be submitted for publication.
(31) (a) Sexton, D. J.; Muruganandam, A.; Mckenny, D. J.; Mutus, B. *Photochem. Photobiol.* **1994**, *59*, 463. (b) Singh, R. J.; Hogg, N.; Joseph, J.; Kalyanaraman, B. *J. Biol. Chem.* **1996**, *271*, 18596. (c) Singh, S. P.; Wishnok, J. S.; Keshive, M.; Deen, W. M.; Tannenbaum, S. R. *Proc. Natl. Acad. Sci. U.S.A.* **1996**, *93*, 14428.
(32) Marazzi, M.; Sancho, U.; Castaño, O.; Frutos, L. M. *Phys. Chem. Chem. Phys.* **2011**, *13*, 7805.
(33) Singh, R. J.; Hogg, N.; Joseph, J.; Kalyanaraman, B. *FEBS Lett.* **1995**, *360*, 47.
(34) (a) Hansch, C.; Leo, A.; Taft, R. W. *Chem. Rev.* **1991**, *91*, 165. (b) Charton, M. *Prog. Phys. Org. Chem.* **1981**, *13*, 119. (c) Hammett, L. P. *J. Am. Chem. Soc.* **1937**, *59*, 96.
(35) Sadlej-Sonowska, N.; Kijak, M. *Struct. Chem.* **2012**, *23*, 359.
(36) See, for example, (a) Kassaee, M. Z.; Nassari, M. A. *J. Photochem. Photobiol., A* **2000**, *136*, 41. (b) Pincock, A. L.; Pincock, J. A.; Stefanova. *J. Am. Chem. Soc.* **2002**, *124*, 9768. (c) Resendiz, M. J. E.; Garcia-Garibay, M. A. *Org. Lett.* **2005**, *7*, 371. (d) Sakamoto, M.; Cai, X.; Hara, M.; Fujitsuka, M.; Majima, T. *J. Phys. Chem. A* **2005**, *109*, 4657. (e) Liddle, B. J.; Silva, R. M.; Morin, T. J.; Macedo, F. P.; Shukla, R.; Lindeman, S. V.; Gardinier, J. R. *J. Org. Chem.* **2007**, *72*, 5637. (f) van Dorp, J. W. J.; Lodder, G. *J. Org. Chem.* **2008**, *73*, 5416. (g) Samori, S.; Tojo, S.; Fujitsuka, M.; Spitler, E. L.; Haley, M. M.; Majima, T. *J. Org. Chem.* **2008**, *73*, 3551. (h) Cordes, T.; Schadendorf, T.; Priewisch, B.; Rück-Braun, K.; Zinth, W. *J. Phys. Chem. A* **2008**, *112*, 581. (i) Kitamura, C.; Tsukuda, H.; Yoneda, A.; Kawase, T.; Kobayashi, T.; Naito, H. *Eur. J. Org. Chem.* **2010**, 3033. (j) Imoto, M.; Ikeda, H.; Ohashi, M.; Takeda, M.; Tamaki, A.; Taniguchi, H.; Mizuno, K. *Tetrahedron Lett.* **2010**, *51*, 5877. (k) Haley, J. E.; Krein, D. M.; Monahan, J. L.; Burke, A. R.; McLean, D. G.; Slagle, J. E.; Fratini, A.; Cooper, T. M. *J. Phys. Chem. A* **2011**, *115*, 265. (l) Mijin, D. Z.; Uščumlić, G. S.; Perišić-Janjić, N. U.; Valentić, N. V. *Chem. Phys. Lett.* **2006**, *418*, 223. (m) Cao, C.; Chen, G.; Yin, Z. *J. Phys. Org. Chem.* **2008**, *21*, 808. (n) Papadakis, R.; Tsolomitis, A. *J. Phys. Org. Chem.* **2009**, *22*, 515. (o) Jankowiak, A.; Kaszynski, P. *J. Org. Chem.* **2009**, *74*, 7441. (p) Chen, G.; Cao, C. *J. Phys. Org. Chem.* **2010**, *23*, 776. (q) Matsui, Y.; Namai, H.; Akimoto, I.; Kan'no, K.-I.; Mizuno, K. *Tetrahedron* **2011**, *67*, 7431. (r) Chen, G.; Cao, C.; Lu, B.; Sheng, B. *J. Phys. Org. Chem.* **2012**, *25*, 327.
(37) Wagner, P. J.; Thomas, M. J.; Harris, E. *J. Am. Chem. Soc.* **1976**, *98*, 7675.
(38) (a) Dust, J. M.; Arnold, D. R. *J. Am. Chem. Soc.* **1983**, *105*, 1221. (b) Jiang, X. K.; Ji, G. Z.; Wang, D. Z.; Xie, J. R. *J. Phys. Org. Chem.* **1995**, *8*, 781. (c) Jiang, X. K. *Acc. Chem. Res.* **1997**, *30*, 283. (d) Wen, Z.; Li, Z.; Shang, Z.; Cheng, J.-P. *J. Org. Chem.* **2001**, *66*, 1466. (e) Creary, X. *Acc. Chem. Res.* **2006**, *39*, 761.
(39) (a) Baldry, P. J. *J. Chem. Soc., Perkin Trans. 2* **1979**, 951. (b) Shim, S. C.; Park, J. W.; Ham, H.-S.; Chung, J.-S. *Bull. Korean*

Chem. Soc. **1983**, *4*, 45. (c) McEwen, J.; Yates, K. *J. Phys. Org. Chem.* **1991**, *4*, 193. (d) Fleming, S. A.; Jensen, A. W. *J. Org. Chem.* **1996**, *61*, 7040.

(40) Fernández-González, M. A.; Marazzi, M.; Zapata, F.; García-Iriepa, C.; Rivero, D.; Lopez-Delgado, A.; Castaño, O.; Temprado, M.; Frutos, L. M. To be submitted for publication.

6.1.2 Structural Substituent Effect in the Excitation Energy of a Chromophore: Quantitative Determination and Application to S-Nitrosothiols

JCTC Journal of Chemical Theory and Computation
Article
pubs.acs.org/JCTC

Structural Substituent Effect in the Excitation Energy of a Chromophore: Quantitative Determination and Application to S-Nitrosothiols

Miguel Ángel Fernández-González, Marco Marazzi, Alberto López-Delgado, Felipe Zapata, Cristina García-Iriepa, Daniel Rivero, Obis Castaño, Manuel Temprado,* and Luis Manuel Frutos*

Departamento de Química Física, Universidad de Alcalá, E-28871 Alcalá de Henares (Madrid), Spain

ABSTRACT: A methodology for the prediction of excitation energies for substituted chromophores on the basis of ground state structures has been developed. The formalism introduces the concept of "*structural substituent excitation energy effect*" for the rational prediction and quantification of the substituent effect in the excitation energy of a chromophore to an excited electronic state. This effect quantifies exclusively the excitation energy variation due to the structural changes of the chromophore induced by the substituent. Therefore, excitation bathochromic and hypsochromic shifts of substituted chromophores can be predicted on the basis of known ground and excited potential energy surfaces of a reference unsubstituted chromophore, together with the ground state minimum energy structure of the substituted chromophore. This formalism can be applied if the chemical substitution does not affect the nature of the electronic excitation, where the substituent effect can be understood as a force acting on the chromophore and provoking a structural change on it. The developed formalism provides a useful tool for quantitative and qualitative determination of the excitation energy of substituted chromophores and also for the analysis and determination of the structural changes affecting this energy. The proposed methodology has been applied to the prediction of the excitation energy to the first bright state of several S-nitrosothiols using the potential energy surfaces of methyl-S-nitrosothiol as a reference unsubstituted chromophore.

I. INTRODUCTION

The substituent effect has become one of the major research topics in physical organic chemistry during the past decades. This fact is due to the need of setting a systematic description of the influence of chemical substitution on physical and chemical molecular properties. In this sense, great strides have been made to explain the effect of different substituents in the description of synthetic, mechanistic, and catalytic properties; in the prediction of chemical reactions and equilibria; and even in the control of agonist/antagonist properties in hormone receptor modulators.[1,2]

In order to make this possible, different relationships between substituent groups and chemical properties have been developed to date. Among them, those providing a quantitative description of these relations are useful tools for predicting and interpreting chemical properties. As a consequence, much emphasis was given to quantitative structure−activity relationships (QSAR) and linear free energy relationships (LFER).

The first empirical quantitative relationship was observed by Hammett (eq 1) in 1937,[3] where a relation between substituted (k) and unsubstituted (k_0) aryl reaction rate constants is proposed to be proportional to the product of a term (ρ) depending on the specific reaction and a term (σ) depending on the specific substituent.

$$\log \frac{k}{k_0} = \rho\sigma \tag{1}$$

He introduced the idea that for any two reactions with two aromatic reactants only differing in the type of substituent (*meta* or *para* positions), the change in Gibbs activation energy is proportional to the change in Gibbs energy. This LFER allowed elucidation of the reaction mechanism concerning the ionization of substituted benzoic acids. Subsequent modifications of the Hammett equation were proposed. The Swain−Lupton equation[4] emerged from the idea of Swain and Lupton that two variables are enough (taking into account resonance effects and field effects) to describe the effects of any substituent, therefore redefining the Hammett's substituent parameter, σ. Other modifications to the Hammett equation are the Taft equation,[5−7] which describes the steric effects of a substituent apart from field, inductive, and resonance effects, and the Yukawa−Tsuno equation,[8] which introduces a new term to the original Hammett relationship that reflects the extent of resonance stabilization for a reactive structure that enhances the transition state's charge. These LFERs were found to be useful tools in interpreting and predicting organic reactions and their mechanisms in the ground state.

Moreover, the substituent effect has important consequences in processes involving excited states, such as the variation of the maximum absorption wavelength of a given chromophore. The prediction of this spectroscopical property, and its eventual modulation, is of special interest in the development of photochromic compounds used as photoresponsive materials,[9] materials with nonlinear optical properties,[10] organic light-emitting diodes,[11,12] etc. In some cases, the Hammett equation has successfully correlated the rates of some reactions in the excited state for a series of molecules differently substituted

Received: July 13, 2012
Published: August 21, 2012

   dx.doi.org/10.1021/ct300597u | J. Chem. Theory Comput. 2012, 8, 3293−3302

with the Hammett constants of the same substituents derived for reactions proceeding in the ground state. Instead, in other cases, it has been observed that the influence of the substituent on the photochemical reaction is different from that found in the ground state,[13] and subsequently $\sigma^{h\nu}$,[14] σ_{ex},[15,16] σ^{*},[17,18] $\sigma^{*h\nu}$,[19] and σ_{cc}^{ex}[20] parameters were introduced as an attempt to describe photochemical substituent effects. As an additional attempt, the Hammett equation has been reformulated in order to correlate the substituent effect with the absorption frequency,[21] in any case leaving the application of the Hammett equation to the description of excited state properties as a non-prominent *trial and error* methodology.

Nevertheless, different empirical rules were developed in order to rationalize substituent effects in chromophores: the Woodward rules are among the most outstanding empirical rules in the study of chemical reactivity in organic chemistry. Woodward demonstrated that the wavelength of the absorption maximum in the UV spectra is strictly correlated with the extent of the carbon−carbon double bond substitution in conjugated systems, including carbonyl compounds, mono/disubstituted benzene derivates, and benzoyl derivatives.[22] These rules have been extensively applied, broadly studied, and expanded by Fieser et al.[23] and Scott[24] by adding a considerable amount of experimental data. Another empirical rule to calculate the absorption band maxima and extinction coefficients of conjugated molecules, especially polyenes, is the Fieser−Kuhn rule,[25] which complements Woodward−Fieser rules that are applicable only to molecules with one to four conjugated double bonds.

Here, we present a general methodology for the prediction of absorption energies in substituted chromophores, focusing on the structural modifications that the substituent causes, with respect to the unsubstituted chromophore. After defining the substituent structural effect with respect to the vertical excitation energy, the methodology is formally developed, realizing how the substituent effect can be used to properly tune the absorption spectra of a molecule and determining which internal coordinates control the excitation energy modulation.

The developed methodology is applied to S-nitrosothiols (RSNOs), a family of compounds of biological and medical relevance for their capability to release nitric oxide (NO) when irradiated in the visible and UV regions,[26−29] therefore making the study of the S−N photocleavage attractive for possible use in phototherapy.[30,31] We recently studied the absorption energy required to initiate photocleavage in a wide variety of RSNOs, showing the possibility of NO release modulation as a function of the substituent.[32]

II. DEVELOPED METHODOLOGY

Substituent Structural Effect and Excitation Energy. Chemical substitution of a given chromophore can alter different physical and chemical properties of the chromophore. Among these properties, the molecular structure is usually affected by substituent groups. These structural changes can affect, in general, all the internal coordinates of the chromophore and can induce modifications on the relative stability of some electronic excited states regarding the ground state. Moreover, if the substituent does not participate in the excitation (i.e., the promoted electrons do not involve orbitals with significant contribution of the substituent), it is expected that the nature of the considered excited electronic state will not change. This situation is quite common, for example when the excited state of a chromophore has a given nature (e.g., π,π^*), and the substituent does not present electrons participating in the excitation, (e.g., no conjugated π electrons). This concept is also present in the widely used multiconfigurational method CASSCF (Complete-Active-Space Self-Consistent-Field),[33] where the selected active space must include those occupied molecular orbitals participating in the electronic excitations, and therefore defining the nature of the excited state to be studied.

In this work, we focus on this situation, where the substituent has no significant effect on the nature of the studied excited state and also does not participate in the excitation itself. Within this premise, which defines the applicability limits of the developed methodology, it is possible to analyze the effect of the structural changes due to chemical substitution, and their effect on the excitation energy.

It is possible to formally divide the molecular entity (chromophore-substituent) into two fragments, being the electronic energy of the system in the ground state (E_{GS}) equal to

$$E_{GS} = E_{GS}^{chrom} + E_{GS}^{subs} + E_{GS}^{chrom/subs} \quad (2)$$

where E_{GS}^{chrom} is the electronic energy of the chromophore, E_{GS}^{subs} is the corresponding energy of the substituent, and $E_{GS}^{chrom/subs}$ is the energy of interaction between both parts of the molecule with all terms referred to the ground state.

Likewise, the energy of the excited state is given by

$$E_{ES} = E_{ES}^{chrom} + E_{GS}^{subs} + E_{GS}^{chrom/subs} \quad (3)$$

Note that the excitation is "localized" in the chromophore (as we assume that the substituent is not participating), and therefore the substituent term is the one corresponding to the ground-state since the energy stabilization/destabilization caused by the substituent is essentially identical for both ground and excited states (i.e., we assume that $E_{GS}^{subs} = E_{ES}^{subs}$). Furthermore, as discussed above, considering only substituents not affecting the excitation significantly, the chromophore-substituent energy term has to be essentially equal for both states ($E_{ES}^{chrom/subs} = E_{GS}^{chrom/subs}$). The larger the extent of validity of this equality, the higher the accuracy of the obtained results from the present formalism.

The excitation energy (E_{exc}) can be easily obtained by subtracting eq 2 from eq 3:

$$E_{exc} = E_{ES} - E_{GS} = E_{ES}^{chrom} - E_{GS}^{chrom} \quad (4)$$

This expression indicates that if the substituent does not contribute differentially to the relative stabilization/destabilization of the ground and excited states, the excitation energy will be governed by the intrinsic properties of the chromophore moiety. Nevertheless, it has to be noted that even if the excitation energy is correctly described by the intrinsic properties of the chromophore, the absolute energy of each state is not. Thus, the ground state of the molecule is affected by the presence of the substituent; specifically it will have an effect on the ground state structure of the molecule. Taking into account the Born−Oppenheimer approximation, every energy term in eq 2 and eq 3 will depend on the molecular coordinates of the chromophore (q_c), substituent (q_s), or both (q_c;q_s). Therefore, if we take the first derivatives of the energy for the ground electronic state (eq 2), we obtain

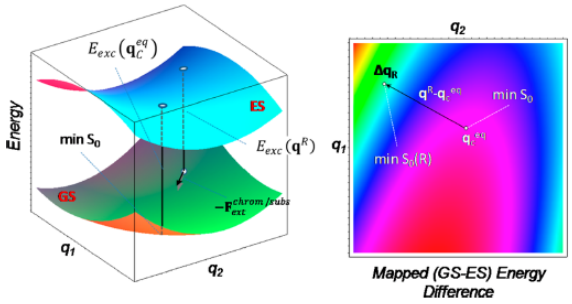

Figure 1. Left: Schematic potential energy surfaces for the ground state (GS) and excited state (ES) of an unsubstituted chromophore as a function of two of its coordinates (q_1, q_2). The substituent provokes a change of the molecular structure from $\mathbf{q}_C^{eq}$ to $\mathbf{q}^R$, which can be explained in terms of the effect of an external force ($\mathbf{F}_{ext}^{chrom/subs}$) acting on the chromophore due to the presence of the substituent. This structural change in the chromophore provokes a shift of the excitation energy from $E_{exc}(\mathbf{q}_C^{eq})$ to $E_{exc}(\mathbf{q}^R)$. Right: Color-mapped excitation energy for the chromophore as a function of the same two coordinates (q_1, q_2). The excitation energy changes due to the substituent effect on the structure of the chromophore, from the unsubstituted chromophore geometry ($\mathbf{q}_C^{eq}$) to the "R" substituted structure ($\mathbf{q}^R$) corresponding to a change of the ground state equilibrium structure from min S_0 to min S_0(R).

$$\nabla E_{GS}(\mathbf{q}_c;\mathbf{q}_s) = \nabla E_{GS}^{chrom}(\mathbf{q}_c) + \nabla E_{GS}^{subs}(\mathbf{q}_s) + \nabla E_{GS}^{chrom/subs}(\mathbf{q}_c;\mathbf{q}_s) \quad (5)$$

The equilibrium geometry of the ground state must fulfill $\nabla E_{GS}(\mathbf{q}_c;\mathbf{q}_s) = 0$. Since we are only interested in the chromophore structure (as the excitation energy only depends on the chromophore), it is straightforward to obtain eq 6 for the equilibrium structure of the molecule.

$$\nabla E_{GS}^{chrom}(\mathbf{q}_c) - \mathbf{F}_{ext}^{chrom/subs} = \mathbf{0} \quad (6)$$

where the term $\mathbf{F}_{ext}^{chrom/subs}$ is interpreted as an external force provoked by the effect of the substituent ($\nabla E_{GS}^{chrom/subs}(\mathbf{q}_c;\mathbf{q}_s)$ term). This external force induced by the substituent is characteristic of the specific chromophore/substituent couple and provokes the displacement of the equilibrium structure of the substituted chromophore regarding the unsubstituted chromophore. The new ground state equilibrium structure of the chromophore is determined by the $\mathbf{F}_{ext}^{chrom/subs}$ force, which exerts a displacement of the energy minimum to a new configuration where $\nabla E_{GS}^{chrom}(\mathbf{q}_c)$ equals $\mathbf{F}_{ext}^{chrom/subs}$ (Figure 1), consequently altering the potential energy surface shape by displacing the minimum. The solution to eq 6 provides the chromophore structure with the attached substituent (R). Finally, by knowing the structure of the substituted chromophore, it is straightforward to predict the excitation shift by using eq 4, which will depend only on the new coordinates of the chromophore under the substituent effect. This procedure is explained in Figure 1.

Substituent Absorption Tuning from Chromophore Potential Energy Surfaces (PESs). As discussed above, if the effect of the substituent in the chromophore is limited to provoke some structural changes but does not affect the nature of the electronic excitation, the electronic transition energy depends only on the new equilibrium structure of the substituted chromophore. Under this assumption, it is possible to predict, avoiding direct *ab initio* calculation, the excitation energy of the substituted chromophore just by correct knowledge of the following information: (i) the ground state structure of the substituted chromophore and (ii) to some extent the PESs (ground and excited) of the unsubstituted chromophore. Usually, the former can be easily obtained with *ab initio* calculations in the ground state; nevertheless, different approaches can be employed in order to have the ground and excited PESs of the unsubstituted chromophore. In the current work, we have used a quadratic approximation of the PESs involved in the excitation to describe the topology of the surfaces.

By using this approximation, the energy of the ground and excited states of the unsubstituted chromophore species can be expanded taking the ground state equilibrium geometry ($\mathbf{q}_C^{eq}$) as the origin according to eq 7 and eq 8.

$$E_{GS}(\Delta\mathbf{q}) = E_{GS}(\mathbf{q}_C^{eq}) + \frac{1}{2}\Delta\mathbf{q}^T\mathbf{H}_{GS}\Delta\mathbf{q} \quad (7)$$

$$E_{ES}(\Delta\mathbf{q}) = E_{ES}(\mathbf{q}_C^{eq}) + \Delta\mathbf{q}^T\mathbf{g}_{ES} + \frac{1}{2}\Delta\mathbf{q}^T\mathbf{H}_{ES}\Delta\mathbf{q} \quad (8)$$

where $\Delta\mathbf{q} = \mathbf{q} - \mathbf{q}_C^{eq}$ is the displacement coordinate vector regarding the ground state equilibrium geometry ($\mathbf{q}_C^{eq}$) for the unsubstituted chromophore, $\mathbf{H}_{GS}$ and $\mathbf{H}_{ES}$ are the Hessian matrices for both states calculated for this geometry, and $\mathbf{g}_{ES}$ is the energy gradient vector in the excited state, also evaluated for the same geometry.

Therefore, according to eqs 7 and 8, the excitation energy for any configuration of the chromophore $E_{exc}(\Delta\mathbf{q})$ is given by eq 9.

$$\begin{aligned} E_{exc}(\Delta\mathbf{q}) &= E_{ES}(\Delta\mathbf{q}) - E_{GS}(\Delta\mathbf{q}) \\ &= E_{ES}(\mathbf{q}_C^{eq}) - E_{GS}(\mathbf{q}_C^{eq}) + \Delta\mathbf{q}^T\mathbf{g}_{ES} \\ &\quad + \frac{1}{2}\Delta\mathbf{q}^T(\mathbf{H}_{ES} - \mathbf{H}_{GS})\Delta\mathbf{q} \end{aligned} \quad (9)$$

Finally, knowing all the parameters in eq 9 ($E_{ES}(\mathbf{q}_C^{eq})$, $E_{GS}(\mathbf{q}_C^{eq})$, $\mathbf{g}_{ES}$, $\mathbf{H}_{ES}$, and $\mathbf{H}_{GS}$), the ground state equilibrium structure for the "−R" substituted chromophore ($\mathbf{q}^R$), and therefore the structural displacement $\Delta\mathbf{q}^R = \mathbf{q}^R - \mathbf{q}_C^{eq}$, it is possible to predict the excitation energy of the "−R" substituted chromophore (E_{exc}^R) according to eq 10.

dx.doi.org/10.1021/ct300597u | J. Chem. Theory Comput. 2012, 8, 3293−3302

Journal of Chemical Theory and Computation Article

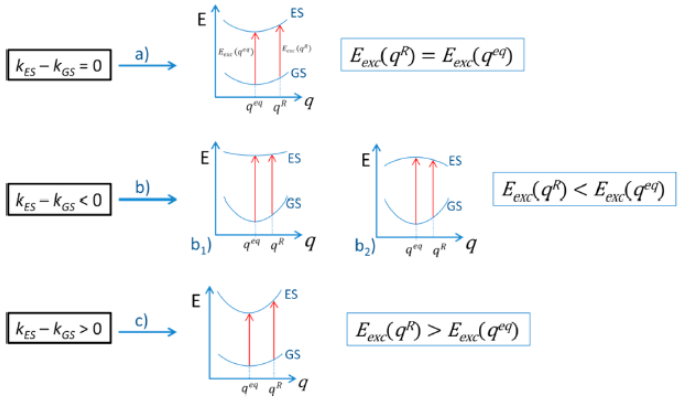

Figure 2. The possible energy difference (excited-ground) force constants (k). Three different cases are possible when distorting the equilibrium structure ($\mathbf{q}^{eq}$) along the corresponding eigenvector ($\mathbf{q}$) to reach the equilibrium geometry for the substituted chromophore ($\mathbf{q}^{R}$): the excitation energy (E_{exc}) does not change significantly (case a); reduction of the excitation energy with positive and negative excited state curvature (cases b_1 and b_2, respectively); increase of the excitation energy (case c).

$$E_{exc}^{R} = E_{ES}(\mathbf{q}_C^{eq}) - E_{GS}(\mathbf{q}_C^{eq}) + (\Delta\mathbf{q}^{R})^T\mathbf{g}_{ES} + \frac{1}{2}(\Delta\mathbf{q}^{R})^T(\mathbf{H}_{ES} - \mathbf{H}_{GS})\Delta\mathbf{q}^{R} \quad (10)$$

Therefore, by using high-level *ab initio* derived PESs and computing ground state structures of substituted chromophores with an affordable method, it is possible to predict (applying eq 10) the excitation energy of a series of substituted chromophore derivatives.

Determination of the Coordinates Controlling the Excitation Energy. According to the discussed methodology, it is possible to have a computationally saving estimation of the excitation energy of a given substituted chromophore on the basis of quadratic ground and excited state PESs of the unsubstituted chromophore—calculation made only once for a given chromophore—and the ground state equilibrium geometry of a substituted chromophore—one calculation in the ground state for each substituent. Moreover, we can take advantage of this situation to analyze the role of each molecular coordinate by predicting their efficiency in modulating the energy gap. According to eq 10, the first order variation of the excitation energy gap is given by the excited state gradient vector ($\mathbf{g}_{ES}$), which will be predominant for small displacements of the substituted chromophore structure. Nevertheless, the second order term in the excitation energy variation (last term in eq 10) can be also relevant, especially when the substituent induces distortions in the ground state that are orthogonal to the energy gradient vector, or when the gradient vector itself ($\mathbf{g}_{ES}$) tends to vanish.

In order to analyze this effect, it is useful to separate the coordinates into two subsets, one corresponding to the energy gradient vector and the rest of coordinates orthogonal to it. The energy gradient vector coordinate provides the first-order correction to the energy difference along $\mathbf{g}_{ES}$, while those orthogonal to $\mathbf{g}_{ES}$ provide the second-order energy gap variation through a projected Hessian difference matrix ($\mathbf{H} \equiv \mathbf{H}_{ES} - \mathbf{H}_{GS}$) which can be obtained by using a projection operator as shown in eq 11.

$$\mathbf{H}^{P} = \mathbf{PHP} \quad (11)$$

where $\mathbf{P}$ is the projector operator defined by

$$\mathbf{P} = \mathbf{I} - \mathbf{g}_{ES}^{N}(\mathbf{g}_{ES}^{N})^T \quad (12)$$

where $\mathbf{I}$ is the identity matrix with $N - 1$ elements, N being the number of molecular coordinates, and $\mathbf{g}_{ES}^{N}$ is the normalized excited state gradient vector . The eigenvalues of the projected Hessian difference ($\mathbf{H}^{P}$) provide the set of force constants difference between ground and excited states ($k_{ES} - k_{GS}$). Close to zero eigenvalues denote that distortions along the corresponding eigenvectors do not provide significant change of the excitation energy (Figure 2, case a). However, negative eigenvalues are related to reduction of the excitation energy (Figure 2, cases b1 and b2) while positive eigenvalues are related to an increase of the energy gap (Figure 2, case c) when structural changes take place along the corresponding eigenvectors. With this information, it is possible to rationalize the influence of the different internal coordinates of a chromophore in tuning the excitation energy.

Electronic-Structure Methods. The implementation of the methodology discussed above has been tested for the prediction of the excitation energy of a wide family of S-nitrosothiol derivatives. All S-nitrosothiol structures, except S-nitrosoglutathione, have been taken from ref 32, all of them being optimized on the ground state at the B3P86 level (Becke's three-parameter hybrid exchange along with Perdew's nonlocal correlation functionals) and calculating the excitation energy by time dependent treatment of the same functional (TD-DFT), as implemented in the Gaussian09 suite of programs.[34] In all cases, a 6-311+G(2df) basis set was applied. This method has been proven to predict excitation energies in good agreement with high-level multiconfigurational methods as Complete Active Space Perturbation Theory to Second Order (CASPT2).[35,36] The analytical PESs for the ground and excited states of *syn*- and *anti*-methyl-S-nitrosothiol have been constructed from energy gradients and Hessians determined at the ground state minima. Numerical Hessians have been

dx.doi.org/10.1021/ct300597u | J. Chem. Theory Comput. 2012, 8, 3293−3302

computed in the case of excited state, while analytical Hessians have been determined for the ground state.

III. APPLICATION TO S-NITROSOTHIOL DERIVATIVES

S-nitrosothiols are a family of compounds where the chromophore corresponds to the −SNO terminal fragment (see Figure 3). The partial double bond character of the S−N

Figure 3. *Anti* (left) and *syn* (right) methyl-S-nitrosothiol ground state equilibrium structures at the B3P86/6-311+G(2df) level of theory. The main geometrical parameters are shown.

bond, caused by delocalization of the sulfur lone pairs in the nitroso group, makes possible the existence of two different RSNO ground state conformers: *syn* and *anti*.[37] In spite of their usual instability at room temperature, the main interest about RSNOs concerns their ability to release nitric oxide (NO), a molecule of fundamental importance in medicine and biology.[38−48] Especially, the generation of NO as a stable radical by irradiating RSNOs at a specific wavelength (i.e., photochemical rupture of the S−N bond) is of potential interest in phototherapy.[29]

One of the simplest members of this family of molecules is methyl-S-nitrosothiol (CH_3SNO, see Figure 3), which was studied theoretically but not experimentally, because of the intrinsic instability shown by the compound.[37,49−51] We have taken this compound as the representative model chromophore for building up the reference PESs (ground and excited state).

As already described by the authors, after irradiation of CH_3SNO to the bright state (S_2 corresponding to a $^1(\pi,\pi^*)$ state), the minimum energy paths lead to a barrierless photocleavage process resulting in the formation of $CH_3S^\bullet$ and $^\bullet NO$ radicals. This implies that an ultrafast process is expected, making possible a modulation of the NO release only by modulation of the vertical excitation energy required to initiate photocleavage.[32]

In the following, the construction of the PESs for ground and excited electronic states is described, and the coordinates modulating the energy gap are identified. Finally, a series of S-nitrosothiols are studied, determining the excitation energy predicted on the basis of CH_3SNO PESs and ultimately compared with the excitation energy directly computed by the above-described TD-DFT methodology.

The PESs of Methyl-S-nitrosothiol. CH_3SNO has two conformations in the ground state, *syn* and *anti* conformers (see Figure 3), where the most relevant structural difference is related to the CSNO dihedral angle (~0° and ~180° for *syn* and *anti* isomers respectively). The absorption spectra for *syn* and *anti* CH_3SNO were previously reported by the authors at the MS-CASPT2/ANO-L level of theory.[32] For both conformers, the two lowest-energy vertical excitations ($S_0\rightarrow S_1$ and $S_0\rightarrow S_2$) correspond to optically dark $^1(n,\pi^*)$ and bright $^1(\pi,\pi^*)$ transitions, respectively. More in detail, the absorption spectrum of *syn* CH_3SNO is characterized by a $S_0\rightarrow S_1$ transition at 530 nm and a $S_0\rightarrow S_2$ transition at 330 nm, while a red shift in *anti* CH_3SNO sets the $S_0\rightarrow S_1$ transition at 600 nm and the $S_0\rightarrow S_2$ transition at 342 nm. For both conformers, the $S_0\rightarrow S_2$ transition is associated with a much higher oscillator strength than for $S_0\rightarrow S_1$ (higher by a factor 33 and 28 for *syn* and *anti* CH_3SNO, respectively). The present study is focused

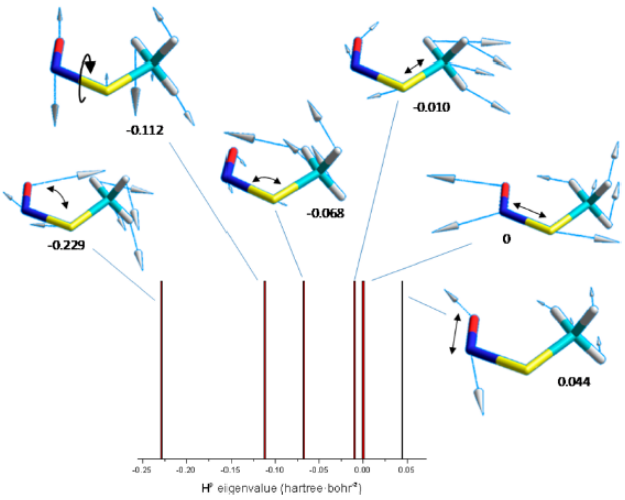

Figure 4. *Syn*-methyl-S-nitrosothiol projected Hessian difference ($\mathbf{H}^P$) eigenvectors and eigenvalues in hartree·bohr^{-2}. The eigenvalue spectrum is displayed with vertical bars, where the $\mathbf{H}^P$ eigenvalue (x axis) indicates the different ability to modify the energy gap (positive for hypsochromic shift and negative for bathochromic shift). The main coordinates associated with each eigenvector are shown with black arrows.

dx.doi.org/10.1021/ct300597u | J. Chem. Theory Comput. 2012, 8, 3293−3302

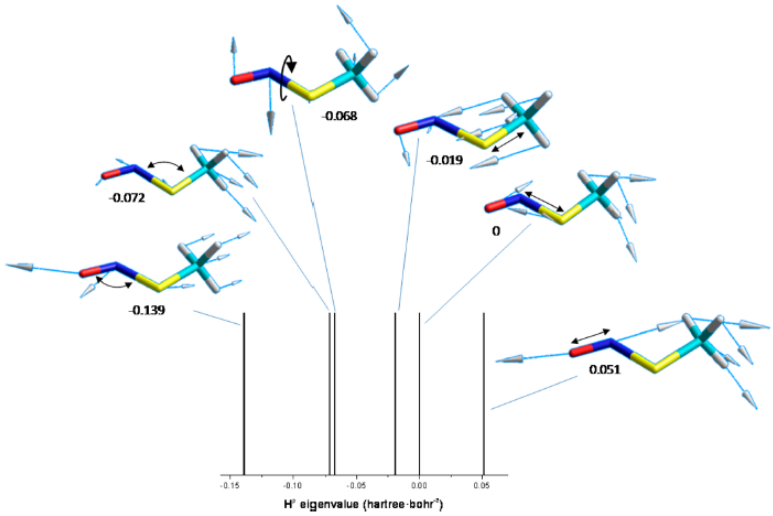

Figure 5. *Anti*-methyl-S-nitrosothiol projected Hessian difference ($\mathbf{H}^P$) eigenvectors and eigenvalues in hartree·bohr^{-2}. The eigenvalue spectrum is displayed with vertical bars, where the $\mathbf{H}^P$ eigenvalue (x axis) indicates the different ability to modify the energy gap (positive for hypsochromic shift and negative for bathochromic shift). The main coordinates associated with each eigenvector are shown with black arrows.

on the prediction of the lowest-energy bright $^1(\pi,\pi^*)$ transition of a series of differently substituted RSNOs.

In order to explore the role of the internal coordinates controlling the $S_0 \rightarrow S_2$ excitation energy, we have determined the second order approximated PESs of both conformers: the excitation energies, the energy gradient vectors, and the projected Hessian difference, $\mathbf{H}^P$ (see eq 11), as well as its eigenvalues and eigenvectors. The later magnitudes provide the directions orthogonal to the excited state gradient vector modulating the $S_0 \rightarrow S_2$ energy gap, while the corresponding eigenvalues quantify the extent of the energy gap variation. Negative eigenvalues of the projected Hessian difference (note that the Hessian difference matrix is defined as $\mathbf{H} \equiv \mathbf{H}_{S_2} - \mathbf{H}_{S_0}$, where ES stands for S_2 and GS for S_0 in Figure 2) are related to distortions where the force constant in S_0 is larger than that of S_2, and consequently, displacements along the corresponding eigenvectors reduce the $S_0 \rightarrow S_2$ excitation energy. On the other hand, positive eigenvalues are related to eigenvectors providing an increase of the energy gap.

Using a minimal set of internal coordinates for the chromophore, the *syn*-methyl-S-nitrosothiol $\mathbf{H}^P$ matrix shows eigenvalues raging from −0.229 to 0.044 hartree·[bohr(rad)]$^{-2}$, indicating that an energy gap increase and decrease can be achieved not only by distortions along the excited state energy gradient vector but also along different coordinates (see Figure 4). On one hand, the excited state energy gradient vector is mainly associated with S−N stretching (corresponding to an eigenvector of the projected Hessian difference with zero eigenvalue). On the other hand, the eigenvectors of $\mathbf{H}^P$ can be associated, to a large extent, with single internal coordinates. The highest eigenvalues (0.044, 0.0, and −0.01) are related to stretching coordinates (N−O, S−N, and C−S, respectively) while the lowest eigenvalues (−0.068, −0.112, and −0.229) correspond to eigenvectors that are mostly related to CSN bending, CSNO torsion, and SNO bending, respectively. With these results, a clear picture of the energy gap variation can be obtained: lowering the $S_0 \rightarrow S_2$ energy gap can be reached by increasing the S−N distance (gradient contribution) and by changing (decrease or increase) the N−O distance (second order contribution). However, an increase of the energy gap is possible by decreasing the S−N distance (gradient contribution) and mainly by varying bendings (CSN and SNO) and torsion (CSNO) and, to a lesser extent, by changing the C−S bond distance.

Similar behavior is observed for the *anti* isomer (see Figure 5). The energy gradient vector is also dominated by the S−N stretching, and the ordering of the corresponding eigenvalues of the projected Hessian difference is equivalent: bendings, torsions, and stretchings in ascending order of the corresponding eigenvalue. Therefore, in order to increase the excitation energy, the coordinates that are able to modulate the energy are the energy gradient vector, mainly described by S−N stretching (by decreasing the S−N distance), while N−O distance variation (increase or decrease) also permits the $S_0 \rightarrow S_2$ energy gap increase. On the other hand, in order to reduce the energy gap, different coordinates can contribute: the increase of the S−N distance (gradient contribution) and the variation of SNO and CSN bendings as well as CSNO torsion and C−S stretching. Of course, the eigenvalues of the diagonal $\mathbf{H}^P$ matrix provide just the excitation energy modulation efficiency of each coordinate per unit displacement. Nevertheless, in order to understand the specific effect of a given substituent, the amplitude of the distortion induced by this substituent has to be taken into account explicitly, obtaining the concrete energy gap variation due to each coordinate.

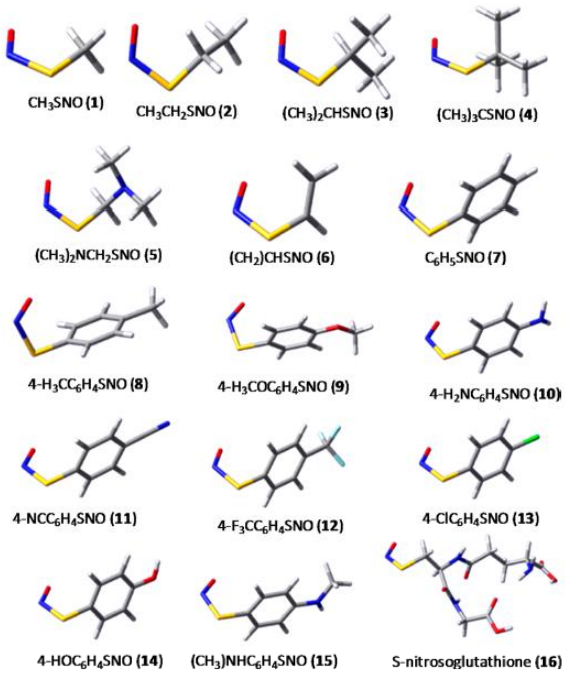

Figure 6. *syn*-S-nitrosothiol derivatives studied (same derivatives for *anti* conformers).

It is therefore concluded that the energy gradient has the same nature for both conformers and is described mainly by C−S stretching. The variation of this coordinate provides a first-order variation of the energy gap, making possible to decrease (or increase) this gap by shortening (enlarging) the C−S distance. Analyzing the second order energy variation, bendings are effective in decreasing the $S_0 \rightarrow S_2$ excitation energy, as well as torsion and, to a lesser extent, the C−S distance. However, the N−O distance variation provokes an increase of the energy gap for both isomers. Finally, the *syn* conformer shows a higher capacity to decrease the energy gap by structural distortions in comparison to the *anti* conformer (as is evident from the higher negative eigenvalues of ΔH^p for the *syn* conformation) while the *anti* conformers show a slightly higher capacity to increase the energy gap.

Excitation Energy Prediction for Substituted S-Nitrosothiols. In order to study the substituent effect on the $S_0 \rightarrow S_2$ energy gap for S-nitrosothiols, we have previously determined the excitation energy for a wide variety of substituted RSNOs: primary, secondary, and tertiary substituted (i.e., alkyl); vinyl; and aryl RSNOs.[32] In Figure 6, the ground state minima (B3P86/6-311+G(2df) level of theory) of different S-nitrosothiols are shown. All kinds of substitution do not affect the nature of the excitation, therefore making it possible to use the developed formalism to study the excitation energy tuning on the basis of structural distortions of the chromophore. Moreover, it was previously shown that aryl substituents do not expand the π-conjugation of the −SNO chromophore, since the aryl group and the −SNO moiety always form a dihedral angle between them ranging from 50 to 90°.[32] Nevertheless, in order to minimize the aryl π-conjugation and being able to measure the structural effect of the substituent, we have restrained to 90° the torsion of those derivatives which are not completely orthogonal. Therefore, these minimum energy conformations completely out of planarity keep the −SNO fragment as the unique chromophore, ranging the absorption maxima for the different substituted derivatives from 350 to 290 nm.[32]

The optimized structures on the ground state have been compared with the reference chromophore (CH_3SNO) and the corresponding structural changes interpreted in terms of the coordinates controlling the excitation energy variation. Finally, on the basis of the ground state optimized structures for the different derivatives, the excitation energies are predicted by using the information of the CH_3SNO PESs.

Before doing the analysis of the structural effect on the excitation energy, the second order approximation made for ground and excited states of the CH_3SNO reference compound has been tested. In this regard, the ground state equilibrium structure coordinates of each derivative have been transferred to CH_3SNO PESs, resulting in a differently distorted CH_3SNO structure for each RSNO. The excitation energy of each "distorted" CH_3SNO was calculated and compared to that obtained from analytical PESs according to the procedure developed in this work (see Figure 7). The correlation between

both magnitudes is quantitative, showing the predictive quality of the second order approximation of the PESs employed.

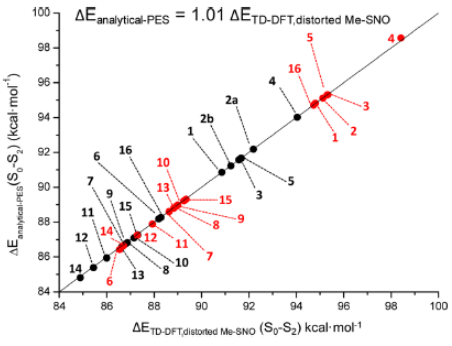

Figure 7. TD-DFT excitation energies of the different distorted Me-SNO (**1**) structures (fitting the corresponding optimized RSNO structures), versus the predicted excitation energies obtained from analytical PESs (black dots, *anti* derivatives; red dots, *syn* derivatives). The correlation shows quantitative agreement in the predictions made on the basis of analytical PESs for Me-SNO (see Figure 6 for numbering).

Finally, the excitation energies of the R-SNO derivatives have been predicted by using the corresponding optimized structures in the ground-state, applying the developed formalism, and then compared with those directly determined with TD-DFT calculations. The excitation energies obtained from analytical PES render exclusively the structural effect of the substituent (i.e., the chromophore structural change induced by the substituent) in the excitation energy. Therefore, the comparison of this energy with that obtained from TD-DFT calculations provides the quantification of the structural role of the substituent in tuning the excitation energy. The correlation between both energies is remarkable, indicating the principal role of the structural substituent effect in tuning S-nitrosothiol excitation energy. In fact, linear regression of these data (see Figure 8) gives a suitable correlation between predicted and TD-DFT computed excitation energies. Since both correlation lines cross the CH_3SNO reference, the slope of the correlation can be easily interpreted as the contribution of the structural substituent effect to the excitation energy variation. In this way, for *syn* derivatives the linear regression provides a slope equal to 0.82, indicating that, on average, 82% of the excitation energy variation is due to the effect of the substituent in the structure of the CSNO chromophore. In the case of *anti* derivatives, this effect rises to 89%.

As previously described, the developed methodology is useful not only to predict the role of the structural effect of a substituent on the excitation energy but also to identify and quantify the role of each coordinate of the chromophore in tuning the transition energy. In this regard, from methyl-S-nitrosothiol PESs analysis, we have obtained the potential role of each internal coordinate of the chromophore in tuning the $S_0 \rightarrow S_2$ excitation energy (*vide supra*). It has to be noted that, at second order, all the coordinates except one (N–O stretching) provide a reduction of the energy gap. Therefore, it is not odd to find that most of the derivatives reduce the energy gap.

We have analyzed the role of each internal coordinate of the chromophore in controlling the excitation energy for all the substituted S-nitrosothiols. The energy gradient component, related mainly to the S–N stretching, is the most important coordinate in tuning the energy gap of S-nitrosothiols (see Figure 9), representing 86% to 99% of the total excitation energy variation, second order contributions being less important (see Figure 10).

The energy gap variation due to the energy gradient ranges from ca. −6 to 3 kcal·mol^{-1} in the case of *anti*-S-nitrosothiols, and from ca. −8 to 4 kcal·mol^{-1} in the case of *syn*-S-nitrosothiols. Moreover, only alkyl derivatives show an energy gap increase, while for vinyl and aryl derivatives the excitation energy is reduced as compared to that of methyl-S-nitrosothiol. Interestingly, for *anti*-S-nitrosoglutathione, which should be more similar to alkyl-derivatives, the energy gap is significantly reduced, indicating an increase of the S–N distance.

Although second order terms in eq 10 are significantly lower than first order contributions, it can be realized that the N–O bond length is the only coordinate able to increase the energy gap (see Figure 10) in both *syn*- and *anti*-S-nitrosothiols, the

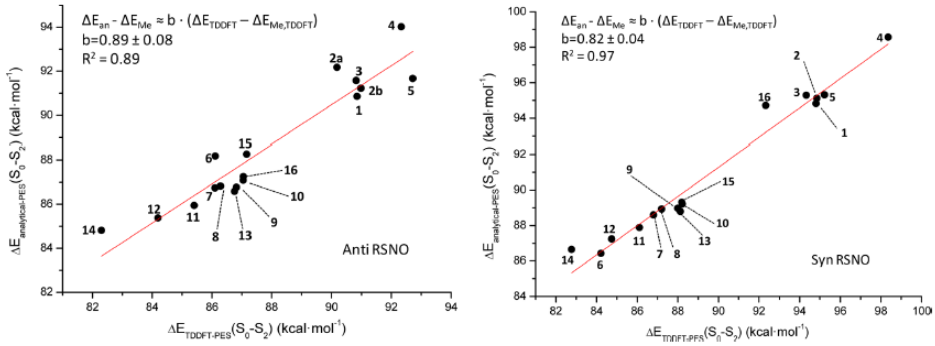

Figure 8. *Anti* (left) and *syn* (right) S-nitrosothiol excitation ($S_0 \rightarrow S_2$) energies obtained from analytical PESs of CH_3SNO versus the computed excitation energies of each S-nitrosothiol derivative (see Figure 6 for numbering).

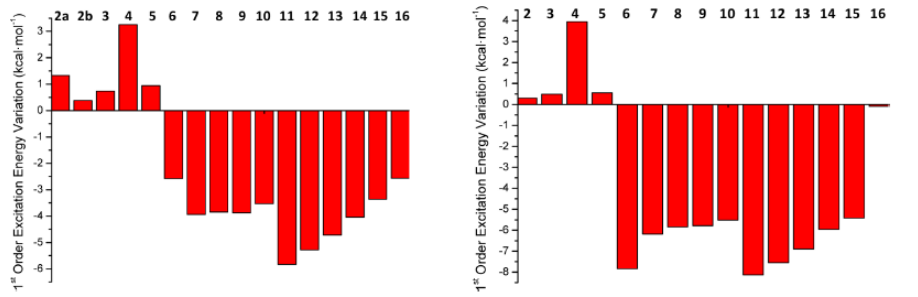

Figure 9. *Anti* (left) and *syn* (right) S-nitrosothiol excitation energy variation with respect to CH_3SNO due to first order (energy gradient component) contribution.

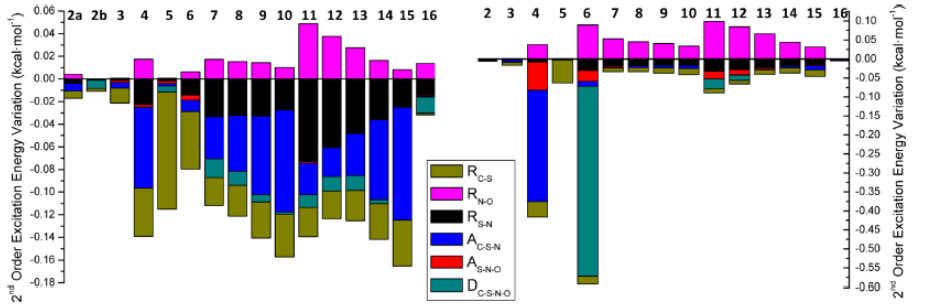

Figure 10. *Anti* (left) and *syn* (right) S-nitrosothiol excitation energy variations due to the second order terms. The individual contribution of each eigenvector of the projected energy Hessian difference ($\mathbf{H}^{\mathrm{P}}$) is shown (the eigenvectors are confidently assigned to distances "R" C−S, N−O, and S−N; to bond angles "A" C−S−N and S−N−O; and to the dihedral angle "D" C−S−N−O).

effect of this coordinate being minimal for alkyl-S-nitrosothiols and small but similar for the rest of substituents. On the other hand, *syn* derivatives show a slightly lower capacity of energy gap reduction in comparison to *anti* derivatives. This is the general rule, except in the case of the *tert*-butyl substituent (compound **4**) where the steric hindrance should be responsible for the large participation of the C−S−N bond angle. Also, compound **6** (vinyl substituent, see Figure 6) exhibits a large participation of the C−S−N−O dihedral angle in energy gap modulation of the *syn* conformer. This contribution highlights the different effects of substituents in the chromophore structure, where a vinyl moiety activates the C−S−N−O dihedral angle while aryl derivatives do not provoke such a change in this coordinate. However, *anti* derivatives show an opposite behavior regarding this coordinate (aryl derivatives are C−S−N bond angle sensitive while vinyl derivative is not). For *anti* isomers, N−O, C−S, and S−N bond lengths contribute in a similar way, taking into account that the former coordinate increases the gap and the rest decrease it. Again, alkyl-S-nitrosothiols are the most energy-gap-insensitive derivatives. The most important coordinate for the decrease of the energy gap is the C−S−N bond angle, showing more pronounced response than *syn* derivates to this coordinate.

IV. CONCLUSIONS

Here, we present a methodology to easily predict the excitation energy shift (bathochromic or hypsonchromic) of substituted chromophores. The formalism is valid for substituted chromophores when the substituent fulfills the following conditions: (i) It does not change the excitation character of the electronic excited state under consideration. (ii) It does not participate directly in the excitation (no molecular orbitals with a significant contribution of the substituent are involved in the excitation process). This methodology only permits one to take into account the structural effect of the substituent in the chromophore excitation energy; therefore, no explicit through-space interaction is considered.

We show that from second-order term PESs for both ground and excited electronic states, it is possible to analyze the role of each molecular coordinate in the excitation energy tuning of the chromophore, being able to identify the ability of each coordinate in the modulation of the gap. The analysis is made on the basis of first- and second-order contributions.

This formalism has been applied to the prediction of excitation energy in a large family of substituted S-nitrosothiols. For these derivatives, 80% to 90% of the total excitation energy shift is due to structural effects induced by the substituent in the chromophore, the gradient vector being the main coordinate controlling the excitation energy variation.

This methodology offers a simple and fast procedure to obtain information regarding the substituent effect in the excitation of a chromophore, permitting the determination of the capability of the chromophore in the excitation energy tuning as well as the identification of the coordinates responsible for such a behavior, which eventually would permit the rational design of substituted derivatives with desired batho- or hypsochromic shifts. Moreover, once the ground and excited PESs (e.g., up to second order) of a chromophore are characterized, only ground-state calculations are needed in order to predict the excitation energy of a substituted derivative, being also possible to use different levels of theory for the prediction of the ground-state structures. Therefore, this methodology could be used for high-level *ab initio* excitation energy prediction where the excited-state calculations are in general computationally expensive, eventually permitting the fast prediction of excitation energies for a large number of substituted chromophores with simple ground state optimizations. Furthermore, the reference compound can be chosen as the simplest possible chromophore, in order to save computational time in the construction of the analytical PESs.

AUTHOR INFORMATION

Corresponding Author

*E-mail: luisma.frutos@uah.es; manuel.temprado@uah.es.

Notes

The authors declare no competing financial interest.

ACKNOWLEDGMENTS

This research was supported by the Spanish MICINN grant CTQ2009-07120 and UAH2011/EXP-041 of the University of Alcalá. M.A.F.-G., M.M., and C.G.-I. are grateful to the UAH and F.Z. to the Spanish MEC for a doctoral fellowship. D.R. acknowledges the University of Alcalá for a research grant. L.M.F. acknowledges receipt of a "Ramon y Cajal" contract from MEC.

REFERENCES

(1) Nguyen, N.-H.; Apriletti, J. W.; Baxter, J. D.; Scanlan, T. S. *J. Am. Chem. Soc.* **2005**, *127*, 4599.
(2) Schultz, D.; Nitschke, J. R. *J. Am. Chem. Soc.* **2006**, *128*, 9887.
(3) Hammett, L. P. *J. Am. Chem. Soc.* **1937**, *59*, 96.
(4) Swain, C. G.; Lupton, E. C., Jr. *J. Am. Chem. Soc.* **1968**, *90*, 4328.
(5) Taft, R. W., Jr. *J. Am. Chem. Soc.* **1952**, *74*, 3120.
(6) Taft, R. W., Jr. *J. Am. Chem. Soc.* **1952**, *74*, 2729.
(7) Taft, R. W., Jr. *J. Am. Chem. Soc.* **1953**, *75*, 4538.
(8) Yukawa, Y.; Tsuno, Y. *Bull. Chem. Soc. Jpn.* **1959**, *32*, 965.
(9) Dong, H.; Zhu, H.; Meng, Q.; Gong, X.; Hu, W. *Chem. Soc. Rev.* **2012**, *41*, 1754.
(10) Khoo, I. C. *J. Nonlinear Opt. Phys. Mater.* **1999**, *8*, 305.
(11) Bruetting, W.; Frischeisen, J.; Scholz, B. J.; Schmidt, T. D. *Europhys. News* **2011**, *42*, 20.
(12) Thejo, K. N.; Dhoble, S. J. *Renewable Sustainable Energy Rev.* **2012**, *16*, 2696.
(13) Sadlej-Sosnowska, N.; Kijak, M. *Struct. Chem.* **2012**, *23*, 359.
(14) McEwen, J.; Yates, K. *J. Phys. Org. Chem.* **1991**, *4*, 193.
(15) Wehry, E. L.; Rogers, L. B. *J. Am. Chem. Soc.* **1965**, *87*, 4234.
(16) Baldry, P. J. *J. Chem. Soc., Perkin Trans. 2* **1979**, 951.
(17) Shim, S. C.; Park, J. W.; Ham, H. S. *Bull. Korean Chem. Soc.* **1982**, *3*, 13.
(18) Shim, S. C.; Park, J. W.; Ham, H. S.; Chung, J. S. *Bull. Korean Chem. Soc.* **1983**, *4*, 45.
(19) Fleming, S. A.; Jensen, A. W. *J. Org. Chem.* **1996**, *61*, 7040.
(20) Cao, C.; Chen, G.; Yin, Z. *J. Phys. Org. Chem.* **2008**, *21*, 808.
(21) Charton, M. *Prog. Phys. Org. Chem.* **1981**, *13*, 119.
(22) Woodward, R. B. *J. Am. Chem. Soc.* **1941**, *63*, 1123.
(23) Fieser, L. F.; Fieser, M.; Rajagopalan, S. *J. Org. Chem.* **1948**, *13*, 800.
(24) Scott, A. I. *The Interpretation of Ultraviolet Spectra of Natural Products*; Pergamon Press: Elmsford, NY, 1962.
(25) Kuhn, H. *J. Chem. Phys.* **1948**, *16*, 840.
(26) Sexton, D. J.; Muruganandam, A.; McKenney, D. J.; Mutus, B. *Photochem. Photobiol.* **1994**, *59*, 463.
(27) Singh, R. J.; Hogg, N.; Joseph, J.; Kalyanaraman, B. *J. Biol. Chem.* **1996**, *271*, 18596.
(28) Singh, S. P.; Wishnok, J. S.; Keshive, M.; Deen, W. M.; Tannenbaum, S. R. *Proc. Natl. Acad. Sci. U. S. A.* **1996**, *93*, 14428.
(29) Wood, P. D.; Mutus, B.; Redmond, R. W. *Photochem. Photobiol.* **1996**, *64*, 518.
(30) Bartberger, M. D.; Houk, K. N.; Powell, S. C.; Mannion, J. D.; Lo, K. Y.; Stamler, J. S.; Toone, E. J. *J. Am. Chem. Soc.* **2000**, *122*, 5889.
(31) Bharatam, P. V.; Amita. *Tetrahedron Lett.* **2002**, *43*, 8289.
(32) Marazzi, M.; Lopez-Delgado, A.; Fernandez-Gonzalez, M. A.; Castano, O.; Frutos, L. M.; Temprado, M. *J. Phys. Chem. A* **2012**, *116*, 7039.
(33) Roos, B. O.; Taylor, P. R.; Siegbahn, E. M. *Chem. Phys.* **1980**, *48*, 157.
(34) Frisch, M. J.; Trucks, G. W.; Schlegel, H. B.; Scuseria, G. E.; Robb, M. A.; Cheeseman; J. R.; Scalmani; G.; Barone; V.; Mennucci; B.; Petersson, G. A.; Nakatsuji, H.; Caricato, M.; Li, X.; Hratchian, H. P.; Izmaylov, A. F.; Bloino, J.; Zheng, G.; Sonnenberg, J. L.; Hada, M.; Ehara, M.; Toyota, K.; Fukuda, R.; Hasegawa, J.; Ishida, M. N.; Honda, Y.; Kitao, O.; Nakai, H.; Vreven, T.; Montgomery, J. A., Jr.; Peralta, J. E.; Ogliaro, F.; Bearpark, M.; Heyd, J. J.; Brothers, E.; Kudin, K. N.; Staroverov, V. N.; Kobayashi, R.; Normand, J.; Raghavachari, K.; Rendell, A.; Burant, J. C.; Iyengar, S. S.; Tomasi, J.; Cossi, M.; Rega, N.; Millam, J. M.; Klene, M.; Knox, J. E.; Cross, J. B.; Bakken, V.; Adamo, C.; Jaramillo, J.; Gomperts, R.; Stratmann, R. E.; Yazyev, O.; Austin, A. J.; Cammi, R.; Pomelli, C.; Ochterski, J. W.; Martin, R. L.; Morokuma, K.; Zakrzewski, V. G.; Voth, G. A.; Salvador, P.; Dannenberg, J. J.; Dapprich, S.; Daniels, A. D.; Farkas, O.; Foresman, J. B.; Ortiz, J. V.; Cioslowski, J.; Fox, D. J. *Gaussian 09*, revision B.01; Gaussian, Inc.: Wallingford, CT, 2009.
(35) Andersson, K.; Malmqvist, P.-A.; Roos, B. O.; Sadlej, A. J.; Wolinski, K. *J. Phys. Chem.* **1990**, *94*, 5483.
(36) Finley, J.; Malmqvist, P.-A.; Roos, B. O.; Serrano-Andres, L. *Chem. Phys. Lett.* **1998**, *288*, 299.
(37) Bartberger, M. D.; Mannion, J. D.; Powell, S. C.; Stamler, J. S.; Houk, K. N.; Toone, E. J. *J. Am. Chem. Soc.* **2001**, *123*, 8868.
(38) Garthwaite, J. *Trends Neurosci.* **1991**, *14*, 60.
(39) Hibbs, J. B., Jr. *Res. Immunol.* **1991**, *142*, 565.
(40) Ignarro, L. J. *Pharm. Res.* **1989**, *6*, 651.
(41) Ignarro, L. J. *Nitric Oxide* **1996**, 111.
(42) Ignarro, L. J.; Byrns, R. E.; Buga, G. M.; Wood, K. S. *Circ. Res.* **1987**, *61*, 866.
(43) Moncada, S.; Palmer, R. M. J.; Gryglewski, R. J. *Proc. Natl. Acad. Sci. U. S. A.* **1986**, *83*, 9164.
(44) Mowbray, M.; McLintock, S.; Weerakoon, R.; Lomatschinsky, N.; Jones, S.; Rossi, A. G.; Weller, R. B. *J. Invest. Dermatol.* **2009**, *129*, 834.
(45) Palmer, R. M. J.; Ferrige, A. G.; Moncada, S. *Nature (London)* **1987**, *327*, 524.
(46) Scatena, R.; Bottoni, P.; Pontoglio, A.; Giardina, B. *Curr. Med. Chem.* **2010**, *17*, 61.
(47) Stamler, J. S.; Jia, L.; Eu, J. P.; McMahon, T. J.; Demchenko, I. T.; Bonaventura, J.; Gernert, K.; Piantadosi, C. A. *Science (Washington, DC, U. S.)* **1997**, *276*, 2034.
(48) Tennyson, A. G.; Lippard, S. J. *Chem. Biol.* **2011**, *18*, 1211.
(49) de Oliveira, M. G.; Shishido, S. M.; Seabra, A. B.; Morgon, N. H. *J. Phys. Chem. A* **2002**, *106*, 8963.
(50) Grossi, L.; Montevecchi, P. C. *Chem.—Eur. J.* **2002**, *8*, 380.
(51) Lü, J. M.; Wittbrodt, J. M.; Wang, K.; Wen, Z.; Schlegel, H. B.; Wang, P. G.; Cheng, J. P. *J. Am. Chem. Soc.* **2001**, *123*, 2903.

6.2 Mimicking a Photoswitch Environment through External Forces

Molecular switches based on *cis-trans* photoisomerization have been already used in different contexts in order to control diverse properties, ranging from peptide conformation to molecular data storage devices, from catalysis to smart materials. During the past years most of the attention has been focused on finding reliable synthetic routes to modify existing switches, in order to meet specific requirements. Among all synthesized and characterized photoswitches, we should mention azobenzenes, overcrowded alkenes, the hemithioindigo chromophore, the green fluorescent protein (GFP) chromophore and protonated Schiff bases (PSBs) based on the retinal chromophore of rhodopsins (*Klajn 2010; Bossi and Aramendia 2011*). Especially, the introduction of azobenzene derivatives and PSBs in peptides and proteins has led to photocontrol of folding and unfolding mechanisms. More in detail, once an azobenzene or PSB derivative is attached to two different residues of an amino acid sequence, UV or visible light irradiation can trigger the photoisomerization, leading to a large conformational change, with effects on the biological activity (*e.g.* interfering with the docking activity of a ligand to its binding site in a target protein). Usually, illuminating the photoswitch with a different wavelength ensures reversibility of the process, resulting in recovery of the initial conformation of the amino acid sequence (*Schrader et al. 2007; Schierling et al. 2010; Beharry et al. 2011; Blanco-Lomas et al. 2012*). Apart from biology, azobenzene was shown to undergo folding/unfolding processes also when incorporated into oligomers, generating the so called foldamers (*Khan and Hecht 2006; Khan et al. 2006; Russew and Hecht 2010; Yu and Hecht 2011; 2012*). One example is oligo(*meta*-phenylene ethynylene), where azobenzene photoswitching is responsible for control over helix-coil transition (*Khan and Hecht 2006*). More in general, the photoswitch is expected to play the role of a foldamer building block, with eventual applications in data storage and actuation.

Therefore, when studying the properties of a photoswitch, we have to pay attention to the effects of the environment where it is applied, since an isolated switch in solution can have different photophysical and

photochemical properties once attached to the backbone of a protein, and therefore result in relevant modifications of its applicability. For instance, the lowest-energy optically bright excited-state of an azobenzene or PSB based photoswitch is a $^1(\pi,\pi^*)$ state, determining a characteristic maximum absorption wavelength of the corresponding $S_0 \rightarrow S_n$ electronic transition which can be largely affected by the presence of eventual residues in the vicinity of the π-conjugated system. Also steric hindrance and the actual residues to which the photoswitch is chemically bound can produce relevant molecular distortions, when compared to the unbounded switch.

For this reason, if we are planning to predict the range of applicability of a certain photoswitch, the simulation of the environment effects becomes a priority. In this Thesis we realized a first step towards the solution of this difficult but necessary task by applying external forces to selected pairs of nuclei of a chromophore, in order to mimic the mechanical stress applied, *e.g.*, when chemically inserted into a peptide or protein. Therefore, this methodology does not take into account eventual electronic or steric effects caused by the medium, but is meant to give a description of the photoswitch behaviour under mechanical stress, identifying the limits for an eventual mechanical isomerization (*i.e.* isomerization provoked by the forces applied), as well as providing a tool to monitor eventual shifts in absorption energy.

We should mention that this approach was previously proposed for optimizing the geometry of a molecule (*Wolinski and Baker 2009; 2010*) and for on-the-fly dynamics, in order to perform mechanochemical studies *(Davis et al. 2009; Kryger et al. 2010; Lenhardt et al. 2010*). The novelty of our method consists in performing force constrained dynamics with analytical potential energy surfaces, therefore reaching considerably higher simulation times with respect to on-the-fly trajectories, at a lower computational expense.

6.2.1 Modulating the Spectroscopical Properties of an Azobenzene Switch by Molecular Dynamics

Azobenzene is composed by two phenyl groups connected by a N=N bond, therefore leading to *cis* and *trans* isomeric forms (Figure 6.1). The *trans* form is basically planar, being ca. 0.6 eV more stable than the *cis* form, where the benzene rings are twisted around the C-N bond to avoid steric hindrance (*Brown and Granneman 1975*).

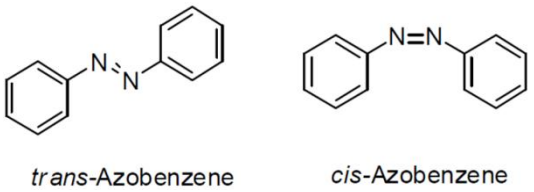

Figure 6.1 Azobenzene isomers.

The photophysics and photochemistry of this system has been extensively studied. The absorption spectrum shows a $^1(n,\pi^*)$ transition at 432 nm (440 nm) for the *trans* (*cis*) isomer, and a $^1(\pi,\pi^*)$ transition at 318 nm (290 nm) for the *trans* (*cis*) isomer (Lednev et al. 1996; Hamm et al. 1997; Lednev et al. 1998). Therefore, visible and near-UV regions are interested by the absorption process. About the photochemistry, isomerization was found to be an ultrafast process for both *cis*-to-*trans* (170 fs) and *trans*-to-*cis* (320 fs) conformational changes (*Naegele et al. 1997; Ishikawa et al. 2001*). The photoisomerization quantum yield measured in *n*-hexane points to higher values when exciting to the $^1(n,\pi^*)$ state (0.40 for *trans*-to-*cis* and 0.53 for *cis*-to-*trans*) than to the $^1(\pi,\pi^*)$ state (0.12 for *trans*-to-*cis* and 0.25 for *cis*-to-*trans*) (*Bortolus and Monti 1979; Siampiringue et al. 1987*). This fact can be eventually explained by different photoisomerization mechanisms initiated in either $^1(n,\pi^*)$ or $^1(\pi,\pi^*)$ states.

In spite of a large number of experimental and theoretical studies which clarified azobenzene excited-state mechanisms (*Monti et al. 1982; Naegele et al. 1997; Fujino and Tahara 2000; Fujino et al. 2001; Ishikawa et al. 2001; Cembran et al. 2004; Ciminelli et al. 2004; Chang et al. 2004; Gagliardi et al. 2004; Satzger et al. 2004; Toniolo et al. 2005; Conti et al. 2008; Pederzoli et al. 2011*), few attempts were made in order to determine

accurately the ground-state potential energy surface. In a recent work (*Klug and Burcl 2010*) the rotational barriers in azobenzene are calculated by DFT methods, connecting transition states and minima by constrained optimization, starting from a geometry slightly displaced from the transition state geometry along the vibrational eigenvector corresponding to the imaginary frequency. In this Thesis, the approach proposed by Klug and Burcl was improved, calculating the reaction path by integrating the intrinsic reaction coordinate, leading to a minimum energy path description of all rotational barriers. The azobenzene ground-state PES, calculated at the CAM-B3LYP/6-311+G(d,p) level of theory, is schematically shown by energy levels in Figure 6.2. In accordance with previous studies, a transition state structure (TS_{tc}) was found to be responsible for *cis-trans* isomerization, being characterized by an almost linear N=N–C_1 angle and the phenyl ring containing C_1 perpendicular to the rest of the molecule. By calculating the reaction paths from TS_{tc} we found two previously unreported saddle points of order higher than two (SP_t and SP_c). These structures are characterized, with respect to TS_{tc}, by a sort of translation of the perpendicular phenyl ring upwards (SP_t) or downwards (SP_c) of the N=N bond, starting to define which will be the final isomer. By calculating the numerical energy gradient vector with different step sizes for differentiation (0.01 Å, 0.02 Å, 0.03 Å), we were able to define only one reaction path for each SP, pointing down in energy and connecting to a transition state which defines the rotational barrier between the two iso-conformers (TS_t for *trans* and TS_{c1} for *cis*). Actually, a second transition state was found at slightly lower energy for the *cis* isomer (TS_{c2}), implying a simultaneous rotation of both phenyl rings from the stable *cis* conformation, in order to reach a symmetric transition state with respect to the N=N bond.

As a result, only 5 kcal·mol^{-1} (2 or 3 kcal·mol^{-1}) are required to overcome rotational barriers for the *trans* (*cis*) form, while a considerable energy of 41 kcal·mol^{-1} (26 kcal·mol^{-1}) is needed to undergo a *trans*-to-*cis* (*cis*-to-*trans*) isomerization on the ground-state.

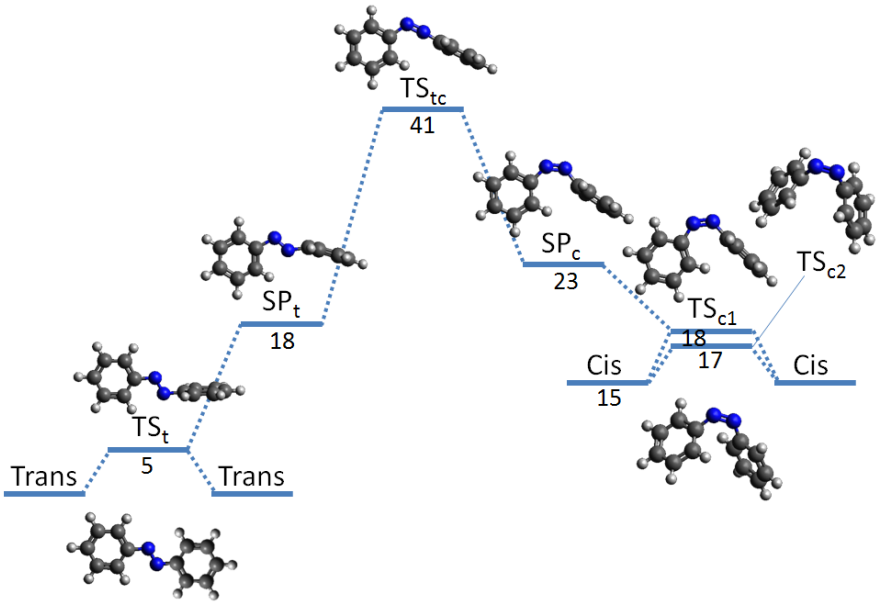

Figure 6.2 Scheme of the azobenzene ground-state potential energy surface, including all stationary points and the relative energy in kcal·mol^{-1} with respect to the most stable isomer.

An exhaustive study of the ground-state was considered fundamental in order to determine quantitatively which is the minimum external force that will cause a mechanically driven isomerization of azobenzene, and which is the maximum external force which can be applied before a bond is broken or van der Waals contact distance is reached.

In this study, the external force was applied to the two carbon atoms of the benzene rings in *para* position with respect to the N=N moiety, in order to simulate the usual environment of azobenzene as a photoswitch in peptides and proteins. The direction of the applied force is therefore the line connecting the two selected atoms. This leads to two possible mechanical stresses: elongation and compression. As shown in Figure 6.3, on the one hand elongation of the *cis* isomer or compression of the *trans* isomer will determine the minimum force for mechanical isomerization; on the other hand, elongation of the *trans* isomer or compression of the *cis* isomer will result in a constant increase of energy,

leading to the maximum force which can be applied before bond breaking or high interatomic repulsion.

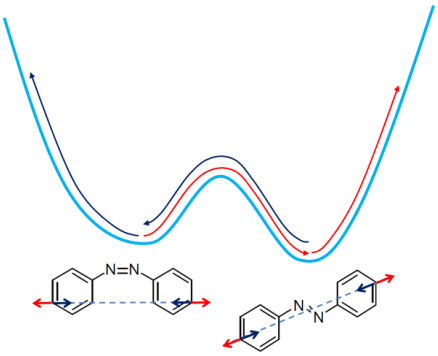

Figure 6.3 Scheme of compression (blue arrows) and elongation (red arrows) forces applied to azobenzene, with consequent response on a simplified ground-state potential energy surface.

A quantitative determination of such minimum and maximum forces was performed as follows: starting from the S_0 minimum structure, the geometry was optimized while constrained at a differently compressed or elongated carbon-carbon distance (by steps of 0.2 Ångström, *i.e.* 0.1 Ångström per benzene ring), in order to determine the minimum energy structures subjected to that externally applied forces. By calculating the force for each optimized structure, we can finally determine minimum and maximum values for azobenzene. As shown by force-strain curves (Figure 6.4), the minimum force is 5.41 nN for *cis*-to-*trans* and 2.69 nN for *trans*-to-*cis* mechanical isomerization; the maximum force which can be applied before reaching the van der Waals contact distance within the *cis* isomer is 19.50 nN, and 6.84 nN before bond breaking of the *trans* isomer.

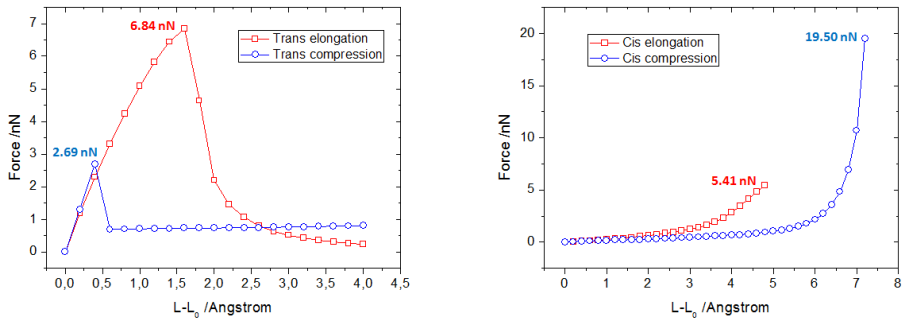

Figure 6.4 Force vs. carbon-carbon strain (L_0 corresponds to the equilibrium structure) curves for *cis* (right) and *trans* (left) azobenzene isomers. Elongation tests (red) and compression tests (blue) are shown.

When looking at elongation and compression tests (Figure 6.4), we observe force-strain curves typical of thermoplastic materials, with an interesting difference between *cis* and *trans* isomer: the force-strain curves of the *cis* isomer reproduce the behaviour of a semicrystalline thermoplastic, while the force-strain curves of the *trans* isomer reproduce the behaviour of a glassy (*i.e.* amorphous) thermoplastic. This could be of interest for the design of photoactive materials, especially photoactive polymers. Indeed, physical and engineering properties of thermoplastics (molding performance, behaviour of the polymer during processing) mainly depend on the molecular structure. Especially in case of a glassy thermoplastic, characterized by a highly disordered solid state structure, a ductile behaviour is expected: the initial nearly-linear portion of the force-strain curve (corresponding to a stress-strain curve in case of macroscopic sample testing) is the elastic region and the slope is the Young's modulus. After the yield point, the force decreases because of limited interaction forces between the polymer chains (Figure 6.4, left), eventually leading to the breaking point. On the other hand in case of a semicrystalline thermoplastic, characterized by a much more ordered structure in the solid state, a brittle behaviour is expected: the force-strain curve do not show any yield point, since the maximum applicable force corresponds to the breaking point (Figure 6.4, right). The novelty here is the eventual possibility to address specific polymer properties by the characterization of

the single monomer, *i.e.* not requiring a model of the overall (bulk phase) polymer.

Once established such limits imposed by the current PES, we can try to answer to the following question: among the force vectors with a module below the defined upper limits, which is the minimum force which can be applied to obtain the maximum shift in absorption energy? Answering this question, we can set a "*photo-response minimum force principle*", which can be of interest to define spectroscopical properties within proteins and, more in general, materials.

Especially, we will focus on the construction of analytical PESs, where classical molecular dynamics simulations are then performed: the PESs of ground and excited-states were built by a quadratic expansion centered on *cis* and *trans* isomer minimum energy structure, by calculating energy gradient and Hessian matrix at the Franck–Condon geometry, and resulting in the analytical expressions (functions of internal coordinates) shown previously in eq. 6.6 and 6.7. To validate this method, the actual CAM-B3LYP/6-311+G(d,p) ground-state energy was computed for a statistic number of geometries (500) which form the calculated trajectory on the analytical PES, in order to determine the error committed by applying a quadratic approximation: 0.85 ± 0.24 kcal·mol^{-1} when applying elongation forces at 1 nN on the trans isomer. To improve this approach, we are actually considering the possibility to build analytical surfaces by interpolation of chemically meaningful structures (*i.e.* energy minima and transition states).

Classical molecular dynamics simulations were computed on the ground-state analytical surface, applying a recently developed methodology (*Zapata et al. 2012*): a canonical ensemble was reproduced by expanding the actual Hamiltonian through the Nosé–Hoover method, which permits to include in the Hamiltonian the required degrees of freedom to simulate a thermostat (*Tuckerman et al. 2001*). This results in a canonical distribution of the harmonic oscillators that form the potential of the molecular system. The equations of motion were integrated by a time reversible integrator, applying the Liouville approach through the Trotter factorization (*Martyna et al. 1996*).

The following procedure was adopted for calculating the absorption spectrum: as first, the lowest and the highest vertical excitation energies

recorded during the dynamics determine the width of the spectrum. The spectrum is then divided into equal intervals of energy covering the whole width, defining the sensitivity of the spectrum. Finally, the vertical excitation energy is determined for each geometry of the dynamics, and assigned to the correspondent energy interval. Therefore, the absorption spectrum results in a histogram of relative intensity as a function of the excitation energy. The relative intensity of $S_0 \rightarrow S_1$ and $S_0 \rightarrow S_2$ vertical transitions is obtained by multiplying oscillator strength *f* times the number of geometries corresponding to a defined excitation energy interval. As expected, the *f* values for $S_0 \rightarrow S_1$ transitions are lower than for $S_0 \rightarrow S_2$, resulting in $^1(n,\pi^*)$ and $^1(\pi,\pi^*)$ transitions, respectively (Table 6-1).

Table 6-1 Oscillator strength (*f*) values for *cis* and *trans* azobenzene isomers at their Franck–Condon geometries. Calculations performed by TD-CAM-B3LYP/6-311+G(d,p) level of theory.

Isomer	$f \cdot 10^{-3}$	
	$S_0 \rightarrow S_1$	$S_0 \rightarrow S_2$
Cis	23	140
Trans	0.01	779

Also for excitation energies, as it was done for ground-state energies, a comparison between predicted (by our method) and calculated absorption energies was performed, resulting in a quantitative remarkable agreement: an error of 0.31 ± 0.11 kcal·mol^{-1} for $S_0 \rightarrow S_1$ (0.38 ± 0.19 kcal·mol^{-1} for $S_0 \rightarrow S_2$) was found when applying elongation forces at 1 nN on the *trans* isomer.

Here, we show the absorption spectra resulting from 1 ns trajectories (10^6 integration steps in total) at a temperature of 300 K, obtained when applying a set of different elongation forces to *trans* azobenzene (the most stable conformer) spanning from 0.1 nN to 6.8 nN (Figure 6.5). The study includes $^1(n,\pi^*)$ and $^1(\pi,\pi^*)$ electronic transitions ($S_0 \rightarrow S_1$ and $S_0 \rightarrow S_2$, respectively).

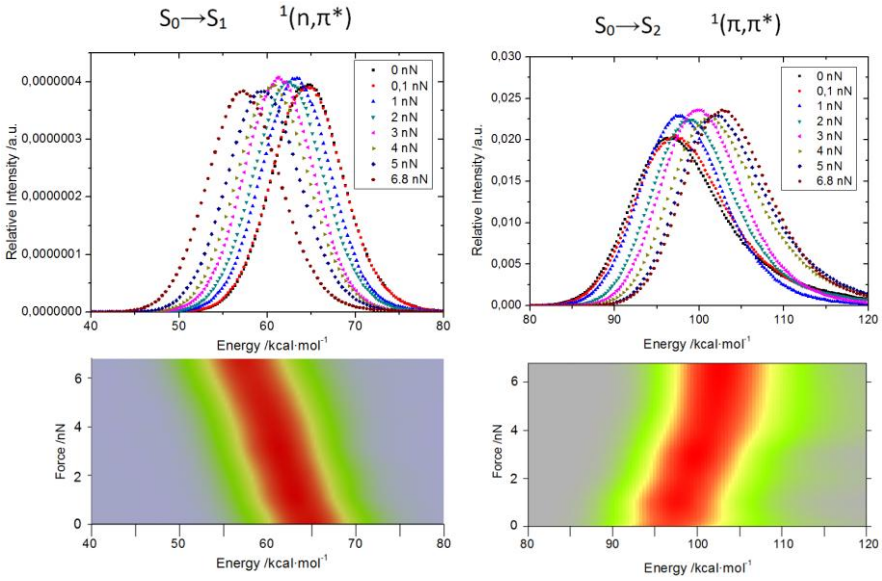

Figure 6.5 *Trans* azobenzene absorption spectra when applying different elongation forces. The results are shown for $S_0 \rightarrow S_1$ (left) and $S_0 \rightarrow S_2$ (right) electronic transitions, with two different types of graph: relative intensity as function of the energy (up) and an image plot where the relative intensity is indicated by colors (increasing from grey, to green, to red) for different energies and applied forces (down).

As shown in Figure 6.5, a force of 0.1 nN does not affect the absorption spectrum which, basically, remains the same as for the unbound *trans* azobenzene. Nevertheless, by increasing the elongation force up to 6.8 nN (which corresponds to the maximum force applicable before bond breaking) a modification of the absorption properties is recorded, clearly indicating a force induced modulation. Especially, a bathochromic shift of ca. 8 kcal·mol^{-1} is shown for the $^1(n,\pi^*)$ electronic transition (from 65 to 57 kcal·mol^{-1}), while a hypsochromic shift of ca. 7 kcal mol^{-1} is shown for the $^1(\pi,\pi^*)$ electronic transition (from 96 to 103 kcal·mol^{-1}).

The elucidation of different possible effects caused by elongations and compression forces on azobenzene constitutes a subject of ongoing work.

7. Summary and Conclusions

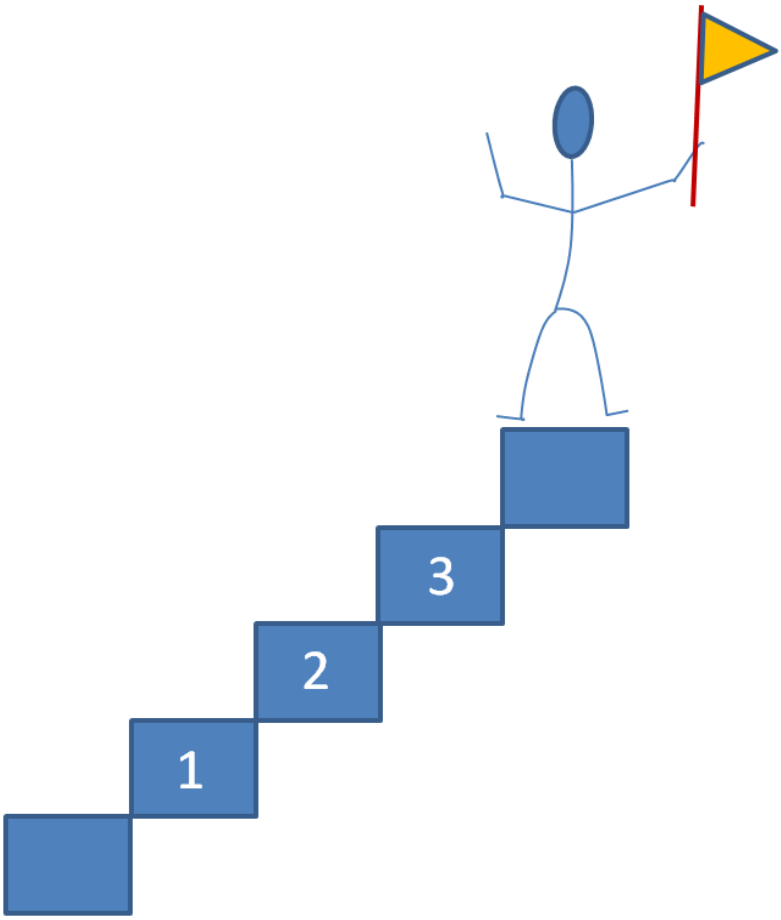

"I am utterly convinced that Science and Peace

will triumph over Ignorance and War"

Louis Pasteur

In this Thesis mechanistic, dynamical and methodological studies are presented, in order to introduce novelties within the research area of photochemistry and photophysics. Especially, attention has been focused on reactions induced by visible and UV light in chemical and biologically relevant systems. The studied phenomena can be summarized as follows:

- Photostability mechanisms within amino acids and proteins have been analyzed, including a $(Gly)_2$ minimal system and the solvated protein of human γB-crystallin, forming the eye lens. In both cases, forward-backward electron coupled proton transfer was found to be the most favorable mechanism, in competition with singlet-singlet Dexter-type energy transfer, allowing population of an initially dark optical state.
- More in general, Dexter-type energy transfer mechanisms between a donor and an acceptor molecule have been studied with the aim of defining an energy transfer reaction coordinate. Special attention has been focused on nonvertical excitation processes studying, as example, triplet-triplet energy transfer (TET) when *cis*-stilbene is an acceptor molecule: a geometrical distortion parameter has been proposed as a quantitative measurement of the nonvertical character, moreover determining the contribution (and therefore the importance) of each individual internal coordinate.
- The substituent effect has been evaluated with respect to the excitation energy of a series of S-nitrosothiols, leading to the conclusion that modulation of nitric oxide release (through S-nitrosothiols photoactivation) is possible, and of potential interest in the design of specific molecules for phototherapies.

All studies were performed applying methods belonging to theoretical and computational chemistry. More in detail, *ab initio* multiconfigurational methods (CASSCF, CASPT2) were applied for an accurate description of electronically excited-states, including the characterization of electronic state crossings. When necessary, the effect of the environment was included through hybrid quantum mechanics/ molecular mechanics modeling.

Different theoretical developments have been proposed:

- In order to improve the CASPT2//CASSCF methodology, a novel method has been developed based on the scaling of the CASSCF energy gradient, in order to approximate the CASPT2 energy gradient. Especially, the proposed method has been implemented for excited-state dynamics, including "on the fly" scaling of the CASSCF energy gradient, and applied to describe the photoisomerization of a retinal model.
- A methodology for the quantitative prediction of excitation energies for substituted chromophores on the basis of ground-state structures has been developed. The formalism introduces the concept of "structural substituent excitation energy effect", since it can be applied only if the chemical substitution does not affect the nature of the electronic excitation, where the substituent effect can be understood as a force acting on the chromophore and provoking a structural change on it. The proposed methodology has been applied to the prediction of the excitation energy to the lowest optically bright state of several S-nitrosothiols.
- A routine to (*i*) predict the maximum forces applicable to a molecular photoswitch, (*ii*) calculate ground-state dynamics on an analytical PES while applying external forces and (*iii*) determine the absorption spectrum has been developed. Its application to azobenzene showed the possibility to tune the absorption maxima assigned to $^1(n,\pi^*)$ and $^1(\pi,\pi^*)$ electronic transitions, for both *cis* and *trans* isomers.

8. Resumen y Conclusiones (Spanish Version)

El proyecto presentado en esta Tesis se basa en la aplicación y desarrollo de métodos teóricos y computacionales con el fine de describir la fotoquímica y la fotofísica de compuestos moleculares químicos y de relevancia biológica.

En particular, este proyecto puede dividirse en dos secciones:

La primera parte incluye la aplicación de métodos *ab initio* de tipo multiconfiguracional para la descripción cualitativa y cuantitativa de procesos fotoinducidos de transferencia de energía, electrónica y protónica. En este caso, el estudio ha sido orientado hacia moléculas que presentan enlaces de hidrógeno, siendo ésta una propiedad característica que proporciona (o por lo menos aumenta) la fotoestabilidad frente la radiación ultravioleta (UV) en aminoácidos, péptidos y proteínas.

La segunda sección surge de las limitaciones encontradas y/o del gasto computacional requerido para realizar cálculos de alto nivel de teoría en el estado excitado.

Más detalladamente, se lograron los siguientes objetivos:

i. Aplicación de la metodología CASPT2//CASSCF al estudio de un modelo de la conformación giro-β, formado por dos glicinas enlazadas a través de un enlace de hidrógeno. Así, se consiguió calcular los caminos de mínima energía encontrados a partir de la irradiación UV que permiten finalmente, la disipación de la energía de excitación como energía vibracional.

ii. Aplicación de la metodología CASPT2//CASSCF/AMBER al estudio de mecanismos de fotoestabilidad en la proteína γB-cristalina, que forma (junto con otras proteínas cristalinas) el cristalino del ojo humano. Especialmente, se destaca el papel que puede jugar el elemento denominado "*Tyrosine corner*", una parte seleccionada de la cadena proteica que permite un giro de aproximadamente

180° a través de un enlace de hidrógeno entre la cadena principal y el grupo lateral de una tirosina.

iii. Propuesta de una definición de coordenada de reacción para procesos de transferencia de energía de tipo Dexter (intercambio electrónico) entre una molécula dadora y una aceptora, dentro del límite de un acoplamiento electrónico débil. El método se aplicó al caso, muy debatido, de transferencia de energía triplete-triplete *no-vertical* con el *cis*-estilbeno como molécula aceptora.

iv. Con el objetivo de superar los límites impuestos por el gradiente de la energía CASPT2 de tipo numérico y de mejorar la metodología CASPT2//CASSCF, se ha propuesto un esquema de escalamiento del gradiente de la energía CASSCF, aplicándolo a modelos del retinal (el cromóforo presente en la rodopsina). Finalmente, se implementó este método propuesto en un programa para dinámicas en el estado excitado.

v. Desarrollo de un método de determinación cuantitativa de la energía de excitación de un cromóforo con diferente sustitución, en el caso de que la sustitución química afecte al cromóforo sólo a nivel estructural y no a la naturaleza electrónica del estado excitado considerado.

vi. Aplicación del concepto antes mencionado de *efecto sustituyente de tipo estructural sobre la energía de excitación* a una amplia serie de S-nitrosotioles, con el objetivo de predecir sus capacidades de liberar óxido nítrico. Los resultados finales sugieren una evidente tendencia en favor de una posible modulación del espectro de absorción.

vii. Tratamiento de los efectos del entorno sobre un interruptor molecular inducido por luz, como fuerzas externas que actúan en los dos extremos del cromóforo. En el caso del azobenceno (uno de los interruptores moleculares inducidos por luz más empleado), los isómeros *cis* y *trans* muestran una fotosensibilidad considerable

respecto a las fuerzas aplicadas, permitiendo la modulación de la longitud de onda del máximo de absorción.

Los enlaces de hidrogeno resultan ser cruciales en la determinación de la conformación y función biológica del ADN y proteínas (*Jeffrey and Saenger 1991*): las bases nitrogenadas del ADN se aparean (adenina-timina, citosina-guanina) formando enlaces de hidrogeno (Figura 8.1); en las proteínas, los grupos C=O y N–H de la cadena principal pueden formar enlaces de hidrogeno (C=O···H–N) entre distintos aminoácidos del mismo polipéptido (Figura 8.1b) que contribuye de manera determinante al tipo de estructura secundaria (hélice-α, β-láminas, etc.) y resultan cruciales en procesos tales como la regulación de la actividad enzimática (a través del reconocimiento de substratos durante la formación de complejos proteicos (*Lyon et al. 2002; Pal and Zewail 2004*)) o la catálisis de reacciones químicas (ej. anhidrasa carbónica (*Lu and Voth 1998*), serín proteasa (*Warshel et al. 1989*), alcohol deshidrogenasa (*Sekhar and Plapp 1988*)).

A parte de la importancia primaria a nivel estructural y funcional, los enlaces de hidrogeno se han propuesto como elementos que pueden conferir estabilidad a un sistema químico o biológico frente a la exposición a la radiación-UV (fotoestabilidad) (*Sobolewski et al. 2005*). La radiación-UV constituye un serio riesgo para distintos sistemas moleculares, causando cambios estructurales y conformacionales que pueden implicar la pérdida de la función o actividad característica de dicho sistema. Por lo tanto, investigar eventuales mecanismos viables de fotoestabilidad en moléculas de relevancia biológica es de primaria importancia para (a) mejorar nuestro conocimiento de los procesos biológicos y (b) eventualmente, proponer modificaciones químicas de aquellas biomoléculas que sufran daños por irradiación-UV (ej. el colágeno en la piel o el cristalino en el ojo de los mamíferos superiores), con la finalidad de conferirles la capacidad de disipar la energía absorbida de manera ultrarrápida.

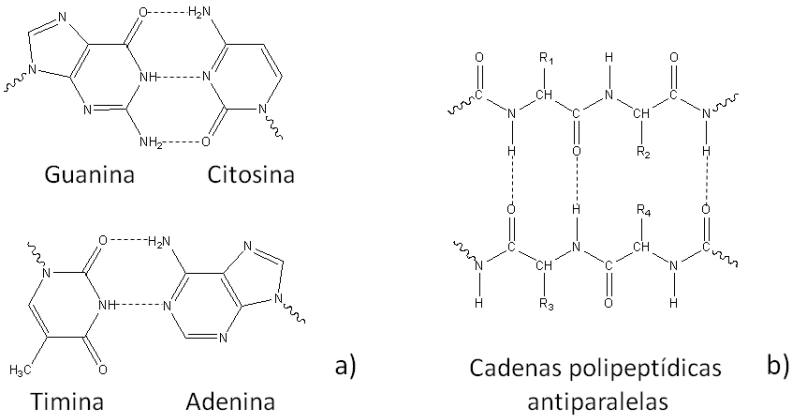

Figura 8.1 Enlaces de hidrógeno entre los pares de bases del ADN (**a**), y entre cadenas polipeptídicas antiparalelas (**b**). R_n: grupo lateral del n-ésimo aminoácido.

La viabilidad del mecanismo de transferencia protónica fotoinducida ha sido estudiada a través de métodos, teóricos y experimentales, en sistemas modelo de las bases del ADN (*Frutos et al. 2007; Zhang et al. 2009*). Sin embargo, la elucidación del mismo en proteínas (*Shemesh et al. 2009*) presenta distintos inconvenientes: un mismo péptido puede adoptar una conformación tridimensional distinta según su entorno biológico además de que el carácter ultrarrápido del proceso pone límites de resolución temporal (del orden de femtosegundos, 10^{-15} s) a estudios experimentales. Por lo tanto, el uso de métodos de química computacional para el estudio de este proceso en un sistema proteico modelo permite solventar dichos inconvenientes ofreciendo una explicación detallada del mecanismo a nivel molecular.

En esta Tesis se aplican métodos pertenecientes a la química cuántica y computacional. Más detalladamente, se han elegido métodos *ab initio* multiconfiguracionales para construir superficies de energía potencial tanto en el estado electrónico fundamental como en los distintos estados electrónicos excitados requeridos para describir la fotoquímica del sistema modelo.

Si se representa la energía potencial en función de la posición relativa *r* de cada uno de los *N* átomos que componen el sistema molecular, el espacio multidimensional resultante (3*N*-6 dimensiones) constituye un campo de fuerzas a través del cual es posible describir los cambios estructurales de las moléculas, la ruptura y la formación de enlaces.

En una reacción fotoquímica convencional, una molécula en el estado electrónico fundamental absorbe un fotón, produciéndose la transición vertical de Franck−Condon a un estado electrónico excitado. La verticalidad de la transición electrónica se debe a la aproximación de Born−Oppenheimer, que permite desacoplar el movimiento relativo de electrones y núcleos: al ser la masa de los núcleos mucho mayor que la de los electrones (un protón es ca. $0{,}18 \cdot 10^4$ veces más pesado de un electrón). De esta manera, se pueden considerar los núcleos como estáticos con respeto a la nube de carga electrónica, cuyo movimiento es mucho más rápido. A la absorción fotónica le sigue un proceso de relajación vibracional en la superficie de energía potencial (SEP) del estado electrónico excitado, hasta alcanzar el nivel vibracional fundamental, es decir, desde el punto de vista de las SEP un punto estacionario, donde los gradientes de la energía son nulos: la fuerza que actúa sobre cada átomo es cero. Un punto estacionario puede corresponder a un mínimo, a un estado de transición o a otro punto crítico de orden superior de la SEP, permitiendo así la explicación del fenómeno de emisión (Figura 8.2a). Las SEPs involucradas en el mecanismo son superficies adiabáticas, en cuanto a que cada punto corresponde a una geometría fija del sistema molecular donde el movimiento de electrones y núcleos está completamente desacoplado (aproximación de Born−Oppenheimer).

En el caso de procesos fotoquímicos ultrarrápidos, se ha demostrado experimentalmente (a través de espectroscopia de femtosegundo), así como teóricamente, que las reacciones implican regiones de cruce entre SEPs, donde es posible estudiar el acoplamiento entre distintos estados electrónicos. Desde el punto de vista físico, esta situación corresponde a una degeneración en energía entre dos (o más) SEPs, que se deriva del hecho de que cuando el sistema pasa a través del cruce, los electrones no consiguen reorganizarse en una escala de tiempos mucho menor respeto a lo que hacen los núcleos. Este hecho hace que la aproximación de Born−Oppenheimer no sea válida y que las superficies se definan como no-adiabáticas. Se puede demostrar matemáticamente (Herzberg and Longuet-Higgins 1963) que el cruce entre dos estados electrónicos requiere la existencia, en la región de cruce, de dos magnitudes independientes representadas a través de dos vectores: el vector diferencia de gradiente (*Gradient Difference,* **GD**) que mide la

distorsión del sistema en la dirección de mayor variación de la diferencia en energía entre los dos estados electrónicos que se cruzan, y el vector de acoplamiento entre estados (*Derivative Coupling,* **DC**) que mide la distorsión del sistema que asegura un máximo acoplamiento entre los estados electrónicos involucrados. **GD** y **DC** definen un plano de intersección (*branching plane*) de tal manera que cualquier distorsión del sistema en este plano hace desaparecer la condición de degeneración energética. Por el contrario, en el restante hiperespacio de dimensión 3*N*-8, cualquier movimiento queda contenido dentro de la región de cruce, manteniéndose la degeneración. La ecuación resultante que expresa la topología de las superficies de energía potencial en función de **GD** y **DC** tiene forma de doble cono (Figura 8.2b), y por tanto el punto de cruce se conoce como intersección cónica (*Conical Intersection, CI*).

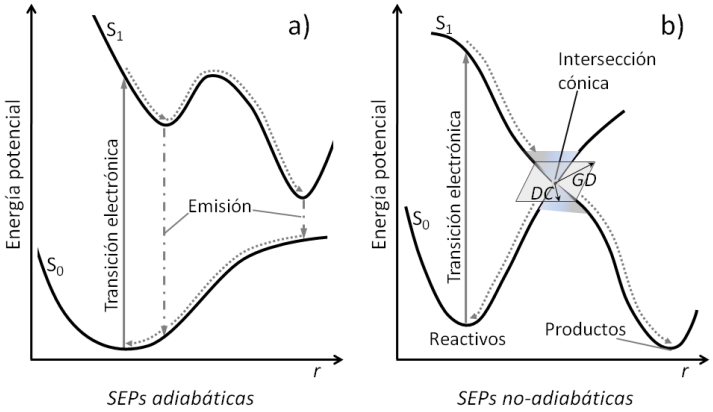

Figura 8.2 (**a**) Mecanismo de excitación del estado electrónico fundamental S_0 al estado electrónico excitado S_1 y sucesiva emisión ($S_1 \rightarrow S_0$), explicado a través de superficies de energía potencial adiabáticas. (**b**) Esquema de una reacción fotoquímica ultrarrápida: a la absorción $S_0 \rightarrow S_1$ le sigue la relajación vibracional del sistema hasta encontrar una intersección cónica, que permite volver a S_0 formando los productos de reacción o regresar hacia los reactivos. Los vectores *GD* y *DC* caracterizan el espacio de cruce.

Entre los métodos *ab initio*, se ha elegido la metodología multiconfiguracional CASPT2//CASSCF. La función de onda multielectrónica CASSCF (*Complete Active-Space Self-Consistent Field*) es de tipo multiconfiguracional ya que se define como la combinación lineal de distintas configuraciones electrónicas. La función incluye todas las posibles excitaciones electrónicas dentro del espacio activo seleccionado, que

contiene los electrones y orbitales moleculares de interés químico para el sistema en estudio. Fuera del espacio activo, los orbitales inactivos permanecen doblemente ocupados y los secundarios (o virtuales) desocupados. La función de onda CASSCF así calculada, constituye la referencia de la función de onda CASPT2 (*Complete Active-Space Perturbation-Theory to the second order*) que incluye la correlación electrónica dinámica, permitiendo obtener energías de excitación de carácter cuantitativo.

La metodología CASPT2//CASSCF (*Andersson et al. 1990*) consiste en calcular los caminos de mínima energía y caracterizar los espacios de cruce a nivel CASSCF, corrigiendo el valor de la energía de geometrías clave de los mecanismos encontrados a nivel CASPT2. En esta tesis se han usado los programas Gaussian 03, Gaussian 09 (*Frisch et al. 2004*), MOLCAS-6 y MOLCAS-7 (*Aquilante et al. 2010*).

A través de la metodología CASPT2//CASSCF se han estudiado las propiedades fotoquímicas y fotofísicas del péptido $(Gly)_3$ con una conformación de giro-β, el cual es un elemento estructural de interés en la estabilización de hojas-β antiparalelas. La estructura optimizada del tripéptido se ha considerado como referencia para reducir el tamaño del sistema molecular, con el fin de hacer asequible computacionalmente el estudio del sistema con la metodología descrita: se ha eliminado la glicina central del tripéptido, que no participa en el enlace de hidrogeno (Figura 8.3), y se ha substituido con una serie de restricciones que reproducen los cambios conformacionales del tripéptido. La estructura final, optimizada en el estado fundamental, permanece en conformación giro-β, como demuestra el puente de hidrogeno entre las glicinas **A** y **B** (*Marazzi et al. 2010; Marazzi et al. 2011*).

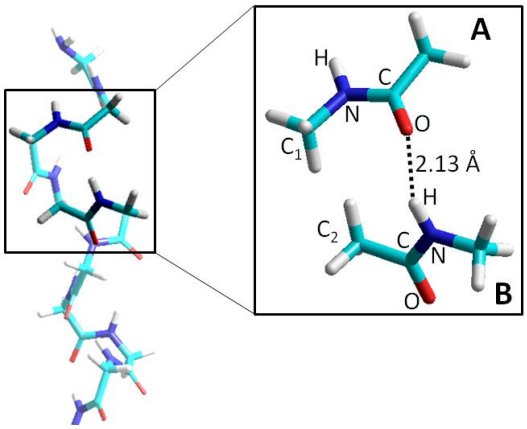

Figura 8.3 Sistema modelo en el estado electrónico fundamental. La posición relativa de los grupos metilos C_1 y C_2 está sometida a restricciones para reproducir la conformación giro-β a través de las glicinas **A** y **B**.

Para una descripción exhaustiva de los estados electrónicos excitados en el modelo propuesto, se ha elegido un espacio activo de 12 electrones en 8 orbitales moleculares, incluyendo de esta manera los estados de naturaleza π,π^* y n,π^*.

Un posible proceso fotofísico que puede tener lugar es la transferencia de energía entre las dos glicinas, que se verifica si dos estados excitados, pertenecientes cada uno a una glicina, se cruzan con un acoplamiento electrónico significativo. El camino de mínima energía, después de la excitación, en el estado excitado $^1(\pi,\pi^*)_A$ indica una relajación vibracional hasta alcanzar un cruce con el estado $^1(n,\pi^*)_B$ (Figura 8.4). La estructura correspondiente al cruce revela cómo ambas glicinas tienden a distorsionar sus geometrías con respecto al estado fundamental: en la glicina **A**, el carbono del enlace peptídico piramidaliza, reorientando el grupo C=O con respecto al grupo N–H de la glicina **B**, la cual se distorsiona de manera complementaria para favorecer el alineamiento del enlace O···H. Como indican los vectores **GD** y **DC**, que son paralelos (resultando en un espacio de cruce unidimensional), el mecanismo implica el acoplamiento de los modos de estiramiento de los grupos C=O, permitiendo la transferencia de energía de la glicina **A** a la **B**. A nivel electrónico, el proceso comporta una migración de energía desde el estado $^1(\pi,\pi^*)_A$, inicialmente poblado a

través de una transición vertical (absorción), al estado $^1(n,\pi^*)_B$. Después de la transferencia de energía, el sistema puede regresar a su geometría inicial (Franck–Condon).

No obstante el acoplamiento entre los estados $^1(\pi,\pi^*)_A$ y $^1(n,\pi^*)_B$ no es despreciable, el módulo del vector **GD** resulta ca. 10 veces mayor que el módulo del vector **DC**, indicando que la mayoría de los paquetes de onda que pasen por el cruce deberían mantenerse en el estado $^1(\pi,\pi^*)_A$, hasta alcanzar un punto de mínimo de la SEP (Figura 8.4).

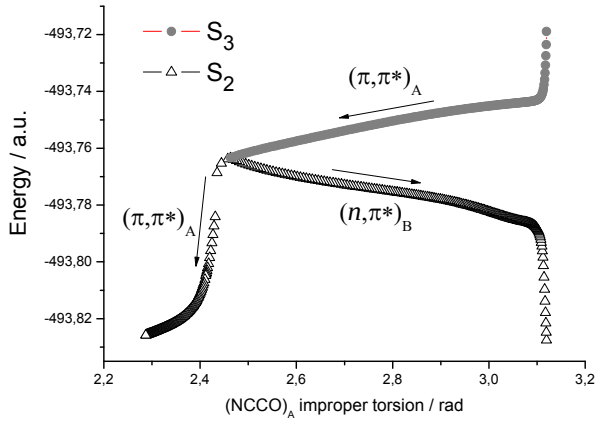

Figura 8.4 Mecanismo de transferencia de energía desde la glicina **A** a la **B** a través de un cruce entre las SEPs correspondientes a los estados singlete S_3 y S_2.

2 kcal·mol^{-1} por encima en energía del mínimo en el estado $^1(\pi,\pi^*)_A$, se ha localizado un cruce entre $^1(\pi,\pi^*)_A$ y un estado de transferencia de carga, $^1(\pi_B\rightarrow\pi_A^*)$. El punto de cruce, donde los vectores *GD* y *DC* son paralelos, actúa como un estado de transición accesible entre los estados $^1(\pi,\pi^*)_A$ y $^1(\pi_B\rightarrow\pi_A^*)$, permitiendo la transferencia de un electrón desde la glicina **B** a la **A**, generando así una separación de carga entre los dos aminoácidos. Para compensar la separación de carga, el protón de la glicina **B** se desplaza hacia el oxígeno de la glicina **A**, rompiendo simultáneamente el enlace con el nitrógeno de la glicina **B**.

El proceso de relajación vibracional en el estado de transferencia de carga conduce a una primera intersección cónica con el estado ópticamente oscuro $^1(n,\pi^*)_A$ (de acoplamiento prácticamente nulo), y una segunda intersección cónica con el estado fundamental, que permite al sistema

volver a la geometría inicial: un electrón se transfiere desde la glicina **A** a la **B** al pasar del estado $^1(\pi_B \rightarrow \pi_A^*)$ al estado fundamental y, durante la relajación final hacia la geometría inicial, el protón sigue al electrón restableciendo el puente de hidrogeno C=O···H–N.

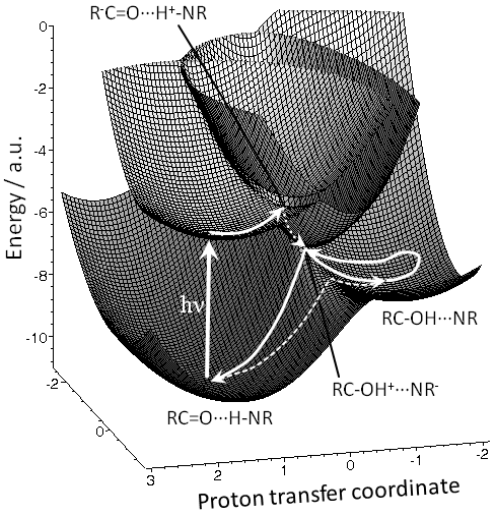

Figura 8.5 Mecanismo de transferencia protónica fotoinducida: transición vertical del estado fundamental (RC=O···H-NR) a un estado localmente excitado; cruce evitado entre el estado localmente excitado y un estado de transferencia de carga ($R^-C=O\cdots H^+$-NR); relajación vibracional e intersección cónica con el estado fundamental (RC-$OH^+\cdots NR^-$): el sistema puede volver a la región de Franck-Condon directamente o a través de un mínimo en el estado de transferencia de carga (RC-OH···NR), mediante un exceso vibracional.

En conclusión, dos mecanismos fotoinducidos son de potencial interés para conferir fotoestabilidad-UV a aminoácidos que presentan enlaces de hidrógeno: la transferencia protónica, que si está acoplada a la transferencia de carga da lugar a una transferencia (por pasos) de hidrógeno (Figuras 8.5, 8.6), y la transferencia de energía (Figura 8.4). Gracias al cálculo de los caminos de mínima energía y de la caracterización de los puntos de cruce entre estados electrónicos a nivel CASPT2//CASSCF, es posible concluir que los mecanismos propuestos tienen carácter ultrarrápido.

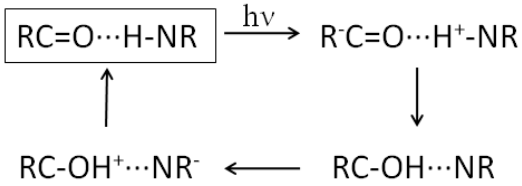

Figura 8.6 Mecanismo propuesto de transferencia protónica fotoinducida mediada por transferencia de carga (electrón).

El efecto de la radiación UV se ha estudiado también en un entorno proteico: el elemento "*Tyrosine corner*" ha sido propuesto como esencial para aumentar la fotoestabilidad de la proteína γB-cristalina, presente en el ojo humano (*Marazzi et al. 2012*). Más detalladamente, se estudiaron distintos procesos ultrarrápidos a través de métodos *ab initio* multiconfiguracionales acoplados con mecánica molecular (nivel de teoría CASPT2//CASSCF/AMBER): transferencia de energía singlete-singlete fotoinducida, transferencia electrónica y protónica fotoinducida, así como población y evolución de los estados triplete. Los caminos de mínima energía indican, como en el caso del sistema formado por dos glicinas, dos posibles eventos inducidos por irradiación UV: transferencia electrónica acoplada a transferencia protónica, proporcionando un mecanismo de conversión interna ultrarrápida, y transferencia de energía, que conduce a posible fluorescencia y fosforescencia. Los resultados obtenidos están de acuerdo con los datos experimentales disponibles, considerando los distintos posibles entornos de la tirosina dentro de la γB-cristalina.

Para un estudio mecanístico de la transferencia de energía, se ha propuesto una definición de coordenada de reacción para la transferencia de energía triplete-triplete, dentro del límite de un acoplamiento electrónico débil. Además, ha sido desarrollado el formalismo teórico para su evaluación cuantitativa en función de las coordenadas internas del sistema, junto con un protocolo para establecer cómo cada coordenada molecular controla el proceso de transferencia. El formalismo presentado permite la separación de las contribuciones del dador y del aceptor para formar la coordenada de reacción, permitiendo la identificación del papel

intrínseco atribuido a cada molécula en el proceso de transferencia de energía triplete.

Este formalismo puede ser aplicado a la transferencia de energía triplete tanto de tipo clásico como *no-vertical*, así como a cualquier reacción de transferencia de energía mediada por un mecanismo de intercambio electrónico.

Se ha ilustrado la utilidad de este novedoso formalismo para el análisis de uno de los casos conflictivos más conocidos de transferencia de energía triplete-triplete *no-vertical*, que involucra el *cis*-estilbeno como molécula aceptora, permitiendo la determinación del aporte de cada coordenada interna en dicho proceso de transferencia de energía.

Teniendo en cuenta las ventajas y los límites de la metodología CASPT2//CASSCF, se ha desarrollado un nuevo método para realizar dinámicas moleculares en el estado excitado, a través del escalamiento local del vector fuerza CASSCF, con el objetivo de generar un vector fuerza pseudo-CASPT2 a un coste computacional razonable, por lo tanto incluyendo los efectos debidos a la teoría de perturbación de segundo orden aplicada a una función de onda multiconfiguracional.

Para probar la validez y los límites del método propuesto, se ha seleccionado un modelo mínimo del retinal (2-*cis*-α-Me-$C_5H_6NH_2^+$) destacando, al mismo tiempo, diferencias y similitudes entre la descripción CASSCF y CASPT2 del mecanismo de isomerización *cis-trans* que conduce a una intersección cónica entre el estado excitado y el fundamental.

Los resultados demuestran que el método desarrollado es capaz de reproducir con éxito el proceso inicial de relajación vibracional que sigue a la absorción de un fotón en el estado excitado, siendo este el proceso donde la descripción CASSCF difiere más de la descripción CASPT2.

Además, se ha aplicado el método desarrollado a un modelo del retinal pre-torsionado, para analizar su conducta en el caso de que la fotoisomerización *cis-trans* sea inducida por un entrono externo (como en la rodopsina), siendo capaz de describir correctamente la región de intersección que permite la población del estado fundamental.

En general, el efecto sustituyente influye en el proceso de absorción de un cromóforo dado. En esta Tesis, se ha desarrollado una metodología

para predecir la energía de excitación de cromóforos sustituidos, considerando solo sus estructuras en el estado fundamental. El formalismo introduce el concepto de *efecto sustituyente de tipo estructural sobre la energía de excitación*, permitiendo alcanzar una predicción racional y una cuantificación del efecto sustituyente en el proceso de excitación de un cromóforo a un estado electrónico determinado. Este efecto cuantifica exclusivamente la variación en energía de excitación debida a cambios estructurales del cromóforo inducidos por el grupo sustituyente. Por lo tanto, es posible predecir desplazamientos batocrómicos e hipsocrómicos de cromóforos sustituidos, teniendo en cuenta las SEPs de los estados fundamental y excitado de un cromóforo de referencia no-sustituido, junto con la estructura de mínima energía en el estado fundamental del cromóforo sustituido.

Es posible aplicar el formalismo desarrollado siempre y cuando la sustitución química no afecte a la naturaleza de la excitación electrónica. En este caso, se puede interpretar el efecto sustituyente como una fuerza que actúa sobre el cromóforo y que provoca un cambio estructural del mismo. Por lo tanto, este formalismo proporciona un instrumento útil para la determinación cualitativa y cuantitativa de la energía de excitación de un cromóforo sustituido, así como el análisis y determinación de los cambios estructurales que la afectan.

Se ha aplicado la metodología propuesta para predecir la energía de excitación al primer estado ópticamente brillante de distintos S-nitrosotioles, usando las SEPs del metil-S-nitrosotiol como cromóforo de referencia no-sustituido (*Fernandez-Gonzalez et al. 2012*). Para esta familia de compuestos, ha sido también estudiada su fotoquímica y fotofísica, a través de métodos computacionales, por su importante característica de modulación de la energía de excitación (*Marazzi et al. 2012*).

Más detalladamente, se ha estudiado a nivel CASPT2 el mecanismo de ruptura inducida por luz del modelo metil-S-nitrosotiol (CH_3SNO) para liberar $CH_3S\cdot$ y $\cdot NO$, resultando ser un proceso energéticamente favorable (sin barreras) en tres distintos casos: irradiando en la región visible (S_1), irradiando en la región UV (S_2) y para una reacción activada por fotosensibilizadores (T_1).

La energía de absorción requerida para iniciar el proceso de ruptura ha sido calculada a nivel CASPT2 y B3P86 (TD-DFT), mostrando la posibilidad

de modular el proceso de liberación de NO en función del sustituyente R. En concreto, se han obtenido correlaciones aceptables entre las longitudes de onda pertenecientes a las transiciones $^1(n,\pi^*)$ y $^1(\pi,\pi^*)$ de más baja energía de los aril-S-nitrosotioles y las correspondientes constantes de Hammett de los sustituyentes.

Otro tema de estudio dentro de la modulación de la longitud de onda para iniciar procesos fotoinducidos es el efecto del entorno. Especialmente, en el caso de que se desee estudiar las propiedades de un interruptor molecular inducido por luz, los efectos del entorno son determinantes ya que el mismo interruptor en disolución o dentro de una proteína puede tener distintas propiedades fotoquímicas y fotofísicas, que modifiquen su aplicabilidad. Por lo tanto, si estamos planeando predecir el intervalo de aplicabilidad de un interruptor dado, la simulación de los efectos del entorno es una prioridad.

Por último, en esta Tesis, se propone la aplicación de un par de fuerzas en los dos extremos de un cromóforo, simulando el caso en el cual, por ejemplo, el cromóforo ha sido introducido en un péptido o proteína a través de la formación de enlaces covalentes. El límite de la metodología que se presenta es no tener en cuenta eventuales efectos electrónicos o estéricos causados por el medio. Sin embargo, esta metodología es capaz de describir el comportamiento de un interruptor molecular bajo estrés mecánico, permitiendo la identificación de los limites para una eventual isomerización mecánica y además, proporcionando una herramienta para monitorear eventuales cambios en la energía de absorción.

La herramienta desarrollada se aplicó al azobenceno, uno de los interruptores inducidos por luz de uso más común en bioquímica, demostrando que las fuerzas externas aplicadas pueden modular considerablemente el espectro de absorción tanto del isómero *cis* como del *trans*, para las transiciones verticales $S_0 \rightarrow S_1$ y $S_0 \rightarrow S_2$. Los resultados obtenidos, junto con la posibilidad de caracterizar las propiedades mecánicas de los dos isómeros a través del cálculo de la fuerza aplicada por cada intervalo en compresión y elongación, podrían ser de gran utilidad para diseñar materiales que posea respuestas morfológicas tanto al irradiar con distintas longitudes de onda como al aplicar distintas fuerzas mecánicas.

List of Publications

I. Marazzi, M.; Sancho, U.; Castaño, O.; Domcke, W.; Frutos, L. M.

Photoinduced Proton Transfer as a Possible Mechanism for Highly Efficient Excited-State Deactivation in Proteins

The Journal of Physical Chemistry Letters **2010**, *1*, 425–428.

II. Marazzi, M.; Sancho, U.; Castaño, O.; Frutos, L. M.

First Principles Study of Photostability within Hydrogen-Bonded Amino Acids

Physical Chemistry Chemical Physics **2011**, *13*, 7805–7811.

III. Marazzi, M.; Blanco-Lomas, M.; Rodríguez, M. A.; Campos, P. J.; Castaño, O.; Sampedro, D.; Frutos, L. M.

On the Mechanism of the Photocyclization of Azadienes

Tetrahedron **2012**, *68***,** 730–736.

IV. Marazzi, M.; Navizet, I.; Lindh, R.; Frutos, L. M.

Photostability Mechanisms in Human γB-Crystallin: Role of the Tyrosine Corner Unveiled by Quantum Mechanics and Hybrid Quantum Mechanics/Molecular Mechanics Methodologies

Journal of Chemical Theory and Computation **2012**, *8*, 1351–1359.

V. Marazzi, M.; López-Delgado, A.; Fernández-González, M. Á.; Castaño, O.; Frutos, L. M.; Temprado, M.

Modulating Nitric Oxide Release by S-Nitrosothiol Photocleavage: Mechanism and Substituent Effects

The Journal of Physical Chemistry A **2012**, *116*, 7039–7049.

VI. Fernández-González, M. Á.; Marazzi, M.; López-Delgado, A.; Zapata, F.; García-Iriepa, C.; Rivero, D.; Castaño, O.; Temprado, M.; Frutos, L. M.

Structural Substituent Effect in the Excitation Energy of a Chromophore: Quantitative Determination and Application to S-Nitrosothiols

Journal of Chemical Theory and Computation **2012**, 8, 3293–3302.

VII. García-Iriepa, C.; Marazzi, M.; Frutos, L. M.; Sampedro, D.

E/Z Photochemical Switches: Syntheses, Properties and Applications

RSC Advances **2012**, accepted.

VIII. García-Iriepa, C.; Marazzi, M.; Zapata, F.; Valentini, A.; Sampedro, D.; Frutos, L. M.

Chiral Hydrogen Bond Environment Providing Unidirectional Rotation in Photoactive Molecular Motors

The Journal of Physical Chemistry Letters **2012**, submitted.

List of Abbreviations

AC	Avoided Crossing
CASSCF	Complete Active-Space Self-Consistent Field
CASPT2	Complete Active-Space Perturbation Theory to the second order
CI	Configuration Interaction
CI	Conical Intersection
c-Stb	*cis*-stilbene
DC	Derivative Coupling
DFT	Density Functional Theory
DNA	DeoxyriboNucleic Acid
DPT	Double Proton Transfer
ET	Electron Transfer
ETPT	stepwise Electron Transfer followed by Proton Transfer
FRET	Förster Resonant Energy Transfer
GD	Gradient Difference
HF	Hartree–Fock
IR	Infra Red
IRC	Intrinsic Reaction Coordinate
IRD	Initial Relaxation Direction
MCSCF	Multiconfigurational Self-Consistent Field
MEP	Minimum Energy Path
MP2	Møller–Plesset Perturbation Theory to the second order
PCET	Proton Coupled Electron Transfer
PES	Potential Energy Surface
PT	Proton Transfer
PTET	stepwise Proton Transfer followed by Electron Transfer
r.h.s	right hand side
RSNO	S-Nitrosothiols

TD-DFT	Time Dependent-Density Functional Theory
TET	Triplet-triplet Energy Transfer
TET-RC	Triplet-triplet Energy Transfer - Reaction Coordinate
UV	Ultra Violet

Bibliography

Andersson, K., P.-A. Malmqvist, B. O. Roos, A. J. Sadlej and K. Wolinski (1990). "Second-order perturbation theory with a CASSCF reference function." J. Phys. Chem. **94**: 5483-5488.

Andruniow, T., N. Ferre and M. Olivucci (2004). "Structure, initial excited-state relaxation, and energy storage of rhodopsin resolved at the multiconfigurational perturbation theory level." Proc. Natl. Acad. Sci. U. S. A. **101**: 17908-17913.

Aquilante, F., V. L. De, N. Ferre, G. Ghigo, P.-a. Malmqvist, P. Neogrady, T. B. Pedersen, M. Pitonak, M. Reiher, B. O. Roos, L. Serrano-Andres, M. Urban, V. Veryazov and R. Lindh (2010). "MOLCAS 7: The Next Generation." J. Comput. Chem. **31**: 224-247.

Aquino, A. J. A., M. Barbatti and H. Lischka (2006). "Excited-state properties and environmental effects for protonated Schiff bases: a theoretical study." ChemPhysChem **7**: 2089-2096.

Atchity, G. J., S. S. Xantheas and K. Ruedenberg (1991). "Potential energy surfaces near intersections." J. Chem. Phys. **95**: 1862-1876.

Baer, M. (2006). "Beyond Born-Oppenheimer. Electronic Nonadiabatic Coupling Terms and Conical Intersections " John Wiley & Sons, Inc., Hoboken, New Jersey.

Balzani, V., A. Credi and M. Venturi (2004). "Molecular devices and machines." Phys. World **17**: 39-42.

Barbara, P. F., T. J. Meyer and M. A. Ratner (1996). "Contemporary Issues in Electron Transfer Research." J. Phys. Chem. **100**: 13148-13168.

Bartberger, M. D., J. D. Mannion, S. C. Powell, J. S. Stamler, K. N. Houk and E. J. Toone (2001). "S-N Dissociation Energies of S-Nitroso thiols: On the Origins of Nitroso thiol Decomposition Rates." J. Am. Chem. Soc. **123**: 8868-8869.

Basilevsky, M. V., G. E. Chudinov and M. D. Newton (1994). "The multi-configurational adiabatic electron transfer theory and its invariance under transformations of charge density basis functions." Chem. Phys. **179**: 263-278.

Beharry, A. A., L. Wong, V. Tropepe and G. A. Woolley (2011). "Fluorescence Imaging of Azobenzene Photoswitching In Vivo." Angew. Chem., Int. Ed. **50**: 1325-1327.

Benedek, G. B. (1997). "Cataract as a protein condensation disease: the Proctor Lecture." Invest Ophthalmol Vis Sci **38**: 1911-1921.

Bernardi, F., S. De, M. Olivucci and M. A. Robb (1990). "The mechanism of ground-state-forbidden photochemical pericyclic reactions:

evidence for real conical intersections." J. Am. Chem. Soc. **112**: 1737-1744.

Betzig, E., G. H. Patterson, R. Sougrat, O. W. Lindwasser, S. Olenych, J. S. Bonifacino, M. W. Davidson, J. Lippincott-Schwartz and H. F. Hess (2006). "Imaging Intracellular Fluorescent Proteins at Nanometer Resolution." Science **313**: 1642-1645.

Bixon, M. and J. Jortner (1999). "Electron transfer-from isolated molecules to biomolecules." Adv. Chem. Phys. **106**: 35-202.

Blanco-Lomas, M., S. Samanta, P. J. Campos, G. A. Woolley and D. Sampedro (2012). "Reversible Photocontrol of Peptide Conformation with a Rhodopsin-like Photoswitch." J. Am. Chem. Soc. **134**: 6960-6963.

Bloemendal, H., J. W. De, R. Jaenicke, N. H. Lubsen, C. Slingsby and A. Tardieu (2004). "Ageing and vision: structure, stability and function of lens crystallins." Prog. Biophys. Mol. Biol. **86**: 407-485.

Blomgren, F. and S. Larsson (2005). "Exploring the potential energy surface of retinal, a comparison of the performance of different methods." J. Comput. Chem. **26**: 738-742.

Born, M. and J. R. Oppenheimer (1927). "Zur quantentheorie der molekeln." Ann. Physik (Leipzig) **84**: 457.

Bortolus, P. and S. Monti (1979). "Cis-trans photoisomerization of azobenzene. Solvent and triplet donors effects." J. Phys. Chem. **83**: 648-652.

Bose, M., D. Groff, J. Xie, E. Brustad and P. G. Schultz (2006). "The incorporation of a photoisomerizable amino acid into proteins in E. coli." J. Am. Chem. Soc. **128**: 388-389.

Bossi, M. L. and P. F. Aramendia (2011). "Photomodulation of macroscopic properties." J. Photochem. Photobiol., C **12**: 154-166.

Braeuer, M., J. L. Perez-Lustres, J. Weston and E. Anders (2002). "Quantitative Reactivity Model for the Hydration of Carbon Dioxide by Biomimetic Zinc Complexes." Inorg. Chem. **41**: 1454-1463.

Brennan, C. M., R. A. Caldwell, J. E. Elbert and D. J. Unett (1994). "Nonvertical Triplet Excitation Transfer to Arylalkene Acceptors: Further Evidence That Double Bond Torsion Is Unimportant." J. Am. Chem. Soc. **116**: 3460-3464.

Brown, E. V. and G. R. Granneman (1975). "Cis-trans isomerism in the pyridyl analogs of azobenzene. Kinetic and molecular orbital analysis." J. Am. Chem. Soc. **97**: 621-627.

Bucksbaum, P. H. (2007). "The Future of Attosecond Spectroscopy." Science **317**: 766-769.

Bylina, A. and Z. R. Grabowski (1969). "Photo-isomerization and the triplet state of stilbene." Trans. Faraday Soc. **65**: 458-463.

Caldwell, R. A., S. J. Riley, A. A. Gorman, S. P. McNeeney and D. J. Unett (1992). "Relaxed triplet energies of phenylnorbornenes. The role of phenyl-vinyl torsions. Origin of nonvertical triplet excitation transfer." J. Am. Chem. Soc. **114**: 4424-4426.

Callegari, A. J. and T. J. Kelly (2006). "UV irradiation induces a postreplication DNA damage checkpoint." Proc. Natl. Acad. Sci. U. S. A. **103**: 15877-15882.

Cantor, C. R. and P. R. Schimmel (1980). "Biophysical Chemistry: The Behavior of Biological Macromolecules; W. H. Freeman & Co.: San Francisco, CA."

Cao, C., G. Chen and Z. Yin (2008). "Excited-state substituent constants σexCC from substituted benzenes." J. Phys. Org. Chem. **21**: 808-815.

Catalan, J. and J. Saltiel (2001). "On the Origin of Nonvertical Triplet Excitation Transfer: The Relative Role of Double-Bond and Phenyl-Vinyl Torsions in the Stilbenes." J. Phys. Chem. A **105**: 6273-6276.

Cavalieri, A. L., N. Mueller, T. Uphues, V. S. Yakovlev, A. Baltuska, B. Horvath, B. Schmidt, L. Bluemel, R. Holzwarth, S. Hendel, M. Drescher, U. Kleineberg, P. M. Echenique, R. Kienberger, F. Krausz and U. Heinzmann (2007). "Attosecond spectroscopy in condensed matter." Nature **449**: 1029-1032.

Celani, P., M. A. Robb, M. Garavelli, F. Bernardi and M. Olivucci (1995). "Geometry Optimisation on a Hypersphere: Application to Finding Reaction Paths from a Conical Intersection." Chem. Phys. Lett. **243**: 1-8.

Celani, P. and H.-J. Werner (2003). "Analytical energy gradients for internally contracted second-order multireference perturbation theory." J. Chem. Phys. **119**: 5044-5057.

Cembran, A., F. Bernardi, M. Garavelli, L. Gagliardi and G. Orlandi (2004). "On the Mechanism of the cis-trans Isomerization in the Lowest Electronic States of Azobenzene: S0, S1, and T1." J. Am. Chem. Soc. **126**: 3234-3243.

Cembran, A., R. Gonzalez-Luque, P. Altoe, M. Merchan, F. Bernardi, M. Olivucci and M. Garavelli (2005). "Structure, Spectroscopy, and Spectral Tuning of the Gas-Phase Retinal Chromophore: The β-Ionone "Handle" and Alkyl Group Effect." J. Phys. Chem. A **109**: 6597-6605.

Cembran, A., R. Gonzalez-Luque, L. Serrano-Andres, M. Merchan and M. Garavelli (2007). "About the intrinsic photochemical properties of the 11-cis retinal chromophore: computational clues for a trap state and a lever effect in Rhodopsin catalysis." Theor. Chem. Acc. **118**: 173-183.

Ceron-Carrasco, J. P., A. Requena, C. Michaux, E. A. Perpete and D. Jacquemin (2009). "Effects of Hydration on the Proton Transfer Mechanism in the Adenine-Thymine Base Pair." J. Phys. Chem. A **113**: 7892-7898.

Ceron-Carrasco, J. P., A. Requena, J. Zuniga, C. Michaux, E. A. Perpete and D. Jacquemin (2009). "Intermolecular Proton Transfer in Microhydrated Guanine-Cytosine Base Pairs: a New Mechanism for Spontaneous Mutation in DNA." J. Phys. Chem. A **113**: 10549-10556.

Ciminelli, C., G. Granucci and M. Persico (2004). "The photoisomerization mechanism of azobenzene: A semiclassical simulation of nonadiabatic dynamics." Chem.--Eur. J. **10**: 2327-2341.

Clark, J. I. (1994). Principle and Practice of Ophthalmology; Saunders College Publishing: Philadelphia, PA: 114−123.

Conti, I., M. Garavelli and G. Orlandi (2008). "The Different Photoisomerization Efficiency of Azobenzene in the Lowest nπ* and ππ* Singlets: The Role of a Phantom State." J. Am. Chem. Soc. **130**: 5216-5230.

Cramer, C. J. (2002). " Essentials of Computational Chemistry." Chichester: John Wiley & Sons, Ltd.: 153–232.

Cramer, C. J. (2004). Essentials of Computational Chemistry. Theories and Models, 2nd edition: 252-254.

Cramer, C. J. (2004). "Essentials of Computational Chemistry. Theories and Models " Ltd John Wiley and Sons, Second Edition: 205-211.

Crespo-Hernandez, C. E., B. Cohen, P. M. Hare and B. Kohler (2004). "Ultrafast Excited-State Dynamics in Nucleic Acids." Chem. Rev. (Washington, DC, U. S.) **104**: 1977-2019.

Cukier, R. I. (1996). "Proton-Coupled Electron Transfer Reactions: Evaluation of Rate Constants." J. Phys. Chem. **100**: 15428-15443.

Cukier, R. I. and D. G. Nocera (1998). "Proton-coupled electron transfer." Annu. Rev. Phys. Chem. **49**: 337-369.

Chang, C.-W., Y.-C. Lu, T.-T. Wang and E. W.-G. Diau (2004). "Photoisomerization Dynamics of Azobenzene in Solution with S1 Excitation: A Femtosecond Fluorescence Anisotropy Study." J. Am. Chem. Soc. **126**: 10109-10118.

Charton, M. (1981). "Electrical effect substituent constants for correlation analysis." Prog. Phys. Org. Chem. **13**: 119-251.

Davis, D. A., A. Hamilton, J. Yang, L. D. Cremar, G. D. Van, S. L. Potisek, M. T. Ong, P. V. Braun, T. J. Martinez, S. R. White, J. S. Moore and N. R. Sottos (2009). "Force-induced activation of covalent bonds in mechanoresponsive polymeric materials." Nature **459**: 68-72.

de Oliveira, M. G., S. M. Shishido, A. B. Seabra and N. H. Morgon (2002). "Thermal stability of primary S-nitrosothiols: Roles of autocatalysis and structural effects on the rate of nitric oxide release." J. Phys. Chem. A **106**: 8963-8970.

De Vico, L., C. S. Page, M. Garavelli, F. Bernardi, R. Basosi and M. Olivucci (2002). "Reaction path analysis of the "tunable" photoisomerization selectivity of free and locked retinal chromophores." J. Am. Chem. Soc. **124**: 4124-4134.

Decornez, H. and S. Hammes-Schiffer (2000). "Model Proton-Coupled Electron Transfer Reactions in Solution: Predictions of Rates, Mechanisms, and Kinetic Isotope Effects." J. Phys. Chem. A **104**: 9370-9384.

Dexter, D. L. (1953). "A theory of sensitized luminescence in solids." J. Chem. Phys. **21**: 836-850.

Dobson, C. M. and P. J. Hore (1998). "Kinetic studies of protein folding using NMR spectroscopy." Nat. Struct. Biol. **5**: 504-507.

Dong, S.-L., M. Loeweneck, T. E. Schrader, W. J. Schreier, W. Zinth, L. Moroder and C. Renner (2006). "A photocontrolled β-hairpin peptide." Chem.-Eur. J. **12**: 1114-1120.

Dougherty, R. C. (1971). "Perturbation molecular orbital treatment of photochemical reactivity. Nonconservation of orbital symmetry in photochemical pericyclic reactions." J. Amer. Chem. Soc. **93**: 7187-7201.

Douhal, A. (2004). "Breaking, Making, and Twisting of Chemical Bonds in Gas, Liquid, and Nanocavities." Acc. Chem. Res. **37**: 349-355.

Douhal, A., S. K. Kim and A. H. Zewail (1995). "Femtosecond molecular dynamics of tautomerization in model base pairs." Nature **378**: 260-263.

Eigen, M. and L. de Maeyer (1958). "Self-dissociation and protonic charge transport in water and ice." Proc. R. Soc. London, Ser. A **247**: 505-533.

Farago, P. (1975). "Interview with Sir George Porter." J. Chem. Educ. **52**(11): 703-705.

Feringa, B. L. (2007). "The Art of Building Small: From Molecular Switches to Molecular Motors." J. Org. Chem. **72**: 6635-6652.

Fernandez-Gonzalez, M. A., M. Marazzi, A. Lopez-Delgado, F. Zapata, C. Garcia-Iriepa, D. Rivero, O. Castano, M. Temprado and L. M. Frutos (2012). "Structural Substituent Effect in the Excitation Energy of a Chromophore: Quantitative Determination and Application to S-Nitrosothiols." J. Chem. Theory Comput. **8**: 3293-3302.

Ferré, N. and J. G. Angyan (2002). "Approximate electrostatic interaction operator for QM/MM calculations." Chem. Phys. Lett. **356**: 331-339.

Fieser, L. F., M. Fieser and S. Rajagopalan (1948). "Absorption spectroscopy and the structures of the diosterols." J. Org. Chem. **13**: 800-806.

Fleming, S. A. and A. W. Jensen (1996). "Substituent Effects on the Photocleavage of Benzyl-Sulfur Bonds. Observation of the "Meta Effect"." J. Org. Chem. **61**: 7040-7044.

Flint, D. G., J. R. Kumita, O. S. Smart and G. A. Woolley (2002). "Using an azobenzene cross-linker to either increase or decrease peptide helix content upon trans-to-cis photoisomerization." Chem. Biol. **9**: 391-397.

Florian, J., V. Hrouda and P. Hobza (1994). "Proton Transfer in the Adenine-Thymine Base Pair." J. Am. Chem. Soc. **116**: 1457-1460.

Florian, J. and J. Leszczynski (1996). "Spontaneous DNA Mutations Induced by Proton Transfer in the Guanine·Cytosine Base Pairs: An Energetic Perspective." J. Am. Chem. Soc. **118**: 3010-3017.

Fores, M., M. Duran and M. Sola (1998). "Intramolecular proton transfer in the ground and the two lowest-lying singlet excited states of 1-amino-3-propenal and related species." Chem. Phys. **234**: 1-19.

Fores, M., M. Duran and M. Sola (2000). "Substituent effects on the intramolecular proton transfer in the ground and lowest-lying singlet excited states of salicylaldimine." Chem. Phys. **260**: 53-64.

Fores, M. and S. Scheiner (1999). "Effects of chemical substitution upon excited state proton transfer. Fluoroderivatives of salicylaldimine." Chem. Phys. **246**: 65-74.

Forster, T. (1946). "Energy migration and fluorescence." Naturwissenschaften **33**: 166-175.

Forster, T. (1949). "Experimental and theoretical investigation of intermolecular transfer of electron activation energy." Z. Naturforsch. **4a**: 321-327.

Forster, T. (1949). "Experiments on intermolecular transition of electron excitation energy." Z. Elektrochem. Angew. Phys. Chem. **53**: 93-99.

Förster, T. (1970). "Diabatic and adiabatic processes in photochemistry." Pure Appl. Chem. **24**: 443-449.

Frisch, M. J., G. W. Trucks, H. B. Schlegel, G. E. Scuseria, M. A. Robb, J. R. Cheeseman, J. A. Montgomery, Jr., T. Vreven, K. N. Kudin, J. C. Burant, J. M. Millam, S. S. Iyengar, J. Tomasi, V. Barone, B. Mennucci, M. Cossi, G. Scalmani, N. Rega, G. A. Petersson, H. Nakatsuji, M. Hada, M. Ehara, K. Toyota, R. Fukuda, J. Hasegawa, M. Ishida, T. Nakajima, Y. Honda, O. Kitao, H. Nakai, M. Klene, X. Li, J. E. Knox, H. P. Hratchian, J. B. Cross, C. Adamo, J. Jaramillo, R. Gomperts, R. E. Stratmann, O. Yazyev, A. J. Austin, R. Cammi, C. Pomelli, J. W. Ochterski, P. Y. Ayala, K. Morokuma, G. A. Voth, P. Salvador, J. J. Dannenberg, V. G. Zakrzewski, S. Dapprich, A. D.

Daniels, M. C. Strain, O. Farkas, D. K. Malick, A. D. Rabuck, K. Raghavachari, J. B. Foresman, J. V. Ortiz, Q. Cui, A. G. Baboul, S. Clifford, J. Cioslowski, B. B. Stefanov, G. Liu, A. Liashenko, P. Piskorz, I. Komaromi, R. L. Marin, D. J. Fox, T. Keith, M. A. Al-Laham, C. Y. Peng, A. Nanayakkara, M. Challacombe, P. M. W. Gill, B. Johnson, W. Chen, M. W. Wong, C. Gonzalez and J. A. Pople (2004). "Gaussian 03, revision C.02; Gaussian, Inc.: Wallingford, CT."

Frutos, L. M., T. Andruniow, F. Santoro, N. Ferre and M. Olivucci (2007). "Tracking the excited-state time evolution of the visual pigment with multiconfigurational quantum chemistry." Proc. Natl. Acad. Sci. U. S. A. **104**: 7764-7769.

Frutos, L. M. and O. Castaño (2005). "A new algorithm for predicting triplet-triplet energy-transfer activated complex coordinate in terms of accurate potential-energy surfaces." J. Chem. Phys. **123**: 104108/104101-104108/104111.

Frutos, L. M., O. Castaño, J. L. Andres, M. Merchan and A. U. Acuna (2004). "A theory of nonvertical triplet energy transfer in terms of accurate potential energy surfaces: The transfer reaction from π,π* triplet donors to 1,3,5,7-cyclooctatetraene." J. Chem. Phys. **120**: 1208-1216.

Frutos, L. M., A. Markmann, A. L. Sobolewski and W. Domcke (2007). "Photoinduced Electron and Proton Transfer in the Hydrogen-Bonded Pyridine-Pyrrole System." J. Phys. Chem. B **111**: 6110-6112.

Fujino, T., S. Y. Arzhantsev and T. Tahara (2001). "Femtosecond Time-Resolved Fluorescence Study of Photoisomerization of trans-Azobenzene." J. Phys. Chem. A **105**: 8123-8129.

Fujino, T. and T. Tahara (2000). "Picosecond Time-Resolved Raman Study of trans-Azobenzene." J. Phys. Chem. A **104**: 4203-4210.

Gagliardi, L., G. Orlandi, F. Bernardi, A. Cembran and M. Garavelli (2004). "A theoretical study of the lowest electronic states of azobenzene: The role of torsion coordinate in the cis-trans photoisomerization." Theor. Chem. Acc. **111**: 363-372.

Garavelli, M., P. Celani, F. Bernardi, M. A. Robb and M. Olivucci (1997). "The C5H6NH2+ Protonated Schiff Base: An ab Initio Minimal Model for Retinal Photoisomerization." J. Am. Chem. Soc. **119**: 6891-6901.

Gorostiza, P. and E. Y. Isacoff (2008). "Optical Switches for Remote and Noninvasive Control of Cell Signaling." Science **322**: 395-399.

Granucci, G. and M. Persico (2007). "Critical appraisal of the fewest switches algorithm for surface hopping." J. Chem. Phys. **126**: 134114/134111-134114/134111.

Green, M. A., K. Emery, Y. Hishikawa and W. Warta (2011). "Solar cell efficiency tables (version 37)." Prog. Photovoltaics **19**: 84-92.

Grossi, L. and P. C. Montevecchi (2002). "A kinetic study of S-nitrosothiol decomposition." Chem.--Eur. J. **8**: 380-387.

Gust, D. and T. A. Moore (1989). "Mimicking photosynthesis." Science **244**: 35-41.

Gust, D., T. A. Moore and A. L. Moore (2009). "Solar Fuels via Artificial Photosynthesis." Acc. Chem. Res. **42**: 1890-1898.

Hamm, P., S. M. Ohline and W. Zinth (1997). "Vibrational cooling after ultrafast photoisomerization of azobenzene measured by femtosecond infrared spectroscopy." J. Chem. Phys. **106**: 519-529.

Hammes-Schiffer, S. (2001). "Theoretical Perspectives on Proton-Coupled Electron Transfer Reactions." Acc. Chem. Res. **34**: 273-281.

Hammes-Schiffer, S. (2009). "Theory of Proton-Coupled Electron Transfer in Energy Conversion Processes." Acc. Chem. Res. **42**: 1881-1889.

Hammett, L. P. (1937). "Effect of structure upon the reactions of organic compounds. Benzene derivatives." J. Am. Chem. Soc. **59**: 96-103.

Hammond, G. S., J. Saltiel, A. A. Lamola, N. J. Turro, J. S. Bradshaw, D. O. Cowan, R. C. Counsell, V. Vogt and C. Dalton (1964). "Mechanisms of photochemical reactions in solution. XXII. Photochemical cis-trans isomerization." J. Am. Chem. Soc. **86**: 3197-3217.

Herz, T., P. Gedeck and T. Clark (1999). "Fast Long-Range Adiabatic Electron Transfer in a Model Polyglycine α-Helix." J. Am. Chem. Soc. **121**: 1379-1380.

Herzberg, G. and H. C. Longuet-Higgins (1963). "Intersection of potential energy surfaces in polyatomic molecules." Discuss. Faraday Soc.: 77-82.

Hess, S. T., T. P. K. Girirajan and M. D. Mason (2006). "Ultra-high resolution imaging by fluorescence photoactivation localization microscopy." Biophys. J. **91**: 4258-4272.

Hilborn, R. C. (1982). "Einstein coefficients, cross sections, f values, dipole moments, and all that." Am. J. Phys. **50**: 982-986.

Hofmann, M., C. Eggeling, S. Jakobs and S. W. Hell (2005). "Breaking the diffraction barrier in fluorescence microscopy at low light intensities by using reversibly photoswitchable proteins." Proc. Natl. Acad. Sci. U. S. A. **102**: 17565-17569.

Hohenberg, P. and W. Kohn (1964). "Inhomogeneous electron gas." Physical Review **136**: B864-B871.

Horwitz, J. (1992). "α-Crystallin can function as a molecular chaperone." Proc. Natl. Acad. Sci. U. S. A. **89**: 10449-10453.

Hratchian, H. P. and H. B. Schlegel (2004). "Accurate reaction paths using a Hessian based predictor-corrector integrator." J. Chem. Phys. **120**: 9918-9924.

Hratchian, H. P. and H. B. Schlegel (2005). "Using Hessian Updating To Increase the Efficiency of a Hessian Based Predictor-Corrector Reaction Path Following Method." J. Chem. Theory Comput. **1**: 61-69.

Irebo, T., O. Johansson and L. Hammarstroem (2008). "The rate ladder of proton-coupled tyrosine oxidation in water: a systematic dependence on hydrogen bonds and protonation state." J. Am. Chem. Soc. **130**: 9194-9195.

Ishikawa, T., T. Noro and T. Shoda (2001). "Theoretical study on the photoisomerization of azobenzene." J. Chem. Phys. **115**: 7503-7512.

James, D. A., D. C. Burns and G. A. Woolley (2001). "Kinetic characterization of ribonclease S mutants containing photoisomerizable phenylazophenylalanine residues." Protein Eng. **14**: 983-991.

Jeffrey, G. A. and W. Saenger (1991). "Hydrogen Bonding in Biological Structures; Springer-Verlag: Berlin."

Johannissen, L. O., T. Irebo, M. Sjodin, O. Johansson and L. Hammarstrom (2009). "The Kinetic Effect of Internal Hydrogen Bonds on Proton-Coupled Electron Transfer from Phenols: A Theoretical Analysis with Modeling of Experimental Data." J. Phys. Chem. B **113**: 16214-16225.

Kandori, H., Y. Shichida and T. Yoshizawa (2001). "Photoisomerization in rhodopsin." Biochemistry (Moscow) **66**: 1197-1209.

Kauzmann, W. (1957). Quantum Chemistry(Academic Press: New York, 1957): 696.

Khan, A. and S. Hecht (2006). "Towards photocontrol over the helix-coil transition in foldamers: synthesis and photoresponsive behavior of azobenzene-core amphiphilic oligo(meta-phenyleneethynylene)s." Chem.--Eur. J. **12**: 4764-4774.

Khan, A., C. Kaiser and S. Hecht (2006). "Prototype of a photoswitchable foldamer." Angew. Chem., Int. Ed. **45**: 1878-1881.

Kitaura, K. and K. Morokuma (1976). "A new energy decomposition scheme for molecular interactions within the Hartree-Fock approximation." Int. J. Quantum Chem. **10**: 325-340.

Klajn, R. (2010). "Immobilized azobenzenes for the construction of photoresponsive materials." Pure Appl. Chem. **82**: 2247-2279.

Klug, R. L. and R. Burcl (2010). "Rotational Barriers in Azobenzene and Azonaphthalene." J. Phys. Chem. A **114**: 6401-6407.

Kobori, Y. and J. R. Norris, Jr. (2006). "1D Radical Motion in Protein Pocket: Proton-Coupled Electron Transfer in Human Serum Albumin." J. Am. Chem. Soc. **128**: 4-5.

Kryger, M. J., M. T. Ong, S. A. Odom, N. R. Sottos, S. R. White, T. J. Martinez and J. S. Moore (2010). "Masked Cyanoacrylates Unveiled by Mechanical Force." J. Am. Chem. Soc. **132**: 4558-4559.

Kuhn, H. (1948). "Free-electron model for absorption spectra of organic dyes." J. Chem. Phys. **16**: 840-841.

Kuki, A. (1991). "Electronic tunneling paths in proteins." Struct. Bonding (Berlin) **75**: 49-83.

Kumita, J. R., O. S. Smart and G. A. Woolley (2000). "Photo-control of helix content in a short peptide." Proc. Natl. Acad. Sci. U. S. A. **97**: 3803-3808.

Lalevee, J., X. Allonas and J. P. Fouassier (2005). "Triplet-triplet energy transfer reaction to cis-stilbene: a dual thermal bond activation mechanism." Chem. Phys. Lett. **401**: 483-486.

Lan, Z., L. M. Frutos, A. L. Sobolewski and W. Domcke (2008). "Photochemistry of hydrogen-bonded aromatic pairs: quantum dynamical calculations for the pyrrole-pyridine complex." Proc. Natl. Acad. Sci. U. S. A. **105**: 12707-12712.

Landau, L. D. (1932). "On the theory of transfer of energy at collisions II." Phys. Z. **2**: 46.

Langhals, H., A. J. Esterbauer, A. Walter, E. Riedle and I. Pugliesi (2010). "Foerster Resonant Energy Transfer in Orthogonally Arranged Chromophores." J. Am. Chem. Soc. **132**: 16777-16782.

Lednev, I. K., T.-Q. Ye, R. E. Hester and J. N. Moore (1996). "Femtosecond Time-Resolved UV-Visible Absorption Spectroscopy of trans-Azobenzene in Solution." J. Phys. Chem. **100**: 13338-13341.

Lednev, I. K., T. Q. Ye, P. Matousek, M. Towrie, P. Foggi, F. V. R. Neuwahl, S. Umapathy, R. E. Hester and J. N. Moore (1998). "Femtosecond time-resolved UV-visible absorption spectroscopy of trans-azobenzene: dependence on excitation wavelength." Chem. Phys. Lett. **290**: 68-74.

Lenhardt, J. M., M. T. Ong, R. Choe, C. R. Evenhuis, T. J. Martinez and S. L. Craig (2010). "Trapping a Diradical Transition State by Mechanochemical Polymer Extension." Science **329**: 1057-1060.

Levine, I. N. (1991). "Quantum Chemistry." Englewood Cliffs, New jersey: Prentice Hall: 455–544.

Li, G. S., B. Maigret, D. Rinaldi and M. F. Ruiz-Lopez (1998). "Influence of environment on proton-transfer mechanisms in model triads from theoretical calculations." J. Comput. Chem. **19**: 1675-1688.

Lin, H. and D. G. Truhlar (2007). "QM/MM: what have we learned, where are we, and where do we go from here?" Theor. Chem. Acc. **117**: 185-199.

Liu, D., J. Karanicolas, C. Yu, Z. Zhang and G. A. Woolley (1997). "Site-specific incorporation of photoisomerizable azobenzene groups into ribonuclease S." Bioorg. Med. Chem. Lett. **7**: 2677-2680.

Lowdin, P. O. (1965). "Quantum genetics and the aperiodic solid. Biological problems of heredity, mutations, aging, and tumors in view of the quantum theory of the DNA molecule." Advan. Quantum Chem. **2**: 213-360.

Lu, D. and G. A. Voth (1998). "Proton Transfer in the Enzyme Carbonic Anhydrase: An ab Initio Study." J. Am. Chem. Soc. **120**: 4006-4014.

Lyon, C. E., E.-S. Suh, C. M. Dobson and P. J. Hore (2002). "Probing the Exposure of Tyrosine and Tryptophan Residues in Partially Folded Proteins and Folding Intermediates by CIDNP Pulse-Labeling." J. Am. Chem. Soc. **124**: 13018-13024.

Marazzi, M., A. Lopez-Delgado, M. A. Fernandez-Gonzalez, O. Castano, L. M. Frutos and M. Temprado (2012). "Modulating Nitric Oxide Release by S-Nitrosothiol Photocleavage: Mechanism and Substituent Effects." J. Phys. Chem. A **116**: 7039-7049.

Marazzi, M., I. Navizet, R. Lindh and L. M. Frutos (2012). "Photostability Mechanisms in Human γB-Crystallin: Role of the Tyrosine Corner Unveiled by Quantum Mechanics and Hybrid Quantum Mechanics/Molecular Mechanics Methodologies." J. Chem. Theory Comput. **8**: 1351-1359.

Marazzi, M., U. Sancho, O. Castano, W. Domcke and L. M. Frutos (2010). "Photoinduced Proton Transfer as a Possible Mechanism for Highly Efficient Excited-State Deactivation in Proteins." J. Phys. Chem. Lett. **1**: 425-428.

Marazzi, M., U. Sancho, O. Castano and L. M. Frutos (2011). "First principles study of photostability within hydrogen-bonded amino acids." Phys. Chem. Chem. Phys. **13**: 7805-7811.

Marazzi, M., A. Valentini, M. Olivucci and L. M. Frutos (2012). In preparation.

Marcus, R. A. and H. Eyring (1964). "Chemical and electrochemical electron-transfer theory." Annu. Rev. Phys. Chem. **15**: 155-196.

Martyna, G. J., M. E. Tuckerman, D. J. Tobias and M. L. Klein (1996). "Explicit reversible integrators for extended systems dynamics." Mol. Phys. **87**: 1117-1157.

Matsui, T., T. Sato, Y. Shigeta and K. Hirao (2009). "Sequence-dependent proton-transfer reaction in stacked GC pair II: The origin of stabilities of proton-transfer products." Chem. Phys. Lett. **478**: 238-242.

Matsui, T., Y. Shigeta and K. Hirao (2007). "Multiple Proton-Transfer Reactions in DNA Base Pairs by Coordination of Pt Complex." J. Phys. Chem. B **111**: 1176-1181.

Mayer, G. and A. Heckel (2006). "Biologically active molecules with a "Light switch"." Angew. Chem., Int. Ed. **45**: 4900-4921.

McEwen, J. and K. Yates (1991). "Substituent effects in the photohydration of styrenes and phenylacetylenes. An attempt to establish a σhν scale for excited-state reactions." J. Phys. Org. Chem. **4**: 193-206.

Merck, K. B., P. J. T. A. Groenen, C. E. M. Voorter, H.-H. W. A. De, J. Horwitz, H. Bloemendal and J. W. W. De (1993). "Structural and functional similarities of bovine α-crystallin and mouse small heat-shock protein. A family of chaperones." J. Biol. Chem. **268**: 1046-1052.

Molcas/Tinker QM/MM (2012). http://sites.univ-provence.fr/lcp-ct/ferre/nf_tinker_qmmm.html (accessed Sep 12, 2012).

Molina, V., M. Merchan and B. O. Roos (1999). "A theoretical study of the electronic spectrum of cis-stilbene." Spectrochim. Acta, Part A **55A**: 433-446.

Monguzzi, A., J. Mezyk, F. Scotognella, R. Tubino and F. Meinardi (2008). "Upconversion-induced fluorescence in multicomponent systems: steady-state excitation power threshold." Phys. Rev. B: Condens. Matter Mater. Phys. **78**: 195112/195111-195112/195115.

Monti, S., G. Orlandi and P. Palmieri (1982). "Features of the photochemically active state surfaces of azobenzene." Chem. Phys. **71**: 87-99.

Moore, A. L., A. Joy, R. Tom, D. Gust, T. A. Moore, R. V. Bensasson and E. J. Land (1982). "Photoprotection by carotenoids during photosynthesis: motional dependence of intramolecular energy transfer." Science **216**: 982-984.

Moore, G. F., M. Hambourger, M. Gervaldo, O. G. Poluektov, T. Rajh, D. Gust, T. A. Moore and A. L. Moore (2008). "A bioinspired construct that mimics the proton coupled electron transfer between P680•+ and the TyrZ-His190 pair of photosystem II." J. Am. Chem. Soc. **130**: 10466-10467.

Muñoz-Losa, A., C. Curutchet, B. P. Krueger, L. R. Hartsell and B. Mennucci (2009). "Fretting about FRET: failure of the ideal dipole approximation." Biophys. J. **96**: 4779-4788.

Muranaka, N., T. Hohsaka and M. Sisido (2002). "Photoswitching of peroxidase activity by position-specific incorporation of a photoisomerizable non-natural amino acid into horseradish peroxidase." FEBS Lett. **510**: 10-12.

Naegele, T., R. Hoche, W. Zinth and J. Wachtveitl (1997). "Femtosecond photoisomerization of cis-azobenzene." Chem. Phys. Lett. **272**: 489-495.

Nakamichi, H., V. Buss and T. Okada (2007). "Photoisomerization mechanism of rhodopsin and 9-cis-rhodopsin revealed by X-ray crystallography." Biophys. J. **92**: L106-L108.

Nakayama, K., M. Endo and T. Majima (2004). "Photochemical regulation of the activity of an endonuclease BamHI using an azobenzene moiety incorporated site-selectively into the dimer interface." Chem. Commun. : 2386-2387.

Naqvi, K. R. and C. Steel (1970). "Exchange-induced resonance energy transfer." Chem. Phys. Lett. **6**: 29-32.

Ni, T., R. A. Caldwell and L. A. Melton (1989). "The relaxed and spectroscopic energies of olefin triplets." J. Am. Chem. Soc. **111**: 457-464.

Nicholson, M. M. (1993). "Phthalocyanine. Properties and Applications." Eds.; VCH: New York, Vol. 3: 71.

Nienhaus, G. U. (2008). "The green fluorescent protein: a key tool to study chemical processes in living cells." Angew. Chem., Int. Ed. **47**: 8992-8994.

Nir, E., K. Kleinermanns and V. M. S. de (2000). "Pairing of isolated nucleic-acid bases in the absence of the DNA backbone." Nature (London) **408**: 949-950.

Oyster, C. W. (1999). The Human Eye: Structure and Function; Sinauer Associates: Sunderland, MA: 595−647.

Page, C. S. and M. Olivucci (2003). "Ground and excited state CASPT2 geometry optimizations of small organic molecules." J. Comput. Chem. **24**: 298-309.

Pal, S. K. and A. H. Zewail (2004). "Dynamics of Water in Biological Recognition." Chem. Rev. **104**: 2099-2123.

Paterson, M. J., M. A. Robb, L. Blancafort and A. D. DeBellis (2005). "Mechanism of an Exceptional Class of Photostabilizers: A Seam of Conical Intersection Parallel to Excited State Intramolecular Proton Transfer (ESIPT) in o-Hydroxyphenyl-(1,3,5)-triazine." J. Phys. Chem. A **109**: 7527-7537.

Pauling, L. and R. B. Corey (1951). "Configurations of polypeptide chains with favored orientations around single bonds: two new pleated sheets." Proc. Natl. Acad. Sci. U. S. A. **37**: 729-740.

Pearson, D., N. Alexander and A. D. Abell (2008). "Improved photocontrol of alpha-chymotrypsin activity: peptidomimetic trifluoromethylketone photoswitch enzyme inhibitors." Chemistry **14**: 7358-7365.

Pederzoli, M., J. Pittner, M. Barbatti and H. Lischka (2011). "Nonadiabatic Molecular Dynamics Study of the cis-trans Photoisomerization of Azobenzene Excited to the S1 State." J. Phys. Chem. A **115**: 11136-11143.

Ramamurthy, V. and R. S. H. Liu (1976). "Photochemistry of polyenes. IX. Excitation, relaxation, and deactivation of dienes, trienes, and higher polyenes in the vitamin A series in the sensitized isomerization reaction." J. Am. Chem. Soc. **98**: 2935-2942.

Reineke, S., F. Lindner, G. Schwartz, N. Seidler, K. Walzer, B. Luessem and K. Leo (2009). "White organic light-emitting diodes with fluorescent tube efficiency." Nature **459**: 234-238.

Renner, C. and L. Moroder (2006). "Azobenzene as conformational switch in model peptides." ChemBioChem **7**: 868-878.

Roos, B. O. (1987). "Advanced Chemistry and Physics: Ab Initio Methods in Quantum Chemistry II." ed Lawley KP (Wiley, Chicester, UK): 399–445.

Russew, M.-M. and S. Hecht (2010). "Photoswitches: from Molecules to Materials." Adv. Mater. **22**: 3348-3360.

Sadlej-Sosnowska, N. and M. Kijak (2012). "Excited state substituent constants: to Hammett or not?" Struct. Chem. **23**: 359-365.

Sadovski, O., A. A. Beharry, F. Zhang and G. A. Woolley (2009). "Spectral tuning of azobenzene photoswitches for biological applications." Angew. Chem., Int. Ed. **48**: 1484-1486.

Sakurai, J. J. (1967). "Advanced Quantum Mechanics (Chapter: Emission and Absorption of Photons by Atoms)." Addison-Wesley, Reading MA.

Salem, L. (1974). "Surface crossings and surface touchings in photochemistry." J. Amer. Chem. Soc. **96**: 3486-3501.

Saltiel, J. and B. W. Atwater (1988). "Spin-statistical factors in diffusion-controlled reactions." Adv. Photochem. **14**: 1-90.

Saltiel, J. and G. S. Hammond (1963). "Mechanisms of photochemical reactions in solution. XVII. Cis-trans isomerization of the stilbenes by excitation transfer from low-energy sensitizers." J. Am. Chem. Soc. **85**: 2515-2516.

Saltiel, J., J. E. Mace, L. P. Watkins, D. A. Gormin, R. J. Clark and O. Dmitrenko (2003). "Biindanylidenes: Role of Central Bond Torsion in Nonvertical Triplet Excitation Transfer to the Stilbenes." J. Am. Chem. Soc. **125**: 16158-16159.

Saltiel, J., G. R. Marchand, E. Kirkor-Kaminska, W. K. Smothers, W. B. Mueller and J. L. Charlton (1984). "Nonvertical triplet excitation transfer to cis- and trans-stilbene." J. Am. Chem. Soc. **106**: 3144-3151.

Samoylova, E., W. Radloff, H.-H. Ritze and T. Schultz (2009). "Observation of Proton Transfer in 2-Aminopyridine Dimer by Electron and Mass Spectroscopy." J. Phys. Chem. A **113**: 8195-8201.

Sampedro, D., A. Migani, A. Pepi, E. Busi, R. Basosi, L. Latterini, F. Elisei, S. Fusi, F. Ponticelli, V. Zanirato and M. Olivucci (2004). "Design and Photochemical Characterization of a Biomimetic Light-Driven Z/E Switcher." J. Am. Chem. Soc. **126**: 9349-9359.

Satzger, H., C. Root and M. Braun (2004). "Excited-State Dynamics of trans- and cis-Azobenzene after UV Excitation in the ππ* Band." J. Phys. Chem. A **108**: 6265-6271.

Sauer, M. (2005). "Reversible molecular photoswitches: A key technology for nanoscience and fluorescence imaging." Proc. Natl. Acad. Sci. U. S. A. **102**: 9433-9434.

Schapiro, I., M. N. Ryazantsev, L. M. Frutos, N. Ferre, R. Lindh and M. Olivucci (2011). "The Ultrafast Photoisomerizations of Rhodopsin and Bathorhodopsin Are Modulated by Bond Length Alternation and HOOP Driven Electronic Effects." J. Am. Chem. Soc. **133**: 3354-3364.

Schapiro, I., O. Weingart and V. Buss (2009). "Bicycle-pedal isomerization in a rhodopsin chromophore model." J. Am. Chem. Soc. **131**: 16-17.

Schierling, B., A.-J. Noel, W. Wende, L. T. Hien, E. Volkov, E. Kubareva, T. Oretskaya, M. Kokkinidis, A. Roempp, B. Spengler and A. Pingoud (2010). "Controlling the enzymatic activity of a restriction enzyme by light." Proc. Natl. Acad. Sci. U. S. A. **107**: 1361-1366, S1361/1361-S1361/1364.

Schlegel, H. B. (1987). "Ab Initio Methods in Quantum Chemistry." Lawley, K. P., Ed.; John Wiley &Sons; Ltd.: New York **1**: 249-286.

Schrader, T. E., W. J. Schreier, T. Cordes, F. O. Koller, G. Babitzki, R. Denschlag, C. Renner, M. Loweneck, S.-L. Dong, L. Moroder, P. Tavan and W. Zinth (2007). "Light-triggered β-hairpin folding and unfolding." Proc. Natl. Acad. Sci. U. S. A. **104**: 15729-15734.

Schreier, W. J., T. E. Schrader, F. O. Koller, P. Gilch, C. E. Crespo-Hernandez, V. N. Swaminathan, T. Carell, W. Zinth and B. Kohler (2007). "Thymine Dimerization in DNA Is an Ultrafast Photoreaction." Science (Washington, DC, U. S.) **315**: 625-629.

Schultz, T., E. Samoylova, W. Radloff, I. V. Hertel, A. L. Sobolewski and W. Domcke (2004). "Efficient deactivation of a model base pair via excited-state hydrogen transfer." Science **306**: 1765-1768.

Sekhar, V. C. and B. V. Plapp (1988). "Mechanism of binding of horse liver alcohol dehydrogenase and nicotinamide adenine dinucleotide." Biochemistry **27**: 5082-5088.

Sekiya, H. and K. Sakota (2008). "Excited-state double-proton transfer in a model DNA base pair: Resolution for stepwise and concerted mechanism controversy in the 7-azaindole dimer revealed by frequency- and time-resolved spectroscopy." J. Photochem. Photobiol., C **9**: 81-91.

Send, R. and D. Sundholm (2007). "Coupled-cluster studies of the lowest excited states of the 11-cis-retinal chromophore." Phys. Chem. Chem. Phys. **9**: 2862-2867.

Send, R. and D. Sundholm (2007). "The role of the β-ionone ring in the photochemical reaction of rhodopsin." J. Phys. Chem. A **111**: 27-33.

Send, R. and D. Sundholm (2007). "Stairway to the conical intersection: a computational study of the retinal isomerization." J. Phys. Chem. A **111**: 8766-8773.

Send, R., D. Sundholm, M. P. Johansson and F. Pawlowski (2009). "Excited State Potential Energy Surfaces of Polyenes and Protonated Schiff Bases." J. Chem. Theory Comput. **5**: 2401-2414.

Serrano-Andres, L. and M. P. Fülscher (1998). "Theoretical Study of the Electronic Spectroscopy of Peptides. III. Charge-Transfer Transitions in Polypeptides." J. Am. Chem. Soc. **120**: 10912-10920.

Serrano-Andres, L. and M. P. Fülscher (2001). "Charge Transfer Transitions in Neutral and Ionic Polypeptides: A Theoretical Study." J. Phys. Chem. B **105**: 9323-9330.

Serrano-Andres, L., M. Merchan and R. Lindh (2005). "Computation of conical intersections by using perturbation techniques." J. Chem. Phys. **122**: 104107/104101-104107/104110.

Servaites, J. D., M. A. Ratner and T. J. Marks (2011). "Organic solar cells: A new look at traditional models." Energy Environ. Sci. **4**: 4410-4422.

Service, R. F. (2011). "Solar energy. Outlook brightens for plastic solar cells." Science **332**: 293.

Shaner, N. C., G. H. Patterson and M. W. Davidson (2007). "Advances in fluorescent protein technology." J. Cell Sci. **120**: 4247-4260.

Shemesh, D., C. Hättig and W. Domcke (2009). "Photophysics of the Trp-Gly dipeptide: Role of electron and proton transfer processes for efficient excited-state deactivation." Chem. Phys. Lett. **482**: 38-43.

Shemesh, D., A. L. Sobolewski and W. Domcke (2009). "Efficient excited-state deactivation of the Gly-Phe-Ala tripeptide via an electron-driven proton-transfer process." J. Am. Chem. Soc. **131**: 1374-1375.

Shemesh, D., A. L. Sobolewski and W. Domcke (2010). "Role of excited-state hydrogen detachment and hydrogen-transfer processes for the excited-state deactivation of an aromatic dipeptide: N-acetyl tryptophan methyl amide." Phys. Chem. Chem. Phys. **12**: 4899-4905.

Shim, S. C., J. W. Park and H. S. Ham (1982). "The new substituent constants in the excited states." Bull. Korean Chem. Soc. **3**: 13-18.

Shim, S. C., J. W. Park, H. S. Ham and J. S. Chung (1983). "The new substituent constants in the excited states. (II)." Bull. Korean Chem. Soc. **4**: 45-47.

Siampiringue, N., G. Guyot, S. Monti and P. Bortolus (1987). "The cis → trans photoisomerization of azobenzene: an experimental re-examination." J. Photochem. **37**(.): 185-188.

Sinicropi, A., C. Bernini, R. Basosi and M. Olivucci (2009). "A novel biomimetic photochemical switch at work: design of a photomodulable peptide." Photochem. Photobiol. Sci. **8**: 1639-1649.

Sjöedin, M., S. Styring, H. Wolpher, Y. Xu, L. Sun and L. Hammarstroem (2005). "Switching the Redox Mechanism: Models for Proton-Coupled Electron Transfer from Tyrosine and Tryptophan." J. Am. Chem. Soc. **127**: 3855-3863.

Smirnova, O. (2010). "Attosecond prints of electrons." Nature **466**: 700-702.

Smitienko, O. A., M. N. Mozgovaya, I. V. Shelaev, F. E. Gostev, T. B. Feldman, V. A. Nadtochenko, O. M. Sarkisov and M. A. Ostrovsky (2010). "Femtosecond formation dynamics of primary photoproducts of visual pigment rhodopsin." Biochemistry (Moscow) **75**(.): 25-35.

Sobolewski, A. L. and W. Domcke (2004). "Ab initio studies on the photophysics of the guanine-cytosine base pair." Phys. Chem. Chem. Phys. **6**: 2763-2771.

Sobolewski, A. L. and W. Domcke (2006). "Relevance of electron-driven proton-transfer processes for the photostability of proteins." ChemPhysChem **7**: 561-564.

Sobolewski, A. L. and W. Domcke (2007). "Computational Studies of the Photophysics of Hydrogen-Bonded Molecular Systems." J. Phys. Chem. A **111**: 11725-11735.

Sobolewski, A. L., W. Domcke and C. Hattig (2005). "Tautomeric selectivity of the excited-state lifetime of guanine/cytosine base pairs: The role of electron-driven proton-transfer processes." Proc. Natl. Acad. Sci. U. S. A. **102**: 17903-17906.

Soudackov, A. and S. Hammes-Schiffer (1999). "Multistate continuum theory for multiple charge transfer reactions in solution." J. Chem. Phys. **111**: 4672-4687.

Soudackov, A. and S. Hammes-Schiffer (1999). "Theoretical Study of Photoinduced Proton-Coupled Electron Transfer through Asymmetric Salt Bridges." J. Am. Chem. Soc. **121**: 10598-10607.

Soudackov, A. and S. Hammes-Schiffer (2000). "Derivation of rate expressions for nonadiabatic proton-coupled electron transfer reactions in solution." J. Chem. Phys. **113**: 2385-2396.

Stamler, J. S., O. Jaraki, J. Osborne, D. I. Simon, J. Keaney, J. Vita, D. Singel, C. R. Valeri and J. Loscalzo (1992). "Nitric oxide circulates in mammalian plasma primarily as an S-nitroso adduct of serum albumin." Proc. Natl. Acad. Sci. U. S. A. **89**: 7674-7677.

Swain, C. G. and E. C. Lupton, Jr. (1968). "Field and resonance components of substituent effects." J. Amer. Chem. Soc. **90**: 4328-4337.

Szymczak, J. J., M. Barbatti and H. Lischka (2008). "Mechanism of Ultrafast Photodecay in Restricted Motions in Protonated Schiff Bases: The Pentadieniminium Cation." J. Chem. Theory Comput. **4**: 1189-1199.

Szymczak, J. J., M. Barbatti and H. Lischka (2009). "Is the Photoinduced Isomerization in Retinal Protonated Schiff Bases a Single- or Double-Torsional Process?" J. Phys. Chem. A **113**: 11907-11918.

Taft, R. W., Jr. (1952). "Linear free-energy relationships from rates of esterification and hydrolysis of aliphatic and ortho-substituted benzoate esters." J. Am. Chem. Soc. **74**: 2729-2732.

Taft, R. W., Jr. (1952). "Polar and steric substituent constants for aliphatic and o-benzoate groups from rates of esterification and hydrolysis of esters." J. Am. Chem. Soc. **74**: 3120-3128.

Taft, R. W., Jr. (1953). "Linear steric energy relationships." J. Am. Chem. Soc. **75**: 4538-4539.

Tautermann, C. S., M. J. Loferer, A. F. Voegele and K. R. Liedl (2003). "About the Kinetic Feasibility of the Lipscomb Mechanism in Human Carbonic Anhydrase II." J. Phys. Chem. B **107**: 12013-12020.

Teller, E. (1937). "Crossing of potential surfaces." J. Phys. Chem. **41**: 109-116.

Therien, M. J., J. Chang, A. L. Raphael, B. E. Bowler and H. B. Gray (1991). "Long-range electron transfer in metalloproteins." Struct. Bonding (Berlin) **75**: 109-129.

Thrush, B. A. (2003). "The genesis of flash photolysis." Photochem. Photobiol. Sci. **2**: 453-454.

Tinker Molecular Modeling (2012). version 5.1; http://dasher.wustl.edu/tinker/ (accessed Sep 12, 2012).

Toniolo, A., C. Ciminelli, M. Persico and T. J. Martinez (2005). "Simulation of the photodynamics of azobenzene on its first excited state: Comparison of full multiple spawning and surface hopping treatments." J. Chem. Phys. **123**: 234308/234301-234308/234310.

Tuckerman, M. E., Y. Liu, G. Ciccotti and G. J. Martyna (2001). "Non-Hamiltonian molecular dynamics: Generalizing Hamiltonian phase

space principles to non-Hamiltonian systems." J. Chem. Phys. **115**: 1678-1702.

Tully, J. C. (1990). "Molecular dynamics with electronic transitions." J. Chem. Phys. **93**: 1061-1071.

Turro, N. J., V. Ramamurthy and J. C. Scaiano (2009). "Principles of Molecular Photochemistry: An Introduction." University Science Books. Sausalito, California.

Umeyama, H., S. Hirono and S. Nakagawa (1984). "Charge state of His-57-Asp-102 couple in a transition state analog-trypsin complex: a molecular orbital study." Proc. Natl. Acad. Sci. U. S. A. **81**: 6266-6270.

Valsson, O. and C. Filippi (2010). "Photoisomerization of Model Retinal Chromophores: Insight from Quantum Monte Carlo and Multiconfigurational Perturbation Theory." J. Chem. Theory Comput. **6**: 1275-1292.

van Boekel, M. A. M., S. E. A. Hoogakker, J. J. Harding and W. W. De Jong (1996). "The influence of some post-translational modifications on the chaperone-like activity of α-crystallin." Ophthalmic Res. **28**: 32-38.

Van Houten, J. (2002). "A century of chemical dynamics traced through the Nobel Prizes. 1." J. Chem. Educ. **79**: 548-550.

von Neumann, J. and E. P. Wigner (1929). "Über merkwürdige diskrete eigenwerte." Z. Physik **30**: 465-467.

Vullev, V. I. and G. Jones, II (2002). "Photoinduced charge transfer in helical polypeptides." Res. Chem. Intermed. **28**: 795-815.

Vura-Weis, J., S. H. Abdelwahed, R. Shukla, R. Rathore, M. A. Ratner and M. R. Wasielewski (2010). "Crossover from Single-Step Tunneling to Multistep Hopping for Molecular Triplet Energy Transfer." Science **328**: 1547-1550.

Wanko, M., M. Garavelli, F. Bernardi, T. A. Niehaus, T. Frauenheim and M. Elstner (2004). "A global investigation of excited state surfaces within time-dependent density-functional response theory." J. Chem. Phys. **120**: 1674-1692.

Wanko, M., M. Hoffmann, P. Strodel, A. Koslowski, W. Thiel, F. Neese, T. Frauenheim and M. Elstner (2005). "Calculating Absorption Shifts for Retinal Proteins: Computational Challenges." J. Phys. Chem. B **109**: 3606-3615.

Warshel, A., G. Naray-Szabo, F. Sussman and J. K. Hwang (1989). "How do serine proteases really work?" Biochemistry **28**: 3629-3637.

Watson, J. D. (1965). "Molecular Biology of the Gene: The Importance of Weak Interactions; Benjamin: New York.".

Watson, J. D. and F. H. C. Crick (1953). "Molecular structure of nucleic acids. A structure for deoxyribose nucleic acid." Nature **171**: 737-738.

Wehry, E. L. and L. B. Rogers (1965). "Application of linear free energy relations to electronically excited states of monosubstituted phenols." J. Am. Chem. Soc. **87**: 4234-4238.

Weingart, O. (2007). "The Twisted C11:C12 Bond of the Rhodopsin Chromophore - A Photochemical Hot Spot." J. Am. Chem. Soc. **129**: 10618-10619.

Westmark, P. R., J. P. Kelly and B. D. Smith (1993). "Photoregulation of enzyme activity. Photochromic, transition-state-analog inhibitors of cysteine and serine proteases." J. Am. Chem. Soc. **115**: 3416-3419.

Windsor, M. W. (2003). "Flash photolysis and triplet states and free radicals in solution." Photochem. Photobiol. Sci. **2**: 455-458.

Wittig, C. (2005). "The Landau-Zener Formula." J. Phys. Chem. B **109**: 8428-8430.

Wolinski, K. and J. Baker (2009). "Theoretical predictions of enforced structural changes in molecules." Mol. Phys. **107**: 2403-2417.

Wolinski, K. and J. Baker (2010). "Geometry optimization in the presence of external forces: a theoretical model for enforced structural changes in molecules." Mol. Phys. **108**: 1845-1856.

Woodward, R. B. (1941). "Structure and the absorption spectra of α,β-unsaturated ketones." J. Am. Chem. Soc. **63**: 1123-1126.

Woolley, G. A. (2005). "Photocontrolling peptide alpha helices." Acc Chem Res **38**: 486-493.

Ye, Y. J. and J. Ladik (1993). "Theory of hopping conductivity in pig insulin." Phys. Rev. B: Condens. Matter **48**: 5120-5126.

Yu, Z. and S. Hecht (2011). "Reversible and Quantitative Denaturation of Amphiphilic Oligo(azobenzene) Foldamers." Angew. Chem., Int. Ed. **50**: 1640-1643.

Yu, Z. and S. Hecht (2012). "Cooperative Switching Events in Azobenzene Foldamer Denaturation." Chem.--Eur. J. **18**: 10519-10524.

Yukawa, Y. and Y. Tsuno (1959). "Resonance effect in Hammett relation. II. Sigma constants in electrophilic reactions and their intercorrelation." Bull. Chem. Soc. Jpn. **32**: 965-971.

Zaari, R. R. and S. Y. Y. Wong (2009). "Photoexcitation of 11-Z-cis-7,8-dihydro retinal and 11-Z-cis retinal: A comparative computational study." Chem. Phys. Lett. **469**: 224-228.

Zapata, F., O. Castaño and L. M. Frutos (2012). "Photoinduced Singlet Oxygen Formation from Triplet Porphyrin: a Molecular Study " To be submitted.

Zener, C. (1932). "Non-Adiabatic Crossing of Energy Levels." Proc. R. Soc. London A **137**: 696-702.

Zener, C. (1932). "Non-Adiabatic Crossing of Energy Levels." Proc. R. Soc. London A **137**: 696.

Zhang, F., Y.-J. Ai, Y. Luo and W.-H. Fang (2009). "Nonradiative decay of the lowest excited singlet state of 2-aminopyridine is considerably faster than the radiative decay." J. Chem. Phys. **130**: 144315/144311-144315/144315.

Zimmerman, H. E. (1966). "Molecular orbital correlation diagrams, Moebius systems, and factors controlling ground- and excited-state reactions. II." J. Am. Chem. Soc. **88**: 1566-1567.

Zundel, G. (1992). "Proton polarizability and proton transfer processes in hydrogen bonds and cation polarizabilities of other cation bonds - their importance to understand molecular processes in electrochemistry and biology." Trends Phys. Chem. **3**: 129-156.